Heavy flavour azimuthal correlations from small to large systems

Ph.D. Thesis

By

RAVINDRA SINGH

DEPARTMENT OF PHYSICS

INDIAN INSTITUTE OF TECHNOLOGY INDORE

APRIL 2023

Heavy flavour azimuthal correlations from small to large systems

A THESIS

Submitted in partial fulfillment of the
requirements for the award of the degree
of
DOCTOR OF PHILOSOPHY

by

RAVINDRA SINGH

DEPARTMENT OF PHYSICS
INDIAN INSTITUTE OF TECHNOLOGY INDORE
APRIL 2023

INDIAN INSTITUTE OF TECHNOLOGY INDORE

I hereby certify that the work which is being presented in the thesis entitled **Heavy flavour azimuthal correlations from small to large systems** in the partial fulfillment of the requirements for the award of the degree of **DOCTOR OF PHILOSOPHY** and submitted in the **DEPARTMENT OF PHYSICS, Indian Institute of Technology Indore**, is an authentic record of my own work carried out during the time period from **December 2017** to **February 2023** under the supervision of **Prof. Ankhi Roy,** Professor, Indian Institute of Technology Indore.

The matter presented in this thesis has not been submitted by me for the award of any other degree of this or any other institute.

Signature of the student with date
(RAVINDRA SINGH)

This is to certify that the above statement made by the candidate is correct to the best of my knowledge.

Ankhi Ray
03/07/2023
Signature of Thesis Supervisor with date
(Dr. ANKHI ROY)

Mr. RAVINDRA SINGH has successfully given his Ph.D. Oral Examination held on 30/06/2023

Ankhi Ray
03/07/2023
Signature of Thesis Supervisor with date
(Dr. ANKHI ROY)

With heartfelt gratitude, I dedicate my thesis to my beloved family, whose unwavering support and encouragement have been my guiding light throughout this journey. To my friends and collaborators, your invaluable contributions and shared passion have shaped this work, fostering growth and inspiration. Finally, to the wondrous nature, captivating physics, and vast universe that continue to unveil their secrets, this thesis stands as a humble tribute to their boundless marvels.

"उद्यमेन हि सिध्यन्ति कार्याणि न मनोरथैः।

न हि सुप्तस्य सिंहस्य प्रविशंति मुखे मृगाः॥" Sanskrit

Meaning: "Through effort, actions are accomplished, not by mere desire. Even the animals do not enter the mouth of a sleeping lion."

ACKNOWLEDGEMENTS

My Ph.D. journey was incredible, and I attribute much of my success to the support and guidance of several individuals. Firstly, I am thankful to my mentor, Dr. Balram Tripathi, and Shiv Shakti Singh, as well as the head of the physics department, Subodh P.G. College, Dr. Subhash C. Agarwal, who encouraged and directed me towards pursuing a Ph.D. degree. Without their support, I may not have pursued this path.

I am also grateful to my supervisor, Prof. Ankhi Roy, who always believed in my potential, provided me with guidance throughout my research work, and stood by me. I want to extend my sincere thanks to Prof. Manvendra Mahato and Prof. Swadesh k. Sahoo for evaluating my progress every year and offering valuable suggestions and constructive criticism that kept me on track. I am indebted to all the faculty members in the Department of Physics, Indian Institute of Technology Indore, including staff members Prashant Gupta, Ved Prakash, Nitin Upadhyay, and Sunny Namdev, Tapesh Parihar, for creating a conducive research environment. Regular outings and discussions with Dr. Biplab Ghosh boosted my confidence levels.

I am also grateful to Deepa Thomas, Fabio Colamaria, Robert Vertesi, Marianna Mazzili, Andra Dubla, Crisitna Terrivoli, Shingo Sakai, Hadi Hasan, M. Innocenti, Ralf Averbeck, and all ALICE Collaboration for providing me with the opportunity to work and for their timely guidance. I want to thank Prof. Subhasis Chattopadhyay, Prof. Bedangadas Mohanty, Prof. Zubayer Ahmed, Dr. Anand Kumar Dubay, Dr. Lokesh kumar, Dr. Partha Pratim Bhaduri.

My journey would have been incomplete without the support of my friends at IIT Indore. Anil, Satyam, and Mukul made it memorable with their delicious cooking and wonderful memories. I am grateful to Sheetal, Himanshu, Shankar, Phushpendra, Mohit, Sonu, Naveen, Sachi, Amita, Dipti, Suman Deb, Rutuparna

Rath, Devesh Pathak, Caption Rituraj Singh, Dhruv Ringe, and others at HJB residence for making my stay at IIT Indore enjoyable.

My lab mates provided me with unconditional support and love that is hard to describe in words. Dr. Sumit Kundu, the most supportive person, Dr. Ajay Kumar, Dr. Sudeep Ghosh, Dr. Ankita Goshwami, Dr. Sudhir, Yoshini Bailung, Swapnesh Khade, Jaswant, Hriday, Prasoon, Ravi, Yatharth, Praveen, Tarun, Rashi, Ajay, Niyathikrishna M R, all made the research journey comfortable and provided me with support during every up and down.

Family support is vital in any achievement, and I have continuously received it from my late grandmother Achhan Kanwar, my parents Birbal Singh and Raj Kanwar, and my dear brother Hansraj Singh, for which I am grateful.

I would like to express my gratitude to the Department of Science and Technology and the Government of India for their support in funding my research.

ABSTRACT

Studying the ultra-relativistic heavy-ion collisions with the A Large Ion Collider Experiment (ALICE) at the Large Hadron Collider(LHC) at European Council for Nuclear Research (CERN) is like peering into the early universe [1–6]. It is believed that in the early universe, some microseconds after the Big Bang, a new state of matter is formed called the quark-gluon plasma (QGP), where quarks and gluons exist as free particles rather than being confined inside hadrons. This state of matter is believed to exist before forming the hadrons. ALICE experiment aims to create and explore the properties of such state, i.e., temperature, energy density, viscosity, and the behavior of quarks and gluons within the medium.

The quark-gluon plasma (QGP) exists for a few microseconds before forming hadrons. Due to that, direct access to this state is not feasible, but various observables,i.e., collective flow, jet quenching, strangeness enhancement, etc., can be used to investigate the QGP. One such probe is through the examination of heavy flavors, such as charm and bottom quarks. Due to their large mass, heavy quarks are primarily produced prior to the formation of the QGP through hard scattering processes with large momentum transfer. [1, 7–10]. While passing, they experience energy loss and witness the full evolution of the QGP. Thus, studying heavy-flavour production can provide information about the dynamics of initial states and the properties of the partons (quarks and gluons) that participate in the scattering. Additionally, heavy-flavour jet, which is a collimated spray of particles in a narrow cone containing a heavy-flavour, can provide information about the fragmentation process of heavy-flavours, which is an essential aspect of understanding the production of hadrons containing heavy-flavours. The fragmentation process is a cascade of partonic splittings and emissions that occurs after a collision and forms the hadrons. Studying heavy-flavour hadrons and heavy-flavour jets can also improve our understanding of quantum chromodynamics (QCD), a

theory of strong interaction, as heavy quarks participate in the strong interaction. In proton-proton (pp) collisions, heavy-flavours can be used to test the predictions of perturbative quantum chromodynamics (pQCD) calculations ($m_{c,b} >> \Lambda_{QCD}$) and also serve the baseline for heavy-ion collisions. Here, $m_{c,b} \approx 1.3, 4.2$ GeV is the mass of charm and beauty quarks, and $\Lambda_{QCD} \approx 200$ MeV is the hard QCD scale. Studying these heavy-flavours in different collision systems (pp, p–Pb, and Pb–Pb) gives us a better understanding of the heavy-ion collisions. Comparing these pp measurements to the p–Pb collisions provide information on modification in fragmentation function due to the cold nuclear matter effect, whereas comparing with Pb–Pb collisions offer information about the hot nuclear matter effect (QGP). By comparing various collision systems, valuable insights can be gained about the density and energy loss mechanisms.

The motivation of this thesis is to study the heavy-flavour azimuthal correlations from small to large systems. The correlation measurement is an alternative way to study the direct jet (parton shower) properties. Jet-like correlation studies give direct access to the initial parton dynamics [11–13]. The typical structure of a two-particle azimuthal correlation distribution of high transverse-momentum (p_{T}) trigger particles with associated charged particles features a "near-side" (NS) peak at $(\Delta\varphi) = (0)$ and an "away-side" (AS) peak at $\Delta\varphi = \pi$, extending over a wide pseudorapidity range. The NS peak is mainly induced by particles emerging from the fragmentation of the same parton that produced the trigger particle. The AS peak is related to the fragmentation of the other parton produced in the hard scattering. Here, $\Delta\varphi$ is the difference in azimuth angle between the trigger and associated particles. The peaks lie on top of an approximately flat continuum extending over the full $(\Delta\varphi)$ range [11]. In this thesis, azimuthal $(\Delta\varphi)$ correlation distributions between heavy-flavour hadron decay electrons and associated charged particles are measured in pp, p–Pb, and Pb–Pb collisions at $\sqrt{s_{\mathrm{NN}}} = 5.02$ TeV with ALICE. Electrons are identified using the ALICE subdetectors, i.e., inner tracking system (ITS), time projection chamber (TPC) and electromagnetic calorimeter (EMCal). Results are reported for electrons with transverse momentum $4 < p_{\mathrm{T}} < 16$ GeV/c and pseudorapidity $|\eta| < 0.6$. The associated charged particles are selected with transverse momentum $1 < p_{\mathrm{T}} < 7$ GeV/c, and relative

pseudorapidity separation with the leading electron $|\Delta\eta| < 1$. The selection of acceptance and p_{T} are based on detector limitation and available statistics. The correlation measurements are performed to study and characterize jet fragmentation and hadronization of heavy quarks. The correlation structures are characterized using a constant and two von Mises functions for each peak to obtain the baseline and the near- and away-side peak observables, respectively. In the measured trigger electron and associated particle kinematic regions, pp and p–Pb collisions systems give consistent results, whereas a modification is seen in Pb–Pb collisions (work is ongoing). The $\Delta\varphi$ distribution and the peak observables in pp and p–Pb collisions are compared with calculations from various Monte Carlo event generators,i.e., PYTHIA8 and EPOS3.

The evolution of the near- and away-side peaks of the correlation functions in pp and p–Pb collisions are found to be similar in all the considered kinematic ranges. This suggests that the modification of the fragmentation and hadronization of heavy quarks due to cold-nuclear-matter effects is not observed within the current precision of the measurements. The extracted near- and away-side per-trigger yields and widths in pp and p–Pb collisions are presented as a function of associated particle p_{T}, which provide access to the momentum distributions of the particles produced in the fragmentation of the hard parton, and allow for a differential study of the jet angular profile. The per-trigger yields decrease with increasing $p_{\mathrm{T}}^{\mathrm{assoc}}$ and are consistent between pp and p–Pb collisions. While the near-side width tends to decrease with increasing $p_{\mathrm{T}}^{\mathrm{assoc}}$, the away-side width does not show a pronounced trend with $p_{\mathrm{T}}^{\mathrm{assoc}}$ for both collision systems. The $\Delta\varphi$ distributions, per-trigger yields, and widths in pp and p–Pb collisions are compared with predictions from PYTHIA8 (with Monash tune for pp and with Angantyr for p–Pb collisions), and EPOS3 Monte Carlo event generators. The PYTHIA8 predictions provide the best description of the data for both yields and widths of the near- and away-side peaks. For the current implementation of the EPOS3 model, the yields are similar to those obtained from data, while the near- and away-side widths are overestimated and underestimated, respectively.

The relative fractions of electrons from charm- and beauty-hadron decays have a strong p_{T} dependence. This feature was exploited by studying the corre-

lation distribution for the kinematic regions, $4 < p_{\mathrm{T}}^{\mathrm{e}} < 7$ GeV/c and $7 < p_{\mathrm{T}}^{\mathrm{e}} < 16$ GeV/c, where the latter $p_{\mathrm{T}}^{\mathrm{e}}$ range is dominated by beauty-hadron decays.

For both collision systems studied, the per-trigger yields are systematically larger for the $7 < p_{\mathrm{T}}^{\mathrm{e}} < 16$ GeV/c range compared to the $4 < p_{\mathrm{T}}^{\mathrm{e}} < 7$ interval due to the larger energy of the initial heavy quark, which allows for the production of more particles in the parton shower. This effect dominates over the increased beauty-origin contribution of the trigger electrons in the $7 < p_{\mathrm{T}}^{\mathrm{e}} < 16$ GeV/c range, which according to PYTHIA8 studies, are characterized by lower correlation peak yields than those of electrons originating from the charm. The near- and away-side widths are observed to be similar for both trigger electron p_{T} ranges for pp and p–Pb collisions.

PYTHIA8 studies indicate that this is due to competing effects, where the larger boost of the initial heavy quark leads to stronger collimation of the peaks with increasing $p_{\mathrm{T}}^{\mathrm{e}}$ for both charm- and beauty-origin contributions, compensating the broader peak widths for trigger electrons originating from beauty-hadron decays, whose contribution increases with $p_{\mathrm{T}}^{\mathrm{e}}$.

In order to explore aspects of fragmentation that are experimentally challenging, we used phenomenological models. Specifically, we used the Angantyr model in PYTHIA8 to investigate medium-like properties without relying on hydrodynamics. Angantyr model combines several nucleon−nucleon collisions to build a proton–nucleus (p–A) or nucleus–nucleus (A–A) collision. This phenomenological study aims to establish the Angantyr model for heavy-ion collisions. Our focus was on examining identified, strange, and multi-strange particle production in Pb–Pb collisions at $\sqrt{s_{\mathrm{NN}}} = 2.76$ TeV. Our results demonstrate how multi-parton interactions (MPI) and color reconnection (CR) influence experimentally measured quantities. As reflected from the name, MPI refers to the multiple interactions between the partons, where, in the color reconnection scheme, strings connecting the partons rearrange in such a way that the length of the final string becomes smaller [14]. We also looked into the role of string shoving within the rope hadronization framework and its effects on particle production. Our study shows that MPI with CR and string shoving configurations produce testable results,

as seen in the charged-particle multiplicity ($N_{\rm ch}$) and mean transverse momentum ($\langle p_{\rm T}\rangle$) distributions. We were able to explain these distributions well using PYTHIA8 Angantyr with appropriate tuning. We also investigated the collective nature of the produced particles by examining the ratio of particle yields to pions and kaons. Our findings suggest that PYTHIA8 Angantyr with MPI+CR and hadronization via string shoving can mimic signs of collectivity. We observed a peak around 3 GeV/c in the ratio of proton over pion, which is consistent with the radial flow observed in experimental data. We also observed a similar rise in all the strange baryon over pion ratios. Overall, our study concludes that PYTHIA+Angantyr provides favorable tunes for studying relevant observables in heavy-ion collisions. However, we found that the model fails in the low $p_{\rm T}$ regime compared to measurements from ALICE. We also found that strangeness enhancement is dominant for heavier strange particles, which is consistent with color strings overlapping at higher densities in accordance with CR and string shoving.

As PYTHIA+Angantyr explains many aspects of the experimental data, therefore, we tried to study the azimuthal angular correlations of electrons from heavy-flavour hadron decays in pp, p–Pb, and Pb–Pb collisions at $\sqrt{s_{\rm NN}}$ = 5.02 TeV using PYTHIA+Angantyr. We study the production of heavy-flavour jets with different parton-level processes, including multi-parton interactions, different color reconnection, and initial and final state radiation processes. In addition, we add the hadron-level processes, i.e., Bose-Einstein and rescattering effects, to quantify the effect due to these processes. The heavy-flavour electron correlations are calculated in the different trigger and associated $p_{\rm T}$ intervals to characterize the impact of hard and soft scattering in the various colliding systems. The yields and the sigmas associated with the near-side (NS) and away-side (AS) correlation peaks are calculated and studied as a function of associated $p_{\rm T}$ for different trigger $p_{\rm T}$ ranges. We observed a small jet-quenching in Pb–Pb collisions compared with pp collisions, probably due to MPI+CR and higher multiplicity compared to a small system. It is also seen that beyond leading color reconnection modes show a small increment of peak height in Pb–Pb collisions. This might be because an additional junction was added to beyond leading color (BLC) tunes, showing the

effect at high-density strings in Pb–Pb collisions. It is observed that MPI has no significant effect on fragmentation, as MPI mostly contributes to the baseline through soft processes. The associated yields are significantly increased by initial and final state radiation effects, as these radiations contribute to more collinear particle production. No significant modifications were observed in fragmentation due to hadron-level processes, i.e., BE effect and rescatter effect. This suggests that associated yields per trigger particle are mainly generated by parton fragmentation.

To investigate the fragmentation of individual heavy quarks and containing hadrons, we studied the azimuthal angular correlations of heavy-flavour hadrons (charm and beauty mesons, and charm baryons) in pp collisions at $\sqrt{s} = 7$ TeV using PYTHIA8 [15]. These measurements across different particle species help to isolate the possible modification in particle production and fragmentation due to different mass and quark contents. We study the production of heavy-flavour jets with different tunes. Similar to the previous studies, the heavy-flavour hadrons correlations are calculated in the different triggers and associated p_{T} intervals. The yields and the widths associated with the near-side and away-side correlation peaks are calculated using double generalized Gaussian function and studied as a function of associated p_{T} for different trigger p_{T} ranges. The near-side correlation distributions and observables of the D mesons derived by PYTHIA are consistent with the ALICE measurements, but PYTHIA needs to reform the physics at the away-side observable as it is slightly overestimated. This may be because PYTHIA does not incorporate NLO explicitly. Due to limited phase space, low $p_{\mathrm{T}}^{\mathbf{assoc}}$ particles are produced more than high $p_{\mathrm{T}}^{\mathbf{assoc}}$ particles; hence for the same $p_{\mathrm{T}}^{\mathrm{trig}}$, yield is higher at low $p_{\mathrm{T}}^{\mathbf{assoc}}$. Near-side associated yields to charm baryons are suppressed in Monash and Shoving tune compared to charm mesons yields. However, the difference is negligible in Mode 2. Similar results were observed in the calculation of the charm baryons production cross sections by the ALICE experiment, where the BLC tune mode 2 was in good agreement with the experimental data. Near-side yields from D mesons are almost 4-5 times larger than B mesons yield for the same $p_{\mathrm{T}}^{\mathrm{trig}}$. A possible reason for this could be the availability of more energy for D meson fragmentation due to smaller mass. No significant difference

is observed in PYTHIA between D and B mesons widths in the same trigger as well as associated p_{T} ranges, i.e., the dead cone effect has no major impact on the widths of D and B mesons at current precision as they are both heavy particles. However, it will be interesting to see the dead-cone effect in heavy quarks while comparing it with light quarks correlation distribution.

In conclusion, this thesis reports on a study of the azimuthal angular correlations of particles produced in pp, p–Pb, and Pb–Pb collisions at the LHC, with a focus on heavy quarks. The study finds that the modification of the fragmentation and hadronization of heavy quarks due to cold-nuclear-matter effects is not observed within the current precision of the measurements, and a clear modification is seen in Pb–Pb collision system. The article also explores the use of phenomenological models, such as Angantyr, to study identified particle production in lead-lead collisions, with a focus on the interplay between multi-parton interactions, color reconnection, and string shoving. The motivation of the phenomenological study by the Angantyr model is to explore an alternative way to explain the heavy-ion collisions and investigate the fragmentation properties of heavy-flavour hadrons.

Publications from the thesis:

Journal Publications:

1. **Ravindra Singh**,Yoshini Bailung, Sumit Kumar Kundu, Ankhi Roy; "*Jet fragmentation via azimuthal angular correlations of electrons from heavy flavor decay in pp, p-Pb, and Pb-Pb collisions using PYTHIA8+Angantyr calculations*"; [PhysRevC.107.024911]

2. **Ravindra Singh**,Swapnesh Khade, Ankhi Roy; "*Jet fragmentation via azimuthal angular correlations of heavy flavors in pp collisions at* $\sqrt{s}$ *=7 TeV*"; [PhysRevC.107.025206]

3. **Ravindra Singh**,Yoshini Bailung, Ankhi Roy; "*Dynamics of particle production in Pb–Pb collisions at* $\sqrt{s_{NN}}$ *= 2.76 TeV using PYTHIA8 Angantyr model*"; [PhysRevC.105.035202]

4. **[PC chair] Ravindra Singh**,ALICE Collaboration; "*Azimuthal correlations of heavy-flavor hadron decay electrons with charged particles in pp and p–Pb collisions at* $\sqrt{s_{\rm NN}}$ *= 5.02 TeV*"; [ArXiv:2303.00591]

Conference Proceedings:

1. **Ravindra Singh**; "*Investigating heavy-flavour jet properties via heavy-flavour particle correlations with ALICE*"; [DOI:10.5281/zenodo.7261226]

2. **Ravindra Singh**; "*Angular correlations of heavy-flavour hadron decay electrons and charged particles in pp collisions at* $\sqrt{s}$ *= 5.02 TeV with ALICE at the LHC*";Published in Proceedings of the 9th Annual Large Hadron Collider Physics (LHCP2021) conference, 7 - 12 June, 2021; [PoS(LHCP2021)191]

Analysis Note:

1. **Ravindra Singh**, Deepa Thomas; "*Azimuthal correlations between heavy flavour decay electrons and charged particles in pp and p-Pb at* $\sqrt{s_{NN}}$ = *5.02 TeV*";ALICE Analysis Note; ID number: ANA-1172; [https://alice-notes.web.cern.ch/node/1172]

Publications beside the thesis:

1. S. Acharya *et al.* [ALICE], "*Data-driven precision determination of the material budget in ALICE*," [arXiv:2303.15317 [physics.ins-det]].

2. S. Acharya *et al.* [ALICE], "*Study of the* $p-p-K^{+}$ *and* $p-p-K^{-}$ *dynamics using the femtoscopy technique*," [arXiv:2303.13448 [nucl-ex]].

3. S. Acharya *et al.* [ALICE], "*Measurement of the angle between jet axes in Pb−Pb collisions at* $\sqrt{s_{\rm NN}} = 5.02$ *TeV*," [arXiv:2303.13347 [nucl-ex]].

4. S. Acharya *et al.* [ALICE], "*Inclusive and multiplicity dependent production of electrons from heavy-flavour hadron decays in pp and p−Pb collisions*," [arXiv:2303.13349 [nucl-ex]].

5. S. Acharya *et al.* [ALICE], "*Measurement of anti-*^{3}*He nuclei absorption in matter and impact on their propagation in the Galaxy*," Nature Phys. **19** (2023) no.1, 61-71 doi:10.1038/s41567-022-01804-8 [arXiv:2202.01549 [nucl-ex]].

6. S. Acharya *et al.* [ALICE], "*Multiplicity dependence of charged-particle jet production in pp collisions at* $\sqrt{\mathbf{s}}$ = **13 TeV**," Eur. Phys. J. C **82** (2022) no.6, 514 doi:10.1140/epjc/s10052-022-10405-x [arXiv:2202.01548 [nucl-ex]].

7. S. Acharya *et al.* [ALICE], "*Measurement of beauty production via non-prompt* D^{0} *mesons in Pb-Pb collisions at* $\sqrt{s_{NN}}$= *5.02 TeV*," JHEP **12** (2022), 126 doi:10.1007/JHEP12(2022)126 [arXiv:2202.00815 [nucl-ex]].

8. S. Acharya *et al.* [ALICE], "*First study of the two-body scattering involving charm hadrons*," Phys. Rev. D **106** (2022) no.5, 052010 doi:10.1103/PhysRevD.106.052010 [arXiv:2201.05352 [nucl-ex]].

9. S. Acharya *et al.* [ALICE], "*Forward rapidity J/ψ production as a function of charged-particle multiplicity in pp collisions at* $\sqrt{s}$ *= 5.02 and 13 TeV*," JHEP **06** (2022), 015 doi:10.1007/JHEP06(2022)015 [arXiv:2112.09433 [nucl-ex]].

10. S. Acharya *et al.* [ALICE], "*Neutral to charged kaon yield fluctuations in Pb – Pb collisions at sNN=2.76 TeV*," Phys. Lett. B **832** (2022), 137242 doi:10.1016/j.physletb.2022.137242 [arXiv:2112.09482 [nucl-ex]].

11. S. Acharya *et al.* [ALICE], "*Constraining hadronization mechanisms with Λc+/D0 production ratios in Pb–Pb collisions at sNN=5.02 TeV*," Phys. Lett. B **839** (2023), 137796 doi:10.1016/j.physletb.2023.137796 [arXiv:2112.08156 [nucl-ex]].

12. S. Acharya *et al.* [ALICE], "*Production of light (anti)nuclei in pp collisions at* $\sqrt{s}$ = 5.02 *TeV*," Eur. Phys. J. C **82** (2022) no.4, 289 doi:10.1140/epjc/s10052-022-10241-z [arXiv:2112.00610 [nucl-ex]].

13. S. Acharya *et al.* [ALICE], "*Observation of a multiplicity dependence in the* p_{T}*-differential charm baryon-to-meson ratios in proton-proton collisions at* $\sqrt{s}$ = 13 *TeV*," Phys. Lett. B **829** (2022), 137065 doi:10.1016/j.physletb.2022.137065 [arXiv:2111.11948 [nucl-ex]].

14. S. Acharya *et al.* [ALICE], "*KS0KS0 and KS0K± femtoscopy in pp collisions at s=5.02 and 13 TeV*," Phys. Lett. B **833** (2022), 137335 doi:10.1016/j.physletb.2022.137335 [arXiv:2111.06611 [nucl-ex]].

15. S. Acharya *et al.* [ALICE], "*Characterizing the initial conditions of heavy-ion collisions at the LHC with mean transverse momentum and anisotropic flow correlations*," Phys. Lett. B **834** (2022), 137393 doi:10.1016/j.physletb.2022.137393 [arXiv:2111.06106 [nucl-ex]].

16. S. Acharya *et al.* [ALICE], "*Investigating charm production and fragmentation via azimuthal correlations of prompt D mesons with charged particles in pp collisions at* $\sqrt{\mathbf{s}} = \mathbf{13}$ *TeV*," Eur. Phys. J. C **82** (2022) no.4, 335 doi:10.1140/epjc/s10052-022-10267-3 [arXiv:2110.10043 [nucl-ex]].

17. S. Acharya *et al.* [ALICE], "*Measurement of prompt D_s^+-meson production and azimuthal anisotropy in Pb–Pb collisions at $\sqrt{s_{NN}}$=5.02TeV*," Phys. Lett. B **827** (2022), 136986 doi:10.1016/j.physletb.2022.136986 [arXiv:2110.10006 [nucl-ex]].

18. S. Acharya *et al.* [ALICE], "$K^*(892)^0$ *and* $\phi(1020)$ *production in p-Pb collisions at* $\sqrt{s_{NN}}$ *= 8.16 TeV*," [arXiv:2110.10042 [nucl-ex]].

19. S. Acharya *et al.* [ALICE], "*Prompt D^0, D^+, and D^{*+} production in Pb–Pb collisions at $\sqrt{s_{NN}}$ = 5.02 TeV*," JHEP **01** (2022), 174 doi:10.1007/JHEP01(2022)174 [arXiv:2110.09420 [nucl-ex]].

20. S. Acharya *et al.* [ALICE], "*General balance functions of identified charged hadron pairs of (π,K,p) in Pb–Pb collisions at sNN= 2.76 TeV*," Phys. Lett. B **833** (2022), 137338 doi:10.1016/j.physletb.2022.137338 [arXiv:2110.06566 [nucl-ex]].

21. S. Acharya *et al.* [ALICE], "*Measurement of inclusive charged-particle b-jet production in pp and p-Pb collisions at $\sqrt{s_{NN}}$ = 5.02 TeV*," JHEP **01** (2022), 178 doi:10.1007/JHEP01(2022)178 [arXiv:2110.06104 [nucl-ex]].

22. S. Acharya *et al.* [ALICE], "*Inclusive quarkonium production in pp collisions at $\sqrt{s}$ = 5.02 TeV*," Eur. Phys. J. C **83** (2023) no.1, 61 doi:10.1140/epjc/s10052-022-10896-8 [arXiv:2109.15240 [nucl-ex]].

23. S. Acharya *et al.* [ALICE], "*Production of light (anti)nuclei in pp collisions at $\sqrt{s}$ = 13 TeV*," JHEP **01** (2022), 106 doi:10.1007/JHEP01(2022)106 [arXiv:2109.13026 [nucl-ex]].

24. S. Acharya *et al.* [ALICE], "*Prompt and non-prompt J/ψ production cross sections at midrapidity in proton-proton collisions at* $\sqrt{s}$ *= 5.02 and 13 TeV*," JHEP **03** (2022), 190 doi:10.1007/JHEP03(2022)190 [arXiv:2108.02523 [nucl-ex]].

25. S. Acharya *et al.* [ALICE], "*Inclusive J/ψ production at midrapidity in pp collisions at $\sqrt{s}$ = 13 TeV*," Eur. Phys. J. C **81** (2021) no.12, 1121 doi:10.1140/epjc/s10052-021-09873-4 [arXiv:2108.01906 [nucl-ex]].

26. S. Acharya *et al.* [A Large Ion Collider Experiment and ALICE], "*Measurement of the groomed jet radius and momentum splitting fraction in pp and Pb−Pb collisions at* $\sqrt{s_{NN}} = 5.02$ *TeV*," Phys. Rev. Lett. **128** (2022) no.10, 102001 doi:10.1103/PhysRevLett.128.102001 [arXiv:2107.12984 [nucl-ex]].

27. S. Acharya *et al.* [ALICE], "*Measurements of the groomed and ungroomed jet angularities in pp collisions at* $\sqrt{s} = 5.02$ *TeV*," JHEP **05** (2022), 061 doi:10.1007/JHEP05(2022)061 [arXiv:2107.11303 [nucl-ex]].

28. S. Acharya *et al.* [ALICE], "*Polarization of* Λ *and* $\bar{\Lambda}$ *Hyperons along the Beam Direction in Pb-Pb Collisions at* $\sqrt{s_{NN}}$*=5.02 TeV*," Phys. Rev. Lett. **128** (2022) no.17, 172005 doi:10.1103/PhysRevLett.128.172005 [arXiv:2107.11183 [nucl-ex]].

29. S. Acharya *et al.* [ALICE], "K_S^0*- and (anti-)*Λ*-hadron correlations in pp collisions at* $\sqrt{s} = 13$ *TeV*," Eur. Phys. J. C **81** (2021) no.10, 945 doi:10.1140/epjc/s10052-021-09678-5 [arXiv:2107.11209 [nucl-ex]].

30. S. Acharya *et al.* [A Large Ion Collider Experiment and ALICE], "*Hypertriton Production in p-Pb Collisions at* $\sqrt{s_{NN}}$*=5.02 TeV*," Phys. Rev. Lett. **128** (2022) no.25, 252003 doi:10.1103/PhysRevLett.128.252003 [arXiv:2107.10627 [nucl-ex]].

31. S. Acharya *et al.* [ALICE], "*Anisotropic flow of identified hadrons in Xe-Xe collisions at* $\sqrt{s_{\rm NN}} = 5.44$ *TeV*," JHEP **10** (2021), 152 doi:10.1007/JHEP10(2021)152 [arXiv:2107.10592 [nucl-ex]].

32. S. Acharya *et al.* [ALICE], "*Study of very forward energy and its correlation with particle production at midrapidity in pp and p-Pb collisions at the LHC*," JHEP **08** (2022), 086 doi:10.1007/JHEP08(2022)086 [arXiv:2107.10757 [nucl-ex]].

33. S. Acharya *et al.* [ALICE], "*Production of* $K^*(892)^0$ *and* $\phi(1020)$ *in pp and Pb-Pb collisions at* $\sqrt{s_{\rm NN}} = 5.02$ *TeV*," Phys. Rev. C **106** (2022) no.3, 034907 doi:10.1103/PhysRevC.106.034907 [arXiv:2106.13113 [nucl-ex]].

34. S. Acharya *et al.* [ALICE], "*Direct observation of the dead-cone effect in quantum chromodynamics*," Nature **605** (2022) no.7910, 440-446 [erratum: Nature **607** (2022) no.7920, E22] doi:10.1038/s41586-022-04572-w [arXiv:2106.05713 [nucl-ex]].

35. S. Acharya *et al.* [ALICE], "*Measurement of Prompt D^0, Λ_c^+, and $\Sigma_c^{0,++}(2455)$ Production in Proton–Proton Collisions at $\sqrt{s}$ = 13 TeV*," Phys. Rev. Lett. **128** (2022) no.1, 012001 doi:10.1103/PhysRevLett.128.012001 [arXiv:2106.08278 [hep-ex]].

36. S. Acharya *et al.* [ALICE], "*Measurement of the production cross section of prompt Ξ_c^0 baryons at midrapidity in pp collisions at $\sqrt{s}$ = 5.02 TeV*," JHEP **10** (2021), 159 doi:10.1007/JHEP10(2021)159 [arXiv:2105.05616 [nucl-ex]].

37. S. Acharya *et al.* [ALICE], "*Experimental Evidence for an Attractive p-ϕ Interaction*," Phys. Rev. Lett. **127** (2021) no.17, 172301 doi:10.1103/PhysRevLett.127.172301 [arXiv:2105.05578 [nucl-ex]].

38. S. Acharya *et al.* [ALICE], "*Kaon–proton strong interaction at low relative momentum via femtoscopy in Pb–Pb collisions at the LHC*," Phys. Lett. B **822** (2021), 136708 doi:10.1016/j.physletb.2021.136708 [arXiv:2105.05683 [nucl-ex]].

39. S. Acharya *et al.* [ALICE], "*Charged-particle multiplicity fluctuations in Pb–Pb collisions at $\sqrt{s_{\rm NN}}$ = 2.76 TeV*," Eur. Phys. J. C **81** (2021) no.11, 1012 doi:10.1140/epjc/s10052-021-09784-4 [arXiv:2105.05745 [nucl-ex]].

40. S. Acharya *et al.* [ALICE], "*Measurement of $K^*(892)^\pm$ production in inelastic pp collisions at the LHC*," Phys. Lett. B **828** (2022), 137013 doi:10.1016/j.physletb.2022.137013 [arXiv:2105.05760 [nucl-ex]].

41. S. Acharya *et al.* [ALICE], "*Inclusive, prompt and non-prompt J/ψ production at midrapidity in p-Pb collisions at $\sqrt{s_{\rm NN}}$ = 5.02 TeV*," JHEP **06** (2022), 011 doi:10.1007/JHEP06(2022)011 [arXiv:2105.04957 [nucl-ex]].

42. S. Acharya *et al.* [ALICE], "*First measurements of N-subjettiness in central Pb-Pb collisions at* $\sqrt{s_{\rm NN}}$ *= 2.76 TeV*," JHEP **10** (2021), 003 doi:10.1007/JHEP10(2021)003 [arXiv:2105.04936 [nucl-ex]].

43. S. Acharya *et al.* [ALICE], "*Measurement of the Cross Sections of* Ξ_c^0 *and* Ξ_c^+ *Baryons and of the Branching-Fraction Ratio BR(*$\Xi_c^0 \to \Xi^- e^+ \nu_e$*)/BR(*$\Xi_c^0 \to \Xi^- \pi^+$*) in pp collisions at 13 TeV*," Phys. Rev. Lett. **127** (2021) no.27, 272001 doi:10.1103/PhysRevLett.127.272001 [arXiv:2105.05187 [nucl-ex]].

44. S. Acharya *et al.* [ALICE], "*Investigating the role of strangeness in baryon–antibaryon annihilation at the LHC*," Phys. Lett. B **829** (2022), 137060 doi:10.1016/j.physletb.2022.137060 [arXiv:2105.05190 [nucl-ex]].

45. S. Acharya *et al.* [ALICE], "*Energy dependence of* ϕ *meson production at forward rapidity in pp collisions at the LHC*," Eur. Phys. J. C **81** (2021) no.8, 772 doi:10.1140/epjc/s10052-021-09545-3 [arXiv:2105.00713 [nucl-ex]].

46. S. Acharya *et al.* [ALICE], "*Exploring the* $N\Lambda$*–*$N\Sigma$ *coupled system with high precision correlation techniques at the LHC*," Phys. Lett. B **833** (2022), 137272 doi:10.1016/j.physletb.2022.137272 [arXiv:2104.04427 [nucl-ex]].

47. S. Acharya *et al.* [ALICE], "*Nuclear modification factor of light neutral-meson spectra up to high transverse momentum in p–Pb collisions at sNN=8.16 TeV*," Phys. Lett. B **827** (2022), 136943 doi:10.1016/j.physletb.2022.136943 [arXiv:2104.03116 [nucl-ex]].

48. S. Acharya *et al.* [ALICE], "*Measurement of beauty and charm production in pp collisions at* $\sqrt{s}$ *= 5.02 TeV via non-prompt and prompt D mesons*," JHEP **05** (2021), 220 doi:10.1007/JHEP05(2021)220 [arXiv:2102.13601 [nucl-ex]].

49. S. Acharya *et al.* [ALICE], "*Measurements of mixed harmonic cumulants in Pb–Pb collisions at* $\sqrt{s_{NN}}$ *= 5.02 TeV*," Phys. Lett. B **818** (2021), 136354 doi:10.1016/j.physletb.2021.136354 [arXiv:2102.12180 [nucl-ex]].

50. S. Acharya *et al.* [ALICE], "*First measurement of the —t—-dependence of coherent* J/ψ *photonuclear production*," Phys. Lett. B **817** (2021), 136280

doi:10.1016/j.physletb.2021.136280 [arXiv:2101.04623 [nucl-ex]].

51. S. Acharya *et al.* [ALICE], "*Coherent J/ψ and ψ' photoproduction at midrapidity in ultra-peripheral Pb-Pb collisions at $\sqrt{s_{\rm NN}}$ = 5.02 TeV*," Eur. Phys. J. C **81** (2021) no.8, 712 doi:10.1140/epjc/s10052-021-09437-6 [arXiv:2101.04577 [nucl-ex]].

52. S. Acharya *et al.* [ALICE], "*Long- and short-range correlations and their event-scale dependence in high-multiplicity pp collisions at $\sqrt{s}$ = 13 TeV*," JHEP **05** (2021), 290 doi:10.1007/JHEP05(2021)290 [arXiv:2101.03110 [nucl-ex]].

53. S. Acharya *et al.* [ALICE], "*Production of pions, kaons, (anti-)protons and ϕ mesons in Xe–Xe collisions at $\sqrt{s_{\rm NN}}$ = 5.44 TeV*," Eur. Phys. J. C **81** (2021) no.7, 584 doi:10.1140/epjc/s10052-021-09304-4 [arXiv:2101.03100 [nucl-ex]].

54. S. Acharya *et al.* [ALICE], "*First measurement of coherent ρ0 photoproduction in ultra-peripheral Xe–Xe collisions at sNN=5.44 TeV*," Phys. Lett. B **820** (2021), 136481 doi:10.1016/j.physletb.2021.136481 [arXiv:2101.02581 [nucl-ex]].

55. S. Acharya *et al.* [ALICE], "*Multiharmonic Correlations of Different Flow Amplitudes in Pb-Pb Collisions at $\sqrt{s_{NN}}$ = 2.76 TeV*," Phys. Rev. Lett. **127** (2021) no.9, 092302 doi:10.1103/PhysRevLett.127.092302 [arXiv:2101.02579 [nucl-ex]].

E. George, R. Singh, P. Sarin and A. Laha, "*Novel Wide Band Gap Semiconductor Devices for Ionizing Radiation Detection*," Springer Proc. Phys. **261** (2021), 1107-1111 doi:10.1007/978-981-33-4408-2_164

56. S. Acharya *et al.* [ALICE], "*Inclusive heavy-flavour production at central and forward rapidity in Xe-Xe collisions at $\sqrt{s_{NN}}$=5.44$ TeV*," Phys. Lett. B **819** (2021), 136437 doi:10.1016/j.physletb.2021.136437 [arXiv:2011.06970 [nucl-ex]].

57. S. Acharya *et al.* [ALICE], "*Jet-associated deuteron production in pp collisions at* $\sqrt{s}$ *= 13 TeV*," Phys. Lett. B **819** (2021), 136440 doi:10.1016/j.physletb.2021.136440 [arXiv:2011.05898 [nucl-ex]].

58. S. Acharya *et al.* [ALICE], "*Jet fragmentation transverse momentum distributions in pp and p-Pb collisions at* $\sqrt{s}$, $\sqrt{s_{\rm NN}}$ *= 5.02 TeV*," JHEP **09** (2021), 211 doi:10.1007/JHEP09(2021)211 [arXiv:2011.05904 [nucl-ex]].

59. S. Acharya *et al.* [ALICE], "*Production of muons from heavy-flavour hadron decays at high transverse momentum in Pb–Pb collisions at sNN=5.02 and 2.76 TeV*," Phys. Lett. B **820** (2021), 136558 doi:10.1016/j.physletb.2021.136558 [arXiv:2011.05718 [nucl-ex]].

60. S. Acharya *et al.* [ALICE], "Υ *production and nuclear modification at forward rapidity in Pb–Pb collisions at sNN=5.02TeV*," Phys. Lett. B **822** (2021), 136579 doi:10.1016/j.physletb.2021.136579 [arXiv:2011.05758 [nucl-ex]].

61. S. Acharya *et al.* [ALICE], "Λ_c^+ *Production and Baryon-to-Meson Ratios in pp and p-Pb Collisions at* $\sqrt{s_{NN}}$*=5.02 TeV at the LHC*," Phys. Rev. Lett. **127** (2021) no.20, 202301 doi:10.1103/PhysRevLett.127.202301 [arXiv:2011.06078 [nucl-ex]].

62. S. Acharya *et al.* [ALICE], "Λ_c^+ *production in pp and in p-Pb collisions at* $\sqrt{s_{NN}}$*=5.02 TeV*," Phys. Rev. C **104** (2021) no.5, 054905 doi:10.1103/PhysRevC.104.054905 [arXiv:2011.06079 [nucl-ex]].

63. S. Acharya *et al.* [ALICE], "*Pseudorapidity distributions of charged particles as a function of mid- and forward rapidity multiplicities in pp collisions at* $\sqrt{s}$ *= 5.02, 7 and 13 TeV*," Eur. Phys. J. C **81** (2021) no.7, 630 doi:10.1140/epjc/s10052-021-09349-5 [arXiv:2009.09434 [nucl-ex]].

64. S. Acharya *et al.* [ALICE], "*Centrality dependence of* J/ψ *and* $\psi(2S)$ *production and nuclear modification in p-Pb collisions at* $\sqrt{s_{\rm NN}}$ *= 8.16 TeV*," JHEP **02** (2021), 002 doi:10.1007/JHEP02(2021)002 [arXiv:2008.04806 [nucl-ex]].

65. S. Acharya *et al.* [ALICE], "*Pion-kaon femtoscopy and the lifetime of the hadronic phase in Pb−Pb collisions at* $\sqrt{s_{\rm NN}}$ *= 2.76 TeV*," Phys. Lett. B **813** (2021), 136030 doi:10.1016/j.physletb.2020.136030 [arXiv:2007.08315 [nucl-ex]].

66. S. Acharya *et al.* [ALICE], "*Production of* ω *mesons in pp collisions at* $\sqrt{\mathbf{s}} = \mathbf{7}$ *TeV*," Eur. Phys. J. C **80** (2020) no.12, 1130 doi:10.1140/epjc/s10052-020-08651-y [arXiv:2007.02208 [nucl-ex]].

67. S. Acharya *et al.* [ALICE], "*J/*ψ *elliptic and triangular flow in Pb-Pb collisions at* $\sqrt{s_{\rm NN}}$ *= 5.02 TeV*," JHEP **10** (2020), 141 doi:10.1007/JHEP10(2020)141 [arXiv:2005.14518 [nucl-ex]].

68. S. Acharya *et al.* [ALICE], "*Soft-Dielectron Excess in Proton-Proton Collisions at* $\sqrt{s}$ *= 13 TeV*," Phys. Rev. Lett. **127** (2021) no.4, 042302 doi:10.1103/PhysRevLett.127.042302 [arXiv:2005.14522 [nucl-ex]].

69. S. Acharya *et al.* [ALICE], "*Measurement of isolated photon-hadron correlations in* $\sqrt{s_{\rm NN}}$ *= 5.02 TeV pp and p-Pb collisions*," Phys. Rev. C **102** (2020) no.4, 044908 doi:10.1103/PhysRevC.102.044908 [arXiv:2005.14637 [nucl-ex]].

70. S. Acharya *et al.* [ALICE], "*Constraining the Chiral Magnetic Effect with charge-dependent azimuthal correlations in Pb-Pb collisions at* $\sqrt{s_{\rm NN}}$ *= 2.76 and 5.02 TeV*," JHEP **09** (2020), 160 doi:10.1007/JHEP09(2020)160 [arXiv:2005.14640 [nucl-ex]].

71. S. Acharya *et al.* [ALICE], "*Elliptic and triangular flow of (anti)deuterons in Pb-Pb collisions at* $\sqrt{s_{\rm NN}}$ *= 5.02 TeV*," Phys. Rev. C **102** (2020) no.5, 055203 doi:10.1103/PhysRevC.102.055203 [arXiv:2005.14639 [nucl-ex]].

72. S. Acharya *et al.* [ALICE], "*Dielectron production in proton-proton and proton-lead collisions at* $\sqrt{s_{NN}}$ *= 5.02 TeV*," Phys. Rev. C **102** (2020) no.5, 055204 doi:10.1103/PhysRevC.102.055204 [arXiv:2005.11995 [nucl-ex]].

A. Collaboration *et al.* [ALICE], "*Unveiling the strong interaction among hadrons at the LHC*," Nature **588** (2020), 232-238 [erratum: Nature **590**

(2021), E13] doi:10.1038/s41586-020-3001-6 [arXiv:2005.11495 [nucl-ex]].

73. S. Acharya *et al.* [ALICE], "*Measurement of the low-energy antideuteron inelastic cross section*," Phys. Rev. Lett. **125** (2020) no.16, 162001 doi:10.1103/PhysRevLett.125.162001 [arXiv:2005.11122 [nucl-ex]].

74. S. Acharya *et al.* [ALICE], "*Production of light-flavor hadrons in pp collisions at* $\sqrt{s} = 7$ *and* $\sqrt{s} = 13$ *TeV*," Eur. Phys. J. C **81** (2021) no.3, 256 doi:10.1140/epjc/s10052-020-08690-5 [arXiv:2005.11120 [nucl-ex]].

75. S. Acharya *et al.* [ALICE], "*Z-boson production in p-Pb collisions at* $\sqrt{s_{\rm NN}} =$ 8.16 *TeV and Pb-Pb collisions at* $\sqrt{s_{\rm NN}} = 5.02$ *TeV*," JHEP **09** (2020), 076 doi:10.1007/JHEP09(2020)076 [arXiv:2005.11126 [nucl-ex]].

76. S. Acharya *et al.* [ALICE], "*Multiplicity dependence of J/*ψ *production at midrapidity in pp collisions at* $\sqrt{s}$ *= 13 TeV*," Phys. Lett. B **810** (2020), 135758 doi:10.1016/j.physletb.2020.135758 [arXiv:2005.11123 [nucl-ex]].

77. S. Acharya *et al.* [ALICE], "*Elliptic Flow of Electrons from Beauty-Hadron Decays in Pb-Pb Collisions at* $\sqrt{s_{NN}}$ *= 5.02 TeV*," Phys. Rev. Lett. **126** (2021) no.16, 162001 doi:10.1103/PhysRevLett.126.162001 [arXiv:2005.11130 [nucl-ex]].

78. S. Acharya *et al.* [ALICE], "ΛK *femtoscopy in Pb-Pb collisions at* $\sqrt{s_{\rm NN}}$ *= 2.76 TeV*," Phys. Rev. C **103** (2021) no.5, 055201 doi:10.1103/PhysRevC.103.055201 [arXiv:2005.11124 [nucl-ex]].

79. S. Acharya *et al.* [ALICE], "*Transverse-momentum and event-shape dependence of D-meson flow harmonics in Pb–Pb collisions at* $\sqrt{s_{NN}}$ *= 5.02 TeV*," Phys. Lett. B **813** (2021), 136054 doi:10.1016/j.physletb.2020.136054 [arXiv:2005.11131 [nucl-ex]].

80. S. Acharya *et al.* [ALICE], "*First measurement of quarkonium polarization in nuclear collisions at the LHC*," Phys. Lett. B **815** (2021), 136146 doi:10.1016/j.physletb.2021.136146 [arXiv:2005.11128 [nucl-ex]].

81. S. Acharya *et al.* [ALICE], "*J/ψ production as a function of charged-particle multiplicity in p-Pb collisions at $\sqrt{s_{\rm NN}}$ = 8.16 TeV*," JHEP **09** (2020), 162 doi:10.1007/JHEP09(2020)162 [arXiv:2004.12673 [nucl-ex]].

82. S. Acharya *et al.* [ALICE], "*Search for a common baryon source in high-multiplicity pp collisions at the LHC*," Phys. Lett. B **811** (2020), 135849 doi:10.1016/j.physletb.2020.135849 [arXiv:2004.08018 [nucl-ex]].

83. S. Acharya *et al.* [ALICE], "*Measurement of nuclear effects on ψ(2S) production in p-Pb collisions at $\sqrt{s_{\rm NN}}$ = 8.16 TeV*," JHEP **07** (2020), 237 doi:10.1007/JHEP07(2020)237 [arXiv:2003.06053 [nucl-ex]].

84. S. Acharya *et al.* [ALICE], "*(Anti-)deuteron production in pp collisions at $\sqrt{s}$ = 13 TeV*," Eur. Phys. J. C **80** (2020) no.9, 889 doi:10.1140/epjc/s10052-020-8256-4 [arXiv:2003.03184 [nucl-ex]].

85. S. Acharya *et al.* [ALICE], "*Multiplicity dependence of π, K, and p production in pp collisions at $\sqrt{s} = 13$ TeV*," Eur. Phys. J. C **80** (2020) no.8, 693 doi:10.1140/epjc/s10052-020-8125-1 [arXiv:2003.02394 [nucl-ex]].

86. S. Acharya *et al.* [ALICE], "*Coherent photoproduction of ρ^0 vector mesons in ultra-peripheral Pb-Pb collisions at $\sqrt{\rm s_{NN}}$ = 5.02 TeV*," JHEP **06** (2020), 035 doi:10.1007/JHEP06(2020)035 [arXiv:2002.10897 [nucl-ex]].

87. S. Acharya *et al.* [ALICE], "*Higher harmonic non-linear flow modes of charged hadrons in Pb-Pb collisions at $\sqrt{s_{\rm NN}}$ = 5.02 TeV*," JHEP **05** (2020), 085 doi:10.1007/JHEP05(2020)085 [arXiv:2002.00633 [nucl-ex]].

88. S. Acharya *et al.* [ALICE], "*Non-linear flow modes of identified particles in Pb-Pb collisions at $\sqrt{s_{\rm NN}}$ = 5.02 TeV*," JHEP **06** (2020), 147 doi:10.1007/JHEP06(2020)147 [arXiv:1912.00740 [nucl-ex]].

89. S. Acharya *et al.* [ALICE], "*Investigation of the p–Σ0 interaction via femtoscopy in pp collisions*," Phys. Lett. B **805** (2020), 135419 doi:10.1016/j.physletb.2020.135419 [arXiv:1910.14407 [nucl-ex]].

90. S. Acharya *et al.* [ALICE], "*Global baryon number conservation encoded in net-proton fluctuations measured in Pb-Pb collisions at $\sqrt{s_{\rm NN}}$ = 2.76*

TeV," Phys. Lett. B **807** (2020), 135564 doi:10.1016/j.physletb.2020.135564 [arXiv:1910.14396 [nucl-ex]].

91. S. Acharya *et al.* [ALICE], "*Longitudinal and azimuthal evolution of two-particle transverse momentum correlations in Pb-Pb collisions at* $\sqrt{s_{\rm NN}}$ *= 2.76 TeV*," Phys. Lett. B **804** (2020), 135375 doi:10.1016/j.physletb.2020.135375 [arXiv:1910.14393 [nucl-ex]].

92. S. Acharya *et al.* [ALICE], "*Multiplicity dependence of K*(892)*^{0} *and* ϕ*(1020) production in pp collisions at* $\sqrt{s}$ *=13 TeV*," Phys. Lett. B **807** (2020), 135501 doi:10.1016/j.physletb.2020.135501 [arXiv:1910.14397 [nucl-ex]].

93. S. Acharya *et al.* [ALICE], "*Underlying Event properties in pp collisions at* $\sqrt{s}$ *= 13 TeV*," JHEP **04** (2020), 192 doi:10.1007/JHEP04(2020)192 [arXiv:1910.14400 [nucl-ex]].

94. S. Acharya *et al.* [ALICE], "*Centrality and transverse momentum dependence of inclusive J/*ψ *production at midrapidity in Pb–Pb collisions at sNN=5.02 TeV*," Phys. Lett. B **805** (2020), 135434 doi:10.1016/j.physletb.2020.135434 [arXiv:1910.14404 [nucl-ex]].

95. S. Acharya *et al.* [ALICE], "*Azimuthal correlations of prompt D mesons with charged particles in pp and p–Pb collisions at* $\sqrt{s_{NN}}$ *= 5.02 TeV*," Eur. Phys. J. C **80** (2020) no.10, 979 doi:10.1140/epjc/s10052-020-8118-0 [arXiv:1910.14403 [nucl-ex]].

96. S. Acharya *et al.* [ALICE], "*Production of (anti-)*^{3}*He and (anti-)*^{3}*H in p-Pb collisions at* $\sqrt{s_{\rm NN}}$ *= 5.02 TeV*," Phys. Rev. C **101** (2020) no.4, 044906 doi:10.1103/PhysRevC.101.044906 [arXiv:1910.14401 [nucl-ex]].

97. S. Acharya *et al.* [ALICE], "*Jet-hadron correlations measured relative to the second order event plane in Pb-Pb collisions at* $\sqrt{s_{\rm NN}}$ *= 2.76 TeV*," Phys. Rev. C **101** (2020) no.6, 064901 doi:10.1103/PhysRevC.101.064901 [arXiv:1910.14398 [nucl-ex]].

98. S. Acharya *et al.* [ALICE], "Υ *production in p–Pb collisions at* $\sqrt{s_{NN}}$*=8.16 TeV*," Phys. Lett. B **806** (2020), 135486 doi:10.1016/j.physletb.2020.135486 [arXiv:1910.14405 [nucl-ex]].

99. S. Acharya *et al.* [ALICE], "*Evidence of Spin-Orbital Angular Momentum Interactions in Relativistic Heavy-Ion Collisions*," Phys. Rev. Lett. **125** (2020) no.1, 012301 doi:10.1103/PhysRevLett.125.012301 [arXiv:1910.14408 [nucl-ex]].

100. S. Acharya *et al.* [ALICE], "*Probing the effects of strong electromagnetic fields with charge-dependent directed flow in Pb-Pb collisions at the LHC*," Phys. Rev. Lett. **125** (2020) no.2, 022301 doi:10.1103/PhysRevLett.125.022301 [arXiv:1910.14406 [nucl-ex]].

101. S. Acharya *et al.* [ALICE], "*Evidence of rescattering effect in Pb-Pb collisions at the LHC through production of* $\mathrm{K}^*(892)^0$ *and* $\phi(1020)$ *mesons*," Phys. Lett. B **802** (2020), 135225 doi:10.1016/j.physletb.2020.135225 [arXiv:1910.14419 [nucl-ex]].

102. S. Acharya *et al.* [ALICE], "*Measurements of inclusive jet spectra in pp and central Pb-Pb collisions at* $\sqrt{s_{\mathrm{NN}}}$ *= 5.02 TeV*," Phys. Rev. C **101** (2020) no.3, 034911 doi:10.1103/PhysRevC.101.034911 [arXiv:1909.09718 [nucl-ex]].

Contents

Figures

Tables

Chapter 1

Introduction

The primary aim of particle physics is to understand the universe by studying the basic constituents and their interactions with matter at the sub-atomic scale. As of now, four fundamental forces exist in the universe, i.e., gravitational, electromagnetic, weak, and strong nuclear interactions, out of which three forces (except gravity) are successfully described by the standard model [43]. This model proposes that matter is composed of quarks and leptons that interact through gauge bosons (such as photons and gluons). Electromagnetism and weak interactions are unified by the electroweak interaction theory, where quantum chromodynamics (QCD) describes the strong interactions between quarks and gluons that reside in a nucleon.

The ALICE (a large ion collider experiment) experiment at CERN, Geneva, has provided the opportunity to investigate the strongly interacting, deconfined coloured medium that was supposed to exist microseconds after the Big Bang called quark-gluon plasma (QGP) [44, 45]. The ultra-relativistic heavy-ion collisions (e.g., Au–Au, Pb–Pb) have enough initial energy densities that are required to form the QGP medium. To study cold nuclear matter (CNM) effects, i.e., nuclear shadowing and hadronic reabsorption, etc., LHC collides protons with lead (p-Pb) ions at high energies. But surprisingly, studies like particle correlations and multiplicity-dependent particle production show hints of the medium formation in small systems like proton-proton (pp) and p–Pb collisions.

Due to the short lifetime of the QGP, a direct study is impossible; therefore, many indirect approaches are used to investigate the properties of this medium. One such approach is via heavy quarks (charm and beauty), as they are produced at the initial stage of collision, mostly by hard scattering processes. These

processes involve large momentum transfer, which allows us to use perturbative quantum chromodynamics (pQCD) methods to calculate the production cross-section of these processes [1, 7–10]. The cross sections of various open heavy-flavor hadrons and their decay leptons have been measured in pp collisions at both mid- and forward-rapidity at the LHC [2–6, 41, 46–61]. They are consistent with pQCD calculations [62–64] within theoretical uncertainties. However, these calculations, along with various Monte Carlo event generators using a fragmentation model tuned on e^+e^- collisions, are unable to describe the recent measurements of charm-baryon production in pp collisions at midrapidity [65–76]. These measurements can be better described by models that incorporate hadronization mechanisms such as quark coalescence [77], additional colour reconnections among parton fragments [78], or by including enhanced feed-down from higher-mass charm-baryon states within a statistical hadronization approach [79], where the higher-mass excited charm-baryon states are predicted by the Relativistic Quark Model [80] but not yet measured. To better understand the fragmentation (parton showering) and hadronization of heavy quarks, more differential measurements are required. In this direction, two types of measurements are generally used in high-energy physics, i.e., jet studies and jet-like azimuthal correlations. The jet-like two-particle azimuthal correlations provide some information about the fragmentation function over the jet measurement, such as the description of particle production processes(leading order)(LO) and next-to-leading order (NLO), description of correlation peaks shape and size, etc. At LO, quark and anti-quark pairs are produced back to back in azimuth, which generates two correlation peaks, while at NLO, correlation peaks are different from LO processes. Quarks and anti-quarks pair at gluon splitting (NLO process) are produced with small opening angles, hence contributing to the broadening of the peaks, while processes like flavour excitation mostly contribute to flat azimuthal correlation. The correlation measurements provide insight into heavy-flavor jet properties at low transverse momentum (p_{T}). By varying the p_{T} interval of the trigger and associated particles, the correlation measurements allow the details of jet fragmentation to be studied, such as the jet angular profile and the momentum distribution of the particles produced in the fragmentation of the hard parton. These measurements in pp collisions, originat-

ing from heavy-flavours provide the test to pQCD calculations, and it serves as a baseline to study the nuclear effects in p–Pb and Pb–Pb collisions. Comparing azimuthal correlation measurements to p–Pb and Pb–Pb collision systems provides information on possible modification due to cold and hot nuclear matter effects, respectively.

This thesis focuses on fragmentation study by correlation measurements in different collision systems. This chapter briefly introduces the Standard Model of particle physics in section 1.1 and the theory of QCD in section 1.2. Section 1.3 shows the overview of the QGP medium and its signatures and formation in ultra-relativistic heavy-ion collisions. Recent experimental measurements of possible medium formation in pp collisions are briefly discussed. Finally, section 1.7 presents the motivation of this thesis.

1.1 The Standard Model

Decades ago, atoms were considered to be the smallest element of matter that could not be split. After discovering the constituents of atoms, i.e., electrons, and nucleons, the scientific community is still trying to figure out the fundamental constituents of matter. Numerous particles were postulated and later found in experiments over time. Many theories and models are introduced for a better understanding of these particles and the interactions between them. In this chain, the Standard Model (SM) gives a complete picture of fundamental particles. The SM describes the behavior of the fundamental particles and forces of nature. It includes the electroweak and quantum chromodynamics theories, which describe the weak and strong nuclear forces, respectively. The Standard Model also includes the Higgs mechanism, which explains the origin of mass. However, it does not describe dark matter, dark energy, neutrino masses, matter-antimatter asymmetry, and the unification of all forces, which indicates the existence of physics beyond the standard model.

The SM contains the following elementary particles,

- Fermions: There are two types of fermions: quarks and leptons. Quarks

come in six "flavors" with three different colour charges (red, green, and blue); up (u), down (d), strange (s) charm (c), top (t), and bottom (b). Leptons are elementary particles that do not experience the strong nuclear force. They include electrons (e), muons (μ), and tau (τ) particles and their corresponding massless and chargeless neutrinos (ν_e, ν_μ, ν_τ). All the particles also have their anti-particles.

- Bosons: These are the particles that mediate the fundamental forces. They include the photon, which mediates the electromagnetic force; the $W^{\pm}$ and Z^0 bosons, which mediate the weak nuclear force; and the gluon (g), which mediates the strong nuclear force.

- Higgs boson (H^0): This is a particle that confirmed the existence of the Higgs field, a fundamental field of the universe that is responsible for giving particles mass. It was discovered at CERN's LHC in 2012 [81].

All the particles except bosons have anti-particles with the same mass but opposite charges. Further, leptons and quarks are grouped into three generations according to their mass. The classification of particles in the standard model can be seen in Figure 1.1.

No evidence of internal structure was found for above mentioned standard model particle; hence, they are considered elementary particles. The combination of quarks together makes hadrons, which interact by the strong nuclear force. The pair of quark and anti-quark make mesons (e.x., pions (π), kaons (K)) while three quarks together form baryons, for e.x., nucleons (proton and neutron). Baryons are fermions having spin 1/2 of integer whereas mesons have integer spin, thus mesons do not follow the Pauli exclusion principle.

This thesis focuses on the dynamics of strongly interacting particles, which govern by the theory of quantum chromodynamics; therefore, QCD will be discussed briefly in the next section.

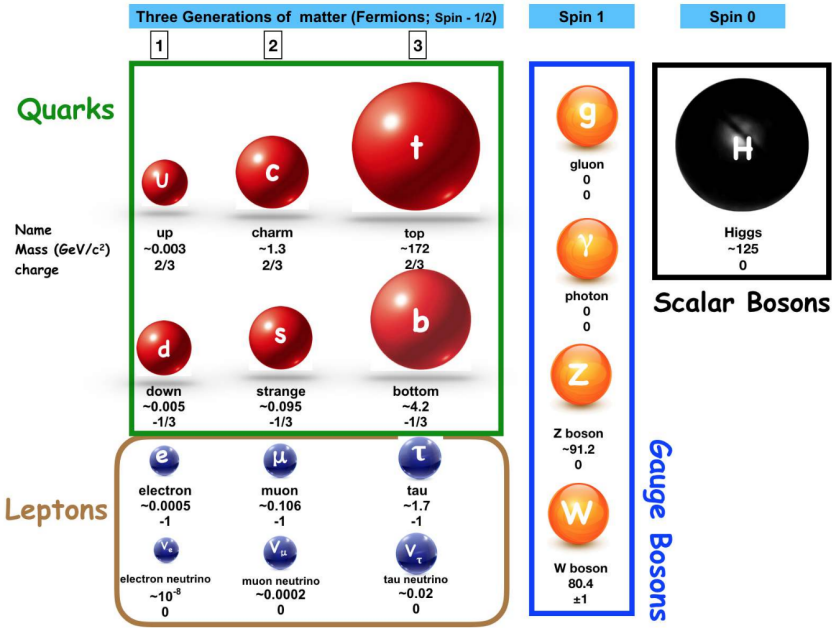

Figure 1.1: Diagram of the Standard Model of particle physics, illustrating the fundamental particles and their interactions through the exchange of force-carrying particles [16].

1.2 QCD: the theory of strong interaction

QCD stands for Quantum Chromodynamics. It is the theory of strong interactions. QCD describes the interactions between quarks and gluons (with colour quantum numbers), which are the building blocks of protons and neutrons, the particles that make up the nuclei of atoms. The strong force is responsible for holding the nucleons together in the nucleus, and it is much stronger than the electromagnetic force, which holds atoms together. However, the strong force only acts at very short distances, so it has very little effect on the behavior of atoms as a whole. Unlike QED, the gauge boson of QCD (gluon) are considered to be self-interacting, meaning that they interact with each other as well as with quarks. This is known as a non-abelian gauge theory, and the gluon interactions are described by the SU(3) gauge group [82, 82]. The SU(3) group has eight different types of gluons, which are divided into three colour charges: red, green, and blue. The colour charge of a quark determines how it interacts with the gluons as gluons are bi-coloured and interact via colour exchange between the uni-coloured quarks.

The QCD has two main peculiarities, viz., colour confinement and asymp-

totic freedom by with gluons and quarks confined together as described below–

- colour Confinement: This refers to the phenomenon where quarks and gluons are confined inside hadrons and are not observed as free particles. The confinement of quarks is a consequence of the non-abelian nature of the strong force, which means that the force depends on the colour charge of the quarks, and the exchange of multiple gluons between quarks leads to an anti-screening effect that makes the force between them stronger at short distances. The confinement of quarks is one of the main challenges in theoretical physics, and several models have been proposed to explain it, such as the confinement through the dual Meissner effect [83] and the confinement through the formation of a string-like flux tube between quarks [84].

- Asymptotic Freedom: It describes the behavior of the strong force between quarks at short distances. Asymptotic freedom states that the strength of the strong force between quarks decreases as the distance between them decreases so that at very short distances, the force is almost zero. This is in contrast to the behavior of other forces, such as the electromagnetic force, which becomes stronger as the distance between particles decreases. It is also a consequence of the non-abelian nature of QCD. It explains why quarks and gluons can exist as a deconfined state in high-energy heavy ion collisions but are confined inside hadrons. It was discovered by David Gross, Frank Wilczek, and David Politzer in 1973, they were awarded the Nobel Prize in Physics in 2004 [85].

  The potential between two coloured charges is defined as,

$$V_{QCD} \approx -\frac{\alpha_S}{r} + \kappa r, \tag{1.1}$$

Where α_S is the coupling constant for strong interaction (running coupling constant), κ is the tension constant of colour string ($\sim$ 1 GeV fm^{-1}) [86], and r is the distance between two coloured charges. This potential is not a simple

Coulombic potential as in QED but rather a more complex function that includes both short-range and long-range components. The short-range component is due to the exchange of multiple gluons, while the long-range component is due to the exchange of a single gluon. This can be understood by the anti-screening effect of gluons. In QCD couplings, two one-loop diagrams in which one virtual gluon and another virtual quark loop are considered. The anti-screening effect is due to the exchange of multiple gluons between quarks, which increases the strength of the force as the distance between the quarks decreases.

The running coupling constant as a function of momentum transfer (Q^2) is defined as follows,

$$\alpha_s(Q^2) = \frac{12\pi}{(33 - 2n_f)\ln(\frac{Q^2}{\Lambda^2_{QCD}})} \tag{1.2}$$

Here, the number of quark flavors accessible at Q^2 is denoted by n_f, and the QCD scale is denoted by Λ_{QCD} ($\Lambda_{QCD} \approx 200$ MeV). When the energy scale is below Λ_{QCD}, non-perturbative QCD effects become significant. The magnitude of the running coupling constant is interpreted as a scale that separates the pQCD (at small $\alpha_s(Q)^2$) and non-pQCD (at large $\alpha_s(Q)^2$).

At non-pQCD regime ($< \Lambda_{QCD} \approx 200$ MeV), quantum chromodynamics can be studied by the theory of lattice QCD (LQCD). The basic idea behind LQCD is to divide space-time into a grid of discrete points, or lattice sites, and to represent the quarks and gluons as variables defined on these lattice sites. The interactions between quarks and gluons are then described by a set of mathematical equations known as the QCD Lagrangian, which are solved numerically using computer simulations [87, 88].

As shown in Figure 1.2, for $Q \gtrsim \Lambda_{QCD}$, the coupling constant is small ($\alpha_s < 1$), and perturbative QCD can be used to study strong interactions. This domain is known as the hard QCD regime, as it is associated with large momentum transfer. On the other hand, at energy scales $Q \lesssim \Lambda_{QCD}$, the coupling constant becomes large ($\alpha_s > 1$), and the dominance of the strong force becomes apparent.

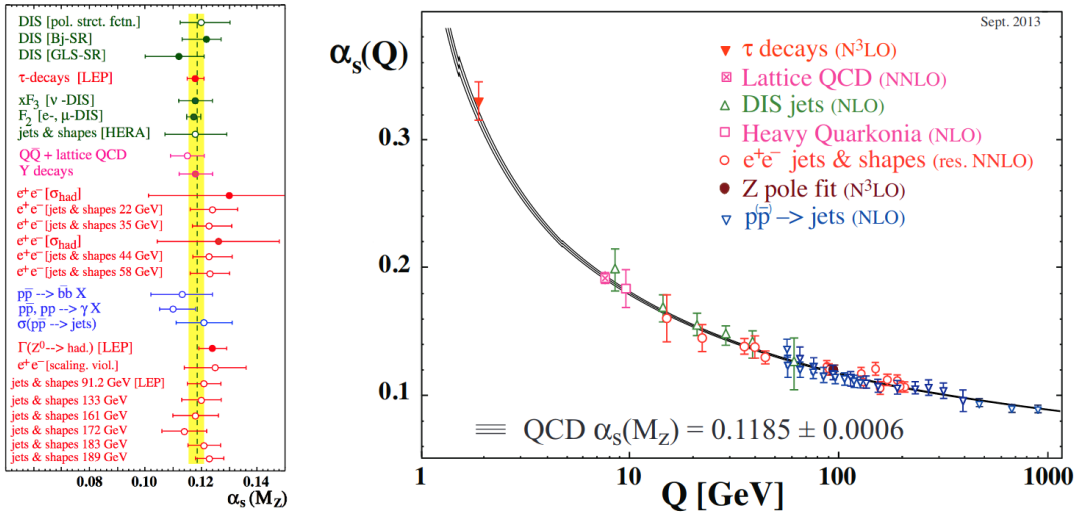

Figure 1.2: Left: List of individual $\alpha_S(M_Z^2)$ measurements and their comparison to the world average from Ref. [17] in 2000; Right: current status of the running of α_S, as summarised in Ref. [18]

This domain is known as the soft QCD regime, as it is associated with low momentum transfer. Due to the high value of the QCD coupling constant in the soft QCD regime, quarks are confined within hadrons, known as colour confinement. Thus, QCD is characterized by two properties, asymptotic freedom, and colour confinement.

1.3 QCD phase diagram and QGP

The QCD phase diagram is a theoretical representation of the phase structure of QCD as a function of temperature (T) and baryon chemical potential (μ_B) as shown in Figure 1.3. In thermodynamics, the baryon chemical potential is defined as the derivative of the thermodynamic potential with respect to the number of baryons (change in energy with respect to the number of baryons). The baryon chemical potential is a measure of the density of net baryons, such as protons and neutrons, in the system. Based on the temperature and density of the system, three main regions of the QCD phase diagram are:

1. **The hadronic phase:** The hadronic phase is characterized by the dominance of hadrons in nuclear matter and occupies the region of the QCD

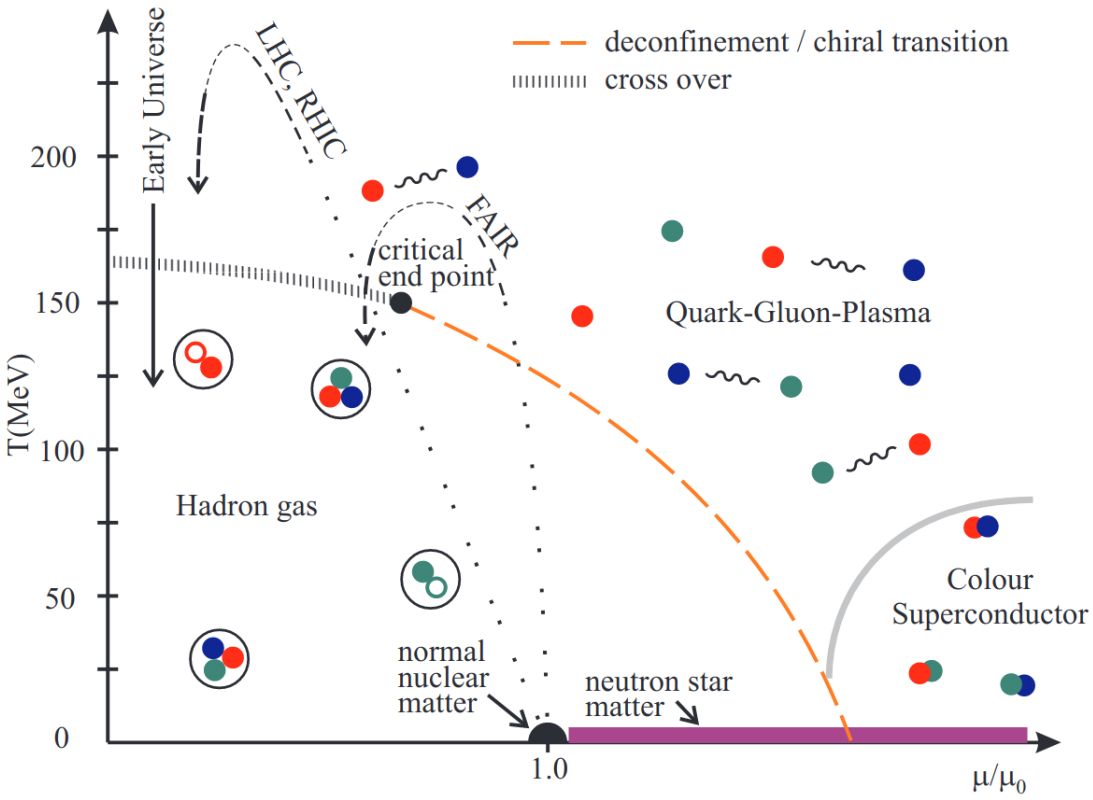

Figure 1.3: A schematic phase diagram of QCD matter in the (T, μ)-plane. The solid black line represents the chemical freeze-out, while the dashed orange line illustrates the chiral/deconfinement transition. Both end at the critical point, which is connected to the $\mu = 0$ axis by a cross-over around $T \approx 170$ MeV. The ground state of nuclear matter is at $T = 0$ MeV and $\mu = \mu_0$. For high chemical potential and low temperature, there exists a phase of colour superconductivity. The dashed black lines indicate the estimated properties of the medium created by various experiments [19]

phase diagram with low temperature and density. In this phase, the coupling between partons is strong enough to bind them together.

2. **The QGP phase:** At high temperatures and/or densities, the hadrons overlap beyond a limit where quarks no longer see the nucleonic density and the strong nuclear force becomes weaker, the protons and neutrons within nuclei "melt" into their constituent quarks and gluons. This is known as the quark-gluon plasma phase. The phase transition at high baryon chemical potential (μ_B or μ) and low temperature is first order, whereas, at high temperature and low μ, the transition is continuous (2^{nd} order phase transition), this region is called "cross-over" region starts after the critical point. Figure 1.4, shows the Lattice QCD predictions of energy density (ϵ) and

pressure of the QCD medium as a function of temperature. In this figure, a sudden rise of ϵ/T^4 in the temperature around 150 MeV, followed by a steady saturation towards a high temperature below the Stefan-Boltzmann limit. This suggests that in this temperature range, thermodynamical characteristics change quickly. This may be understood by a phase transition to a rise in the partonic number of degrees of freedom from hadronic degrees of freedom. It is supposed that this unconfined state of matter existed in the early universe. The study of QCD at non-zero baryon chemical potential is challenging due to the so-called "sign problem" in lattice QCD simulations. Lattice QCD is a numerical approach to study QCD on a discrete space-time lattice. In lattice QCD simulations, the partition function of QCD is expressed as a path integral over all possible configurations of the quark and gluon fields. However, at non-zero baryon chemical potential, the fermion determinant in the partition function becomes complex, leading to a "sign problem". This makes it difficult to use standard Monte Carlo methods to sample configurations of the quark and gluon fields, which are necessary to calculate thermodynamic quantities. Experimentally, this distinct state of matter may be produced by heavy ion collisions (HIC) in ultra-relativistic space. Once created, QGP immediately expands out due to large pressure gradients. The coloured quarks subsequently bond back to hadrons due to colour confinement when it cools down and expands in volume. The QGP phase's lifespan is calculated to be 10^{-22} s.

3. **The colour superconducting phase** At high densities but low temperatures, the quarks within nucleons are expected to form Cooper pairs, behaving like a superconductor [89]. colour superconductivity is thought to occur in the cores of neutron stars and in the early universe and is an active area of research in the field of high-energy physics.

The exact boundary between these regions is not known and is an active area of research. It is believed that the transition between the hadronic phase and the QGP phase is a smooth crossover [90], while the transition between the QGP phase and the colour superconducting phase is a first-order phase transition. The

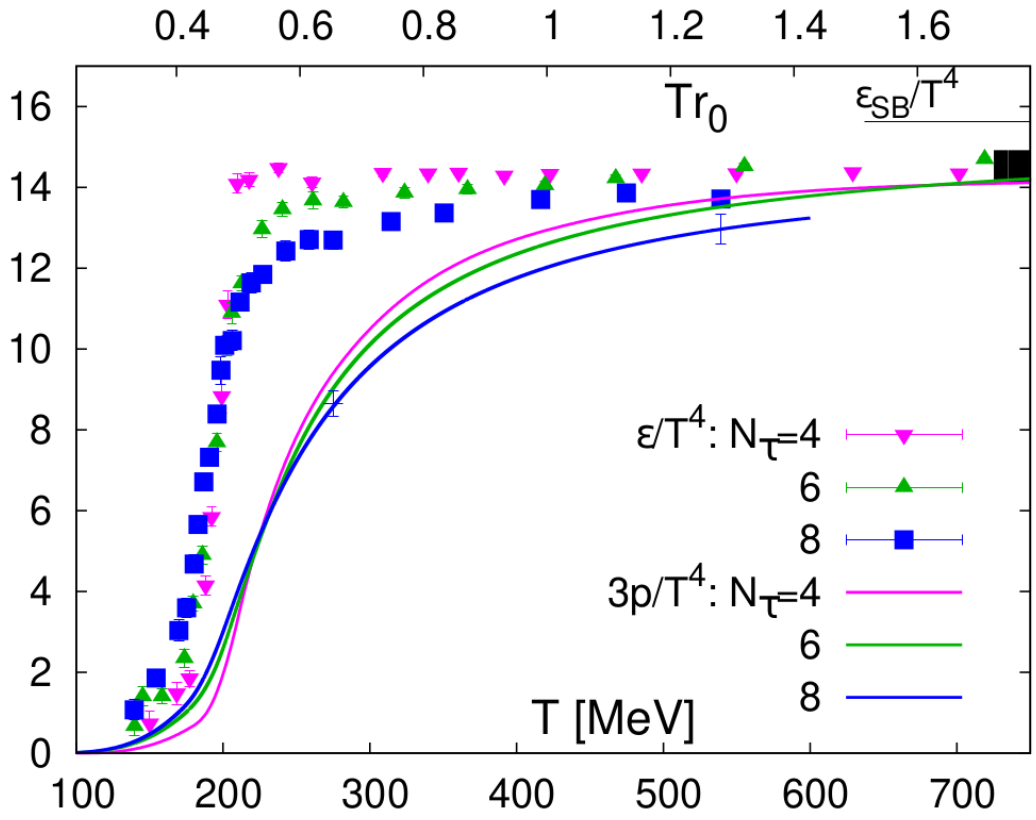

Figure 1.4: Lattice QCD predictions of energy density (marker points) and pressure (lines) of the QCD medium as a function of temperature and normalized by the critical temperature (T_C). ϵ_{SC}/T^4 is the Stefan-Boltzmann limit. Different colours are for different lattice constants [20, 21]

more details of this QGP medium we will show in the section 1.4.1

The phases of QCD can be investigated through the study of heavy-ion collisions in particle accelerators, such as the large hadron collider [91] and relativistic heavy ion collider (at high temperature) [45], and the facility for antiproton and ion research [92] and nuclotron-based ion collider facility (at high baryon density) [93].

1.4 Ultra-relativistic heavy-ion collisions

Ultra-relativistic heavy-ion collisions refer to the collision of two heavy atomic nuclei, such as gold (Au) or lead (Pb), at extremely high energies and velocities that approach the speed of light. These collisions are typically carried out using large particle accelerators. to generate extremely high-energy densities and tem-

peratures that can reach up to several trillion degrees. The goal of these collisions is to recreate the conditions that existed a fraction of a second after the Big Bang in order to study the properties of matter at extremely high temperatures and densities [94].

Heavy-ion collisions have been studied since the early 1960s, starting with low-energy experiments at the Bevatron accelerator. In the 1970s and 1980s, experiments using heavy ions such as sulfur and lead at the Alternating Gradient Synchrotron (AGS) and Super Proton Synchrotron (SPS) demonstrated the possibility of creating a new state of matter, the quark-gluon plasma. The Relativistic Heavy Ion Collider (RHIC) was constructed in the 1990s, where experiments with gold ions confirmed the existence of the quark-gluon plasma and provided new insights. In 2010, the LHC began conducting heavy-ion collisions with lead ions at even higher energies and is currently providing new information about the quark-gluon plasma and the strong force [95].

In recent years, several other heavy-ion facilities have been proposed or are under construction around the world to study the high baryon density region, such as the Facility for Antiproton and Ion Research (FAIR) in Germany, the Nuclotron-based Ion Collider fAcility (NICA) in Russia. These facilities will continue to expand our understanding of the properties of matter at extreme temperatures and densities.

In these collisions, the degree of overlap between the two ions and, therefore, the degree of energy deposited in the collision is determined by impact parameter (b) in units of distance, typically femtometers (fm). It is a measure of the distance between the centers of the two colliding ions at the point of closest approach.

1.4.1 QGP formation

The formation of the QGP in relativistic heavy-ion collisions is a complex process that is still not fully understood. It is believed that it occurs through a combination of several mechanisms and stages, such as deconfinement, chiral symmetry restoration, thermalization, and strong interactions between quarks and gluons in the initial stage of the collision. These mechanisms work together to create a hot,

dense system of particles that collectively form the QGP [45, 91].

Currently, the color glass condensate (CGC) theory is considered as one of the potential explanations for the formation of the quark-gluon plasma (QGP) [96]. This hypothesis is based on the observation that the gluon density increases rapidly as the Bjorken scale, represented by x_T, decreases. The Bjorken scale is the fraction of a hadron's transverse momentum carried by a parton. In CGC theory, as the x_T decreases, the gluon density increases, eventually reaching a point at which the gluons saturate at a specific energy scale (Q). This saturation results in the formation of extremely dense gluonic fields, which are compressed in the lab frame due to the Lorentz contraction. The compression leads to poor coupling among the low x_T gluons, resulting in a loosely coupled and extremely high energy density of gluons in the hadron. The ultra-relativistic velocities of the colliding ions also cause time dilation during the lifespan of the gluons, resulting in a slower evolution of the gluonic fields than the time scales involved in the collision. When these two gluon densities pass one another during the collision, significant electric and magnetic forces are generated. The medium created by these fields is referred to as glasma. The quark-gluon plasma is created when this glasma equilibrates and decays into gluons. In summary, the CGC theory posits that the formation of the quark-gluon plasma in relativistic heavy-ion collisions is a result of the saturation of gluon densities, leading to the formation of dense gluonic fields and the subsequent equilibration and decay of the glasma.

1.4.2 Dynamics of Ultra-Relativistic Collisions: A Study of Space-Time Evolution

The space-time evolution of ultra-relativistic collisions can be described using the theory of special relativity and the principles of quantum field theory. These collisions occur when two particles, each with very high energy and momentum, collide with one another. The resulting interactions can produce new particles and phenomena that are not observed in lower energy collisions [97]. The evolution of ultra-relativistic collisions can be seen in Fig. 1.5. A brief explanation of each evolution step is described below.

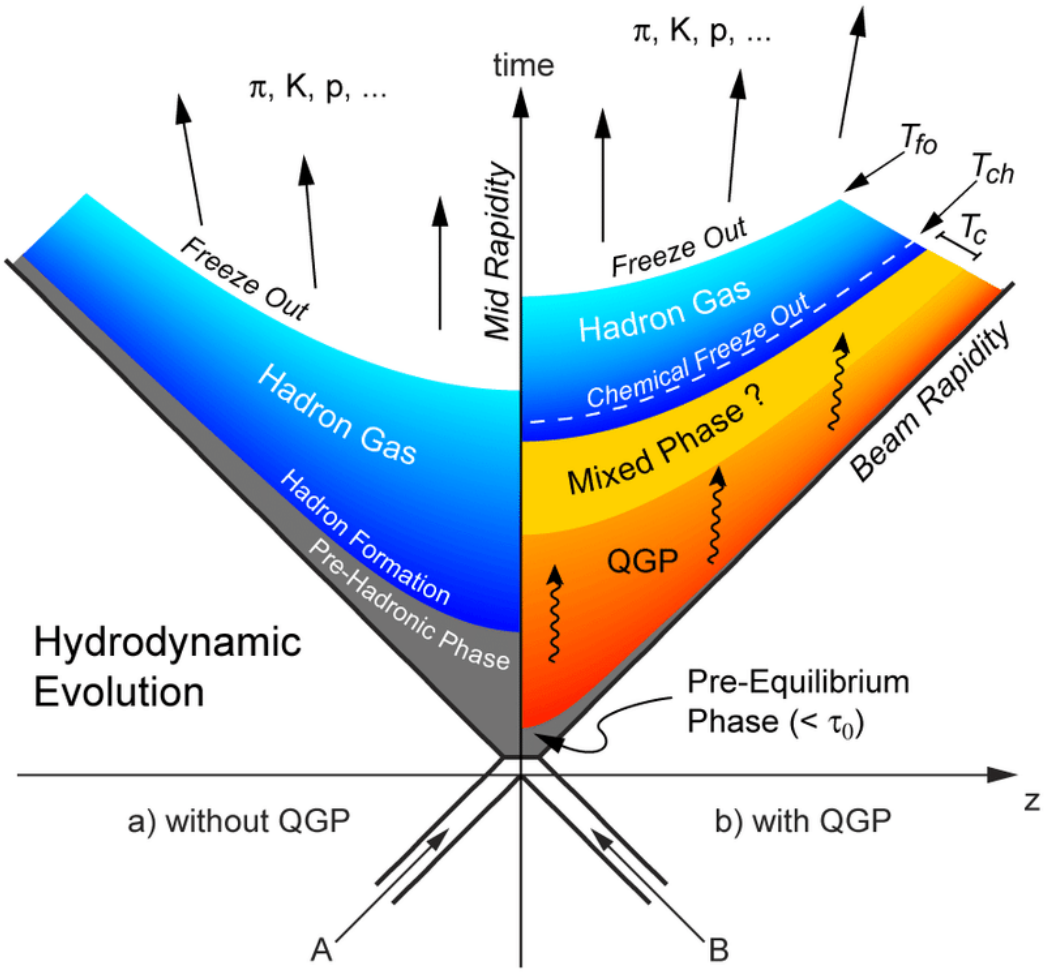

Figure 1.5: Space-time evolution of relativistic heavy-ion and hadronic collisions [19].

- **The pre-equilibrium phase:** This phase of ultra-relativistic collisions refers to the evolution time $\tau \leq 1fm/c$. During this phase, the colliding particles interact, producing subatomic particles and phenomena such as initial state radiation (ISR), colour fields, and jets. ISR occurs when the incoming particles emit radiation before they collide, reducing their energy and momentum. colour fields associated with the strong nuclear force are formed between the colliding particles and can produce a variety of subatomic particles. In this stage, particles are mainly generated by the hard QCD process, which later creates Jets (collimated streams of particles). Also, in this stage, colliding particles interact with one another and create a high-energy and dense region known as the "fireball." The temperature and density of the fireball can reach trillions of degrees and densities comparable to that of an

atomic nucleus.

- **Formation and evolution of QGP:** The initial pre-equilibrium state of the collision can evolve to the final stage through interactions among the partons, which can be both elastic and inelastic. These interactions become increasingly important in central collisions, where the energy density is high enough to push the produced partons to interact with one another. As these interactions occur, the system approaches thermal equilibrium, with a thermalization time of roughly one femtosecond. This state is known as the QGP, a high-temperature state of matter in which quarks and gluons are liberated from the confinement of protons and neutrons. The behavior of the QGP can be described using the principles of relativistic hydrodynamics, which is the study of the flow and behavior of fluids. Hydrodynamic theories are able to account for the behavior of the locally thermalized QGP, indicating that the medium generated in heavy-ion collisions behaves as a strongly correlated liquid rather than a weakly interacting gas [98]. This is the result of the high-pressure gradients within the QGP, which arise from inhomogeneities in the densities of the medium. As the system expands and cools, it eventually reaches a phase transition, beyond which the coloured partons begin to form colourless hadronic states, known as hadronization. At this point, a hadronic description of the system is required. This phase is also known as the mixed phase, where both hadrons and partons are present in the system.

- **Chemical freeze-out:** This occurs when the density of the hot matter drops below a critical value, and particle interactions become rare. At this point, the chemical composition of the matter becomes fixed, and the number of particles of each type (protons, neutrons, mesons, and baryons) is determined. The temperature at which chemical freeze-out occurs is typically around 150-170 MeV, which corresponds to a few times the temperature of the center of the Sun [99].

- **Kinetic freeze-out:** At this stage, the particle interactions become less frequent, and the momentum of each particle becomes fixed. [99] This phe-

nomenon is known as kinetic freeze-out. During this process, the particle interactions become so rare that the particles can be considered to move freely, with no further interactions among them. Finally, these particles reach the detector. Kinetic freeze-out typically occurs at a temperature around 100-120 MeV. The momentum distribution of the particles at kinetic freeze-out can provide valuable information about the properties of the quark-gluon plasma, such as its temperature, pressure, and viscosity.

1.5 Experimental observables

As discussed, a direct study of the QGP in heavy ion collisions is not possible due to its very short lifetime of less than 10 fm/c. Therefore, indirect probes are required to investigate the properties of this medium. The investigation of the characteristics of the QCD medium is carried out by gauging multiple final state observables, including particle yields, multiplicity, and transverse momentum distribution. In this segment, we present the azimuthal anisotropy and nuclear modification factor of heavy-flavour decay electrons that are employed to characterize the QGP. Ultimately, we explore the relative contribution of beauty quarks to heavy-flavour decay electrons, together with its theoretical forecasts, and examine the alterations in the fragmentation of heavy quarks in the QGP, which form the focal point of this thesis.

1.5.1 Heavy-flavour production

Heavy-flavour hadrons, which are made up of c or b valence quarks and a light quark, are of particular interest. These quarks have a large mass, which causes them to be mainly produced in the early stages of the collision, before the formation of the QGP, unlike the light quarks, which can be produced from a thermal medium. By studying heavy-flavour hadrons, important information on the properties of the QGP can be obtained [100].

According to pQCD, the production cross-section for heavy quarks is computed through the factorization theorem, expressed as:

$$d\sigma^{\text{hard}}_{AB\to C} = \Sigma_{a,b,X} f_{a/A}(x_a, Q^2) \otimes f_{b/B}(x_b, Q^2) \otimes \ d\sigma^{\text{hard}}_{ab\to cX}(x_a, x_b, Q^2) \otimes D_{c\to C}(z, Q^2) \quad (1.3)$$

This equation uses several terms to describe the various probabilities and functions involved. For example, $f_{a/A}(x_a, Q^2)$ and $f_{b/B}(x_b, Q^2)$ are parton distribution functions that describe the probability of finding a parton "a" or "b" inside particles "A" or "B" given a fraction of momentum (x) and a factorization scale (Q^2). The term $d\sigma^{\text{hard}}_{ab\to cX}(x_a, x_b, Q^2)$ represents the partonic hard scattering cross-section, and $D_{c\to C}(z, Q^2)$ is the fragmentation function of the produced parton "C", which can be studied using jet and correlation measurements.

The motivation for studying heavy-flavour production lies in the fact that heavy quarks, particularly charm and beauty quarks, are excellent probes of the QGP. When traversing the QGP, heavy quarks experience elastic and inelastic interactions with the partons in the plasma. Thus, they undergo the full evolution of the QGP. Heavy quarks also lose less energy than light quarks due to the absence of gluon radiation at forward angles, below $\theta < \text{M/E}$, where M is the quark mass and E is its energy. This phenomenon, predicted by QCD, is called the dead-cone effect [101]. This is a universal effect as it does not depend on the nature of the gauge interaction nor the spin of the particle.

Heavy-flavour hadrons can be studied in two different ways, either by fully reconstructing the D and B hadrons through their hadronic decay channels or by studying the leptons from the semi-leptonic decays of heavy-flavour hadrons. Reconstruction through their hadronic decay channels requires a very good tracking system and large statistics. In contrast, semi-leptonic decay offers the advantage of a relatively large branching ratio, of the order of 10% for both charm and beauty hadrons. Additionally, electrons can be identified directly using calorimeters and hence can be used as trigger particles. The disadvantage of studying heavy-flavour via leptons is that the hadron momentum cannot be reconstructed due to the missing neutrino.

1.5.2 Azimuthal anisotropy

The azimuthal distribution of emitted particles in the plane perpendicular to the beam direction is a sensitive experimental observable that provides insights into the dynamics of the early stages of heavy-ion collisions. In non-central collisions, the initial matter distribution is anisotropic due to the almond-shaped geometrical overlap region. If the matter is strongly interacting, this spatial asymmetry is converted into an anisotropic momentum distribution through multiple collisions between partons. The anisotropy of the produced particles is decomposed into the Fourier coefficients.

$$\frac{dN}{d\varphi} \propto 1 + 2\sum_{n=1}^{\infty} v_n \cos[n(\varphi - \Psi_n)], \tag{1.4}$$

Here φ is the azimuthal angle, and Ψ_n is the azimuthal angle of the initial state symmetry plane for the n$^{\text{th}}$ harmonic. The first coefficient of Fourier series decomposing is called direct flow (v_1), whereas the second coefficient is called the elliptic flow (v_2) [102].

Hydrodynamical models predict and explain most of the measurements of the elliptic flow of light hadrons at low transverse momentum ($p_T < 2-3$ GeV/c). The elliptic flow measurements provide evidence that the created matter equilibrates in an early stage of the collision and evolves according to the laws of hydrodynamics, behaving nearly like a perfect fluid [45, 103].

The measurements of elliptic flow for heavy quarks provide additional insight into the transport properties of the medium. Since heavy quarks are produced in the initial stages of the collision, they experience the full evolution of the system, providing information about the medium's properties and its interaction with heavy quarks. The measurement of heavy quark elliptic flow can also help constrain the transport coefficients, such as the heavy quark diffusion coefficient, which is sensitive to the medium's transport properties.

Fig. 1.6 depicts the v_2 of D mesons, which is found to be of similar magnitude to that of charged particles, which is dominated by light-flavour hadrons [22].

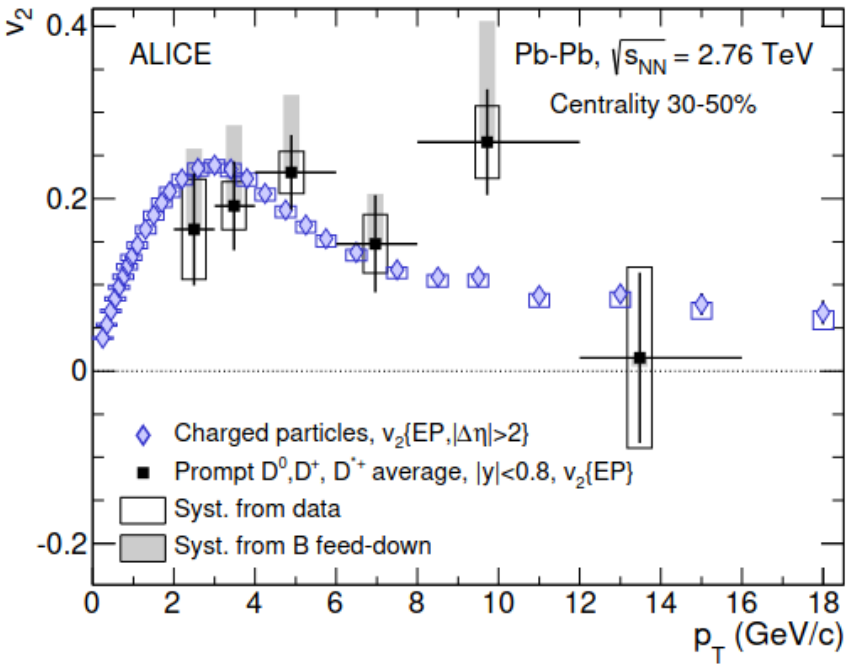

Figure 1.6: The average v_2 of D^0, D^+, and D^{*+} as a function of p_T is compared to the v_2 of charged particles measured using the event plane (EP) method. The symbols representing the D mesons are placed horizontally at the mean p_T of the three species [22].

The average v_2 of D mesons in the $2 < p_T < 6$ GeV/c range is measured to be $0.204 \pm 0.030(\text{stat}) \pm 0.020(\text{syst})^{+0.092}_{-0}$, indicating a positive deviation from zero with a significance of 5.7σ. This suggests that the interactions between the charm quarks and the medium constituents transfer information on the azimuthal anisotropy of the system, indicating that low momentum charm quarks are involved in the collective motion of the system. A positive v_2 is also observed for $p_T > 6$ GeV/c [22], which is likely due to the path-length dependence of the partonic energy loss, although the large uncertainties prevent a definitive conclusion.

1.5.3 Nuclear modification factor

The nuclear modification factor (R_{AA}) is a key observable in the study of high-energy nuclear collisions, particularly in the search for the QGP [104]. It is defined as the ratio of the yield of particles produced in heavy-ion collisions to the yield of particles produced in proton-proton collisions, scaled by the number of binary nucleon-nucleon collisions ($\langle N_{coll} \rangle$) to account for the different sizes and densities of the colliding systems,

$$R_{AA}(p_T) = \frac{dN^{AA}/dp_T}{\langle N_{coll}\rangle dN^{pp}/dp_T}, \tag{1.5}$$

Here, dN^{AA}/dp_T and dN^{pp}/dp_T represent the transverse momentum distribution of particles in heavy-ion and proton-proton collisions, respectively. $R_{AA}(p_T)$ measures the degree to which the particle production is suppressed in heavy-ion collisions compared to proton-proton collisions. If the QGP is formed in heavy-ion collisions, the partons produced in the initial stages of the collision will interact strongly with the surrounding medium, leading to parton energy loss and suppression of high-p_T particle production. As a result, $R_{AA}(p_T)$ is expected to be less than unity at high p_T.

The measurement of $R_{AA}(p_T)$ provides important information about the properties and evolution of the QGP. The suppression of high-p_T particles observed in $R_{AA}(p_T)$ measurements suggests that the QGP behaves as a strongly interacting and dense medium, with a large energy density that can modify the properties of the produced particles. Moreover, the measurement of $R_{AA}(p_T)$ as a function of the collision centrality provides information about the parton energy loss as a function of the QGP density and temperature.

In recent years, $R_{AA}(p_T)$ measurements have been extended to different particle species, including hadrons containing heavy quarks. The measurement of $R_{AA}(p_T)$ for heavy quarks provides a powerful tool to study the interaction of heavy quarks with the QGP, which is sensitive to the heavy quark mass and the QGP transport properties. Furthermore, the measurement of $R_{AA}(p_T)$ for hadrons containing heavy quarks, such as D mesons and B mesons, can provide information about the modification of the heavy quark fragmentation in the QGP.

- **Quarkonia suppression**

  One of the most important probes of the QGP is the suppression of quarkonia states, such as charmonia ($c\bar{c}$) and bottomonia ($b\bar{b}$). The suppression of these states is attributed to the dissociation of the bound state due to the screening effect of the QGP [105].

  Charmonium Suppression

Charmonia states are formed by a $c\bar{c}$ pair bound by the strong nuclear force. The ground state of charmonium is the J/ψ particle, which is composed of a charm quark and a charm anti-quark. In the QGP medium, the charm quarks interact with the gluons and light quarks, leading to the screening of the potential between the charm quark and anti-quark [106]. This results in the dissociation of the J/ψ state, which is the dominant source of charmonium suppression in heavy-ion collisions [107].

In addition to the screening effect, other mechanisms contribute to charmonium suppression, such as the regeneration of $c\bar{c}$ pairs from the QGP and the cold nuclear matter effect. These effects make it challenging to extract the precise contribution of the QGP screening to the charmonium suppression. However, it has been observed that the suppression of the J/ψ state increases with the centrality of the collision, indicating that the QGP plays a dominant role in charmonium suppression in central collisions.

Bottomonium Suppression

Bottomonium states, such as the Υ particle, are composed of a $b\bar{b}$ pair. The suppression of bottomonium states in heavy-ion collisions is less pronounced than that of charmonium states due to the larger binding energy of the bottomonium states. The $\Upsilon(1S)$ state, which is the ground state of bottomonium, is expected to be suppressed by the QGP screening effect. However, the suppression of higher bottomonium states, such as the $\Upsilon(2S)$ and $\Upsilon(3S)$, is expected to be less sensitive to the QGP screening effect.

Experimental studies have confirmed the suppression of bottomonium states in heavy-ion collisions. The suppression of the $\Upsilon(1S)$ state has been observed to increase with the centrality of the collision, similar to the suppression of the J/ψ state [106]. However, the precise contribution of the QGP screening effect to bottomonium suppression remains to be determined due to the various mechanisms that contribute to the suppression.

- **Strangeness enhancement** The concept of strangeness enhancement has been put forward as a potential marker for the occurrence of QGP formation. The notion was initially proposed in [108]. It has been determined that $s\bar{s}$

pairs are predominantly produced in QGP via the gluonic ($gg \rightarrow s\bar{s}$) channel. At the RHIC and LHC energies, QGP is characterized by a high density of gluons, creating the necessary conditions for $s\bar{s}$ pair production.

The strange quark's mass is approximately 95 MeV, which is comparable to the critical temperature ($T \sim 170$ MeV) for the QCD phase transition, implying that the strange quark reaches thermal equilibrium before the QGP undergoes a phase transition [109]. The process of Pauli blocking of light quarks (u, d) also plays a role in enhancing the production of strange quark pairs. All quarks are fermions and adhere to the Pauli Exclusion Principle. As more up and down quarks are generated in the collision, they fill up the lower Fermi energy levels, making $s\bar{s}$ pair production more favorable.

Thus, the QGP is expected to be made up of gluons, u, d, and s quarks, with an increase in strange hadron production compared to other light hadrons in collisions where a QGP medium is anticipated to form. Experimental observations from the ALICE experiment in Pb-Pb collisions at $\sqrt{s_{\rm NN}} = 2.76$ TeV have confirmed the phenomenon of strangeness enhancement [25], providing compelling evidence for the existence of QGP in heavy-ion collisions at ultra-relativistic energies.

1.5.4 Jet quenching

In high-energy nuclear collisions, jets are formed when energetic partons (quarks or gluons) are produced in the early stages of the collision and subsequently fragment into collimated sprays of hadrons in a narrow cone. These collimated particles are called the jet. When these jets pass through the hot and dense medium, they lose energy due to interactions with the medium. This phenomenon is called jet quenching.

The jet quenching phenomenon is a consequence of the strong interactions between the high-energy particles in the jet and QGP medium. These interactions can cause the particles in the jet to lose energy. This energy loss results in the reduction of the number of particles and the modification in the fragmentation pattern of the jet.

Jet quenching is an essential phenomenon in the study of QGP because it provides information about the properties of this hot and dense medium, such as its viscosity and transport properties. As shown in Fig. 1.7, the energy loss of a jet generated in the central collision would be greater than that of a jet produced at the peripheral collision due to the strength of the QGP medium [23]. In the next section, we will discuss these jet properties using jet-like two particle correlation.

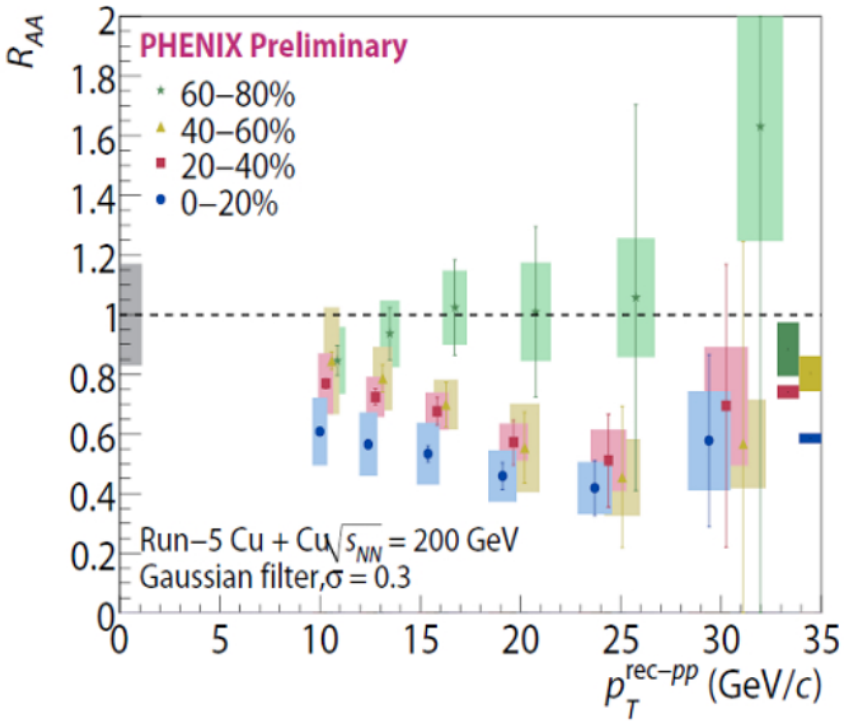

Figure 1.7: Jet nuclear modification factors measured in Cu–Cu collisions at $\sqrt{s_{\mathrm{NN}}} = 200$ GeV [23].

1.5.5 Modification of jet-like two particle correlation yield

The study of jet properties provides insight into the properties of the dense matter produced in these collisions, including the QGP. One of the key observables for the study of jet properties is the two-particle correlation function, which measures the probability of finding a particle at a certain angle and momentum relative to the trigger particle. In this thesis, we will discuss the modification of jet-like two-particle correlation yields in heavy-ion collisions compared to proton-proton collisions.

The two-particle correlation function is defined as:

$$C(\Delta\eta, \Delta\phi) = \frac{1}{N^{trig}} \frac{d^2 N_{pairs}}{d\Delta\eta d\Delta\phi}, \tag{1.6}$$

where $\Delta\eta$ and $\Delta\phi$ are the differences in pseudorapidity and azimuthal angle, respectively, between the two particles in the pair. $d^2N_{pairs}/d\Delta\eta d\Delta\phi$ is the distribution of particle pairs as a function of $\Delta\eta$ and $\Delta\phi$, and N^{trig} is the number of triggered particles. In heavy-ion collisions, the two-particle correlation function is sensitive to the underlying jet structure, as the produced partons may interact with the surrounding medium and lose energy before fragmenting into hadrons.

The modification of jet-like two-particle correlation yields is quantified by the I_{AA}, similar to the nuclear modification factor, R_{AA}, defined as:

$$I_{AA} = \frac{Y_{\mathrm{AA}}}{Y_{\mathrm{pp}}}. \tag{1.7}$$

I_{AA} measures the deviation of the two-particle correlation function in heavy-ion collisions from that in proton-proton collisions and provides information about the modifications of jet-like correlations due to the presence of the QGP. In particular, I_{AA} can reveal the energy loss of partons as they traverse the QGP, as well as the modification of jet fragmentation due to the medium.

The typical structure of a two-particle azimuthal correlation function contains two peaks and a baseline as shown in Fig 1.8. The correlation function is characterized by the following components:

- **Baseline** The baseline contribution to the correlation function represents the uncorrelated pairs of particles, which arise from various sources, such as the underlying event and detector effects.
- **Near-side peak** The near-side peak in the correlation function is typically located at small azimuthal angles ($\Delta\varphi \approx 0$) and is associated with the triggered particle.
- **Away-side peak** The away-side peak in the correlation function is typically located at large azimuthal angles ($\Delta\varphi \approx \pi$) and is associated with the

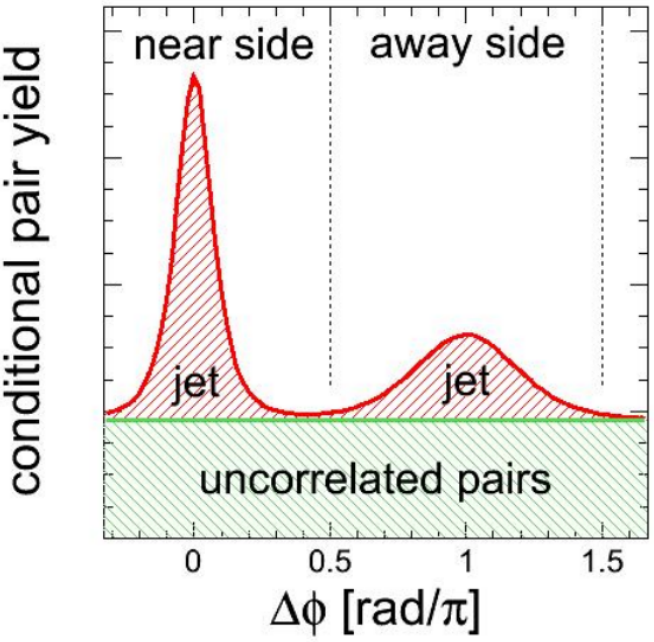

Figure 1.8: A typical structure of the two particle azimuthal-correlation distribution containing the near- and away-side peaks with baseline.

recoiled jet. This type of peak arises in a back-to-back configuration.

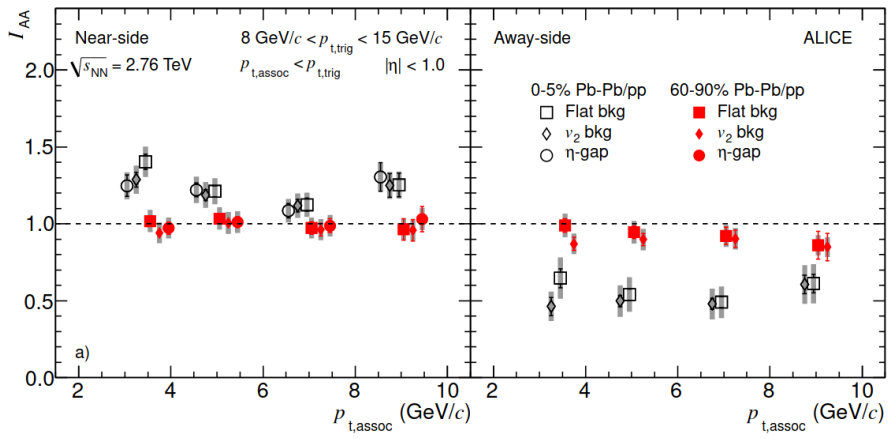

Figure 1.9: IAA for near-side (left panel) and away side (right panel) for central ($0-5\%$ PbPb/pp) and peripheral ($60-90\%$ PbPb/pp) collisions measured by the ALICE detector [24].

The results are presented in Fig. 1.9, which shows the yield ratio, I_{AA}, for central (0-5%) and peripheral (60-90%) Pb–Pb collisions at $\sqrt{s_{\mathrm{NN}}} = 2.76$ TeV. In central collisions, there is an away-side suppression ($I_{\mathrm{AA}} \approx 0.6$), which indicates in-medium energy loss. Additionally, the near-side I_{AA} displays an enhancement of around 20-30% above unity, which has not been significantly observed in RHIC experiments at similar momenta. This near-side enhancement suggests

that the near-side parton is also subject to medium effects, possibly due to various factors such as a change in the fragmentation function, a possible change of the quark/gluon jet ratio in the final state due to their different coupling to the medium, or a bias on the parton p_{T} spectrum after energy loss due to the trigger particle spectrum [24]. The sensitivity of I_{AA} and R_{AA} to different properties of the medium makes their combination particularly effective in constraining jet quenching models.

1.6 QGP-like signatures in small systems

One of the hallmarks of the formation of QGP is the generation of a significant number of particles. Heavy-ion collisions, such as Pb–Pb collisions, produce several thousand final state charged particles, thereby increasing the likelihood of creating highly dense matter. In the central rapidity region, it has been observed indirectly that pp collisions at LHC energies produce an average of (5-10) particles, with some events producing 100 or more particles, which are known as high-multiplicity events. Recent arguments suggest that QGP-droplets could potentially form during such events if they occur. In this discussion, we will briefly consider some observations related to the possible formation of QGP-droplets in high-multiplicity pp collisions.

- **Strangeness enhancement**

  Fig. 1.10 displays the yield ratio of the strange and multi-strange particle with non-strange particle (pions), integrated over transverse momentum (p_{T}), as a function of charged particle multiplicities. The data reveals a significant increase in the production of strange particles in high-multiplicity collisions.

- **Ridge-like structure in multi-particle correlations**

  The ridge-like structures observed in high-multiplicity proton-proton collisions at $\sqrt{s} = 13$ TeV are depicted in Fig. 1.11. In heavy-ion collisions, the development of such structures, which exhibit a long-range in pseudorapidity with large $\Delta\eta$ and a near-side peak in azimuthal angle with small $\Delta\varphi$, can

be attributed to the collective expansion of the strongly interacting matter.

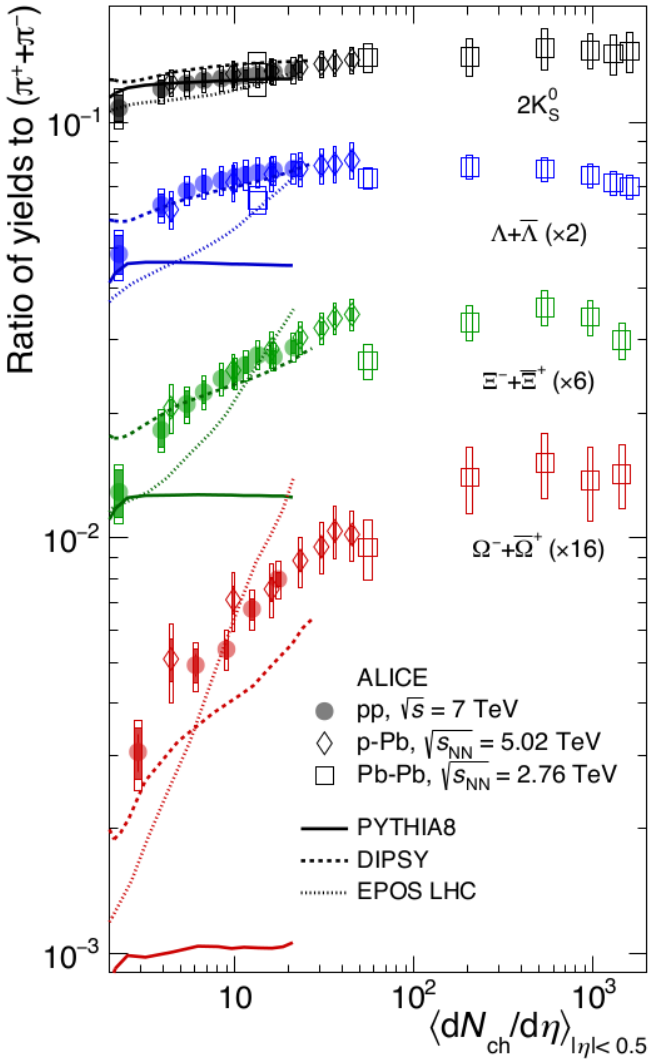

Figure 1.10: The correlation between the charged particle pseudorapidity density and the ratio of multi(strange) particles to pions varies across proton-proton, proton-lead, and lead-lead collisions at LHC energies. [25].

- **Large radial flow velocity**

  Fig. 1.12 displays the determination of the kinetic freeze-out temperature ($T_{\rm kin}$) and radial flow velocity ($\langle\beta_T\rangle$) obtained from the Blast-wave fit of the low-$p_{\rm T}$ spectra of identified particles [110]. The analysis reveals a radial flow velocity of 0.49 ± 0.02 in proton-proton collisions at $\sqrt{s} = 7$ TeV. This indicates a significant degree of collectivity in high-multiplicity proton-proton collisions, akin to what is observed in heavy-ion collisions. These intriguing observations at LHC energies raise the possibility of the formation of a

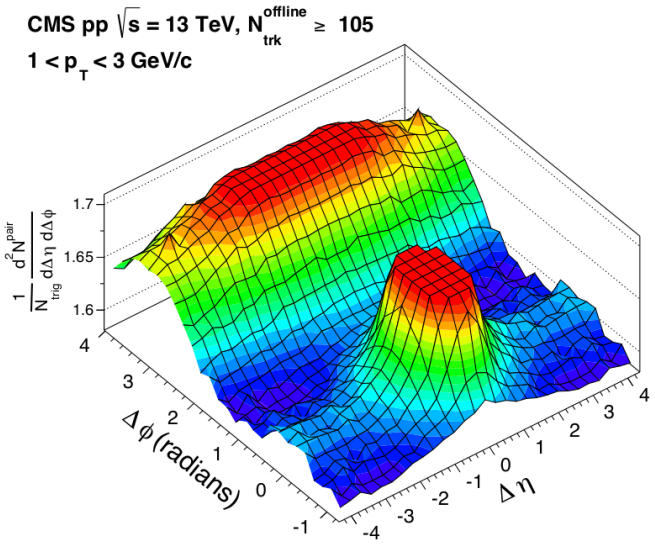

Figure 1.11: The correlation function for pairs of charged particles with each particle having a transverse momentum between 1 and 3 GeV/c, displaying a ridge-like structure in high-multiplicity proton-proton collisions at 13 TeV [26].

medium in high-multiplicity proton-proton collisions. Additionally, the presence of a hadronic phase in proton-proton collisions has been experimentally confirmed, as discussed in references [111, 112], which calls for further investigations. These findings challenge our understanding of small systems, which were once thought to be devoid of any thermalized medium.

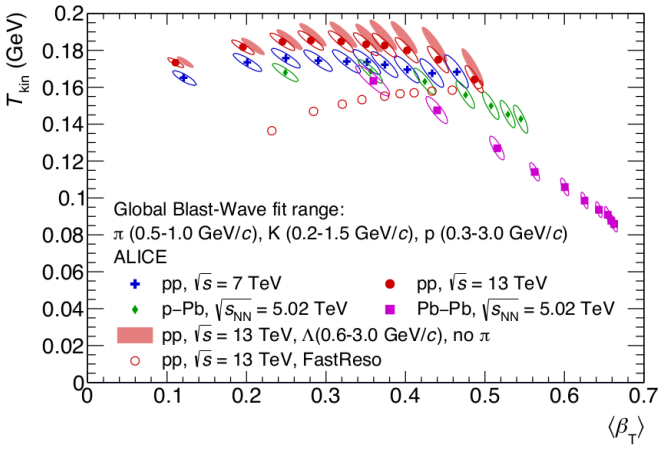

Figure 1.12: The kinetic freeze-out temperature and radial flow velocity were measured for pp, p–Pb, and Pb–Pb collisions at LHC energies [26].

1.7 Motivation of the thesis

The ALICE experiment at the large hadron collider allows us to study ultra-relativistic heavy-ion collisions. The goal is to explore the properties of the QGP. The ALICE experiment specializes in studying the QGP and other properties of matter produced in heavy-ion collisions, including the temperature, energy density, and viscosity, as well as the behavior of quarks and gluons within the medium. This helps us to determine the properties of the QGP and study it at different energy scales.

One motivation of this thesis is to study the properties of heavy flavor jets using two particle azimuthal correlation, specifically, the production and fragmentation process of heavy flavors like charm and bottom quarks. Heavy flavors are produced in initial hard scattering processes and are sensitive to the dynamics of the underlying process. By studying heavy flavor production, we can learn about the properties of the partons participating in the scattering and the dynamics of the initial state. The ALICE Collaboration measured the azimuthal correlation distributions of prompt D mesons with charged particles in pp collisions at $\sqrt{s}$ = 5.02, 7, and 13 TeV for D mesons with transverse momentum ($p_{\mathrm{T}}^{\mathrm{D}}$) up to 36 GeV/$c$ and transverse momentum of associated charged particle ($p_{\mathrm{T}}^{\mathrm{assoc}}$) up to 3 GeV/$c$ [11–13]. The measurements were compared with Monte Carlo (MC) simulations using different event generators, such as PYTHIA [15, 113, 114], HERWIG [115, 116], EPOS [117, 118], and POWHEG coupled with PYTHIA8. By measuring the correlation distribution between heavy-flavor decay electrons and charged particles, a much larger sample of correlation pairs was obtained, allowing for a significant extension of the $p_{\mathrm{T}}^{\mathrm{assoc}}$ range and providing a complete picture of heavy quark fragmentation [11, 12]. Electrons from beauty-hadron decays dominate the heavy-flavor hadron decay electron spectrum at high $p_{\mathrm{T}}^{\mathrm{e}}$ [119], and probing large enough trigger electron transverse momenta enables the study of the correlation function of particles originating from beauty-hadron decays, which can provide information on the different correlation structures for charm and beauty quarks. This additional information can be used to constrain MC simulations further.

In addition, we endeavored to examine the properties of fragmentation in regions where the experimental study is currently unfeasible. In this direction, azimuthal correlations between heavy flavour with charged particles are measured in pp, p–Pb, and Pb–Pb collisions. We expanded the range of kinematics for electrons resulting from the decay of heavy flavor hadrons which is currently not possible in experimental data due to statistics. We predicted the modification of the fragmentation function in heavy-ion collisions using the PYTHIA8 Angantyr model. Our investigation aimed to understand how parton and hadron-level processes can impact fragmentation properties, and we compared the correlation of charm mesons with charm baryons and beauty mesons. This thesis reports the results for various kinematic regions of heavy flavour hadrons, their decay electron, and associated charged particles. The measurements are used to study and characterize jet fragmentation and hadronization of heavy quarks. The results from different collision systems are compared to study the effects of cold-nuclear matter and hot-nuclear matter, and comparison between different particle species helps us to investigate the individual particle fragmentation properties. Additionally, this thesis also tried to establish the PYTHIA8 Angantyr model for heavy ion collisions, though it does not include the quark-gluon plasma medium. This thesis also delves into the production of identified, strange, and multi-strange particles in Pb–Pb collisions. Through this, we sought to investigate how multi-parton interactions, colour reconnection, and string shoving affects the experimentally measured quantities and to gain insights into the collective nature of the produced particles. We also attempt to study the p_{T} spectra and integrated yields of identified, strange, and multi-strange particles.

1.8 Thesis layout

The thesis is organized in the following manner:

In chapter 1, we have introduced high-energy physics by discussing the early stage of the Universe, the Standard Model, and QCD. A description of the QCD phase diagram and quark-gluon plasma has also been provided. Finally, we talked about the motivation of the thesis.

In chapter 2, a brief description of the LHC has been provided. ALICE experiment and its detectors are explained in detail. The motivation of some particle event generators is also mentioned.

Chapter 3 presents a detailed study of the azimuthal correlation between heavy-flavour hadron decay electrons with charged particles. The methodology, electron identification, and construction of the correlation function are discussed in detail.

In chapter 4, detailed calculations and assignment of systematic uncertainties are discussed.

Chapter 5 explains the results that we obtained using ALICE data analysis on the azimuthal correlation of heavy-flavour hadron decay electron with charged particles.

Chapter 6 presents the phenomenological study using the PYTHIA8 Anagantyr model.

In chapter 7, finally, the results and outcomes of the thesis have been summarized.

Chapter 2

Experimental setup and event generators

2.1 The large hadron collider

Physicists are now able to go beyond the Standard Model [43, 120] with the LHC, which is pushing the boundaries of human understanding. The LHC is at the vanguard of efforts to comprehend the fundamental nature of the cosmos in this period for cosmology, astrophysics, and high-energy physics.

The discovery of the Higgs boson in 2012 [121] is undoubtedly a major milestone in the history of physics. Beyond this, the LHC has the ability to help find answers to some of the most critical problems of the day as:

- The existence, or not, of supersymmetry
- The nature of dark matter
- The presence of extra dimensions

It is also essential to continue to study the properties of the Higgs.

The Large Hadron Collider (LHC) [122], a synchrotron accelerator, is currently the world's biggest and most potent particle accelerator. It is located at the Conseil Européen pour la Recherche Nucléaire (CERN), close to the Swiss-French border and the city of Geneva. The ring's circumference is $\sim$ 27 kilometers long and is typically installed between 45 to 100 meters below the earth. The beam pipes cross at the four interaction points where the collisions happen. The beams

share a 130 meter long common beam pipe at these locations. It was constructed in 1984 to host the Large Electron Positron Collider (LEP) [123], which was demolished in 2001 to make space for the actual accelerator, which is used to study proton-proton (pp), proton-lead (p-Pb), and lead-lead (Pb-Pb) collisions. The LHC is made up of two independent beam pipes with opposing magnetic fields that are connected by a twin-bore magnet. This configuration enables the acceleration of proton beams with a maximum center-of-mass energy of $\sqrt{s} = 14$ TeV with the luminosity $\mathcal{L} = 10^{34}$ cm^{-2}s^{-1} [124], as well as lead nuclei beams providing collisions at $\sqrt{s_{\mathrm{NN}}} = 5.02$ TeV with a peak luminosity of $\mathcal{L} = 10^{27}$ cm^{-2}s^{-1}.

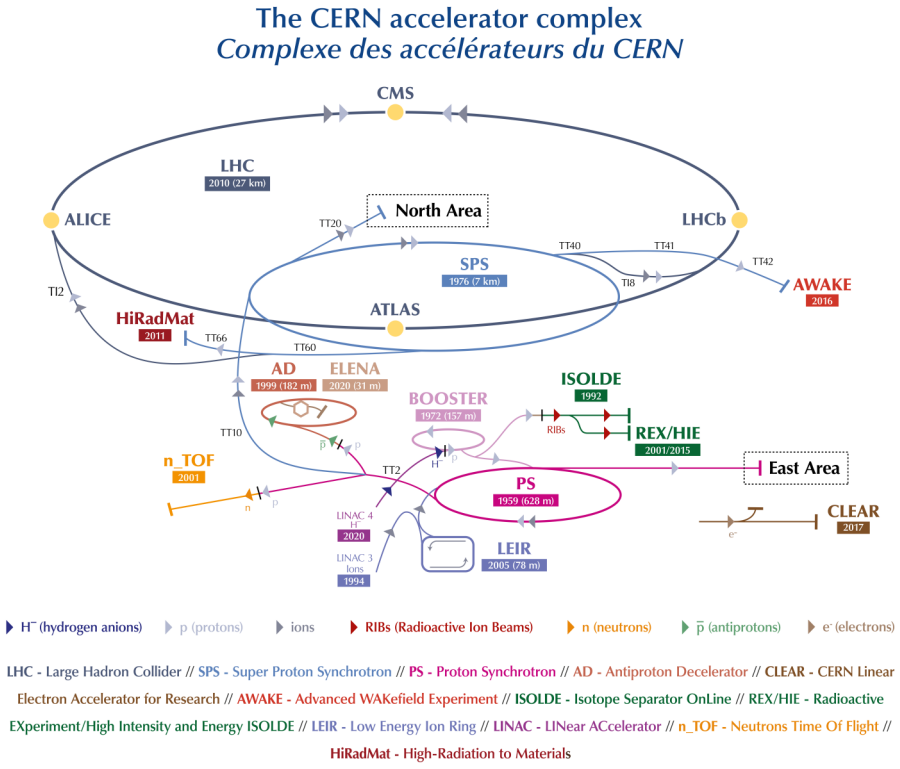

Figure 2.1: The Large Hadron Collider (LHC) and it's injection points [27].

Fig. 2.1 depicts an overview of the LHC as well as the locations of the four main LHC-connected experiments. These are

- **ALICE (A Large Ion Collider Experiment):** This experiment specializes in detecting events with a large multiplicity of generated particles obtained by heavy-ion collisions, is located at site 2 [91]. The purpose of this experiment is to understand the QGP better. A detailed description of this facility can be found in Section 2.2.

- **ATLAS (A Toroidal LHC Apparatus):** This general-purpose detector, situated in site 1 [125], is an experiment developed for novel physics research and designed for pp collisions measurement with the highest interaction rate. It is used for studying dark matter, Super Symmetric particles (SUSY), evidence of extra dimensions, etc.

- **CMS (Compact Muon Solenoid):** This detector serves the same physics goal as the ATLAS experiment [126].

- **LHCb (LHC beauty):** The location of the Large Hadron Collider beauty (LHCb) experiment is at site 8, which is dedicated to the research of heavy flavour physics, specifically the study of hadrons containing beauty quarks and CP violation [127].

The LHC injection mechanism can be seen in Fig. 2.1. The extensive device chain that accelerates protons and drives ions to higher energies ends with this collider. The Linear Accelerator 2 (LINAC2) accelerates protons obtained from hydrogen atoms to a maximum energy of 50 MeV. Once they are accelerated to an energy of about 1.4 GeV inside the proton synchrotron booster (PSB), protons are sent to the proton synchrotron (PS), where they are accelerated to an energy of around 25 GeV. After then, protons are accelerated in the Super Proton Synchrotron (SPS) to an energy of around 450 GeV before entering the LHC collider. The acceleration of Pb ions is different from those of protons. The evaporation of metallic lead creates them, followed by ionization and initial acceleration to an energy of around 4.2 MeV/nucleon is done by the LINAC3 (LINAC3). Later they enter the Low Energy Ion Ring (LEIR), where they reach an energy of around 72 MeV/nucleon. Before being injected into the LHC, the ions travel the same path as the protons, going via PS (5.9 GeV/nucleon) and SPS (177 GeV/nucleon).

2.2 The ALICE experiment

The A Large Ion Collider Experiment (ALICE detector) [91] is a heavy-ion detector situated in IP2 at the LHC. This experiment's primary objectives are the

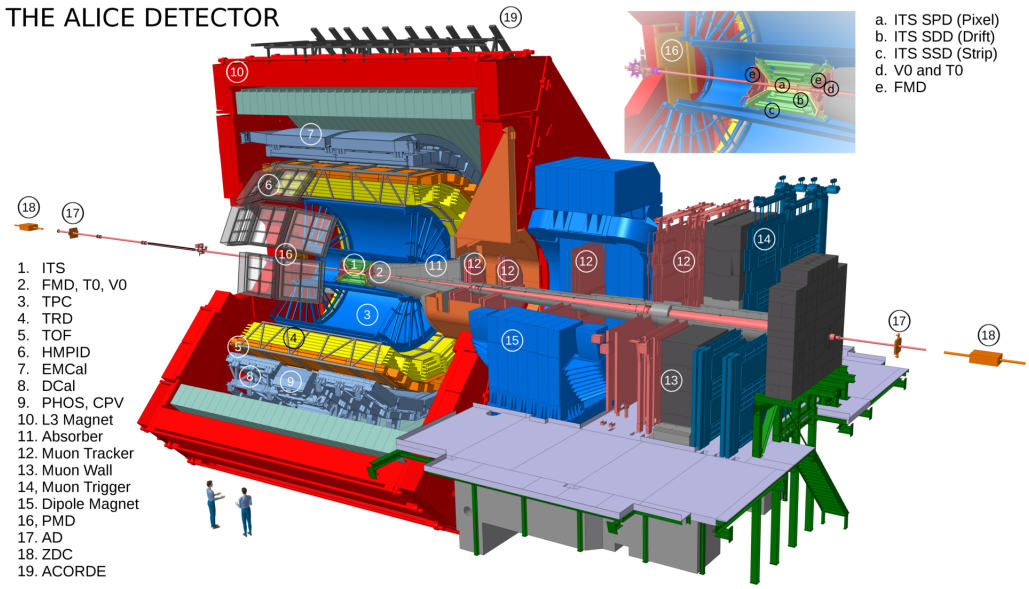

Figure 2.2: A detailed view of the ALICE detector at LHC [28].

characterization of QGP at extremely high energies and densities generated by Pb-Pb collisions to explore the QCD phase diagram and to investigate the physics of strongly interacting matter. The field of experimental relativistic heavy-ion physics was still in its infancy at the time of design in the early 1990s. It was exceedingly challenging to forecast what would happen at the center of mass energies that were hundreds of times higher than those previously attained. Therefore, it was necessary to build a versatile "general-purpose" detector capable of picking up a wide range of potential signals, both anticipated and unexpected. The numerous improvements that have been made since the initial design was demonstrated (the muon spectrometer approved in 1995, the transition-radiation detector in 1999, and the electromagnetic calorimeter in 2007, in addition to a host of upgrades planned for the 2017-2018 shutdown). The huge number of detector subsystems that make use of almost all known detection techniques show that the ALICE detector has the ability to detect a wide range of signals. With the help of its 18 subsystems, which each have their own respective advantages and disadvantages, it is possible to monitor up to 8000 particles in a single event with momenta ranging from 10 MeV/c to more than 100 GeV/c and conduct particle identification over a broad energy range and reconstruct interesting decay vertices. According to the spatial region they occupy, the detector sub-components can be divided into two groups: forward detectors (muon spectrometer) at forward rapidity, used for

triggering, and central-barrel detectors at mid-rapidity for particle identification and tracking. The charged particle multiplicity at mid-rapidity reaches values of several thousand per event in central Pb–Pb collisions. For this reason, only detectors with high granularity and a low material budget to reduce multiple scattering are adopted in the region surrounding the interaction point, like the Inner Tracking System and the Time Projection Chamber, as described below. Cylindrical systems surround the nominal interaction point with increasing radii, namely the Inner Tracking System (ITS), the Time Projection Chamber (TPC), the Transition Radiation Detector (TRD), and the Time Of Flight (TOF). Two detectors, namely electromagnetic calorimeters (EMCal) and a Ring Imaging Cherenkov (HMPID) detector with a restricted azimuthal acceptance, are added on top of them. A heavy absorber apparatus (muon spectrometer) composed of a dipole magnet and fourteen layers of Resistive Plate Chambers (RPC) triggers muon events and reconstruct them at forward rapidity. After that, the experiment is outfitted with a number of smaller detectors operating at backward and forward rapidity (V0, T0, FMD, PMD, and ZDC), whose primary functions are the characterization of the global event properties. The last step involves installing an array of scintillators (ACORDE) outside the L3 solenoid to trigger and expel cosmic rays, which may also be utilized for alignment.

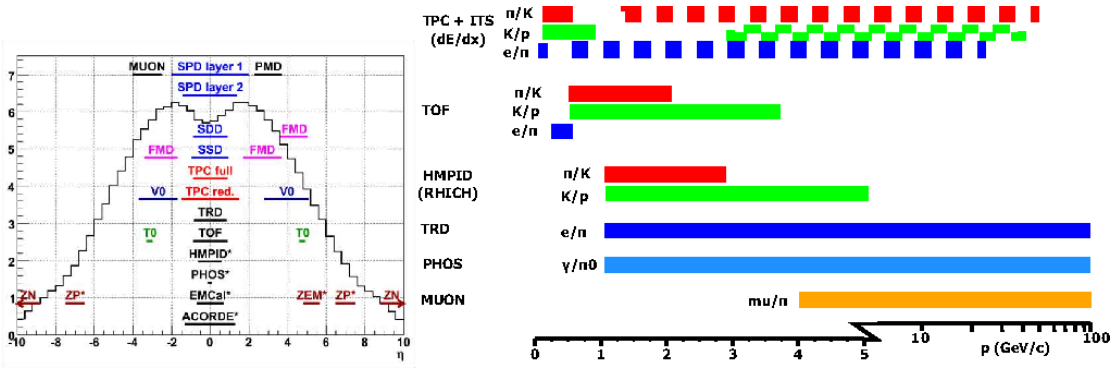

Figure 2.3: Pseudo-rapidity (η) coverage of various sub-detectors of ALICE at LHC [29].

Figure 2.3 illustrates the pseudorapidity ranges for the various detector subsystems. The pseudorapidity acceptance, position, and purpose of all subdetectors are listed in Table 2.1. Except for ACCORDE, all of the central barrel detectors are placed inside a solenoid that was first employed by the L3 experi-

Table 2.1: Detail description of sub-detectors in ALICE at the LHC. The detectors marked with an asterisk (*) are used for triggering [16, 42]

Detector	**Acceptance (η)**	**Acceptance (ϕ)**	**Position**	**Main Purpose**
SPD*	$\pm$2.0	full	r = 3.9 cm	tracking, vertex
	$\pm$1.4	full	r = 7.6 cm	tracking, vertex
SDD	$\pm$0.9	full	r = 15.0 cm	tracking, PID
	$\pm$0.9	full	r = 23.9 cm	tracking, PID
SSD	$\pm$1.0	full	r = 38.0 cm	tracking, PID
	$\pm$1.0	full	r = 43.0 cm	tracking, PID
TPC	$\pm$0.9	full	85 < r/cm < 247	tracking, PID
TRD*	$\pm$0.8	full	290 < r/cm < 368	tracking, $e^{\pm}$ id
TOF*	$\pm$0.9	full	370 < r/cm < 399	tracking, PID
PHOS*	$\pm$0.12	220^0 — 320^0	460 < r/cm < 478	photons
EMCal*	$\pm$0.7	80^0 — 187^0	430 < r/cm < 455	photons and jets
HMPID	$\pm$0.6	1^0 — 59^0	r = 490.0 cm	PID
ACORDE*	$\pm$1.3	30^0 — 150^0	r = 850.0 cm	cosmics
PMD	2.3 — 3.9	full	z = 367.0 cm	photons
FMD	3.6 — 5.0	full	z = 320.0 cm	charged particles
	1.7 — 3.7	full	z = 80.0 cm	charged particles
	(-3.4) — (-1.7)	full	z = -70.0 cm	charged particles
V0*	2.8 — 5.1	full	z = 329.0 cm	charged particles
	(-3.7) — (-1.7)	full	z = -88.0 cm	charged particles
T0*	4.6 — 4.9	full	z = 370.0 cm	time, vertex
	(-3.3) — (-3.0)	full	z = -70.0 cm	time, vertex
ZDC*	> 8.8	full	z = $\pm$ 113.0 m	forward neutrons
	6.5 — 7.5	< 10^0	z = $\pm$ 113.0 m	forward neutrons
	4.8 — 5.7	$2\phi < 10^0$	z = 7.3 3 m	photons
MCH	(-4.0) — (-2.5)	full	-14.2 < z/m < -5.4	muon tracking
MTR*	(-4.0) — (-2.5)	full	-17.1 < z/m < -16.1	muon trigger

ment when LEP was using the LHC tunnel. This solenoid creates a 0.5T bending magnetic field inside the center barrel. This is the largest non-superconducting solenoid that has ever been built, and while it offers all the necessary qualities at a low cost (a weak solenoidal field as the best compromise between low momentum acceptance, tracking resolution, and tracking efficiency), It places some limitations on the overall detector design (for instance, the depth of the EMCal is restricted by the existing structure). The complete detector has a volume of 16mx16mx26m = 6656m^3, and weighs over 10,000 tonnes. The arrangement of the ALICE detector and its different subsystems is shown in Figure 2.2. Except for the Electromagnetic Calorimeter, Transition Radiation Detector, and PHOS (photon spectrometer), all detector subsystems were installed and were operational when the LHC started running in 2008. In 2010, the installation of 4 out of 10 EMCal super-modules, 7 out of 18 TRD modules, and 3 of 5 PHOS modules was done. The last three TRD modules and the remaining EMCal modules were installed in 2011 (the year of the data taken for this analysis), and the remainings were implemented during the 2013 shutdown. To increase the acceptance (psydorapidity) of the calorimeter, a new calorimeter called ALICE DCal (Dijet calorimeter) was constructed with plans to add one additional PHOS module and utilize empty space around PHOS. This would increase the overall calorimeter coverage to almost 60% of the central barrel. A detailed description of the ALICE coordinate system can b found in the Ref. [91]

2.2.1 Inner Tracking System (ITS)

Due to its proximity to the beam pipe, ITS [30] is the essential detector in responsible for monitoring the primary vertex of the collisions. ITS incorporates six layers of concentric cylindrical silicon detectors (pixels, drifts, and strips) based on the three different silicon detector technologies. These cylindrical layers span the whole azimuth and are positioned around the beryllium beam pipe of the LHC, which has a 2.9 cm radius and an 800 m thickness. It is situated between the radii of 4 to 43 cm. Figure 2.4 shows the corresponding geometrical arrangement of the ITS. The major goal of ITS is the precise measurement of primary and secondary

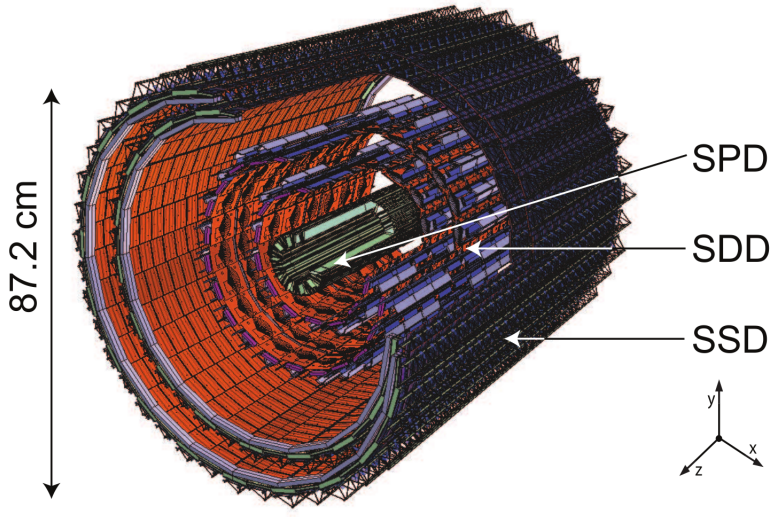

Figure 2.4: Schematic diagram of ALICE Inner Tracking System [30].

vertices, which is essential for reconstructing light or heavy flavoured resonance and weak decay particles. Furthermore, ITS improves the tracking and detection of low-momentum particles. By offering more tracking points closer to the interaction point, it also helps to improve the measurement of the TPC. The Silicon Pixel Detector (SPD), based on hybrid silicon pixels, is a two-dimensional matrix (sensor ladder) of reverse-biased silicon detector diodes bump-bonded to readout chips. Each diode is linked to a conductive solder bump to contact the readout chip that corresponds to the input of an electronics readout cell. The half-stave module, which is a fundamental detector module, consists of two ladders, one Multi-Chip Module (MCM), and one High-Density Aluminum/Polyamide Multi-Layer Interconnect. The ladder silicon sensor matrix bump adheres to five front-end chips. The sensor matrix has 256 x 160 cells that measure 50 µm (r) by 425 µm (z) in size. To provide coverage between readout chips, longer sensor cells are employed in the border area. The active area of the sensor matrix is 12.8 mm (r) x 70.7 mm (z). The front-end chip reads out a sub-matrix made up of 256 (r) x 32 (z) detector cells. The SPD (60 staves) contains 9.8 x 106 cells overall in 240 ladders and 1200 chips. An average distance of 3.9 cm (7.6 cm) separates the inner (outer) SPD layer from the beam axis. To reduce the material budget, the detector design employs a number of particular strategies. The SPD offers the highest spatial resolution of all ITS detectors, making it possible to measure impact parameters with a resolution suitable for detecting heavy flavours. The Silicon Drift Detector

(SDD) is built on modules with a sensitive area of 70.17 (r) x 75.26 (z) mm2, which is split into two drift areas where electrons travel in the opposite direction under a drift field of around 500 V/cm. The SDD modules are attached to a ladder-like linear framework. The outer layer of the SDD consists of 22 ladders with eight modules, whereas the inner layer consists of 14 ladders with six modules apiece. The centroid of the charge accumulated along the anodes is used to reconstruct the particle's location along z. The measured drift time relative to the trigger time is used to determine the particle's position along the drift coordinate (r). Given that the drift speed strongly depends on the humidity and temperature gradients in the SDD volume, detailed information of the drift speed that is measured during many calibration runs is required for this reconstruction. The Silicon Strip Detector (SSD) building block is a module made up of one double-sided strip detector with two hybrids front-end electronics. The sensors have an active area of 73 (r) x 40 (z) mm2 and are 300 µm thick. There are 768 strips, nearly parallel to the direction of the z beam, with a pitch of 95 m on each side. The innermost SSD layer is made up of 34 ladders with 22 modules along the beam direction, while the outer SSD layer is made up of 38 layers with 25 modules each. The outer four layers are employed for energy loss ($\mathrm{d}E/\mathrm{d}x$) measurement in the non-relativistic (1/ 2) area for low momentum particles as low as pT $\sim$ 100 MeV through analog readout. In pp collisions at $\sqrt{s} = 13$ TeV, LHC15f pass2 period, Figure 2.5 depicts the average energy loss ($\mathrm{d}E/\mathrm{d}x$) distribution of charged particles vs their momentum using the ITS alone (ITS pure standalone track and reconstruction). The lines in Figure 2.5 represent a parametrization of the detector response based on a hybrid parametrization using a polynomial function at low p/m and a "PHOBOS" Bethe-Bloch formula (p and m are particle momentum and mass, respectively). This outcome demonstrates the dE/dx-based particle detection capacity of ITS, and It is shown that pions, kaons, and the proton are clearly separated.

With these mystical abilities, ITS helps in the tracking and identification of low-momentum particles. We now move to the Time Projection Chamber (TPC), another essential tracking detector in the central barrel detector systems, in the next section 2.2.2.

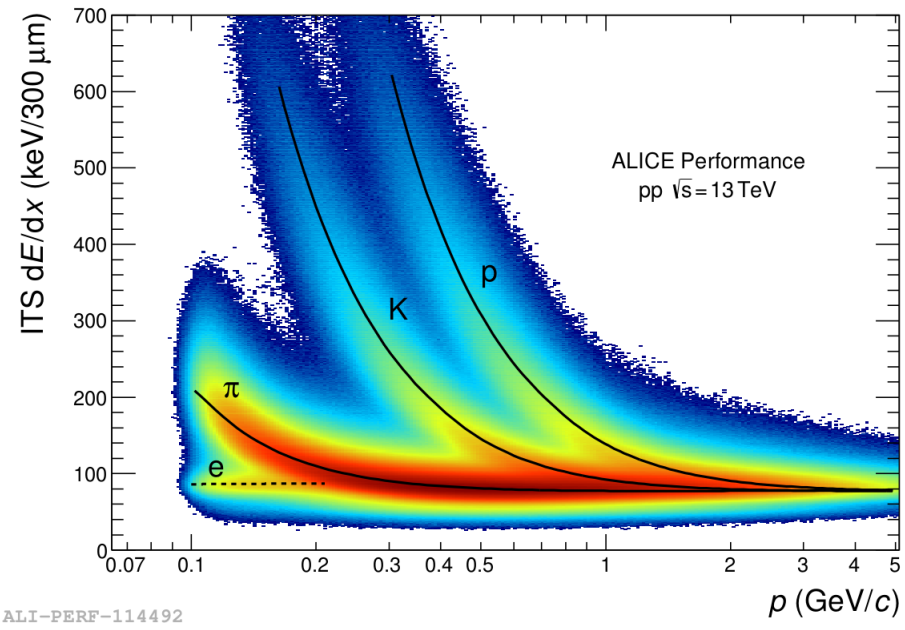

Figure 2.5: Average energy loss (dE/dx) distribution of charged particles vs their momentum (p) for ITS pure standalone tracks measured in pp collisions at $\sqrt{s}$ = 13 TeV [31]. The lines are the parametrization of the detector response based on the Bethe-Bloch formula.

2.2.2 The Time Projection Chamber (TPC)

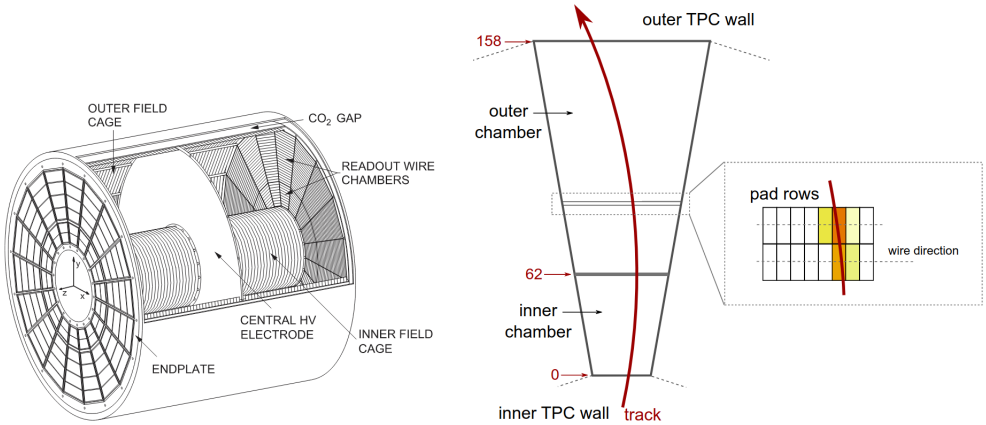

Figure 2.6: (Left)Schematic diagram of ALICE Time Projection Chamber detector [32]. (Right) Bases azimuthal sections of TPC detector. Every trapezoidal section is divided in an inner region (Inner ReadOut Chamber, IROC) and an outer region (Outer ReadOut Chamber, OROC) [33].

The ALICE experiment's primary tracking detector is the Time Projection Chamber (TPC) [128, 129]. Along with the ITS, it is designed to measure the momentum of charged particles, identify them, and determine the interaction vertex. The covered pseudorapidity range is $|\eta| < 0.9$, whereas the azimuthal acceptance

is 360°. This is presently the biggest TPC placed on an experimental apparatus. It is cylindrical in form, with an internal radius of $\sim$ 85 cm, an exterior one of $\sim$ 247 cm, and a length of $\sim$ 510 cm, giving a total active volume of $\sim$ 88 m^3. It is separated into two sectors by the presence of a central cathode, maintained at a high negative potential of V $\sim$ -100 kV, and produces an electric field that was constant and measured E $\sim$ 400 V/cm due to the action of the external field cage. The interior volume is split into two 2.5 m long portions, each filled with a $Ne/CO_2/N_2$ (Run 1) combination (90/10/5). Neon was replaced by argon in Run 2. The maximum drift time $\sim$ 90 µs, produced by the electron drift velocity of 2.7 cm/s over 250 cm (each of the two TPC drift zones separated by the central cathode), limits the highest event rate that the TPC can support. The two primary issues that constrain ALICE to operate at a lower instantaneous luminosity than the other LHC experiments at a high interaction rate are pile-up effects and the longer TPC dead time. This mixture's significant temperature dependency on velocity requires appropriate thermal stability (T $\leq$ 0.1 K [130]) for the TPC. Electrons produced by traversing charged particles in the gas are subject to a drift velocity towards the cylinder basis, which is azimuthally segmented into 18 trapezoidal sections, divided into an inner and an outer region, each of which is equipped with a Multi-Wire Proportional Chamber (MWPC), for a total of 36. (see the right panel in Figure 2.6). Together, the two MWPCs count 159 rows of readout pads, with the cathodes capturing the initial electrons' avalanche. The spatial information along the beam direction is given by the drift time, which is recorded by buffering the collected charge with a defined frequency. This signal is utilized to rebuild the x-y projection of the particle trajectory. With a magnetic field of 0.5 T and a resolution of 1% for low-momentum particles ($p_T \sim 1$ GeV/c), the TPC detector guarantees a tri-dimensional track reconstruction for charged particles. The resolution increases to 3.5% for p_T 100 GeV/c. The MWPC signal's amplitude is used to detect charged particles by measuring their energy loss per unit length as they move through the gas.

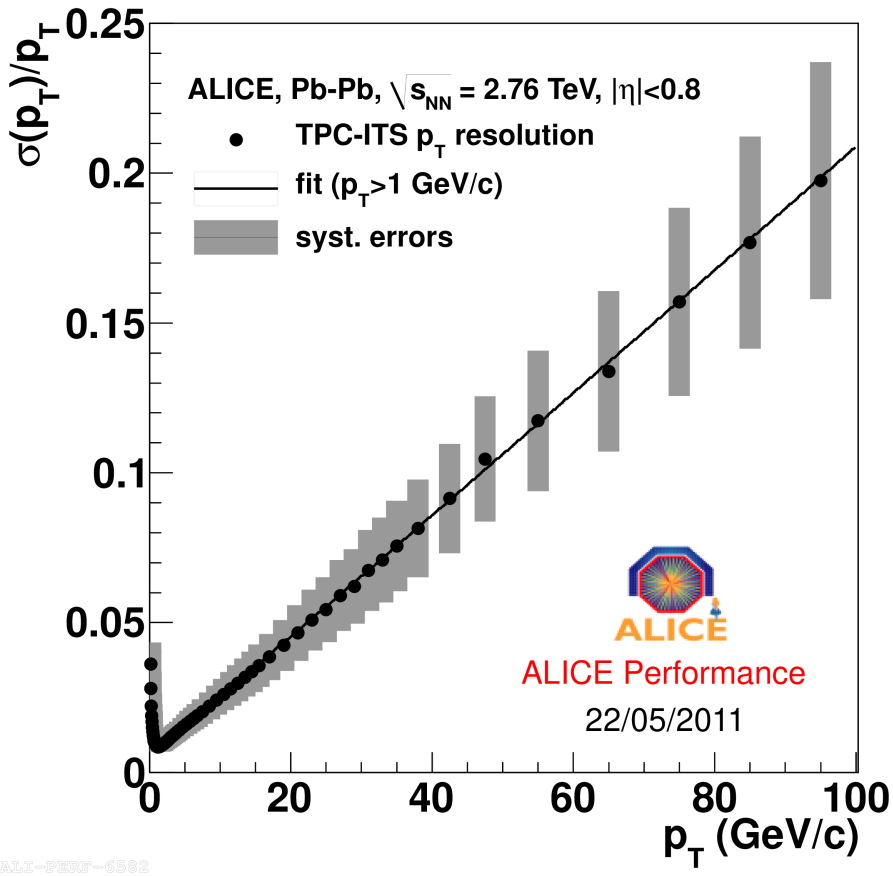

Figure 2.7: Combine TPC + ITS transverse momentum resolution [34].

Particle identification and track reconstruction

The TPC can reconstruct a primary track across a large momentum range, with a very good momentum resolution, from roughly $p_{\mathrm{T}} \sim 0.1$ -100 GeV/c. And it is noted that efficiency $> 90\%$ for $p_{\mathrm{T}} > 100$ MeV/c, where the interactions in the ITS material are the limiting factor. As demonstrated in Figure 2.7, the ITS and TPC are able to measure the momentum of the charged particles with a resolution greater than 1% for low p_{T} and 20% for $p_{\mathrm{T}} \sim 100$ GeV/c by monitoring the deflection in the magnetic field. The charge collected in the TPC readout pads is used to evaluate the particle energy loss. Both the momentum and the particle energy loss are measured at the same time. Additionally, this information makes it possible to distinguish between the different charged particle species in the low momentum range. The Bethe-Bloch formula is used to calculate the energy loss ($\mathrm{d}E/\mathrm{d}x$) of a charged particle in the detector medium as follows:

$$-\langle\frac{dE}{dx}\rangle = \frac{4\pi \mathrm{Ne}^4}{mc^2\beta^2}\left(\ln\frac{2mc^2\beta^2\gamma^2}{I} - \beta^2 - \frac{\delta(\beta)}{2}\right) \tag{2.1}$$

Where β is the velocity of the moving particle, γ is the Lorentz factor ($\gamma^2 = 1/(1-\beta^2)$), and z is its associated charge, and N, e, and m are the number density, electric charge, and mass of the electron, respectively. I stands for the atom's mean excitation energy. The density effect correction term is $\delta(\beta)$[131]. It can be seen from Eq. 2.1 that the $1/\beta^2$ term causes a reduction in energy loss in the low-velocity region. The ionization value becomes minimum for the relativistic limit, and particles in this region are called ionized particles. The $\mathrm{d}E/\mathrm{d}x$ factor and $\beta\gamma$ are simply parametrized in this approach of particle identification by energy loss. The Beth-Bloch curve utilized in the ALICE experiment is parameterized similarly to ALEPH collaboration [131, 132] as:

$$f(\beta\gamma) = \frac{P_1}{\beta^{P_4}}\left[P_2 - \beta^{P_4} - \ln\left(P_3 + \frac{1}{(\beta\gamma)^{P_5}}\right)\right] \tag{2.2}$$

Where γ is the Lorentz factor, β is the particle velocity, and P_{1-5} is the fit parameter. Figure 2.8 represents the dE/dx distribution for several charged particles, with the solid line representing what is predicted by the Bethe-Bloch formula. The track-by-track analysis identifies the low-momentum particles. Additionally, higher momentum particles are identified using multi-Gaussian fits to compare observed and parameterized values of dE/dx (as stated in Eq. 2.2).

Another method to identify the particles is the TPC $n/sigma$ (σ) selection. It defines as

$$n\sigma = \frac{(dE/dx)_{measured} - (dE/dx)_{expected}}{\sigma^{PID}_{TPC}} \tag{2.3}$$

where, $(\mathrm{d}E/\mathrm{d}x)_{expected}$ is the expectation of the modified Bethe-Bloch function and $(\mathrm{d}E/\mathrm{d}x)_{measured}$ is the energy loss of the TPC measured tracks. The

σ_{TPC}^{PID} is the particle identification resolution of the TPC.

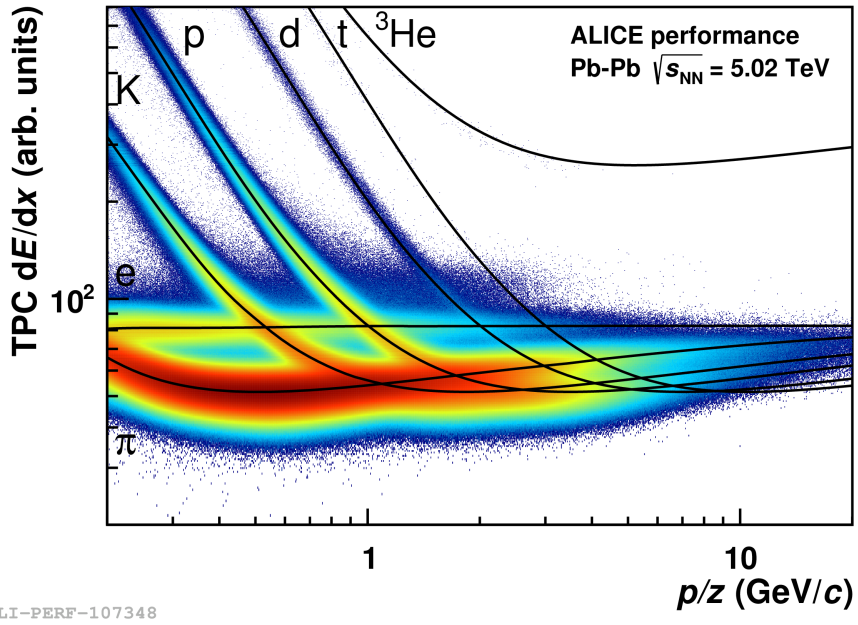

Figure 2.8: The information of TPC energy loss (dE/dx) performed on Run2 ALICE data [35].

The $n\sigma$ technique of particle identification is extensively used for the electron identification in this thesis.

2.2.3 Electromagnetic Calorimeter (EMCal) and Dijet Calorimeter (DCal)

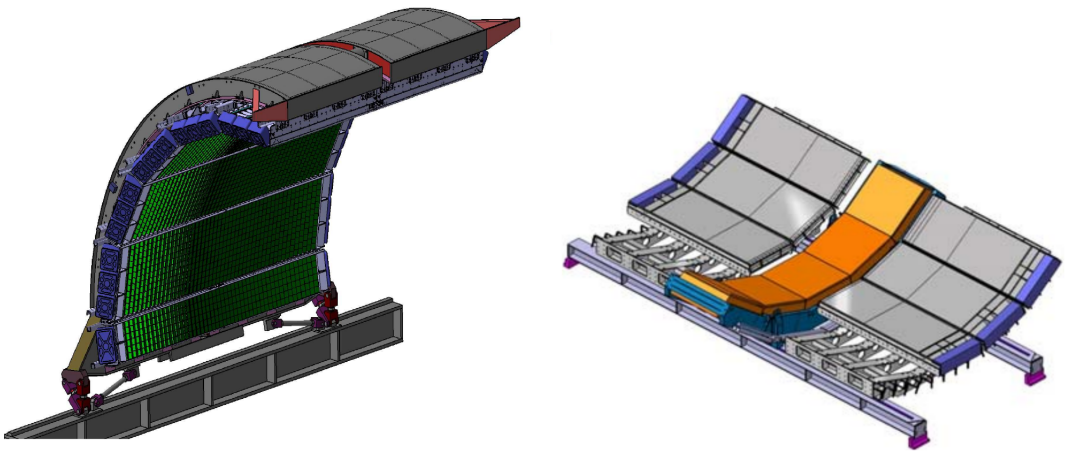

Figure 2.9: Array of Electromagnetic Calorimeter (EMCal) Super-modules [36] (Left) and Dijet Calorimeter (DCal) super-modules in gray with the PHOS super-modules in Orange in the middle [37] (Right).

The Electromagnetic Calorimeter (EMCal) and Dijet Calorimeter (DCal) are cylindrical-shaped Pb-scintillator sampling calorimeters placed next to the ALICE magnet coil at a radial distance of r $\sim$ 4.6 m from the beam line. A sampling calorimeter contains layers of active material to measure the observable signal/energy deposited in between layers of absorber material that degrades the particle energy used to produce the particle shower. The EMCal (and DCal) improves ALICE's jet measuring capabilities in addition to its superb particle tracking and identification capabilities. These detectors also provide improved photon, electron, and neutral particle measurements at high momentum and trigger on high-energy jets.

The EMCal spans the range between $|\eta| < 0.7$ and $\Delta\varphi = 107°(80° < \varphi < 187°)$. The maximum weight that the L3 magnet can support sets a limit on the size of EMCal. The DCal is an expansion of the EMCal acceptance that was added to the system to increase the range. The DCal covers an azimuthally $\Delta\varphi = 67°$ $(260° < \varphi < 327°)$ and covers pseudorapidity acceptance $0.22 < |\eta| < 0.7$. Because the space is occupied by the current PHOS detector, the DCal coverage is not uniform. To increase the acceptability of the EMCal and enable the measurement of hadron-jet and di-jet correlations, the ALICE EMCal system was specifically designed. Figure 2.9 shows a schematic representation of the EMCal and DCal arrays. A super module, which is the fundamental component of both the EMCal and the DCal, is an injection-molded scintillator consisting of two 2×2 towers/cells with 76 alternating layers of 1.44 mm Pb and 77 layers of 1.76 mm polystyrene. Each tower has a transverse dimension $\sim$ 6.0 x 6.0 cm^2, with an acceptable range $\Delta\eta \times \Delta\varphi \sim 0.014$ x 0.014. The EMCal detector system is designed to be a compact detector with a sampling fraction 1:22 Pb to scintillator ratio by volume and a detector thickness of 20.1 radiation lengths ($20.1X_0$, where X_0 = 12.3 mm) and an effective Moliere radius (R_M) of 3.20 cm. The mean path of an electron such that its energy is lowered by a factor of 1/e is known as the radiation length (X_0). It is a property of the material in which particles traversed. The Moliere radius (RM), a measurement of the transverse dimension of electromagnetic showers, is the circumference of a cylinder that contains, on average, 90% of the shower's energy deposition. The EMCal detects the energy

that particles deposit as they pass through the detector material. While moving through the calorimeter, electrons and photons predominantly interact through electromagnetic interactions and create electromagnetic showers. Photons are absorbed by pair production (γ + nucleus $\rightarrow$ e + γ + nucleus). On the other hand, electrons lose energy by bremsstrahlung (e + nucleus $\rightarrow$ e + γ + nucleus). Since the aim of this thesis is the azimuthal correlation of heavy-flavour hadron decay electrons with charged particles, the description of the EMCal in this section is mostly focused on the identification of electrons. Since the detector is 20.1X0 in thickness, electrons (and photons) tend to deposit all of their energy in the EMCal clusters through an electromagnetic shower. As a result, the total energy (E) deposited by the electrons in the EMCal should be equal to its momentum (p) (E/p $\approx$ 1), which is determined from the TPC. However, because the hadrons interact mainly through the strong nuclear force and the thickness of the towers is about equal to one nuclear interaction length, they do not entirely deposit their energy in the EMCal. The E/p for hadrons should be lower than 1. Since photons don't produce a signal in the TPC, electrons and photons are distinguished from one another by matching the EMCal clusters to the TPC tracks. With an increase in the incident particle's energy, the calorimeter's energy resolution improves. For electrons with energies larger than 10 GeV, the ALICE EMCal's energy resolution is lower than 5%.

It is challenging to choose high-purity electrons with $p \geq 6$ GeV/c because, as discussed in section 2.2.2 and is clear from figure 2.8, the hadron dE/dx band from TPC starts to mix with the electrons band as the momentum increases. A distribution of E/p from EMCal vs. TPC $n\sigma_e$ is shown in Figure 2.10. The figure shows a clear separation between the electron region and other hadrons. The shape of the shower is another distinguishing characteristic of the EMCal clusters that may be utilized to differentiate between electrons and hadrons. Additionally, the EMCal detector is also used as high momentum trigger.

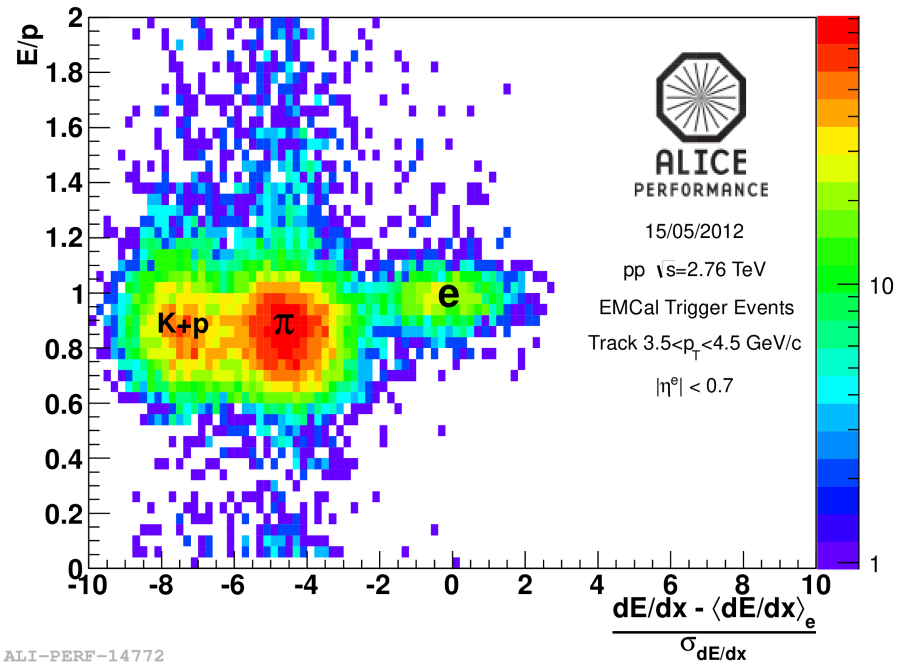

Figure 2.10: The E/p vs TPC $n\sigma_e$ distribution in pp collisions at $\sqrt{s} = 2.76$ TeV. Energy (E) is obtained from the EMCal, and momentum (p) is measured from the TPC detector.

2.2.4 VZERO detectors (V0)

The VZERO (V0) detector [38, 133] is a compact angle detector made up of the V0A and V0C scintillator counter arrays. They are mounted on either side of the ALICE interaction point. As shown in figure 2.11, the V0C is positioned to the front face of the front absorber 0.90 m from the vertex, and the V0A is situated 3.4 m from the vertex, on the side opposite the muon spectrometer. The pseudorapidity acceptance of V0A and V0C detectors are $2.8 < \eta < 5.1$ and -3.7 $< \eta <$ -1.7, respectively.

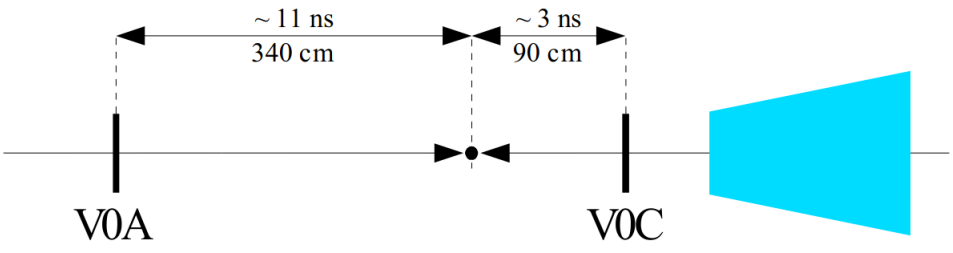

Figure 2.11: Time alignment condition on V0A and V0C [38].

In pp and A-A collisions, the V0 detector offers minimum-bias (MB) triggers for the central barrel detectors. In addition to the initial beam collisions, interactions caused by the presence of materials, such as the beam pipe and the front absorber, lead to the generation of secondary particles, which will distort the physical information that should have been obtained from the main charged particles. Therefore, a minimum-bias trigger is employed to detect particles from beam-beam (BB) collisions. If hits are found on each disc (V0A and V0C) at the anticipated time, i.e., 11 ns after the collision on V0A and 3 ns after the collision on V0C, the minimum-bias trigger verifies that an event has happened. The van der Meer scan method [134] is used to assess luminosity in pp collisions using the V0 detector.

The V0 detector is also used to measure centrality and multiplicity based on the energy deposited in the scintillator.

2.3 ALICE off-line and on-line system

2.3.1 Off-line computation in ALICE

The raw data collected from the detectors must be processed before being ready in the form of events for further analysis. This section presents the off-line data processing and tools used for analysis (ALICE Grid and AliRoot framework).

ROOT and AliRoot

A large portion of the high-energy physics experimental community, including ALICE, uses a scientific software called the ROOT analysis framework [135], which was primarily written in C++. At the same time, other languages, such as R and Python, are also integrated into ROOT. ROOT was invented at CERN, and it has features for handling and analyzing large amounts of data in high-energy physics. In addition to offering data management and storage capabilities, ROOT packages are loaded with several tools for doing mathematical and statistical analysis. The AliRoot framework is a ROOT modification built specifically for ALICE

simulation and reconstruction. [136].

Simulation

Analysis of high-energy collision experiments heavily relies on the simulation of actual data collected from experiments. To optimize physics data for detector efficiency and acceptance constraints, simulated samples are used. The transport code and the event generator are the two components that make up a simulation. Event generators use the theoretical concepts of collision dynamics to produce events and particles with the same average behavior as in real data. To produce events as closely as feasible to the known real data, many event generators employ various theories and physical procedures. Since Monte Carlo techniques are employed for the simulations, the simulated data produced by the event generators is sometimes referred to as a "Monte Carlo sample" or "MC sample." ALICE's most popular event generator to simulate pp events is PYTHIA [113, 137]. EPOS [138] and HIJING [139], which are used to simulate both pp and heavy-ion collisions, are two further well-known event generators. Event generator outputs are subsequently incorporated into the input of the transport models. Transport models that replicate the behavior of detectors, i.e., GEANT [140, 141]. The output from the transport models aims to replicate the quantity and characteristics of particles collected by the experiments as closely as possible. A simulation can be defined as a computer-simulated version of an experiment.

ESD and AOD files

The unprocessed data is stored in the Event Summary Data (ESD) files after reconstruction. The ESD files contain the complete information of reconstructed data from every sub-detector, including trigger data, collision vertex measurements, and specific particle track data from various sub-detectors, etc. However, because of their size, the ESD files are complicated and unsuitable for local analysis. As a result, Analysis Object Data (AOD) files are produced from the ESD files, which only include data that is necessary for particular studies. The input for local analysis is AOD files.

Data reconstruction procedure and tracking

Calibration is the first step in reconstructing raw data, which will be recorded in ESD and AOD files. Each detector's clustering is then completed independently. A cluster is a fired group of nearby cells that is utilized as an input for reconstructing a track or tracklet by a tracking detector. The ESD files also contain clusters from calorimeter-based detectors. Algorithms that use the correlation between SPD tracklets are used to reconstruct the location of the interaction vertex [142]. Within a narrow azimuthal window (order of 0.01 rad), tracklets are created by nearby clusters of both layers of the SPD aligned with the primary vertex that was successfully reconstructed. The space point where the highest number of lines from a linear extrapolation of the tracklets converge is considered to be the primary interaction vertex. The tracklet multiplicity affects the vertex determination efficiency [142]. Track recognition (finding) and reconstruction in the ALICE are done in the central barrel of ALICE using the Kalman filter approach [143] in three steps. The first step starts at the TPC's outer radius. A track seed is created using pairs of TPC clustered in nearby pad rows, and the primary vertex is predicted using SPD. If a proximity cut is met, the track seed is pushed inwards toward the inner radius of TPC and updated at each step with the closest TPC cluster. At this stage, a preliminary particle identification based on the dE/dx is performed. These tracks are called "TPC-only tracks." These tracks are then extended to the point of closest distance to the main interaction vertex and transmitted toward the ITS for track finding in the ITS. Using the clusters identified in the first iteration, these tracks from the primary vertex are transmitted back to the TPC's outer radius in the second iteration. The specific energy loss is used to update the particle identification as well. These tracks are then extended in the direction of the cluster-matching detectors TRD, TOF, HMPID, EMCAL, and PHOS. The clusters from the second iteration are used to re-fit the tracks inward to their closest approach to the SPD vertex in the final iteration. These are called "global tracks Compared." to the primary interaction vertex, the final interaction vertex is computed utilizing the global tracks with better accuracy.

Clustering in EMCal

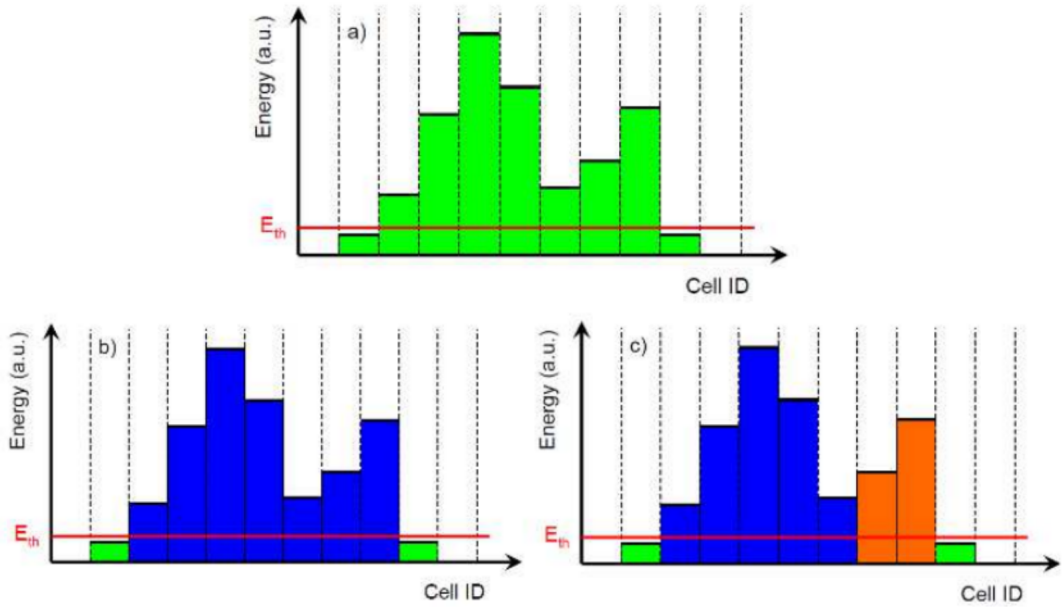

Figure 2.12: Different clusterization algorithms. Boxes represent energy in cells. E_{th} is the threshold energy for clusterization. a) Energy in cells before clusterization (marked in green color). b) Result of Clusterizer V1. There is one big cluster made of cells in blue color. Green cells are below the threshold and not associated with the cluster. c) Result of Clusterizer V2. There are two clusters made of blue and orange cells. Green cells are below the threshold and not associated with any cluster. [39].

Photons and electrons passing the Electromagnetic Calorimeter deposit their energy in different towers through electromagnetic shower. The showers cover a group of nearby towers because of the size of the tower. These groupings of nearby towers or cells are known as clusters. A digit is a group of data that describes a cell, such as the location of the cell, the amount of energy deposited, etc. Using any of the existing clusterization techniques, clusters are created from digits with the same particle's energy deposited. Currently, the EMCal supports four different types of clusterizers: Clusterizer V1, Clusterizer V2, Clusterizer 3×3, and Clusterizer V1 with unfolding. The Clusterizer V1 and Clusterizer V2 have been utilized in this study and are briefly discussed in this section. The Clusterizer V1 is the most straightforward clustering technique, aggregating nearby digits or cells until no more is left over a specified energy threshold. A "working array" of digits is chosen by initializing a set of clustered parameters [39]. Finding the digit in the working array with the highest energy deposit serves as the algorithm's

first seed digit. The energy of the digits must be greater than the minimal energy threshold (Eth = 500 MeV utilized for this research) in order to be selected. The cluster is related to the adjacent digits to the seed digits that are over the threshold energy. The adjacent digits that have a common edge with the seed are known as neighboring digits. To guarantee that no two clusters contain the same digit, the digits added to the cluster are subtracted from the working array. The algorithm keeps searching for neighbors of the already-added digits to the cluster. This operation keeps going until there are no more neighboring digits in the working array. The clustering procedure begins again once the cluster has been produced and while there are still digits in the working array that may generate fresh seeds and their neighbors for a new cluster. This process continues until there are no more seed digits in the array. The Clusterizer V2 algorithm is identical to the Clusterizer V1 technique, except in order to become a neighbor, the digit's energy must be lower. The V1 and V2 clusterization techniques are displayed in Figure 2.12. Boxes represent energy in cells, and the threshold energy for clustering is E_{th}. The energy in cells prior to clustering is shown in panel (a) in the top panel. Clusterizer V1 output can be seen in the bottom left panel (b). There is a large blue cell cluster that is present. Clusterizer V2 output is seen in the bottom right panel (c). There are two clusters made of blue and orange cells. The green cells in both bottom panels are below the threshold and not connected to any cluster. The Clusterizer V2 has been utilized in this thesis study to get the final results.

Shower Shape of clusters

To distinguish electrons from neutrons and hadrons, an extra parameter is employed to analyze the lateral form of showers in the $\eta - varphi$ plane of EMCal. The shower shape describes by the squared eigenvalues of the shower form ellipse's dispersion matrix, which were determined from the energy distribution of the individual detector cells [144]. Figure 2.13 [39]shows a toy model of such a cluster. The long and short axes of the ellipse are λ^2_{long} (M02) and λ^2_{short} (M20), respectively. The readout electronics of the scintillator in the EMCal are damaged by neutrons, which results in abnormally high energy signals that are often confined in one cell with a few nearby low-energy cells [145]. As a result, a lower

threshold for the shower shape axis is used (for example, $\lambda^2_{long} > 0.1$) to exclude contamination from neutron contributions. The shower shape parameter is also used to deny contribution from hadrons such as neutral pions at high p_{T} ($p_{\mathrm{T}} \geq$ 10 GeV/c) [145]. Neutral pions can form overlapping showers as they decay into pairs of photons, which allows for reconstructing a single elongated cluster. The study employed a p_{T} dependent higher threshold of the shower shape parameter to minimize effects from such contamination. Further details on the shower shape parameters can be found [39].

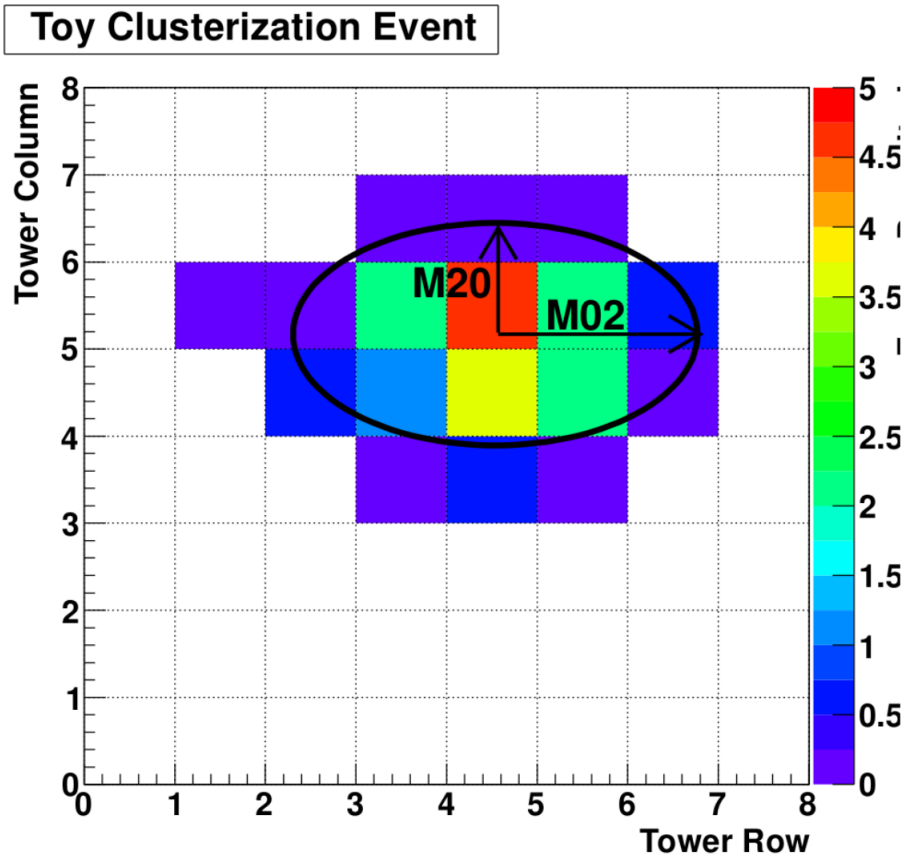

Figure 2.13: A sample of clusterization event. The cluster is fitted with an ellipse, and the two axes are labeled M02 and M20. Each square corresponds to a tower/cell [39].

2.3.2 ALICE online system

Centralized web services manage the data collection processes in ALICE. It consists of the following components: the Data Acquisition (DAQ), the High-Level Trigger (HLT), the Trigger System (TRG), and the Experiment Control System

(ECS) [146, 147]. While DAQ, integrated with TRG and HLT system, specifies the setup of the detectors during data-taking times, DCS manages hardware operation. The coordination of all the core systems is under the purview of ECS. The detectors are organized in partitions with a certain set of trigger inputs so that they can work simultaneously, despite the fact that they can operate independently (in a mode known as a standalone mode). This is carried out during the physics data collection phase. Running in standalone mode is primarily used for calibration, commissioning, and debugging tasks.

Trigger System

The primary function of the Trigger system (TRG) is to determine within microseconds if the resulting event is worthy of being recorded for each bunch-crossing of the LHC. It comprises a High-Level Trigger (HLT) and a Central Trigger Processor (CTP). CLP has three levels of triggers, depending upon the arrival times of the trigger inputs and the time synchronization of the detector, namely, level-0 (L0) or first-level trigger, level-1 (L1) or second-level, and level-2 (L2) or final level. L0 gave the aggregate signal information from different detectors in 1.2 µs after passing each bunch, whereas L1 took 6.5 µs. The final level trigger that decides everything takes 100 seconds. The system determines whether the selected event will be asserted, negated, or irrelevant after the last and final level trigger. Following that, the data is recorded using the DAQ system.

High Level Trigger

At the conclusion of the trigger selection procedure, the ALICE High-Level Trigger (HLT) is in charge of compiling inputs from all major detectors and selecting events of interest. This is accomplished by a firmware and software-based filtering process. Through Detector Data Links (DDL), the raw data is gathered and entered into HLT. Following the event's unique reconstruction for each detector, the selection of events is carried out using the event's reconstruction of the physics observables. The reconstruction of events for each detector independently comes next. Therefore, by choosing and compressing the events, HLT aids in reducing

the volume of physical events.

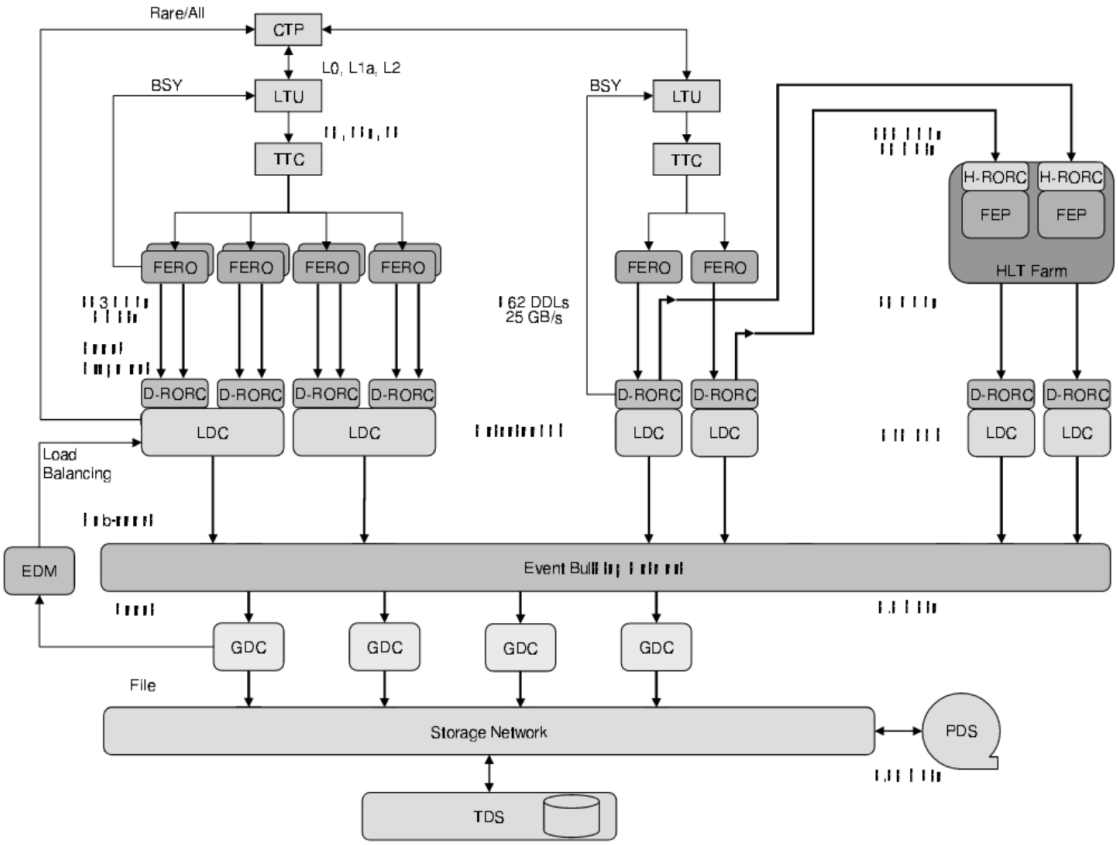

Figure 2.14: The overall architecture of the ALICE DAQ system and the interface to the HLT system [40].

Data Acquisition

The management of data flow from detector-related electronics to long-term storage is the responsibility of the DAQ system. The Local Data Concentrators (LDCs), which read the events from the optical Detector Data Links, are used to do this. The information about the events that have been collected is then sent to Global Data Collectors (GDCs), which record the events to Transient Data Storage. It is then put into permanent storage. It also consists of software programs for doing system performance and data monitoring. An overview of the ALICE DAQ architecture is shown in Figure 2.14.

Detector and Experimental Control System

The main goal of the Detector Control System (DCS) is to make it possible for the ALICE to operate at the LHC securely. It controls and handles all the services associated with detectors, such as gas, magnet, cooling, and high and low-voltage power supply. Even during shutdown periods, it is continuously in operation. All the on-line systems' actions must be coordinated through the ALICE Experiment Control System (ECS) in order to achieve their shared objective.

2.4 Event generators

Event generators are computer programs used in high-energy physics and particle physics to simulate the interactions of particles. These generators use theoretical models of particle interactions and can predict the properties of the final-state particles produced in high-energy collisions. In this section, we will discuss a few event generators for hadronic collisions as well as heavy ion collisions.

2.4.1 Event generators for hadronic collisions

1. **Herwig:** Herwig is a general-purpose event generator for the simulation of high-energy lepton-lepton, lepton-hadron, and hadron-hadron collisions. It includes several features as

    - Initial- and final-state QCD jet evolution taking account of soft gluon interference via angular ordering.
    - A detailed treatment of the suppression of QCD radiation from massive particles, the dead-cone effect.
    - The simulation of BSM physics includes correlations between the production and decay of the BSM particles together with the ability to add new models by simply encoding the Feynman rules.
    - An eikonal model for multiple partonic scatterings to describe the underlying event.

- A cluster model of the hadronization of jets based on non-perturbative gluon splitting.
- A sophisticated model of hadron and tau decays using matrix elements to give the momenta of the decay products for many modes and including a detailed treatment of off-shell effects and spin correlations.

2. **SHERPA:** Sherpa simulations can be achieved for lepton–lepton collisions, as explored by the CERN LEP experiments, for lepton–photon collisions, for photon–photon collisions with both photons either resolved or unresolved, for deep-inelastic lepton-hadron scattering, as investigated by the HERA experiments at DESY, and, in particular, for hadronic interactions as studied at the Fermilab Tevatron or the CERN LHC Gleisberg:2008ta,sherpa. The physics processes that can be simulated with Sherpa cover all reactions in the Standard Model. The Sherpa program owes versatility to the two inbuilt matrix-element generators, AMEGIC++ and Comix, and to it's phase-space generator, Phasic, which automatically calculates and integrates tree-level amplitudes for the implemented models. This feature enables Sherpa to be used as a cross-section integrator and parton-level event generator as well. The algorithms used in Sherpa improved descriptions of multijet production processes.

3. **PYTHIA:** PYTHIA is a Monte Carlo event generator that simulates the hadronic interactions of particles, such as protons or heavy ions, with the matter. The main features of PYTHIA are hard and soft interactions, parton distributions, initial/final-state parton showers, multi-parton interactions, fragmentation, and decay.

   PYTHIA is an event generator that is extensively and successfully used for the study of proton-proton and proton-lepton collisions. Recent advancement in PYTHIA8 enables the study of heavy nuclei collisions, namely proton-nuclei (pA) and nuclei-nuclei (AA). In this work, the PYTHIA8 event generator is used to simulate ultra-relativistic Pb–Pb collisions with Angantyr [148]. PYTHIA8 natively does not support heavy-ion systems; however, the Angantyr model combines several nucleon-nucleon collisions into one

heavy-ion collision. It is a combination of many-body physics (theoretical) models suitable for producing hard and soft interactions, initial and final-state parton showers, particle fragmentation, multi-partonic interactions, color reconnection mechanisms, and decay topologies [113]. In this study, we use PYTHIA8, which includes multi-parton interactions (MPI), color reconnection (CR), and rope hadronization mechanisms in particle production. MPI is vital to expostulate the underlying events, multiplicity distributions, and charmonia production. In general, an event generator at high colliding energies produces around four to ten partonic interactions, which depend on the overlapping region of colliding particles [149]. The perturbative scattering processes are implemented by Initial State Radiation (ISR) and Final State Radiation (FSR)[150, 151].

Hadronization in PYTHIA8 is done using the Lund string fragmentation model. The beam remnants and the produced partons are interconnected via strings storing potential energy. The string interactions in PYTHIA8 can be carried out in coordinate and color space via ropes, color reconnection, and string shoving mechanisms. The mode of interaction between the strings governs the hadronization mechanism. These underlying mechanisms are responsible for the signatures in heavy-ion measurements without any thermalized medium within PYTHIA8. The rope hadronization model allows strings to overlap in transverse space to create a "rope". Within these overlapping strings in the impact parameter space, the energy density between the region of overlap and outside creates a pressure gradient that pushes the strings outside. This mechanism in PYTHIA8 is accomplished by making the strings "shove" each other apart. String shoving in PYTHIA8/Angantyr influences the ratio to strange and non-strange hadrons, which can explain the strangeness enhancement in pp and heavy-ion measurements. In the CR mechanism, color strings are effectively shorter. This leads to a decrease in particle production and consequently the multiplicity (N_{ch}). This is compensated by the addition of MPI as a parton-level phenomenon in PYTHIA8, which increases particle production. On the contrary, strings are effectively

longer in string shoving, which leads to an increase in particle production. In literature, flow-like effects in pp collisions are well mimicked by string shoving and CR mechanisms [14] in PYTHIA8.

In Angantyr, positions and the number of the interacting nucleons and binary nucleon-nucleon collisions are performed by Glauber model-based eikonal approximation in impact-parameter space. Furthermore, Gribov's corrections are implemented in order to include diffractive excitation, which appears due to the fluctuations in the nucleon substructure. Angantyr is the first model which implements diffractive excitation in both projectile and target nuclei via individual fluctuations. This is essential to generalize for a AA system [148]. The contribution to the final state from each participating nucleon is induced from the Fritiof model with the concept of wounded nucleons (diffractive and non-diffractive). The hard partonic sub-collisions, normalized by nucleon-nucleon sub-collisions, play a crucial role at high energies. The model treats the projectile and target nucleons via two interaction scenarios. In one case, the interactions between the species are considered as pp like non-diffractive (ND) processes. This is entirely driven by PYTHIA8. However, in the second scenario, a wounded projectile nucleon can have ND interactions with many target nucleons, which are termed secondary ND (SD) collisions. Subevents are generated solely through PYTHIA8, where these SD collisions are put into play as modified SD processes [152]. Depending on the interaction probability, interactions between wounded nucleons are classified as elastic, non-diffractive, secondary non-diffractive, single-diffractive, and double-diffractive.

2.4.2 Event generators for heavy ion collisions:

1. **HIJING:** HIJING is a Monte Carlo event generator that simulates the interactions of heavy ions, such as gold or lead nuclei, with the matter. It is particularly well-suited for simulating the early stages of heavy ion collisions, including the formation of the quark-gluon plasma.

2. **AMPT:** AMPT (A Multi-Phase Transport Model) is a hybrid model that combines a microscopic transport model. It is designed to simulate the entire evolution of a heavy ion collision, from the initial stages to the final hadronic state. The AMPT model consists of several components, including the initial condition generator, which produces the initial state of the collision; the partonic transport model, which describes the evolution of the quark-gluon plasma, and the hadronic cascade model, which simulates the formation of hadrons from the quark-gluon plasma. The AMPT model also includes the effects of resonance decay, parton coalescence, and hadronization mechanisms.

   The AMPT model has been used to study a wide range of phenomena in heavy ion collisions, including the production of quarkonia, the formation of jet quenching, and the behavior of the quark-gluon plasma under extreme conditions.

3. **UrQMD:** UrQMD (Ultra-Relativistic Quantum Molecular Dynamics) is a microscopic transport model that simulates the interactions of heavy ions at high energies. It is particularly well-suited for simulating the late stages of heavy ion collisions, including the hadronization and decay of particles.

4. **EPOS:** EPOS is a Monte-Carlo event generator for minimum bias hadronic interactions, used for both heavy ion interactions and cosmic ray air shower simulations. The acronym stands for energy conserving multiple scattering; Partons, parton ladders, and strings; Off shell remnants; and Saturation. Unlike PYTHIA, which is based on a factorization approach, EPOS is based on the Parton-based Gribov-Regge theory, a multiple scattering theory that combines the eikonalized parton model. The program uses a parton model where each binary interaction is represented by a parton ladder, which can be considered as quasi-longitudinal color fields or relativistic strings or string fragments. EPOS also implements the idea of Pomerons, which exhibit the interaction between incoming partons.

   EPOS 3, the version used in the referenced thesis, employs full (3+1D) viscous hydrodynamical calculations followed by a hadronic cascade, mak-

ing it, unlike any other event generator. The separation of collision zones into "core" and "corona" regions is another novel aspect of EPOS, based on string densities at earlier times of the collision. The high energy density region above a certain critical string density is called the "core," where hadronization is achieved through imposing radial flow for all hadron species. This produces a full collective expansion that creates QGP in heavy-ion collisions. The low string density region is called the "corona," where particle production occurs similarly to pp scattering.

EPOS aims to reproduce various LHC observables such as multiplicity, jets, and collective behavior. It is a well-suited simulation model for describing collisions at LHC and higher energies. EPOS has been successful in explaining LHC data for different collision systems at various energies.

These are just a few examples from various event generators available for simulating high-energy physics and particle physics processes. The choice of event generator depends on the specific physics phenomena being studied and the accuracy and computational resources required for the simulation.

Chapter 3

Analysis strategy

This chapter outlines the approach employed to investigate the azimuthal angular correlations between heavy-flavour decay electrons and charged hadrons in pp and p–Pb collisions. The methodology involves several steps, such as event selection, electron identification, and background removal, to obtain the heavy-flavour decay electron sample. The analysis also entails constructing the $\Delta\varphi$ distribution between the heavy-flavour hadron decay electrons (HFE) and charged particles, which will be discussed in the next section. This chapter begins with the general strategy, as well as the datasets, including Monte-Carlo samples and event selection criteria. Subsequently, it describes the track selection criteria and criteria for the pp and p–Pb datasets, followed by the electron identification process. The chapter then details the identification and removal of different backgrounds to obtain the heavy-flavour decay electron sample and then explains how the azimuthal angular correlations between heavy-flavour decay electrons and charged hadrons are determined. Finally, we will provide a brief discussion of Pb–Pb analysis in section 3.17. Although it will not be the main focus of this thesis as the analysis of the Pb–Pb system is still ongoing.

3.1 General strategy

This section presents a broad overview of the measurement process for the azimuthal angular correlation distributions between heavy-flavour decay electrons and charged hadrons. The subsequent sections will provide a detailed explanation of each of these steps. Throughout the thesis, the symbol Φ will be used as a

shorthand for the $\Delta\varphi$ distribution between electrons and charged hadrons as,

$$\Phi \equiv \frac{dN}{d\Delta\varphi} \tag{3.1}$$

To obtain the electron sample, various sub-detectors (ITS, TPC, EMCal, and V0) of the ALICE detector are utilized. In the electron sample, some hadrons may be misidentified as electrons and need to be removed. The resulting $\Delta\varphi$ distribution for inclusive electrons (pure electron sample) is then obtained,

$$\Phi^{\text{Inclusive}} = \Phi^{\text{ec}} - \Phi^{\text{had}}, \tag{3.2}$$

Here, we use Φ^{ec} to denote the distribution of electron candidates, while Φ^{had} is obtained from di-hadron correlations that are scaled as per the hadron contamination in electron sample. The inclusive electrons are defined as electrons that may originate from the decay of heavy-flavour hadrons or from non-HFE, such as gamma conversion and Dalitz decay of η and π^0 mesons.

The $\Delta\varphi$ distribution between heavy-flavour decay electron (Φ^{HFE}) and charged particle is measured by subtracting $\Delta\varphi$ distribution of Non-HFE ($\Phi^{\text{Non-HFE}}$) from inclusive electron $\Delta\varphi$ distribution ($\Phi^{\text{Inclusive}}$) as

$$\Phi^{\text{HFE}} = \Phi^{\text{Inclusive}} - \Phi^{\text{Non-HFE}}, \tag{3.3}$$

To determine the Non-HFE background, we use the invariant mass method, which involves calculating the invariant mass of electron-positron pairs. This method is explained in more detail later in section 3.7. The electron-positron pairs with a low invariant mass peak are considered to originate from a non-heavy flavour source. However, the random pairing of electron-positron pairs results in the combinatorial background in the invariant mass distribution. To account for this background, we subtract the invariant mass of electron pairs with the same charges to calculate the true pair of electron-positron (Non-HFE) as

$$\Phi_{\text{r}}^{\text{Non-HFE}} = \Phi^{\text{ULS}} - \Phi^{\text{LS}}. \tag{3.4}$$

Here, $\Phi_{\rm r}^{\rm Non-HFE}$ is the distribution for reconstructed Non-HFE, $\Phi^{\rm ULS}$ and $\Phi^{\rm LS}$ are the distribution for unlike-sign and like-sign electrons, respectively.

Due to limited detector acceptance and efficiency, the number of identified non-HFE is not true, this number is corrected by using the tagging efficiency ($\epsilon_{\rm tagging}$), which is obtained from Monte-Carlo simulations. The total Non-HFE ($\Phi^{\rm Non-HF}$) background is calculated using the efficiency as

$$\Phi^{\rm Non-HF} = \left(\frac{1}{\epsilon_{\rm tagging}}\right) \Phi_{\rm r}^{\rm Non-HF}. \tag{3.5}$$

3.2 Experimental dataset

The vast amount of data collected between 2015 and 2018 during the Run-2 data-taking period at the LHC is organized into "production cycles" or "data-taking periods." During data collection from the collisions, the data-taking configurations are occasionally reset under software control [153], which marks the beginning of a new "run" with a unique "run number" that increases with each subsequent run. The run-list for each data-taking period is obtained with a specific set of detectors requirements, e.g., SSD, SPD, SDD, V0, TPC, EMCal, e.g., TPC-EMCal analysis [154]. The azimuthal angular correlations between heavy-flavour decay electrons and charged particles analysis used TPC-EMCal datasets and were measured on pp and p–Pb collision systems at $\sqrt{s_{\rm NN}}$ = 5.02 TeV collected by the ALICE detector. As explained in section 3.17, the raw data from the detector systems undergo processing to store it as events in Event Summary Data (ESD), and for further analysis, Analysis Object Data (AOD) files can be used. This processing, which includes alignment, calibration, simulation, and reconstruction, occurs in several successive reconstruction passes [91]. The datasets used for this measurement are LHC17p and LHC17q for pp collisions and LHC16q and LHC16t for p–Pb collisions. The data samples are used without SDD information as they are fast compared to datasets that include SDD, as SDD has a finite readout time. In both collision systems, minimum-biased (MB) datasets are used. A minimum bias event requires a signal in both VZERO-A and VZERO-C detectors. After elimi-

nating events from beam-gas collisions, events resulting from hadronic interactions were selected. To ensure a consistent reconstruction efficiency in the mid-rapidity region, only events with a primary vertex position falling within the z-coordinate axis range of -10 to 10 cm were chosen. About 800M and 546M events were analyzed for measurements in pp and p–Pb collisions, respectively, corresponding to integrated luminosities of (16.63 ± 0.32) nb^{-1} [155] and (250 ± 10) μb^{-1} [156]. The integrated luminosity is defined as the ratio of the number of events (N_{events}) over the interaction cross-section (σ).

$$\mathcal{L}_{int} = \frac{N_{\text{events}}}{\sigma} \tag{3.6}$$

3.3 Monte-Carlo samples

To determine the reconstruction and tracking efficiency of non-heavy flavour decay electron (NHFE), Monte-Carlo (MC) simulations are employed. In the pp and p–Pb analyses, the MC sample was obtained using PYTHIA 6.4.25 event generator [113], with the Perugia 2011 tune [157], and HIJING 1.36 [158] generators, respectively. They will be referred to as PYTHIA6 and HIJING in the following. The generated particles were propagated through the ALICE apparatus using GEANT 3.21.11 [159]. In order to increase the statistical precision of the tagging efficiency, π^0 and η mesons generated with PYTHIA6 were embedded in the simulated events. The detector configuration and beam vertex conditions are consistent with those during data collection. the MC production `LHC18a4b2_Geant3_fast_HFE` (pp) and `LHC21g8_fast` (p–Pb) are used to calculate NHFE reconstruction efficiency and `LHC17l3b_centWoSDD and 17l3b_fast` (pp) and `LHC20f11c2_fast` (p–Pb) are used to calculate the tracking efficiency of charged particles.

3.4 Event selection

This section discusses the event selection criteria utilized in this analysis to choose relevant events for study. Due to the high collision rate in ALICE, a trigger system is employed to select relevant data segments containing the physics information of interest, which is subsequently stored for analysis. The selection of triggers depends on the selection of events that meet the analysis requirements and interests. In this analysis, a minimum-bias (MB) trigger is used. The minimum bias trigger is a selection of inelastic events with minimal bias, as the name implies. In ALICE, the minimum bias trigger selection (kINT7 trigger) necessitates a hit on both sides of the V0 detector, indicating that a collision has taken place.

To ensure uniform reconstruction efficiency of charged particles, a selection criterion is applied on the primary z vertex position ($|z_{\rm vtx}|$ <10 cm) from the center of the ALICE detector system along the beam direction. The primary Z vertex range is limited to ±10 cm. For this analysis, events were selected based on the number of contributors to the primary vertex. Only events with at least two contributors from tracks to match with the SPD vertex were used. Pile-up events, where multiple collisions are recorded as a single event, were removed. There are two types of pile-up that can occur. Same-bunch-crossing pile-up, where more than one collision occurs in the same bunch crossing, and out-of-bunch pile-up, where one or more collisions occur in bunch crossings different from the one which triggered the data acquisition. Pile-up events were rejected at the physics selection level if another collision occurred in a given time window before and after the trigger. In pp collisions, based on the multiple reconstructed vertices, the SPD vertexer (vertex finding algorithm) was also used to tag pile-up events. An event is tagged as pile-up if more than one vertex is present. After finding the first vertex, referred to as the "main" vertex, tracklets that do not point to this vertex are used to check if there are other vertices from which particles originate.

3.5 Track reconstruction and selection

The charged particle tracks that are reconstructed by the ALICE tracking system, consisting of the ITS and TPC detectors, are extended to the EMCal detector and subjected to a geometric matching with the EMCal cluster, which is a reconstructed electromagnetic shower. To ensure high-quality tracks for electron identification, various selection criteria are employed. The selection criteria applied on tracks for electron identification are presented in TABLE 3.1 for both the pp and p–Pb data sets.

Table 3.1: Track selection criteria applied in pp and p–Pb collisions at $\sqrt{s_{\rm NN}}$ = 5.02 TeV.

Track property	criteria applied
Minimum NCrossedRowsTPC	70
Minimum RatioCrossedRowsOver	
FindableClustersTPC	0.8
Maximum χ^2 per TPC cluster	4
Reject kink candidates	yes
ITS and TPC refit	yes
Hit on SPD layer	kAny
Maximum χ^2 per ITS cluster	36
DCA to Vtx 2D	kTRUE
Require sigma to Vtx	kFALSE
Min number of ITS cluster	2
EMCAL acceptance	$\lvert\eta\rvert < 0.6$, $80 < \phi < 187$
DCAL acceptance	$0.22 < \lvert\eta\rvert < 0.6$, $260 < \phi < 320$
	$\lvert\eta\rvert < 0.6$, $320 < \phi < 327$
Maximum DCAxy	0.5
Maximum DCAz	1.

The charged particle tracks reconstructed using ITS and TPC are propagated towards the EMCal and DCAL (will be together referred as EMCAL) detector using the Kalman filter approach [160]. The tracks which have geometri-

cal matching with EMCal cluster are selected, requiring the track-cluster pair to satisfy $(|\varphi_{\text{track}} - \varphi_{\text{cluster}}|) < 0.01$ and $|\eta_{\text{track}} - \eta_{\text{cluster}}| < 0.01$.

A pseudo-rapidity range of $|\eta| < 0.8$ for charged particles is enforced due to the acceptance of the TPC detector, and $|\eta| < 0.6$ for electrons due to EMCal detector acceptance. When a charged particle passes through the TPC, it generates a signal in the TPC's pad-rows by depositing energy. This deposited energy is considered a cluster if it exceeds a certain threshold; therefore, the maximum number of clusters in a given TPC sector is equivalent to the number of pad-rows, which is 159. As the pad length increases with radial distance, the number of crossed rows is used as a selection criterion for electrons. The number of crossed rows is defined as the number of clusters plus the number of missing clusters [161], which may occur due to various factors such as baseline shifts. Missing clusters can be identified by examining neighboring clusters. A minimum of 70 crossed rows is required for track selection. Clusters at the TPC sector edges or overlapping tracks are excluded from the $\mathrm{d}E/\mathrm{dx}$ calculation due to potential distortion caused by edge effects. Electrons are relatively light particles and lose energy more slowly as they travel through the gas. As a result, they tend to stop in a narrow energy range known as the "Fermi plateau region." In this region, the number of ionization clusters produced by an electron is relatively high, leading to more hits per track in the TPC. On average, electrons have more clusters per track than hadrons because electron tracks are already in their fermi plateau region, which is not the case for hadrons. To ensure the validity of each track candidate, a minimum of 2 ITS clusters, at least one hit on any layer of the SPD, and minimum criteria of 0.8 on the ratio of found TPC cross rows to the number of findable clusters are required [161]. Furthermore, a final refit of the global track with the Kalman filter back to the identified primary vertex must be performed to pass the ITS and TPC for each track candidate. Criteria on the distance of the closest approach (DCA) in the transverse plane (xy) and in the beam direction (z) to the primary vertex are applied to differentiate tracks from the primary vertex and those originating from decays of strange hadrons or interactions with the beam as they have wider DCA. Additionally, a criterion on the χ^2 per degree of freedom (χ^2/ndf) of the momentum fit in the TPC is applied to each track to suppress

random, uncorrelated combinations of clusters in TPC during momentum reconstruction. Any tracks that deviate from the track model of continuous particle trajectories, such as those showing deviations due to emission of bremsstrahlung or due to decay in flight, are discarded from the analysis by rejecting the kink mother (mother particle of a deviated particle). It should be noted that the TPC dE/dx resolution of kink tracks is typically poorer than that of regular tracks.

3.6 Electron identification

In this analysis, we utilize particle identification (PID) information from the TPC and EMCal detectors to perform electron identification. In TPC, particles are identified using the information of specific energy loss (dE/dx). Figure 3.1 displays the n$\sigma^{e}_{\mathrm{TPC-d}E/\mathrm{d}x}$ distribution (deviation of measured dE/dx relative to the expected dE/dx for electrons) as a function of momentum for both pp and p–Pb collisions. To select electron candidates, a criterion of $-1 <$ n$\sigma^{e}_{\mathrm{TPC-d}E/\mathrm{d}x}$ < 3 is applied. The criteria are asymmetric, with higher pion contamination in the $-3 <$ n$\sigma^{e}_{\mathrm{TPC-d}E/\mathrm{d}x} < -1$ region. The number of n$\sigma^{e}_{\mathrm{TPC-d}E/\mathrm{d}x}$, defined as the difference between the measured dE/dx signal in the detector and the expected value for electrons divided by the energy-loss resolution in TPC. To extend the momentum range of electrons and to distinguish them from hadrons, the EMCal detector is used. The momentum information for each track is provided by the TPC and ITS track reconstruction algorithm, while the corresponding energy deposit is measured in the EMCal. Electrons are identified based on their E/p ratio, which is around 1 since the mass of electrons can be ignored for relativistic particles. On the other hand, pions have a lower E/p ratio as they deposit only a fraction of their initial energy in the EMCal. Parameters describing the shape of the particle shower (ellipsoid shape) in the EMCal detector are also utilized to improve the purity of the electron sample. In this analysis, a selection on the long axis (M02) is applied as it proves to be more effective than a selection on the short axis in improving electron purity, as detailed in [162].

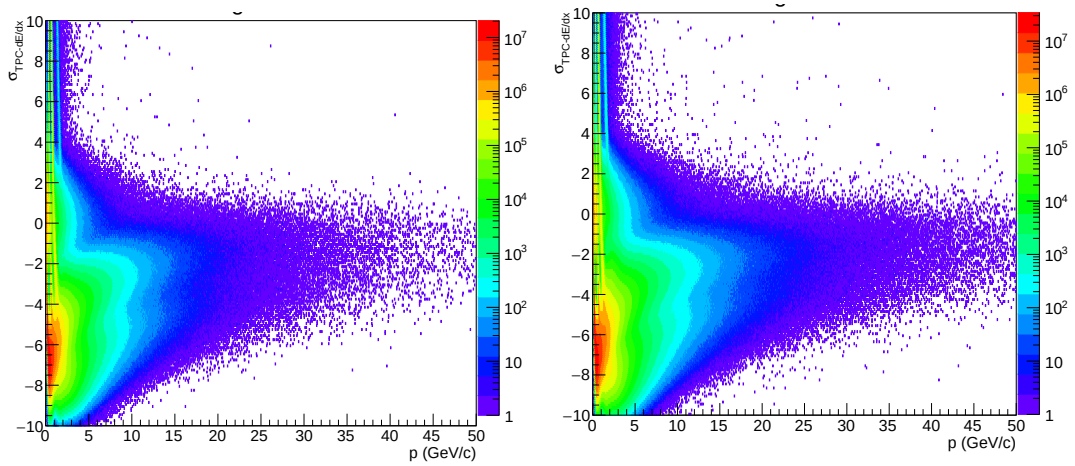

Figure 3.1: $\mathrm{n}\sigma^{e}_{\mathrm{TPC-d}E/\mathrm{d}x}$ distribution is shown for pp collisions (left) and in p–Pb collisions (right) at $\sqrt{s_{\mathrm{NN}}} = 5.02$ TeV.

Figure 3.2 and 3.3 illustrate the E/p distribution in various p_{T} ranges from 3 to 12 GeV/c for pp and p–Pb events, respectively, after applying criteria of $-1 < \mathrm{n}\sigma^{e}_{\mathrm{TPC-d}E/\mathrm{d}x} < 3$ and $0.02 < \mathrm{M02} < 0.9$. To estimate the hadron contamination, the E/p ratio for hadrons ($-10 < \mathrm{n}\sigma^{e}_{\mathrm{TPC-d}E/\mathrm{d}x} < -3.5$) is taken after applying shower shape criteria that are scaled to match the E/p distribution in the range $0.3 < E/p < 0.6$. The resemblance between the shapes of electrons and hadrons in this region indicates that the predominant contribution is likely to be from hadrons. Since electrons and hadrons exhibit similar shapes in this region, it is likely that the majority of the contribution comes from hadrons. This information is useful in estimating the level of hadron contamination in the electron region with an E/p value ranging from 0.8 to 1.2. The purity of the electron sample is shown in Figure 3.4. The purity is calculated as the ratio of the number of all electron candidates (Alle) minus the number of hadrons (Had) to the number of all electron candidates for $0.8 < E/p < 1.2$.

$$Purity = \frac{N^{\mathrm{Alle}} - N^{\mathrm{Had}}}{N^{\mathrm{Alle}}}. \tag{3.7}$$

The purity of the electron sample for the p_{T} bin considered in the correlation analysis ($4 < p^{\mathrm{e}}_{\mathrm{T}} < 12$ GeV/c) is 95.5% in pp collisions and 97.8% in p–Pb collisions.

The values for $\mathrm{n}\sigma^{e}_{\mathrm{TPC-d}E/\mathrm{d}x}$, E/p , and shower shape criteria applied are

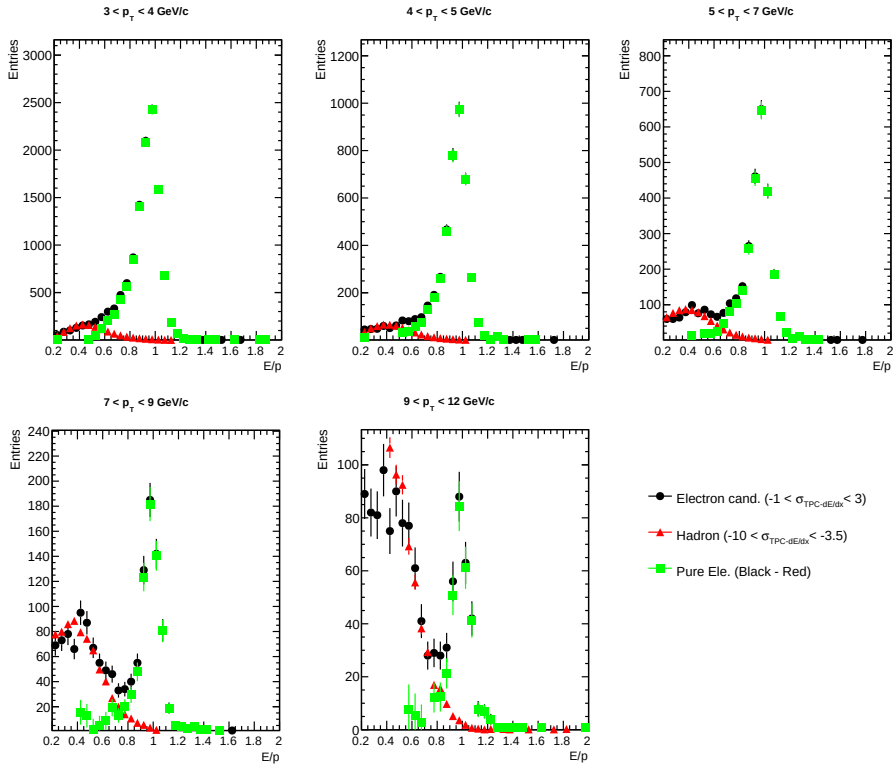

Figure 3.2: E/p distribution after $-1 < \mathrm{n}\sigma^{e}_{\mathrm{TPC}-\mathrm{d}E/\mathrm{d}x} < 3$ and $0.02 <$ M02 $<$ 0.9 criteria in pp collisions at $\sqrt{s} = 5.02$ TeV. Hadron contamination is shown in the red distribution. E/p distribution for electrons after subtracting hadron contamination is shown in green points.

summarized in Table 3.2.

Table 3.2: Electron identification criteria

criteria parameters	criteria applied
$\mathrm{n}\sigma^{e}_{\mathrm{TPC}-\mathrm{d}E/\mathrm{d}x}$	(-1, 3)
Shower shape long axis (M02)	(0.02, 0.9)
E/p	(0.8, 1.2)

After applying the electron identification criteria, any remaining hadron contamination is removed by scaling the hadrons to the E/p distribution, resulting in an inclusive electron sample.

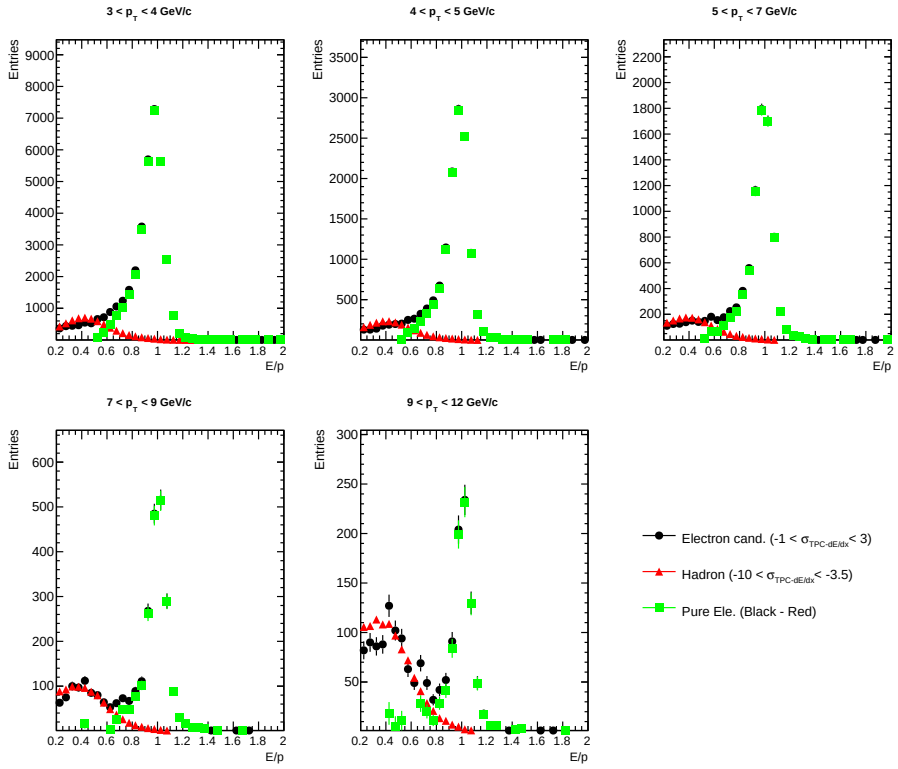

Figure 3.3: E/p distribution after $-1 < \mathrm{n}\sigma^{e}_{\mathrm{TPC-d}E/\mathrm{d}x} < 3$ and $0.02 < \mathrm{M02} < 0.9$ criteria in p–Pb collisions at $\sqrt{s_{\mathrm{NN}}} = 5.02$ TeV. Hadron contamination is shown in the red distribution. E/p distribution for electrons after subtracting hadron contamination is shown in green.

3.7 Estimation of Non-HFE contribution

The inclusive electron spectrum arises from several sources, which include:

- Heavy-flavour electrons originating from the semi-leptonic decay of heavy-flavour hadrons (c, b $\rightarrow$ e).
- Electrons resulting from Dalitz decays of light neutral mesons ($\pi^0 \rightarrow \gamma e^+ e^-$) and from photon conversion in the detector material.
- Electrons produced from weak K $\rightarrow$ e$\pi\mu$ (K_{e3}) decays and dielectron decays of light vector mesons.
- Electrons generated from dielectron decays of heavy quarkonia ($J/\psi \rightarrow e^+ e^-$).

- Electrons originating from partonic hard scattering processes, including Drell-Yan processes and prompt photon production ($q\bar{q} \rightarrow \gamma/Z \rightarrow e^+e^-$).

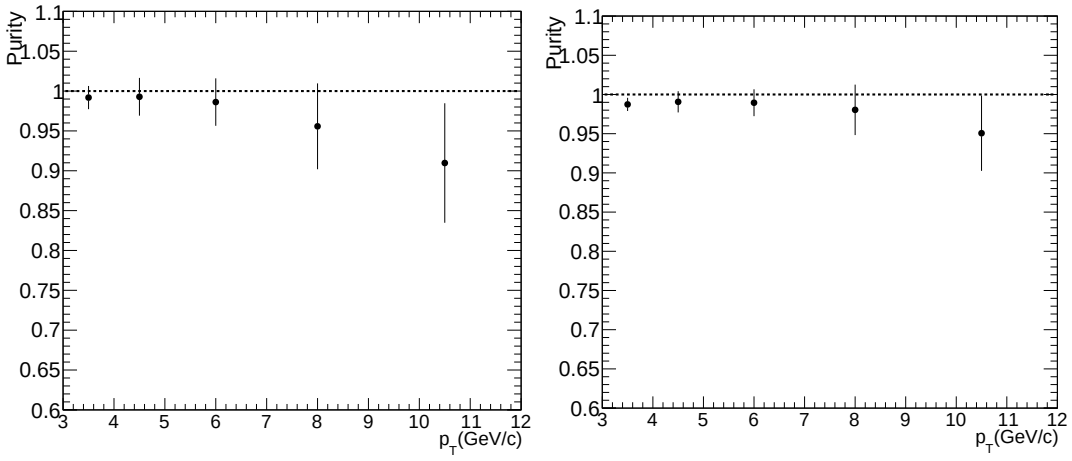

Figure 3.4: purity of the electron sample in pp (left) and p–Pb (right) collisions for $4 < p_{\mathrm{T}}^{\mathrm{e}} < 12$ GeV/c at $\sqrt{s_{\mathrm{NN}}} = 5.02$ TeV.

The dominant sources of non-heavy-flavour electrons (non-HFE), especially in the considered p_{T} range, are electrons from Dalitz decay and photon conversions, which are depicted in Figure 3.5 [41]. The other sources contribute negligibly; as a result, the analysis focuses on reconstructing the non-HFE background.

The invariant mass distribution of electron pairs from conversions and Dalitz decay (i.e., non-HFE sources) peaks at low invariant mass due to zero photon mass, while no such correlation exists for HFE. Therefore, the non-HFE background can be estimated by pairing the $\mathrm{e}^{\pm}$ with their partners and calculating their invariant mass.

The procedure starts with applying electron identification criteria to tag one of the $\mathrm{e}^{\pm}$ tracks from the primary collision vertex. Next, all other tracks in the same event are looped over to find the partner electron. Partner electrons are selected from AOD tracks passing the selection criteria summarized in Table 3.3. In order to improve the probability of reconstruction, loose criteria are imposed on partner electrons.

A loose $\mathrm{d}E/\mathrm{d}x$ criteria is implemented for the partner electron around the electron band to increase the likelihood of detecting the electron pair.

To eliminate electrons originating from photon conversion, a criterion is ap-

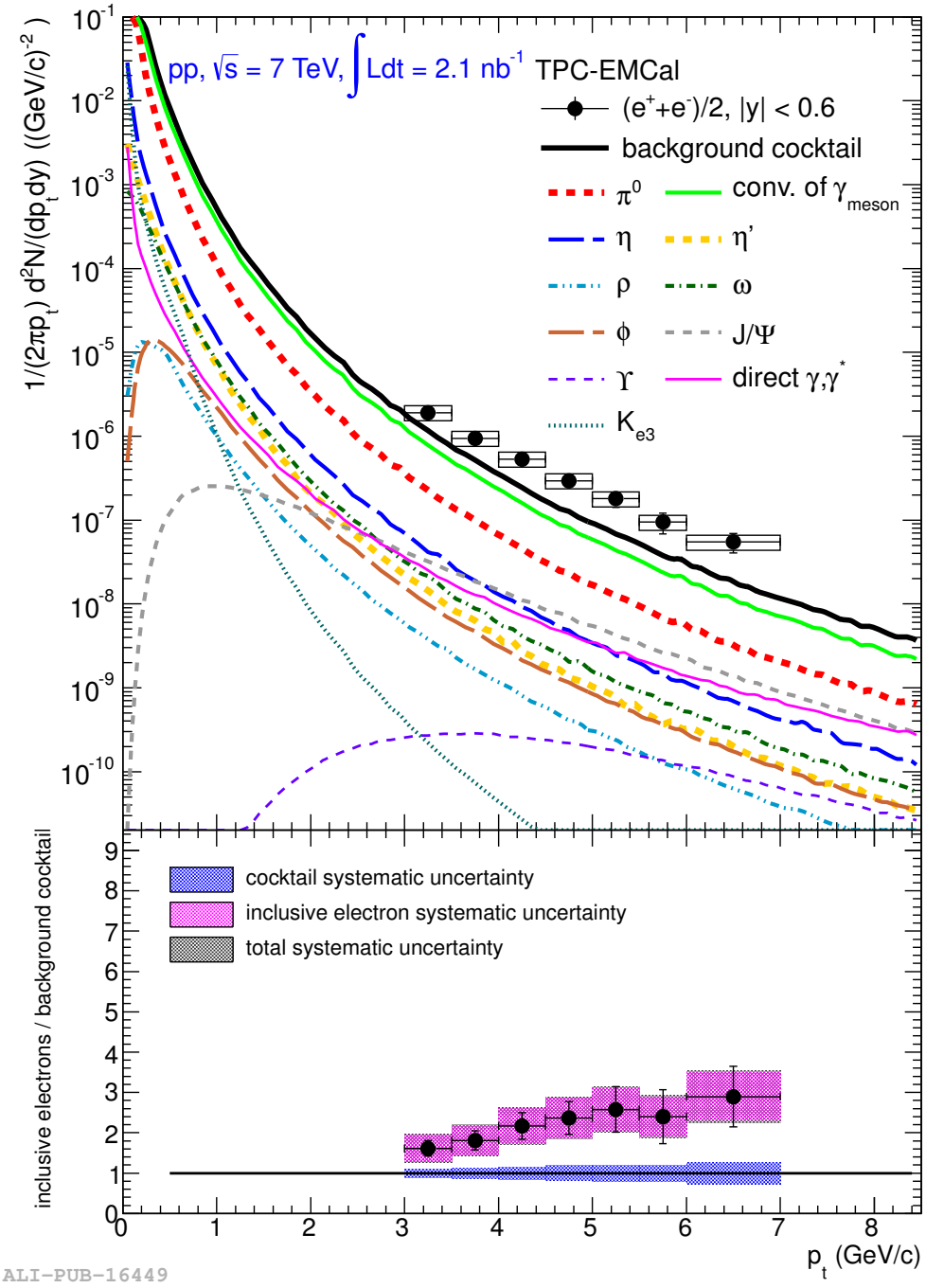

Figure 3.5: Inclusive electron yield per minimum bias pp collision as function of p_{T} at $\sqrt{s} = 7$ TeV in comparison with different background sources calculated using an MC hadron-decay generator. Lower panels show the ratio of the inclusive electron yield to the background electron cocktail [41].

plied on the invariant mass of $M_{e^{\pm}} < 0.14$ GeV/c^2 . The unlike-sign electron pairs include both true Non-HFE and combinatorial background. The combinatorial background is estimated from the like-sign pairs. The Non-HFE sample can be obtained by subtracting the like-sign (LS) paired electrons from the unlike-sign

Table 3.3: Selection criteria for partner electron selection.

Track property	criteria applied
Min number of TPC clusters	50
Maximum χ^2 per TPC cluster	4
Reject kink candidates	yes
Maximum DCAxy	2.4
Maximum DCAz	3.2
DCA to Vtx 2D	kTRUE
Minimum NCrossedRowsTPC	60
Minimum RatioCrossedRowsOverFindableClustersTPC	0.6
Min p_{T} (GeV/c)	0.1
TPC and ITS refit	yes
Pseudorapidity	$-0.9 < \eta < 0.9$
PID criteria	$-3 < \mathrm{n}\sigma^{e}_{\mathrm{TPC}-\mathrm{d}E/\mathrm{d}x} < 3$
Maximum DCAxy	0.5
Maximum DCAz	1.

(ULS) sample.

$$N_e^{\mathrm{Non-HF-reco}} = N_e^{\mathrm{ULS}} - N_e^{\mathrm{LS}}. \tag{3.8}$$

The invariant mass distribution for like-sign (LS) and unlike-sign (ULS) electron pairs is shown in Figure 3.6.

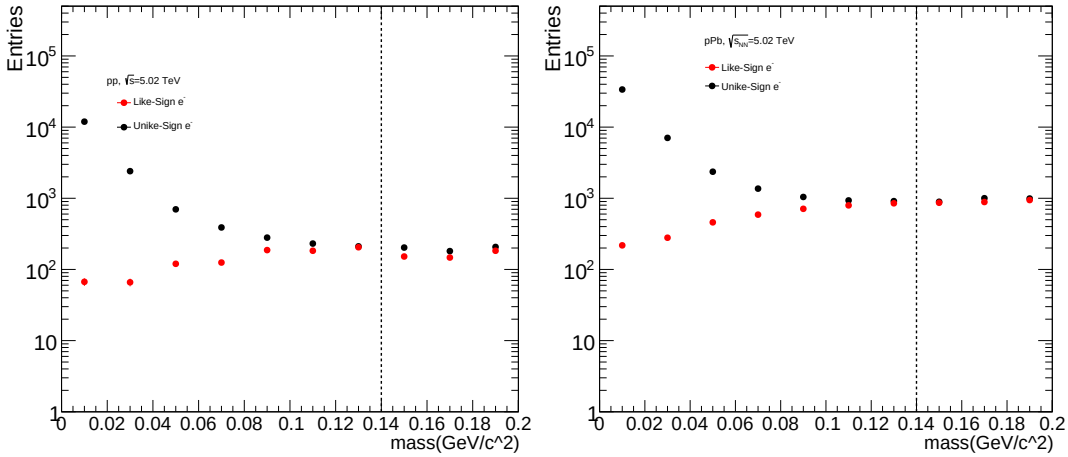

Figure 3.6: Invariant mass distribution for the like-sign (red symbols) and unlike-sign (black symbols) electron pairs for $4 < p_{\mathrm{T}}^{e} < 12$ GeV/c in pp and p–Pb collisions at $\sqrt{s_{\mathrm{NN}}} = 5.02$ TeV.

3.8 Non-HFE identification efficiency

Some photonic decays may not be detected in the data due to various reasons, such as a partner photon being outside the detector's range, not meeting certain requirements, or not being chosen during track reconstruction. As a result, the initial count of photonic electrons is corrected by the tagging efficiency (ϵ_{tag}) obtained from a Monte-Carlo (MC) sample, which represents the likelihood of correctly identifying photonic electrons. The Non-HFE tagging efficiency using the invariant mass method is calculated by applying the same analysis criteria to the MC samples mentioned in section 3.3. The tagging efficiency can be calculated by taking the ratio of the number of true photonic pairs originating from the same mother (N_{Found}) that have passed the associated track selection criteria to the total number of electrons (positrons) originating from photonic sources (N_{Total}) obtained from the enhanced MC sample. The enhanced MC sample is used in order to reduce the statistical uncertainty arising from using a general-purpose sample at high p_{T}.

$$\epsilon_{\mathrm{tag}} = \frac{N_{\mathrm{Found}}}{N_{\mathrm{Total}}}. \tag{3.9}$$

Due to the presence of π^0 and η enhancement in the MC sample, the p_{T} distribution of electrons is biased. This bias is corrected by calculating the weight

of the π^0 and η enhancement (HIJING/Enhancement) and applying it to the p_{T} distribution of electrons.

3.8.1 Weight calculation

The weight is determined by selecting π^0 and η from HIJING and enhanced events while ensuring that the enhanced π^0 and η do not originate from enhanced HF decays by selecting only those π^0 and η that have no mother. The ratio of the p_{T} distribution of HIJING and embedded events is then calculated. This ratio is fitted with a Hagedorn function $\frac{A}{(\exp(-Bx-Cx^2)+\frac{x}{D})^E}$ [163] to parameterize the enhanced sample, as shown in Figure 3.7 for pp collisions. Here, A,B,C,D, and E are the free parameters.

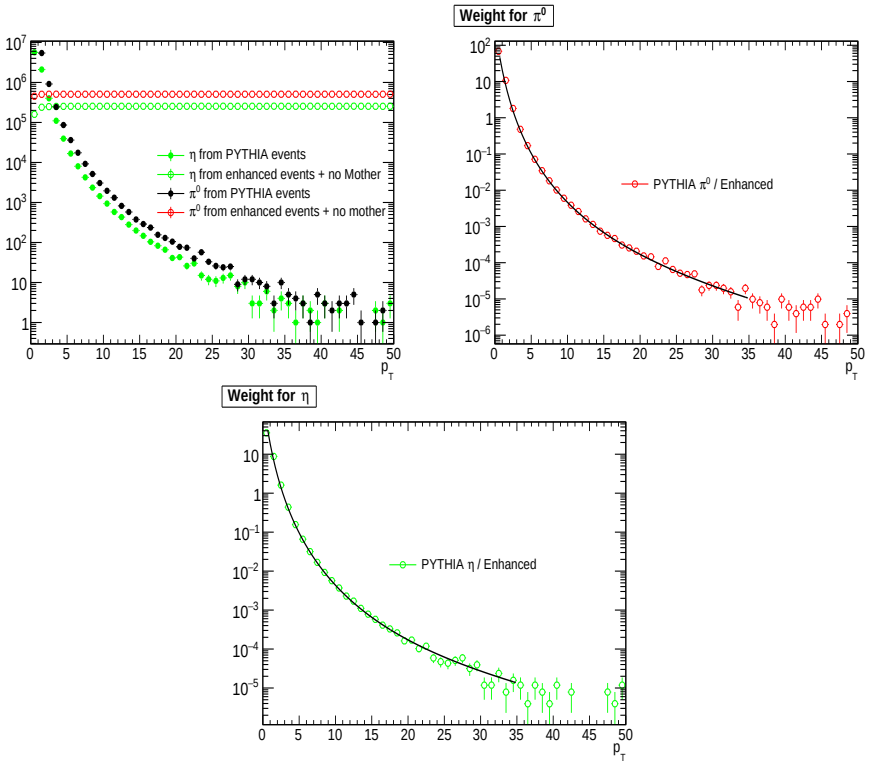

Figure 3.7: p_{T} distribution of π^0 and η (top Left) from PYTHIA and embedded events. Weight = PYTHIA/Embedded p_{T} distribution fit with a Hagedorn function for π^0 (top Right)and η (bottom) in pp collisions at $\sqrt{s} = 5.02$ TeV.

The obtained weight from the fit function is used to adjust the electron p_{T} spectrum and remove the enhancement bias. Specifically, the electron p_{T} is multiplied by the weight obtained from the fit function using the parent particle's

p_{T} (π^0 and η) as input. Figure 3.8 illustrates the electron p_{T} distribution before and after the weight adjustment in pp collisions. The same weight adjustment procedure is also applied to the p–Pb MC sample.

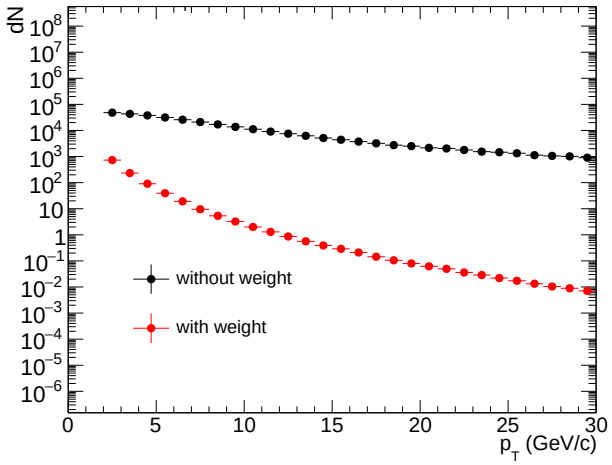

Figure 3.8: p_{T} distribution of electrons before and after applying the weight in pp collisions at $\sqrt{s} = 5.02$ TeV.

The efficiency of non-HFE tagging as a function of $p_{\mathrm{T}}^{\mathrm{e}}$ is presented in Figure 3.9 in pp and p–Pb collisions before and after applying the weight to remove the bias from enhancement. The efficiency varies from 66% for low momenta to 79% for momenta above 10 GeV/c.

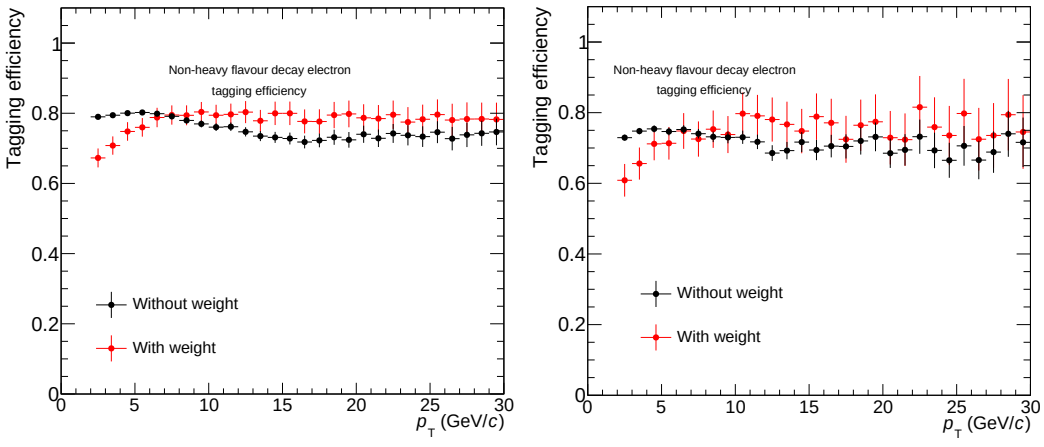

Figure 3.9: Non-HFE reconstruction efficiency as a function of $p_{\mathrm{T}}^{\mathrm{e}}$ before and after applying the weight for pp (left) and p–Pb (right) collisions at $\sqrt{s_{\mathrm{NN}}} = 5.02$ TeV.

3.9 Azimuthal angular correlations between heavy flavour electrons and charged particles

The purpose of this analysis is to examine the characteristics of heavy-flavour production in pp and p–Pb collisions by constructing azimuthal angular correlations ($\Delta\varphi$) between the charged particle and heavy-flavour hadron decay electrons. The initial stage involves creating a $\Delta\varphi$ distribution for charged particle and inclusive electrons as

$$\Delta\varphi(e,h) = \varphi^{e} - \varphi^{h} \tag{3.10}$$

Section 3.6 explains the method used to identify electrons, while TABLE 3.4 outlines the criteria applied to select charged hadrons from the TPC detector. The hadron sample does not undergo any particle identification process.

The azimuthal correlations between heavy-flavour hadron decay electrons and charged particle are calculated as

$$\frac{dN^{\mathrm{HF}}}{d\Delta\varphi_{e-h}} = \frac{dN^{\mathrm{Incl}}}{d\Delta\varphi_{e-h}} - \frac{1}{\epsilon^{\mathrm{tagging}}} \times \frac{dN^{\mathrm{Non-HF-reco}}}{d\Delta\varphi_{e-h}}, \tag{3.11}$$

In this equation, the first term refers to azimuthal correlation distribution between inclusive and charged particle, whereas the second term refers to correlation distribution between non-HFE and charged particle. To select the hadron candidate tracks, the AOD track sample is utilized and filtered using the selection criteria detailed in Table 3.3. This chapter outlines the approach employed to investigate the azimuthal angular Figure 3.10 and 3.11 display the $\Delta\varphi$ distribution of inclusive electrons and charged particles in pp and p–Pb collisions, respectively. Since the distributions are not normalized, the peaks in p–Pb collisions appear higher in amplitude due to the larger statistics.

Table 3.4: Track selection criteria for associated particles.

Track property	criteria applied
Min number of TPC clusters	50
Maximum χ^2 per TPC cluster	4
Reject kink candidates	yes
Maximum DCAxy	2.4
Maximum DCAz	3.2
DCA to Vtx 2D	kTRUE
Minimum NCrossedRowsTPC	60
Minimum RatioCrossedRowsOverFindableClustersTPC	0.6
TPC and ITS refit	yes
Pseudorapidity	$-0.8 < \eta < 0.8$
PID criteria	$-3 < \mathrm{n}\sigma^{e}_{\mathrm{TPC}-\mathrm{d}E/\mathrm{d}x} < 3$
Maximum DCAxy	0.5
Maximum DCAz	1.

3.10 Mixed event correction

The distribution of the azimuthal angular correlation can be distorted by several factors, such as pair acceptance and dead or noisy channels in detectors. To mitigate such distortions, the $(\Delta\eta, \Delta\varphi)$ distributions from mixed events are utilized. This involves creating a distribution by selecting electrons from one event and charged particles from other events. In an ideal scenario, if there is no acceptance or detector impact, the distribution of $\Delta\varphi$ in mixed events should be flat as there is no correlation between electrons and hadrons from separate events, and the $\Delta\eta$ distribution should be triangular structure due to the limited η acceptance of the detector. Any deviation from this flat distribution can be attributed due to detector effects and must be corrected for.

To acquire the correlation distribution using the event mixing method, a mixed event pool is constructed using charged particles from different events except for the same-event. The hadron tracks in this mixed event pool are selected using the same criteria as in the same-event analysis. The mixed event $\Delta\varphi$ dis-

tributions are built utilizing events with similar characteristics, such as centrality and primary vertex position along the z-axis (VtxZ). Consequently, the mixed event pool is divided into one centrality and four VtxZ bins for pp analysis and four multiplicity percentile and six VtxZ bins for p–Pb analysis.

pp events:

- Centrality bin : (0,100)
- VtxZ(cm) bin : (-10,-3), (-3,0.9), (0.9,3), (3,10)

p–Pb events:

- Centrality bin: (0,25), (25,50), (50,75), (75,100)
- VtxZ(cm) bin : (-10,-4.6), (-4.6,-1.6), (-1.6,0.9), (0.9,3.4), (3.4,6.1), (6.1,10)

In mixed-event pool, the centrality pool is divided into equally-sized bins based on a uniform distribution, while the asymmetry in VtxZ bins accounts for the shift of mean in the z-vertex distribution from $VtxZ = 0.$, which is centered around $VtxZ = 0.9$ in pp and p–Pb collisions. Only events within the same centrality and VtxZ bins are used to construct the mixed event distribution, and at least three events must be present in each bin to ensure a sufficient number of particles for the distribution. The mixed event $(\Delta\eta, \Delta\varphi)$ distribution in pp and p–Pb collisions are shown in Figures 3.12 and 3.13, respectively.

When $(\Delta\eta, \Delta\varphi) \approx 0$, the trigger electron and its corresponding hadrons that originate from the same event must be within the detector's range. This characteristic can be utilized to calculate the normalization factor for the mixed event distribution. The $\Delta\varphi$ distribution, which compares the heavy-flavour decay electrons to the charged hadrons from the mixed event approach, is standardized so that the output at $\Delta\varphi \approx 0$ is equivalent to one. This standardization coefficient is known as β.

To correct for acceptance and detector effects on the $(\Delta\eta, \Delta\varphi)$ distribution from the same event, the ratio of the distributions from the same event and mixed events are taken.

$$\frac{d^2N^{pair}}{d\Delta\eta d\Delta\varphi} = \beta \times \frac{S_{SE}(\Delta\eta, \Delta\varphi)}{B_{ME}(\Delta\eta, \Delta\varphi)} \tag{3.12}$$

The signal distribution is the particle yield of pairs in the same event, given by

$$S_{SE}(\Delta\eta, \Delta\varphi) = \frac{d^2N^{same}}{d\Delta\eta d\Delta\varphi} \tag{3.13}$$

where, N^{same} is the number of pairs within a $(\Delta\eta, \Delta\varphi)$ bin. The background distribution from mixed-event is given by

$$B_{ME}(\Delta\eta, \Delta\varphi) = \frac{d^2N^{mix}}{d\Delta\eta d\Delta\varphi} \tag{3.14}$$

where, N^{mix} is the number of mixed-event pairs. To correct for mixed events, each correlation component necessary to construct the heavy-flavour decay electron correlation, such as $(\Delta\eta, \Delta\varphi)$ of inclusive, ULS, and LS electrons, etc., are subject to mixed event correction in all p_{T} bins. However, the mixed event distribution may experience significant statistical fluctuations at high associated track p_{T} ($p_{\mathrm{T}} > 4$ GeV/c), so to reduce this fluctuation, the mixed event $(\Delta\eta, \Delta\varphi)$ distribution for $p_{\mathrm{T}} > 4$ GeV/c is merged and used for all p_{T} bins, as the shape of the mixed event $\Delta\varphi$ distribution is independent of p_{T}, as depicted in Figure 3.14.

As defined in eq. 3.13, the mixed-event corrected same-event $(\Delta\eta, \Delta\varphi)$ distribution is shown in Figure 3.15 and 3.16 in pp and p–Pb collisions, respectively. Note that the mixed-event distribution is limited to $|\Delta\eta| < 1$ to avoid the "wing effect," which is a large fluctuation that occurs at large $\Delta\eta$ due to limited entries of correlation bins in that region. The final distribution used for this analysis is the one projected to $\Delta\varphi$, as the available statistics are limited and would not allow for a correlation study in both $(\Delta\eta, \Delta\varphi)$.

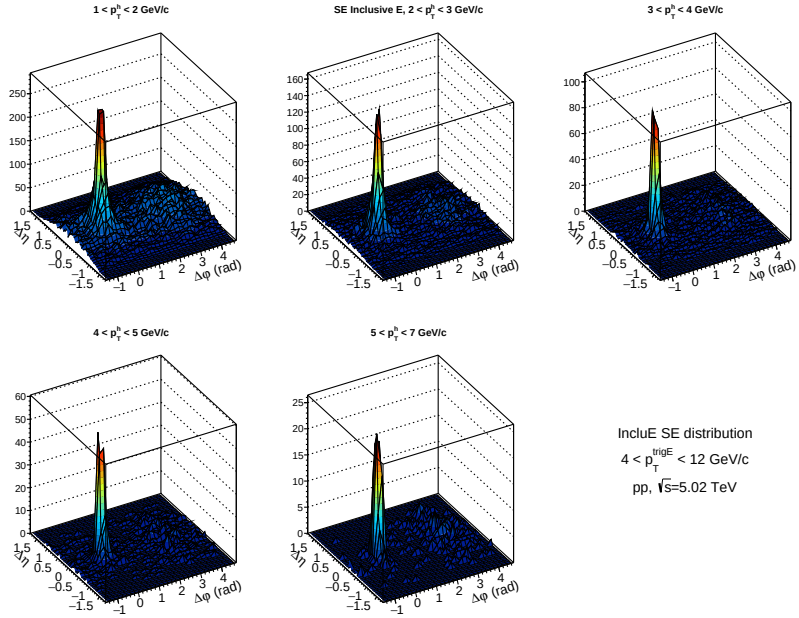

Figure 3.10: Same event $(\Delta\eta, \Delta\varphi)$ distribution between inclusive electrons and charged particles for $4 < p_{\mathrm{T}}^{\mathrm{e}} < 12$ GeV/c and in different associated charged particle p_{T} ranges in pp collisions at $\sqrt{s} = 5.02$ TeV.

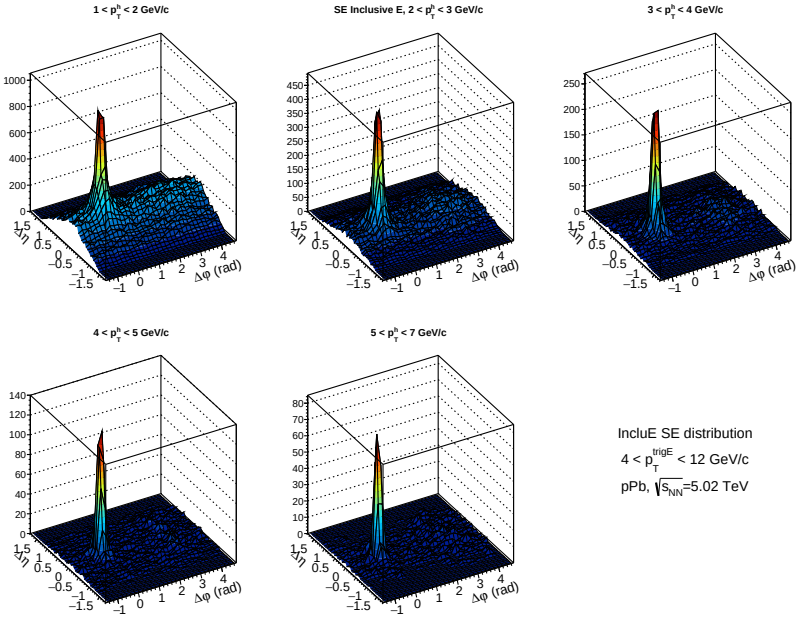

Figure 3.11: Same event $(\Delta\eta, \Delta\varphi)$ distribution between inclusive electrons and charged particles for $4 < p_{\mathrm{T}}^{\mathrm{e}} < 12$ GeV/c and in five associated charged particle p_{T} ranges for p–Pb collisions at $\sqrt{s_{\mathrm{NN}}} = 5.02$ TeV.

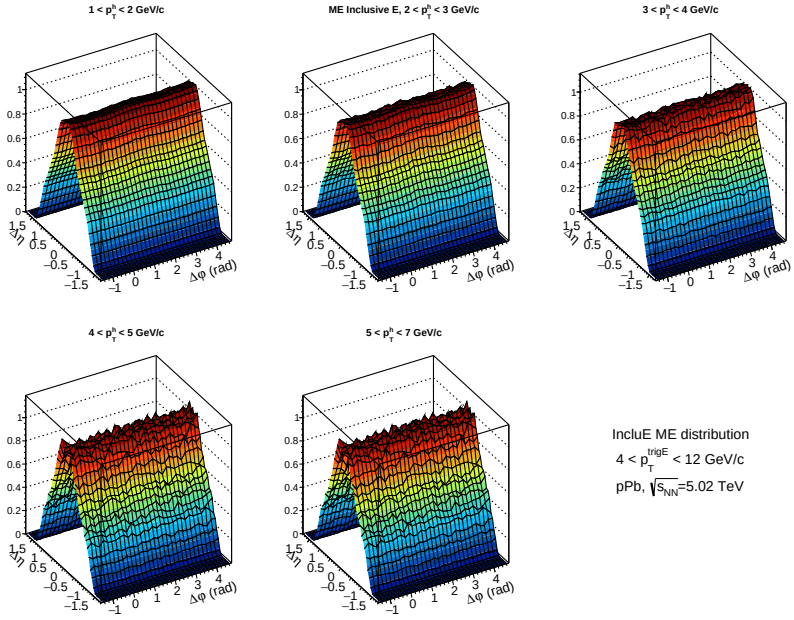

Figure 3.13: Mixed event $(\Delta\eta, \Delta\varphi)$ distribution between inclusive electrons and charged particles normalized by β $(N^{\Delta\varphi=0})$ for $4 < p_{\mathrm{T}}^{\mathrm{e}} < 12$ GeV/c and in five associated charged particle p_{T} ranges for p–Pb collisions at $\sqrt{s_{\mathrm{NN}}} = 5.02$ TeV.

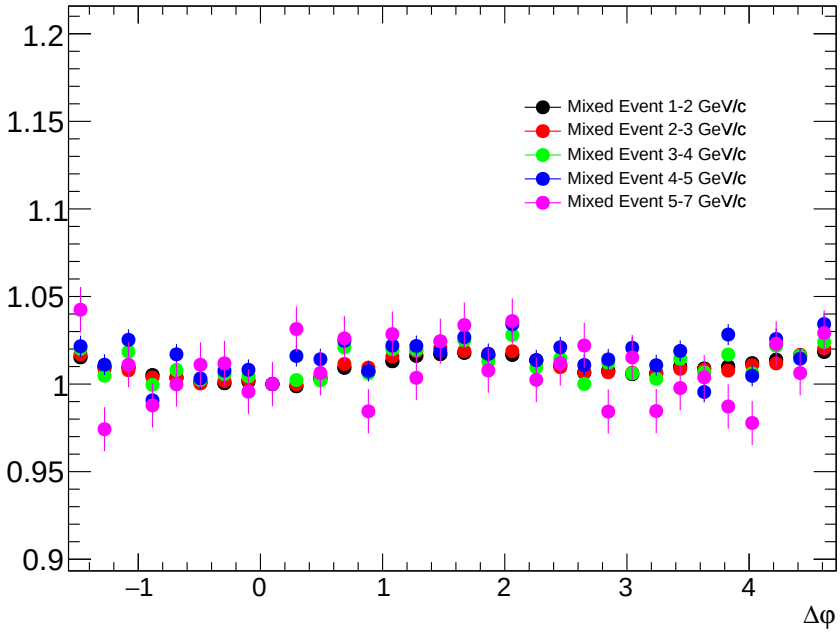

Figure 3.14: Mixed event $\Delta\varphi$ distribution for different $p_{\mathrm{T}}^{\mathrm{assoc}}$ ranges normalized by the yield at $\Delta\varphi = 0$ in pp collisions at $\sqrt{s} = 5.02$ TeV.

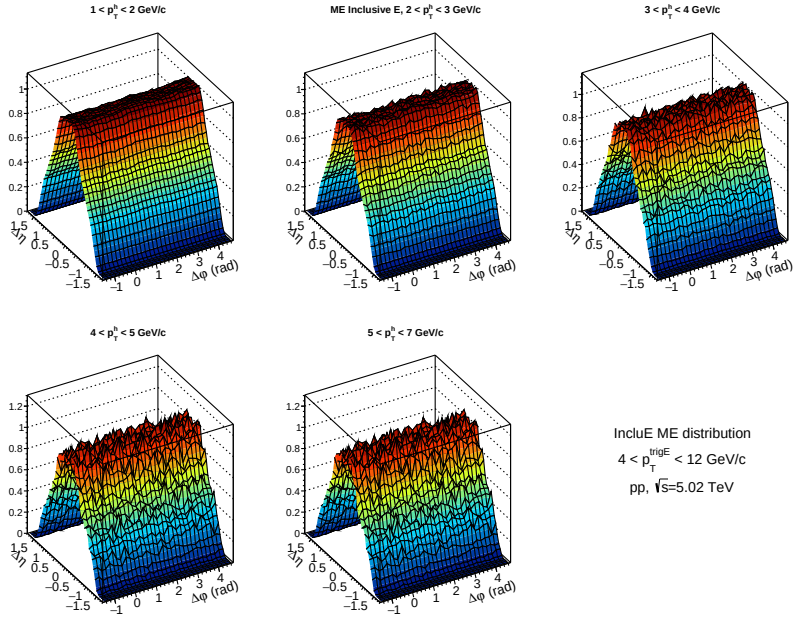

Figure 3.12: Mixed event $(\Delta\eta, \Delta\varphi)$ distribution between inclusive electrons and charged particles normalized by β $(N^{\Delta\varphi=0})$ for $4 < p_{\mathrm{T}}^{\mathrm{e}} < 12$ GeV/c and in five associated charged particle p_{T} ranges in pp collisions at $\sqrt{s} = 5.02$ TeV.

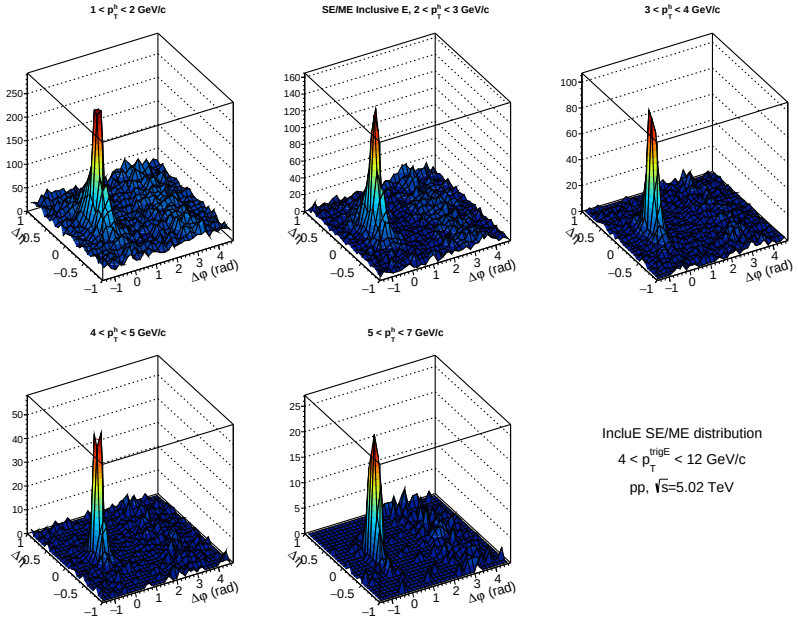

Figure 3.15: SE/ME $(\Delta\eta, \Delta\varphi)$ distribution between inclusive electrons and charged particles for $4 < p_{\mathrm{T}}^{\mathrm{e}} < 12$ GeV/c and in five associated charged particle p_{T} ranges in pp collisions at $\sqrt{s} = 5.02$ TeV.

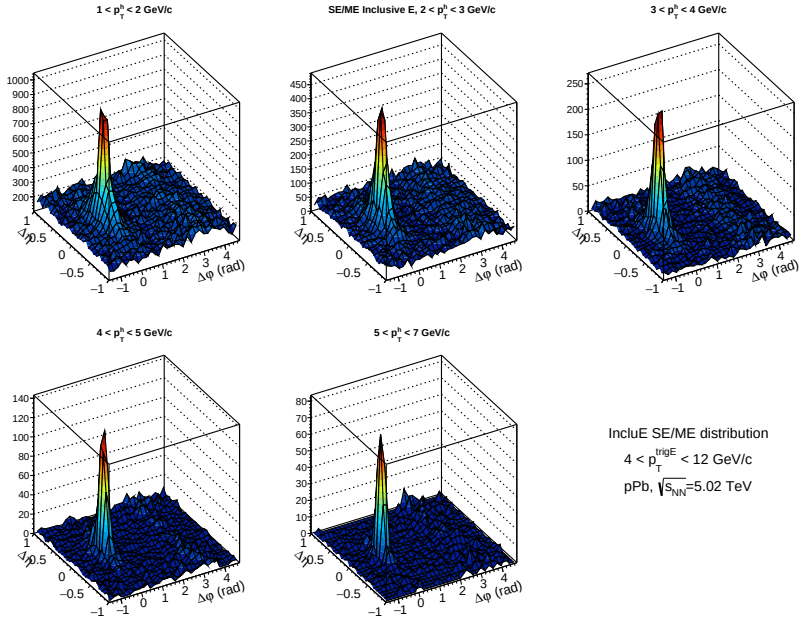

Figure 3.16: SE/ME $(\Delta\eta, \Delta\varphi)$ distribution between inclusive electrons and charged particles for $4 < p_{\mathrm{T}}^{\mathrm{e}} < 12$ GeV/c and in five associated charged particle p_{T} ranges for p–Pb collisions at $\sqrt{s_{\mathrm{NN}}} = 5.02$ TeV.

3.11 Hadron contamination

As we know, the inclusive electron sample can contain some unwanted hadron contamination. To reduce this contamination, a hadron-hadron $\Delta\varphi$ distribution is constructed. The correlation distribution is obtained using hadron triggers with $\mathrm{n}\sigma^{e}_{\mathrm{TPC-d}E/\mathrm{d}x}$ in the range of $(-10, -4)$, and it is then scaled to the yield of hadron contamination in the E/p distribution (explained in section 3.6). The $\Delta\varphi$ distribution for inclusive electrons before and after the removal of hadron contamination is shown in Figure 3.17 and 3.18 for pp and p–Pb collisions. In these figures, the black points represent the $\Delta\varphi$ distribution for inclusive electrons, the blue distribution represents the hadron contamination, and the red distribution is the result of removing the hadron contamination from the inclusive electron sample. The contamination from charged hadrons was estimated to be around 1% at $p_{\mathrm{T}} = 4$ GeV/c increasing to about 12% at 16 GeV/c in both pp and p–Pb collisions.

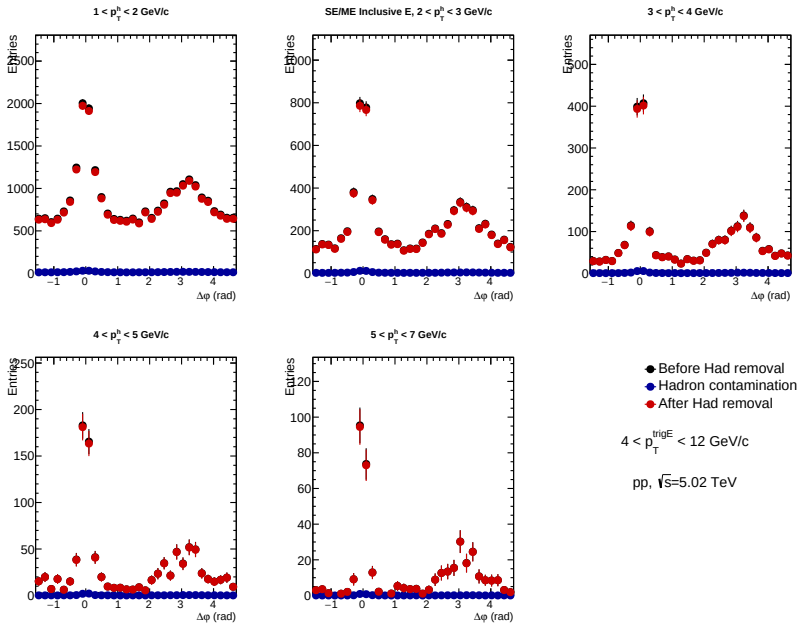

Figure 3.17: $\Delta\varphi$ distribution for inclusive electrons before and after subtraction of hadron contamination $4 < p^{\mathrm{e}}_{\mathrm{T}} < 12$ GeV/c and in five associated charged particle p_{T} ranges in pp collisions at $\sqrt{s} = 5.02$ TeV.

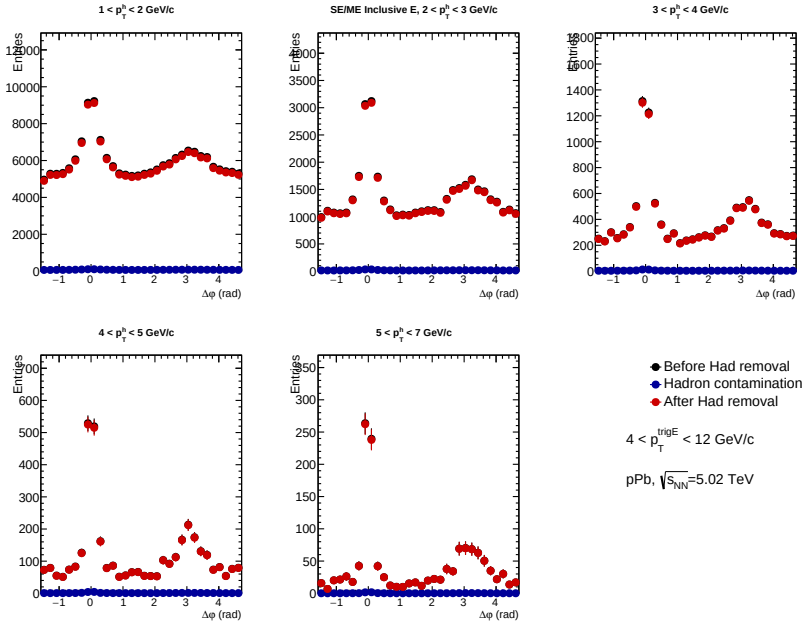

Figure 3.18: $\Delta\varphi$ distribution for inclusive electrons before and after subtraction of hadron contamination $4 < p_{\mathrm{T}}^{\mathrm{e}} < 12$ GeV/c and in five associated charged particle p_{T} ranges in p–Pb collisions at $\sqrt{s_{\mathrm{NN}}} = 5.02$ TeV.

3.12 Non-HF decay electron correlation

The $\Delta\varphi$ correlation between inclusive electrons and charged particles comprises of electrons from heavy-flavour hadron decay as well as non-heavy-flavour electron. To identify the non-heavy flavour electron background, the invariant mass method is used as described in Section 3.7.

The $\Delta\varphi$ distribution for the reconstructed non-heavy flavour electron background, denoted as Non-Hf$_{\rm r}$, is obtained by subtracting the $\Delta\varphi$ distribution of unlike-sign pairs from that of like-sign pairs for electrons, i.e.,

$$\Phi_{\rm r}^{\rm Non-HF} = \Phi_{\rm r}^{\rm ULS} - \Phi_{\rm r}^{\rm LS} \tag{3.15}$$

The $\Delta\varphi$ distribution for ULS, LS and Non-Hf$_{\rm r}$ electrons are shown in Figure A.1, A.2 and A.5 in pp collisions, and in Figure A.3, A.4, A.6 for p–Pb events, respectively.

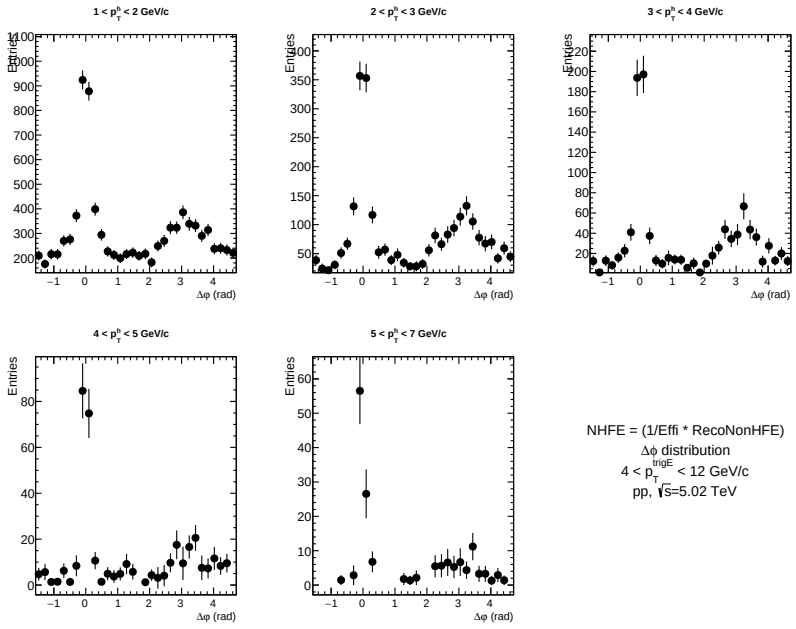

Figure 3.19: $\Delta\varphi$ distribution for non-heavy flavour electron $4 < p_{\rm T}^{\rm e} < 12$ GeV/c and in five associated charged particle $p_{\rm T}$ ranges in pp collisions at $\sqrt{s} = 5.02$ TeV.

The Non-Hf$_{\rm r}$ $\Delta\varphi$ distribution is need to correct by the tagging efficiency (ϵ_{tag}) as reported in the section 3.8. The Non-HFE $\Delta\varphi$ distribution after efficiency correction is shown in Figure 3.19 and 3.20 for pp and p–Pb, respectively.

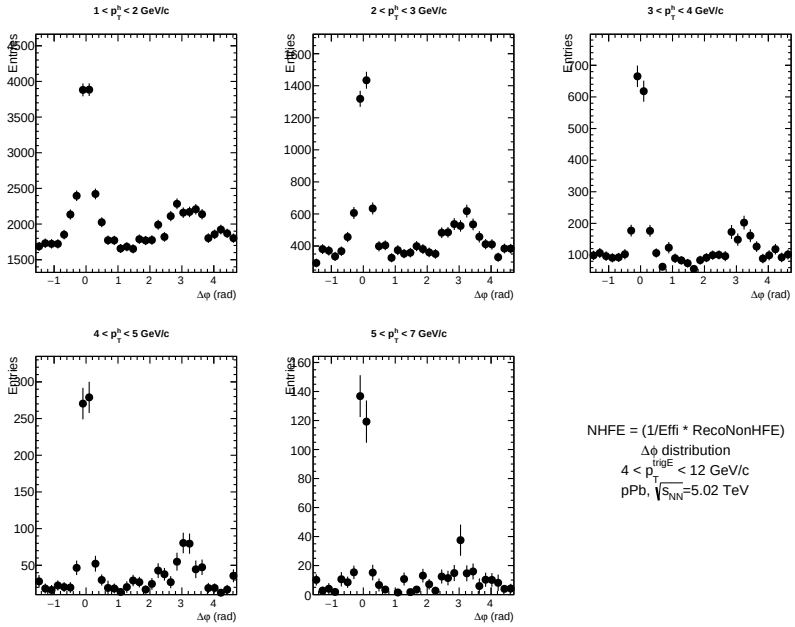

Figure 3.20: $\Delta\varphi$ distribution for non-heavy flavour electron for $4 < p_{\mathrm{T}}^{\mathrm{e}} < 12$ GeV/c and in five associated charged particle p_{T} ranges in p–Pb collisions at $\sqrt{s_{\mathrm{NN}}} = 5.02$ TeV.

To obtain the $\Delta\varphi$ distribution for HFE, the contribution of the non-HFE $\Delta\varphi$ distribution needs to be subtracted from the inclusive electron $\Delta\varphi$ distribution. This process is illustrated in Figure 3.21 and 3.22 for pp and p–Pb events, respectively. The resulting $\Delta\varphi^{\mathrm{HF}}$ distribution is then normalized by the number of heavy-flavour decay electrons (N_e^{HF}) in the sample to obtain the per-trigger electron correlation distribution.

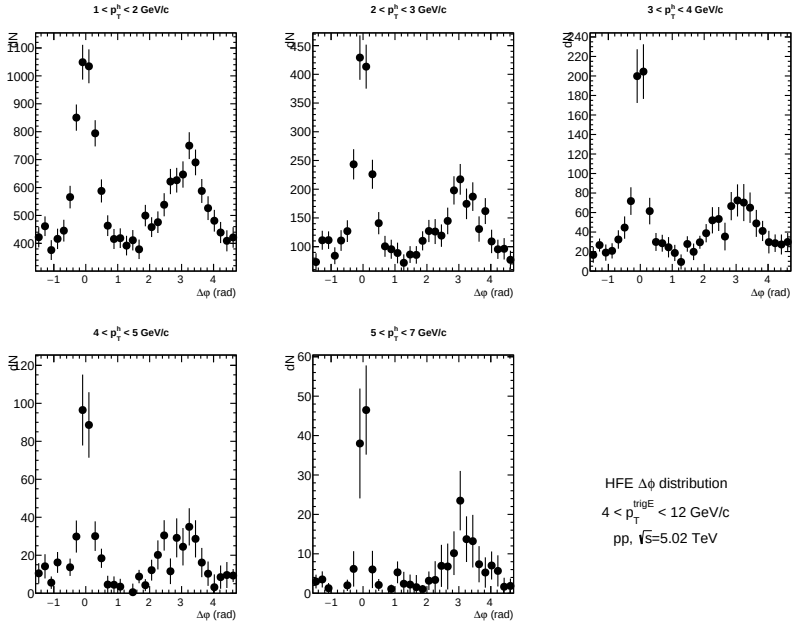

Figure 3.21: $\Delta\varphi$ distribution for HFE after subtracting Non-HFE from inclusive electrons for $4 < p_{\mathrm{T}}^{\mathrm{e}} < 12$ GeV/c and in five associated charged particle p_{T} ranges in pp collisions at $\sqrt{s} = 5.02$ TeV.

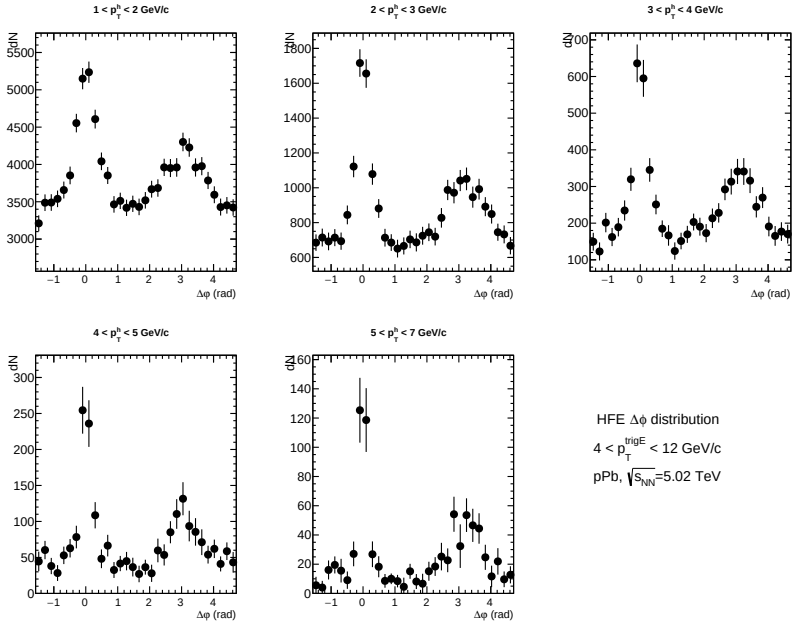

Figure 3.22: $\Delta\varphi$ distribution for HFE after subtracting Non-HFE from inclusive electrons for $4 < p_{\mathrm{T}}^{\mathrm{e}} < 12$ GeV/c and in five associated charged particle p_{T} ranges in p–Pb collisions at $\sqrt{s_{\mathrm{NN}}} = 5.02$ TeV.

3.13 Charged particle tracking efficiency

The purpose of this analysis is to evaluate the differential yield of charged particles associated with each triggered electron. As the electron reconstruction efficiency remains consistent throughout the analyzed p_{T} range and its impact nullifies upon normalization by the number of triggered particles (electrons), it is not employed in this analysis. Instead, the tracking efficiency for associated charged particles is computed using general-purpose MC samples, which are discussed in section 3.3. This efficiency is defined as the ratio of reconstructed "physical primary" tracks to all "physical primary" tracks in the MC stack after implementing track selection criteria. Physical primary particles are those that are created in the collision, including strong and electromagnetic decay products but not feed-down from weak decays of strange particles. The tracking efficiency with respect to p_{T} is illustrated in Figure 3.23 for both pp and p–Pb collisions.

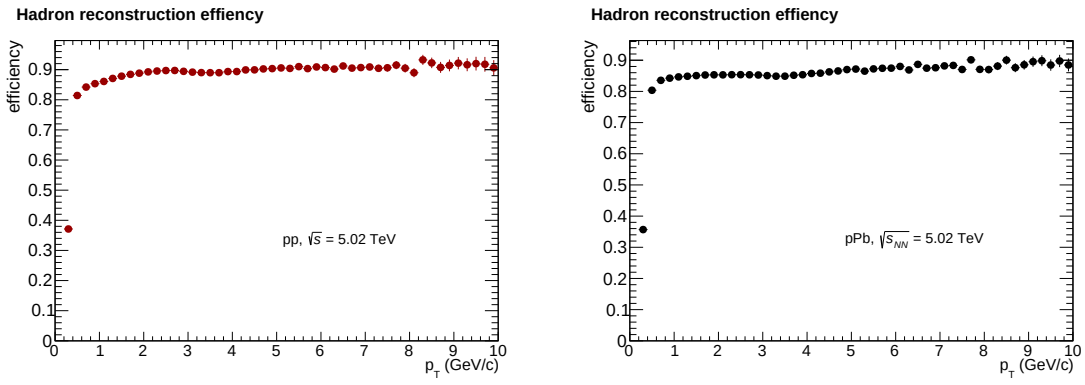

Figure 3.23: Tracking efficiency for associated particles obtained using MC simulations for $4 < p_{\mathrm{T}}^{\mathrm{e}} < 12$ GeV/c and in five associated charged particle p_{T} ranges in pp (left) and p–Pb (right) collisions at $\sqrt{s_{\mathrm{NN}}} = 5.02$ TeV.

3.14 Purity estimation

To estimate the secondary particle (decay of primary particles [164]) contamination in the associated track selection, general-purpose Monte-Carlo simulations are used. The fraction of tracks that are not "physical primary" tracks are selected to estimate the level of secondary contamination. The contamination as a function of p_{T} is illustrated in Figure 3.24 for both pp and p–Pb collisions.

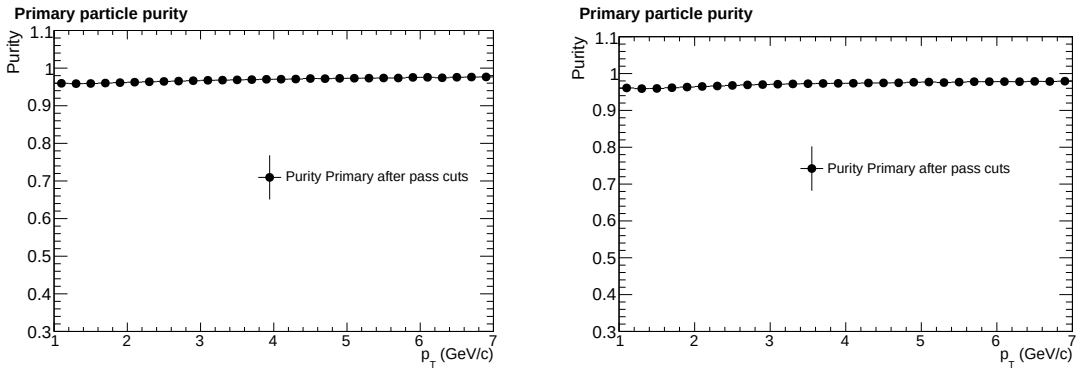

Figure 3.24: Secondary particle contamination in associated particle sample obtained using MC simulations after passing selection cuts for $4 < p_{\mathrm{T}}^{\mathrm{e}} < 12$ GeV/c and in five associated charged particle p_{T} ranges in pp (left) and p–Pb (right) collisions at $\sqrt{s_{\mathrm{NN}}} = 5.02$ TeV.

Figure 3.25 and 3.26 display the differential yield of associated particles per trigger electron, corrected for both tracking efficiency and secondary particle contamination, for pp and p–Pb collisions.

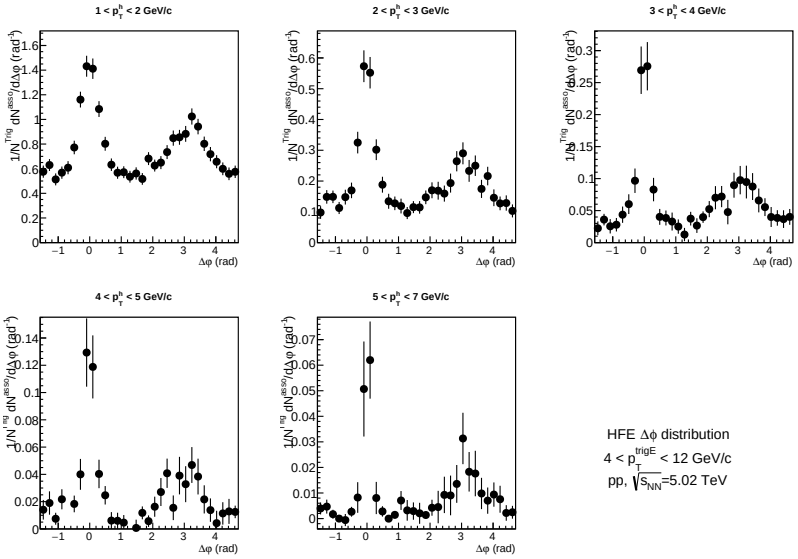

Figure 3.25: Azimuthal angular correlation per trigger between HF-decay electrons and charged particles after tracking efficiency and secondary particle correction for $4 < p_{\mathrm{T}}^{\mathrm{e}} < 12$ GeV/c and in five associated charged particle p_{T} ranges in pp collisions at $\sqrt{s} = 5.02$ TeV.

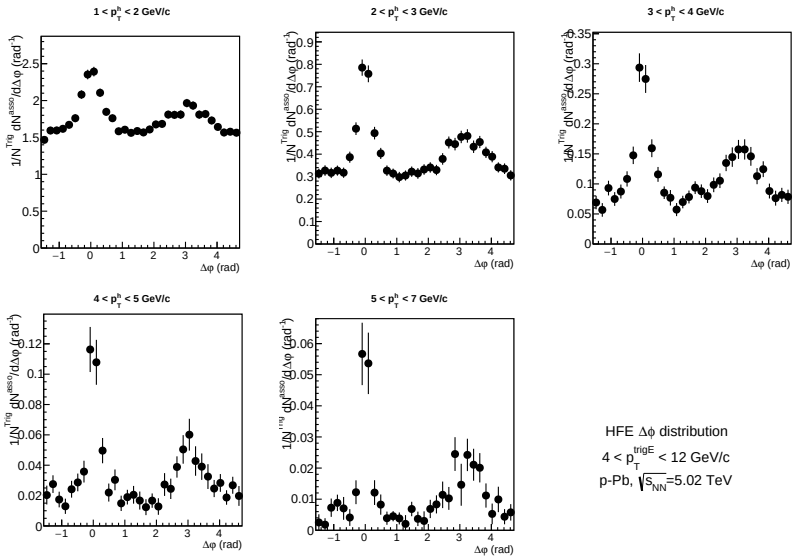

Figure 3.26: Azimuthal angular correlation per trigger between HF-decay electrons and charged particles after tracking efficiency correction and secondary particle correction for $4 < p_{\mathrm{T}}^{\mathrm{e}} < 12$ GeV/c and in five associated charged particle p_{T} ranges in p–Pb collisions at $\sqrt{s_{\mathrm{NN}}} = 5.02$ TeV.

3.15 Pedestal estimation

In order to compare the jet signal on the near and away side of the $\Delta\varphi$ distribution for various associated p_{T} bins of both pp and p–Pb events, it is necessary to subtract the uncorrelated pairs of HFE and associated particles that lie under the signal region. In this analysis, firstly, the pedestal is estimated by fitting a 0^{th} order polynomial with a Generalized Gaussian function for both the near-side and away-side peak fitting. The total fit function is presented below,

$$f(\Delta\varphi) = b + \frac{Y_{NS} \times \beta_{NS}}{2\alpha_{NS}\Gamma(1/\beta_{NS})} \times e^{-(\frac{\Delta\varphi}{\alpha_{NS}})^{\beta_{NS}}} + \frac{Y_{AS} \times \beta_{AS}}{2\alpha_{AS}\Gamma(1/\beta_{AS})} \times e^{-(\frac{\Delta\varphi-\pi}{\alpha_{AS}})^{\beta_{AS}}}, \quad (3.16)$$

The total fit function used in this analysis comprises of two generalized Gaussian terms that describe the near- and away-side peaks, along with a constant term that represents the baseline. A periodicity condition is imposed on the function to ensure $f(0) = f(2\pi)$.

The integrals of the generalized Gaussian terms, Y_{NS} and Y_{AS}, correspond to the associated-particle yields for the near (NS)- and away (AS)-side peaks, respectively. In the function, the parameter α is related to the variance of the function and thus to its width, while the parameter β controls the shape of the peak (a Gaussian function is obtained for $\beta = 2$). The widths of the correlation peaks are determined by the square root of the variance of their fitting terms, which is given by $\alpha\sqrt{\Gamma(3/\beta)/\Gamma(1/\beta)}$ [12]. The mean of the generalized Gaussian functions is fixed at $\Delta\varphi = 0$ and $\Delta\varphi = \pi$. The baseline b represents the minimum value of the $\Delta\varphi$ distribution.

To reduce the impact of statistical fluctuations on the estimation of yields in experimental data for both pp and p–Pb collisions, the value of β is fixed while fitting the $\Delta\varphi$ distribution, as shown in Table 3.5. The fixed β values are obtained from the $\Delta\varphi$ distributions of electrons from heavy-flavour hadron decays and charged hadrons from PYTHIA8 Monte Carlo (MC) simulations. The MC $\Delta\varphi$ distributions are fitted with the generalized Gaussian function given in Eq 6.5, as illustrated in Figure 3.27.

The $\Delta\varphi$ distributions from experimental data are fitted using the generalized Gaussian function (Eq 6.5), with the fixed β parameter obtained from the MC (PYTHIA8) distributions. The fitting results are shown in Figure 3.28 and 3.29 for pp and p–Pb events, respectively. The generalized Gaussian fitting is depicted by the black line in these figures, while the green line represents the pedestal (baseline). The red data points and lines correspond to the baseline subtracted data points and fitting, respectively.

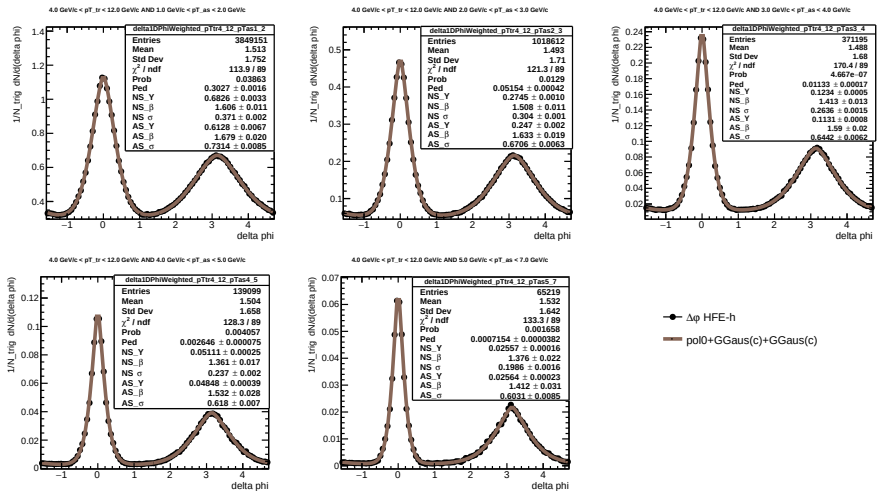

Figure 3.27: HFE-h $\Delta\varphi$ distribution which is generated from MC (PYTHIA8) and fitted with generalized Gaussian function for $4 < p_{\mathrm{T}}^{\mathrm{e}} < 12$ GeV/c and in five associated charged particle p_{T} ranges in pp collisions at $\sqrt{s} = 5.02$ TeV.

Table 3.5: Near-side and away-side β values obtained by MC (PYTHIA) in pp.

p_{T}^{h} in GeV/c	β_{NS}	β_{AS}
1-2	1.60596	1.67864
2-3	1.50754	1.63330
3-4	1.41302	1.58953
4-5	1.36122	1.53177
5-7	1.37647	1.41160

As the generalized Gaussian function has a large number of free parameters and we have to fix the β parameter from the fitting of Monte-Carlo data. Hence, the von Mises function was employed as a new fit function due to its ability to accurately describe the peak structure with only a very few free parameters [165] and used it as a default function to subtract the baseline and estimate the near-

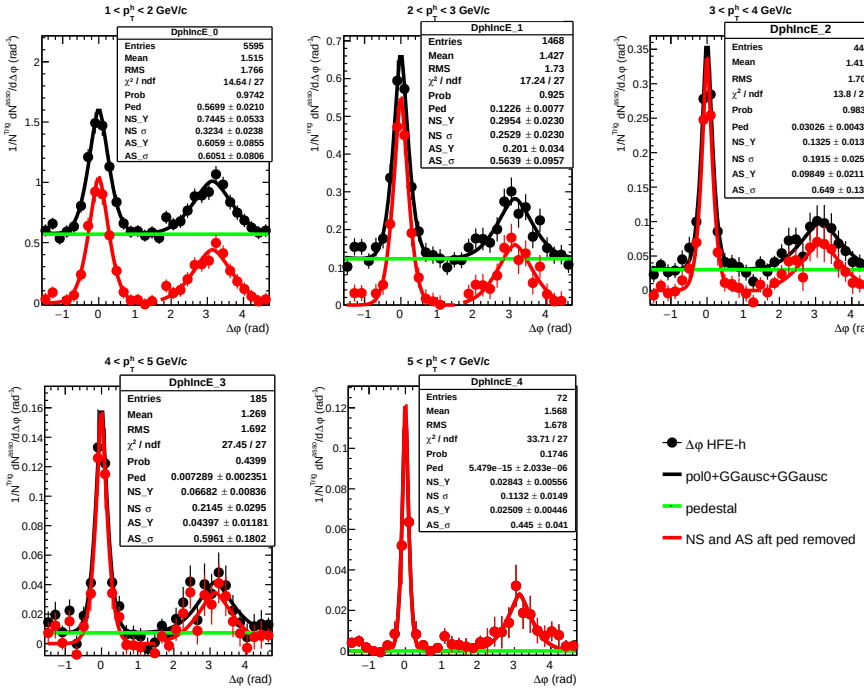

Figure 3.28: HFE-h $\Delta\varphi$ distribution for $4 < p_{\mathrm{T}}^{\mathrm{e}} < 12$ GeV/c and in five associated charged particle p_{T} ranges fitted with generalized Gaussian function in pp collision at $\sqrt{s} = 5.02$ TeV showing in black markers, baseline in the green line, and $\Delta\varphi$ distribution after baseline subtraction showing in red markers.

and away-side observables.

The function is defined as:

$$f(\Delta\varphi) = b + \frac{e^{\kappa_{NS}\cos(\Delta\varphi)}}{2\pi I_0(\kappa_{NS})} + \frac{e^{\kappa_{AS}\cos(\Delta\varphi-\pi)}}{2\pi I_0(\kappa_{AS})} \tag{3.17}$$

Here, b is the baseline, κ is the reciprocal of dispersion, which means it gives a measure of the concentration, I_0 is the 0^{th} order modified Bessel function. The mean for near- and away-side peaks are fixed to "0" and "π," respectively.

The near- and away-side width is estimated by measuring the sigma (σ) from the von Mises function as given by the relation:

$$\sigma = \sqrt{-2\log\frac{I_1(\kappa)}{I_0(\kappa)}} \tag{3.18}$$

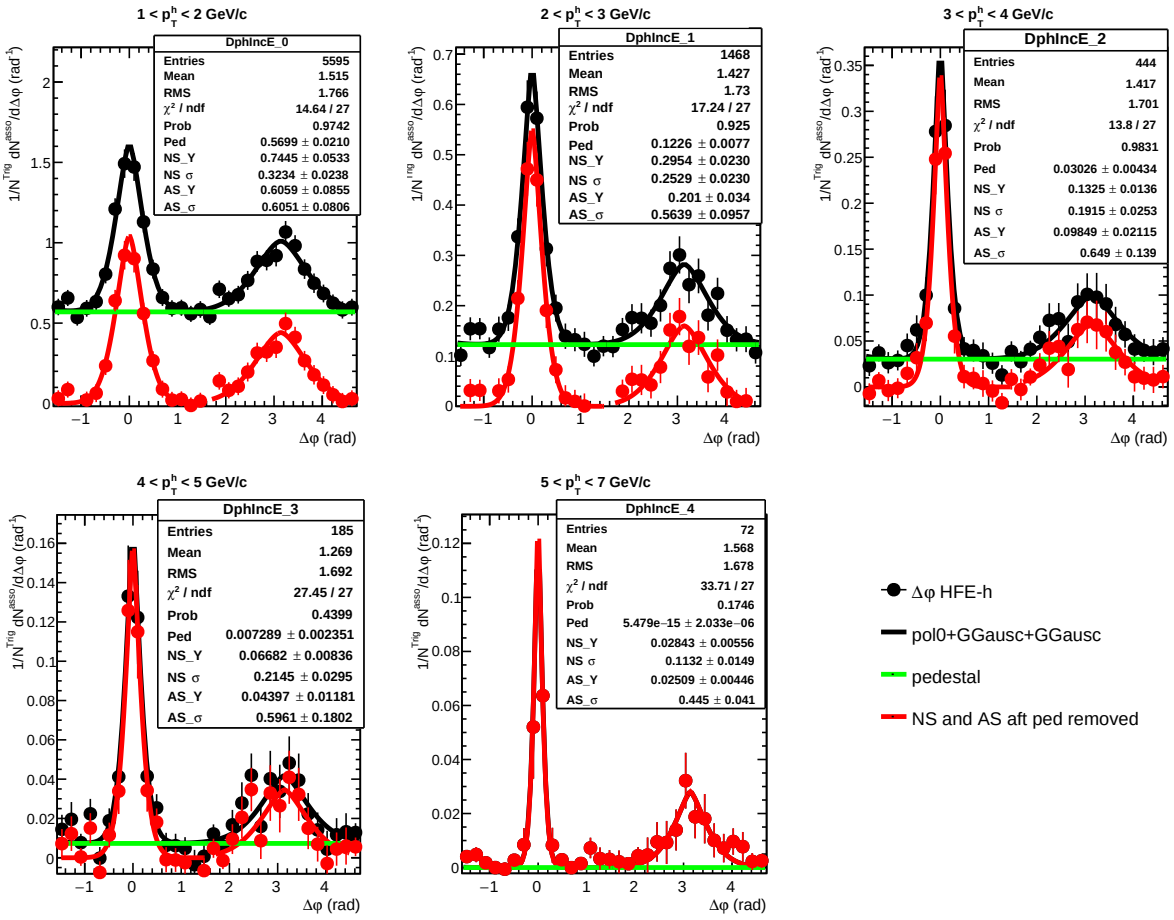

Figure 3.29: HFE-h $\Delta\varphi$ distribution for different $p_{\mathrm{T}}^{\mathrm{e}}$ ranges fitted with generalized Gaussian function in p–Pb collision at $\sqrt{s} = 5.02$ TeV showing in black markers, baseline in the green line, and $\Delta\varphi$ distribution after baseline subtraction showing in red markers for five associated p_{T} ranges.

Here, I_0 and I_1 are the modified Bessel function of 0^{th} order and 1^{st} order, and κ is measured by the von Mises function fit parameter.

The error in the width (dσ) is propagated by the relation:

$$\mathrm{d}\sigma = \frac{1}{\sigma} \times \left(\frac{\mathrm{I}_1}{\mathrm{I}_0} - \frac{\mathrm{I}_0}{\mathrm{I}_1} + \frac{1}{\kappa} \right) \mathrm{d}\kappa \tag{3.19}$$

Where dκ is the uncertainty in κ, obtained by von Mises function fitting.

The von Mises fitted $\Delta\varphi$ is shown in Fig. 3.30 and 3.31 in pp and p–Pb collisions, respectively.

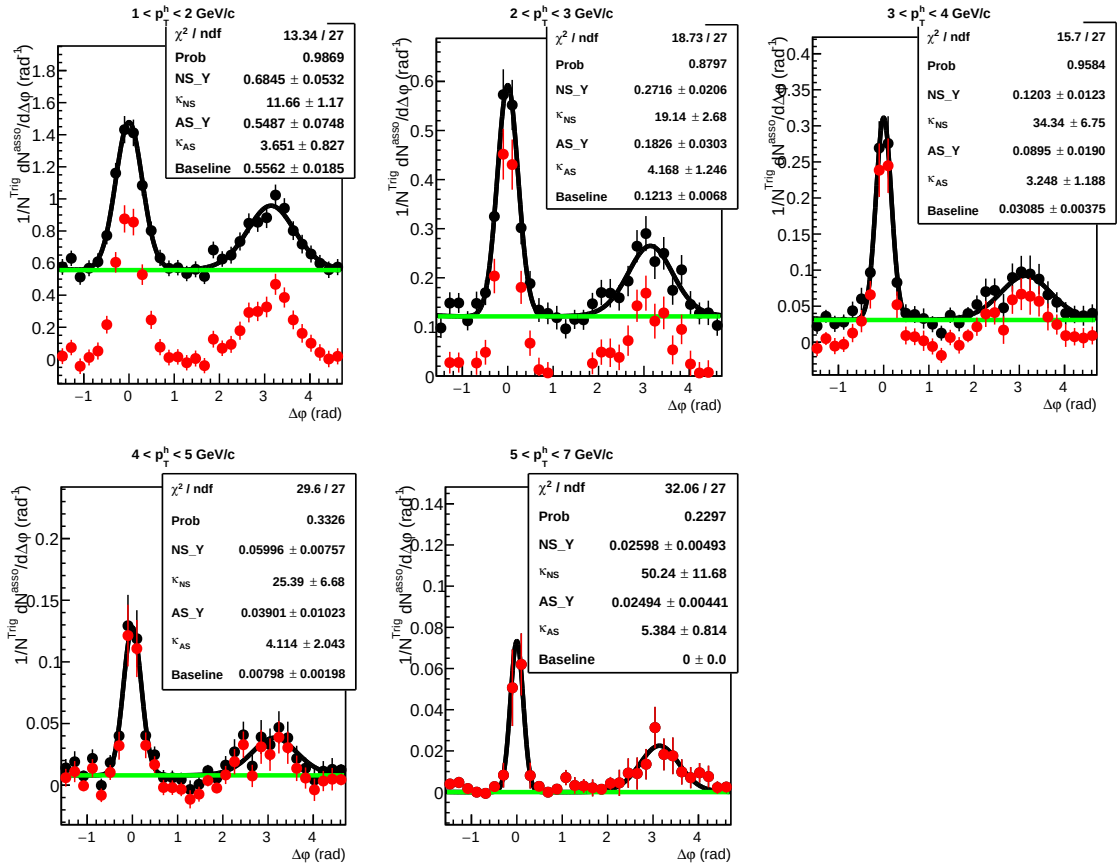

Figure 3.30: HFE-h $\Delta\varphi$ distribution fitted with von Mises function for $4 < p_{\mathrm{T}}^{\mathrm{e}} < 12$ GeV/c and in five associated charged particle p_{T} ranges in pp collisions at $\sqrt{s} = 5.02$ TeV.

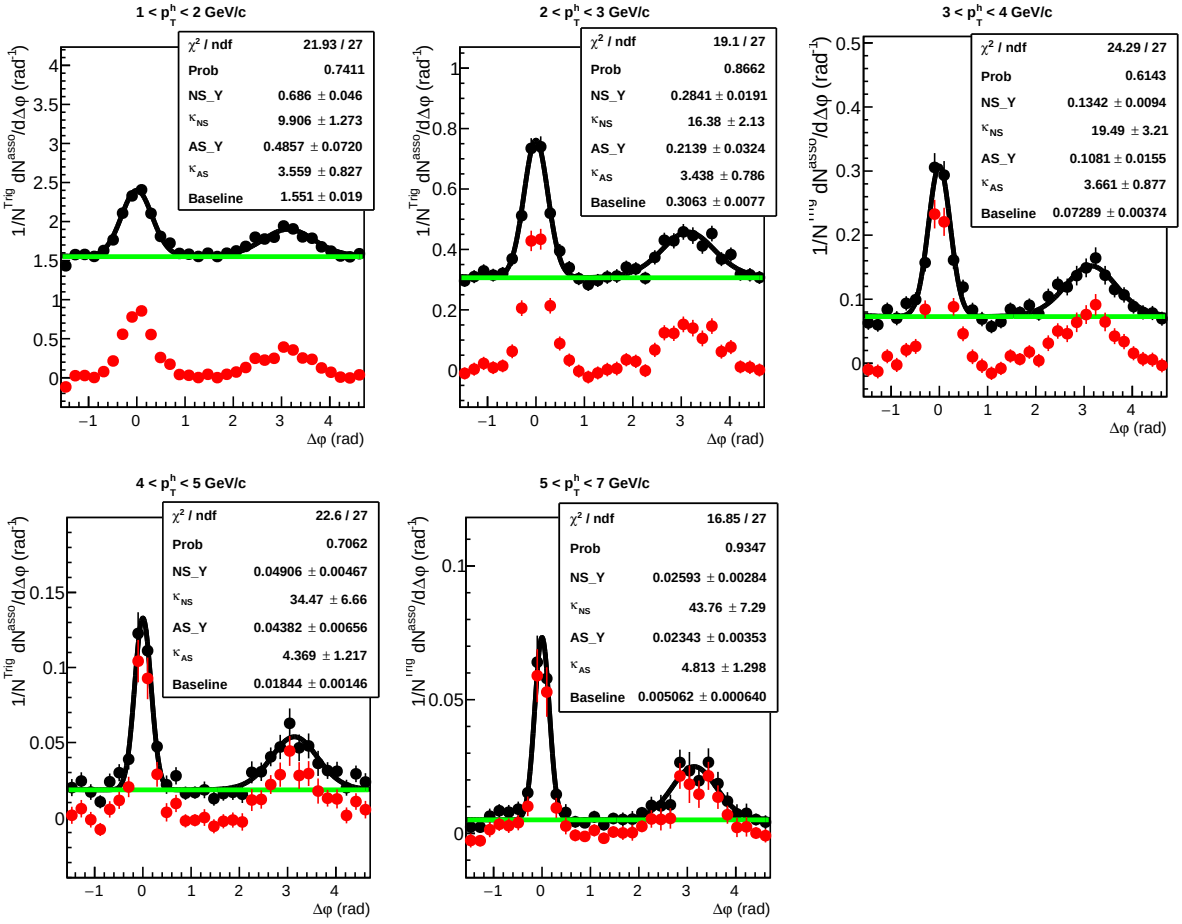

Figure 3.31: HFE-h $\Delta\varphi$ distribution fitted with von Mises function for $4 < p_{\mathrm{T}}^{\mathrm{e}} < 12$ GeV/c and in five associated charged particle p_{T} ranges in p–Pb collisions at $\sqrt{s_{\mathrm{NN}}} = 5.02$ TeV.

3.16 Near- and away-side yields and sigma

To determine the near-side and away-side yields of the $\Delta\varphi$ distribution, the integral of the correlation distribution is calculated within the range of -3σ to 3σ from the mean value for near-side (mean =0) and away-side (mean =π), after pedestal subtraction. In this case, σ is obtained from the fit. A comparison of the near-side and away-side yields and sigma (σ) in pp and p–Pb collisions provides insight into the possible modification of the fragmentation function of heavy-quarks. The near-side and away-side yields in pp and p–Pb collisions are displayed in Figure 3.32, and the near-side and away-side sigma (σ) are illustrated in Figure 3.33.

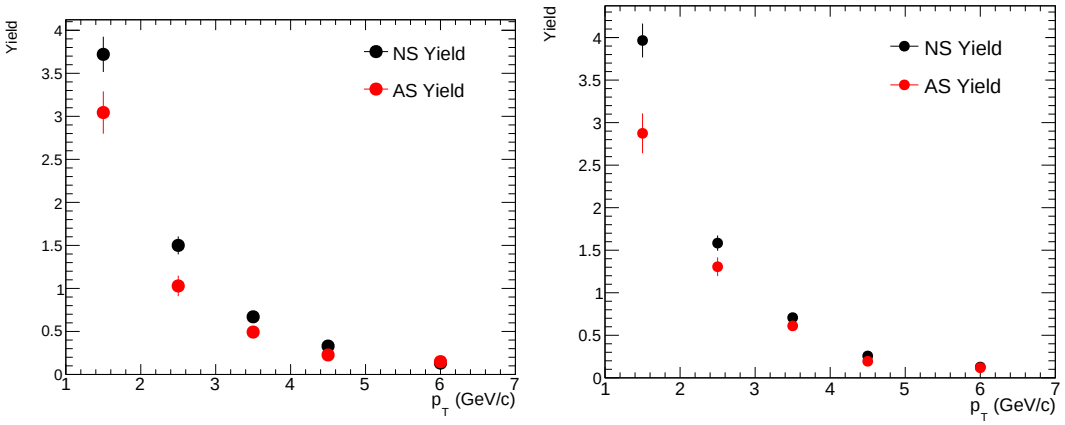

Figure 3.32: Near-side and away-side yield for $4 < p_{\mathrm{T}}^{\mathrm{e}} < 12$ GeV/c and in five associated charged particle p_{T} ranges in pp (left) and p–Pb (right) collisions at $\sqrt{s_{\mathrm{NN}}} = 5.02$ TeV.

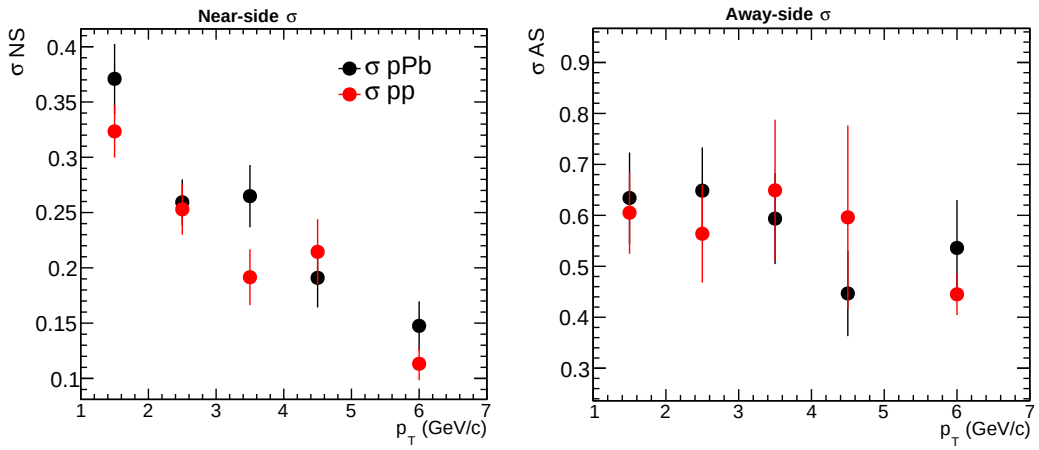

Figure 3.33: Near-side (left) and away-side (right) sigma (σ) for $4 < p_{\mathrm{T}}^{\mathrm{e}} < 12$ GeV/c and in five associated charged particle p_{T} ranges in pp and p–Pb collisions at $\sqrt{s_{\mathrm{NN}}} = 5.02$ TeV.

3.17 Pb–Pb analysis

Heavy quarks experience energy loss as they move through the QCD medium, which occurs as a result of elastic and inelastic collisions with the constituents of the medium. Because of their high mass, heavy quarks may have a shorter hadronization time compared to light quarks, potentially resulting in hadronization occurring within the QGP while the heavy quarks are traversing the medium. This could lead to modifications in the fragmentation function of heavy quarks. By studying the azimuthal angular correlation of high-p_{T} particles originating from heavy-flavour (charm and beauty) decays, we can investigate their interaction with the Quark Gluon Plasma. The near-side correlation distribution of heavy-flavour decay electrons and charged hadrons in Pb–Pb collisions is examined in this chapter to quantify the modification of the fragmentation function caused by the interaction of heavy quarks with the medium. The near-side yield per trigger particle is calculated to assess this modification and the near-side yield in Pb–Pb collisions is compared to that in pp collisions (I_{AA}) to study the modification of the particle correlation yield. Moreover, the study of the away-side correlation distribution provides information on jet quenching, while the near-side correlation distribution gives insight into the fragmenting jet leaving the medium. However, Pb–Pb analysis is ongoing at the time of writing the thesis.

The analysis technique used for Pb–Pb analysis differs slightly from that used for pp and p–Pb analysis. In contrast to pp and p–Pb analysis, where the flow component was negligible, in Pb–Pb analysis, the elliptical flow contribution in $\Delta\varphi$ is considerable and must be subtracted from the $\Delta\varphi$ distribution to isolate the jet contribution.

The expression gives the elliptic flow contribution to trigger-associated particle correlation.

$$\frac{dN}{d\Delta\varphi_{e-h}} \propto 1 + 2v_2^e v_2^{assoc} \cos(2\Delta\varphi), \tag{3.20}$$

In Fig. 3.34, the von Mises function is used to fit the $\Delta\varphi$ distribution, and the cyan lines indicate the flow contribution. The presence of flow contribution is

significant in the Pb–Pb collision system.

Fig. 3.35 presents a comparison between the $\Delta\varphi$ distributions in Pb–Pb and pp collisions to observe qualitative modifications. At low $p_{\mathrm{T}}^{\mathrm{assoc}}$, the near-side peak of the correlation distribution is higher in Pb–Pb collisions, while the away-side peaks appear smaller than those in pp collisions. This suggests that jet fragmentation is altered by the medium in Pb–Pb collisions.

Moreover, the near-side yield modification effect is demonstrated in Fig. 3.36, indicating that the near-side yield in Pb–Pb collisions at lower $p_{\mathrm{T}}^{\mathrm{assoc}}$ is approximately 50% higher than that in pp collisions. This study is currently ongoing, and we anticipate exciting results in the near future.

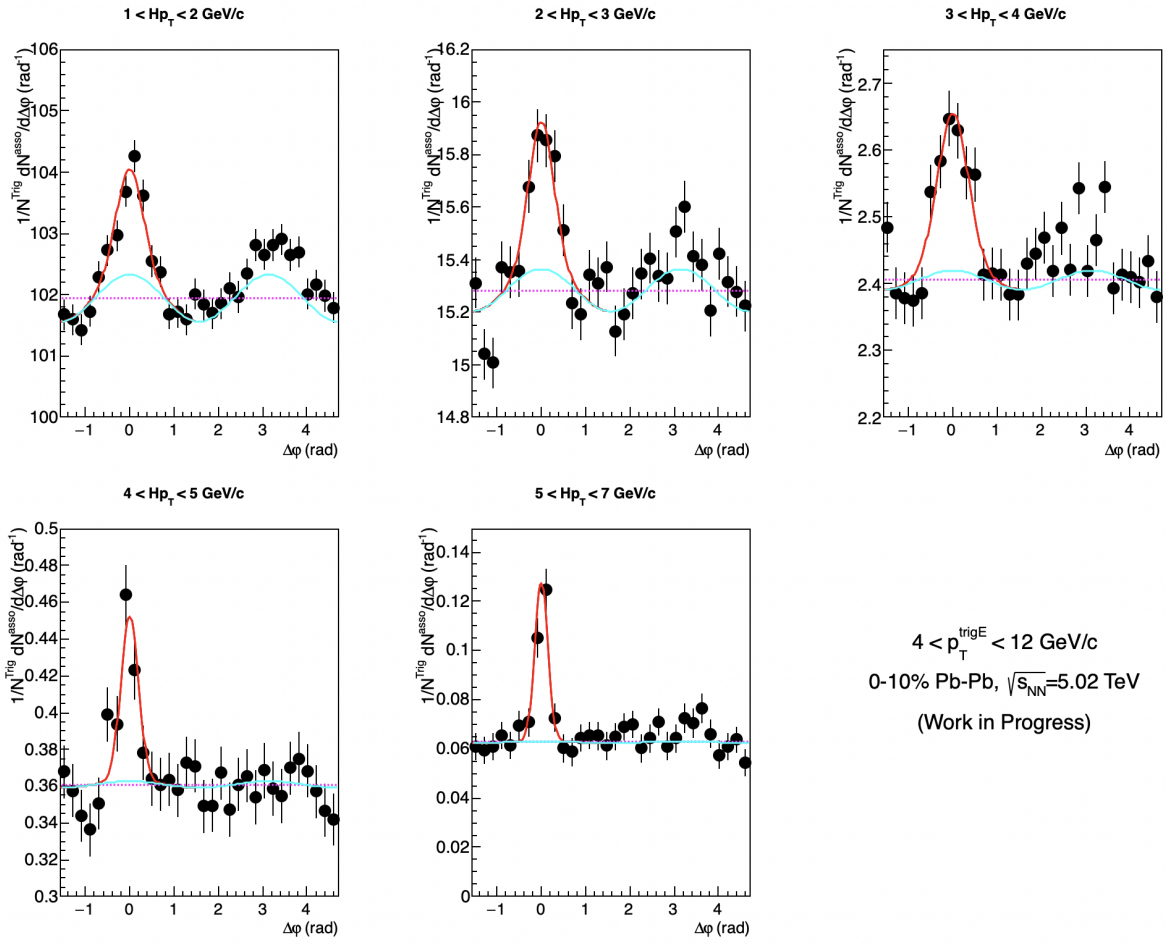

Figure 3.34: Azimuthal-correlation distributions for $4 < p_{\mathrm{T}}^{\mathrm{e}} < 12$ GeV/c for different associated p_{T} ranges Pb–Pb collisions at $\sqrt{s_{\mathrm{NN}}} = 5.02$ TeV. The distribution is fitted with the von Mises function (red), baseline (magenta), and contribution of elliptical flow (cyan).

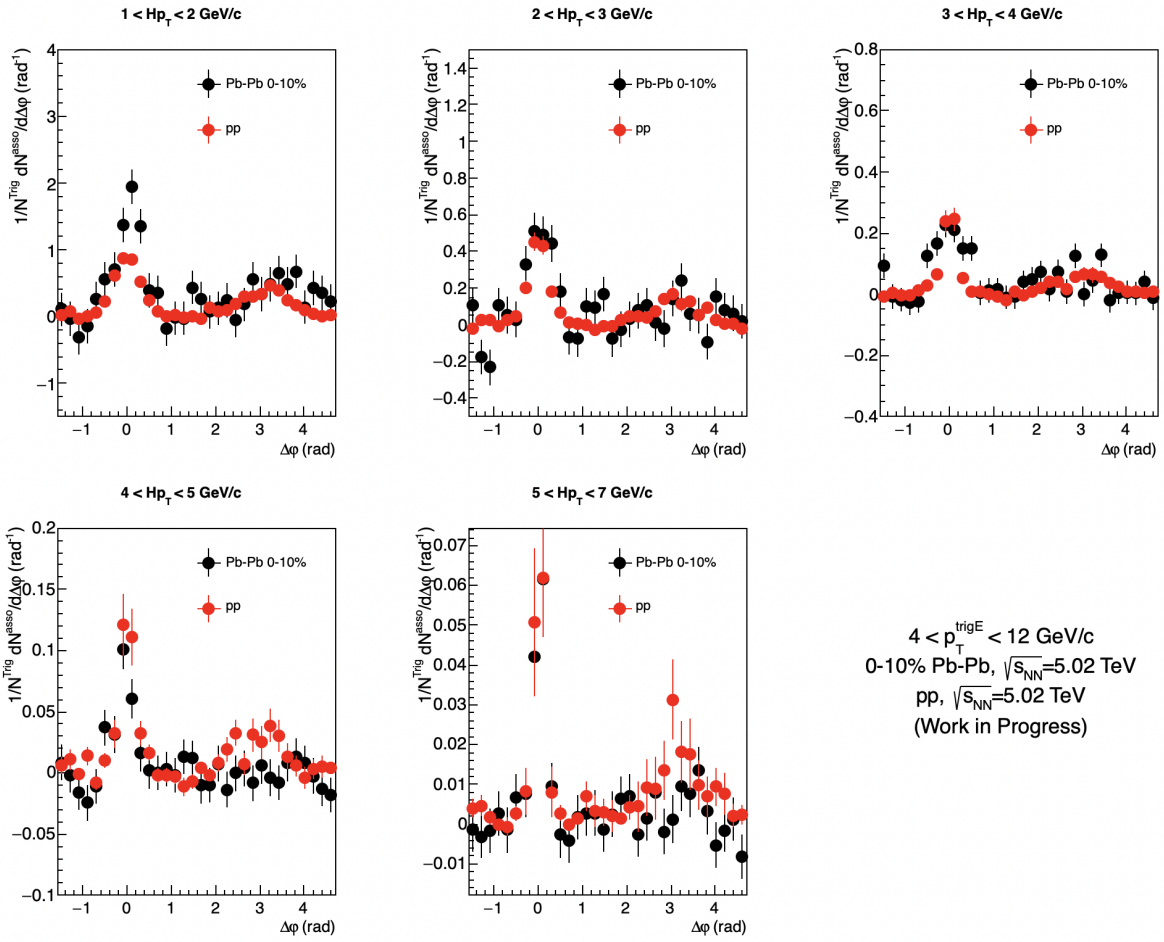

Figure 3.35: Azimuthal-correlation distributions after baseline subtraction for $4 < p_{\mathrm{T}}^{\mathrm{e}} < 12$ GeV/c for different associated p_{T} ranges in pp and Pb–Pb collisions at $\sqrt{s_{\mathrm{NN}}} = 5.02$ TeV.

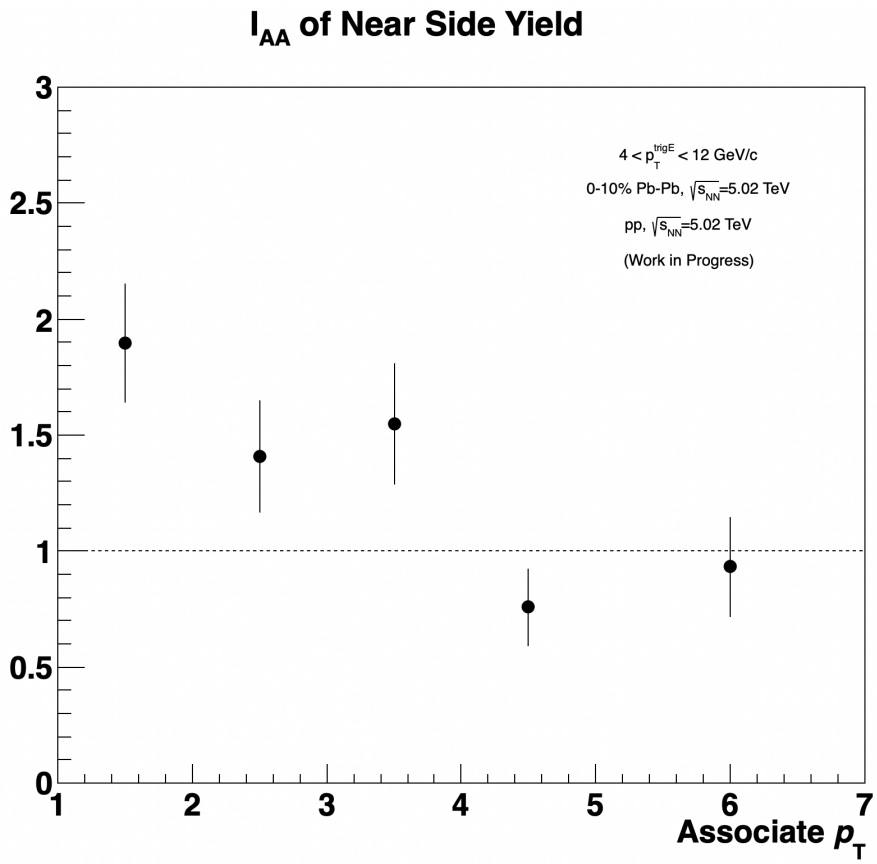

Figure 3.36: Near-side per-trigger yields ratio for $4 < p_{\mathrm{T}}^{\mathrm{e}} < 12$ GeV/c and $1 < p_{\mathrm{T}}^{\mathrm{assoc}} < 7$ GeV/c in Pb–Pb over pp collisions at $\sqrt{s_{\mathrm{NN}}} = 5.02$ TeV.

Chapter 4

Systematic uncertainties

When measuring a physical quantity, there is inherent systematic uncertainty associated with the equipment used, assumptions made, and models employed to make inferences based on the observed data. Systematic uncertainties are evaluated by varying the parameters used for electron identification, NHFE reconstruction, associated track selection,mixed-event correction, and fitting procedures. The uncertainties are estimated separately for the near-side and away-side yields and sigma and are evaluated for the per-trigger HFE $\Delta\varphi$ distribution. These systematic studies are carried out on the correlation distribution to quantify their impact on the results.

The following systematic sources are used to estimate the systematic uncertainties for the correlation distribution.

1. Electron track selection
    - Minimum number of TPC crossed rows required for the track
    - TPC crossed rows over findable clusters
2. Electron identification
    - $\mathrm{n}\sigma^{e}_{\mathrm{TPC-d}E/\mathrm{d}x}$
    - E/p
    - Shower shape (M02)
3. Associated track selection
    - Minimum number of TPC crossed rows required for the track

- TPC crossed rows over findable clusters
- Hit in any of the SPD layer
- η cut

4. Non-HFE identification
   - Invariant mass cut
   - Minimum TPC number of clusters required for the track
   - Partner electron track p_{T}
5. mixed-event correction
   - Normalization factor
   - VtxZ and centrality binning
6. Pedestal estimation methods

To estimate the systematic uncertainties, the pedestal in the $\Delta\varphi$ distribution is removed to obtain the uncertainty on the near and away side. To illustrate the procedure, systematic uncertainties for associated track selection are used as an example in the next section.

4.0.1 Associated particle track selection

The $\Delta\varphi$ distribution is acquired by altering the selection cuts for associated particles, as presented in Table 4.1. To assess the impact on the near-side and away-side, a pedestal is defined by fitting the $\Delta\varphi$ distribution with two generalized Gaussian functions and is then subtracted from the $\Delta\varphi$ distribution. The correlation distribution with the pedestal removed is illustrated in Figure 4.1 for pp.

The $\Delta\varphi$ distribution ratio for each variation in track cut to default settings is obtained after pedestal subtraction for both pp and p–Pb events. These ratios are presented in Figure 4.2 and 4.3. To determine the systematic uncertainties, a zero-order polynomial fit is applied to the ratio obtained after pedestal subtraction for the highest and lowest variation within the range of $-0.5 < \Delta\varphi < 0.5$ and

Table 4.1: Hadron track cut variations

Variables	Cut applied
Minimum number of TPC crossed rows required for the track	60 (default)
Minimum number of TPC crossed rows required for the track	70
Minimum number of TPC crossed rows required for the track	80
Minimum number of TPC crossed rows required for the track	90
TPC crossed rows over findable clusters	0.6 (default)
TPC crossed rows over findable clusters	0.7
TPC crossed rows over findable clusters	0.8
TPC crossed rows over findable clusters	0.9

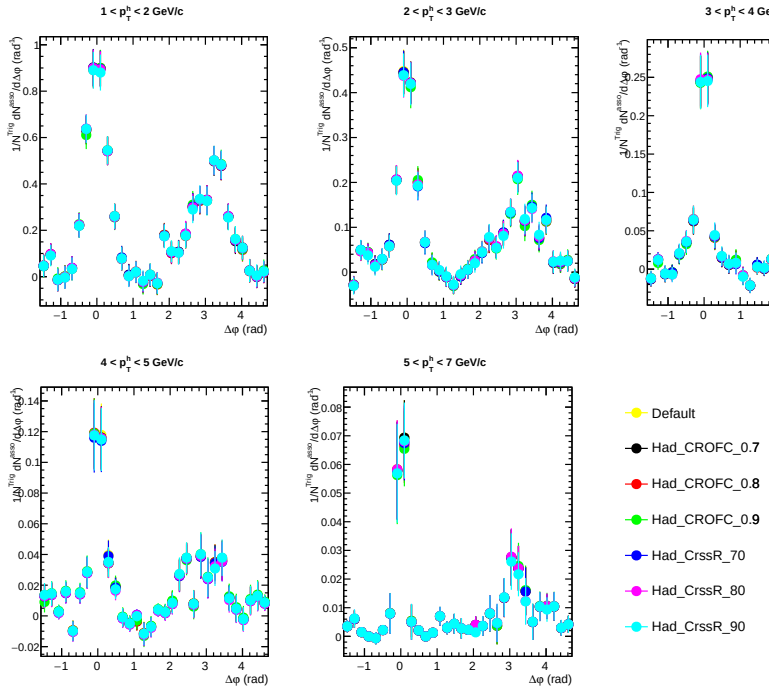

Figure 4.1: The $\Delta\varphi$ distribution of different track cut variations for $4 < p_{\mathrm{T}}^{\mathrm{e}} < 12$ GeV/c and $1 < p_{\mathrm{T}}^{\mathrm{assoc}} < 7$ GeV/c compared to the default cut values after pedestal subtraction in pp collisions at $\sqrt{s} = 5.02$ TeV.

$2.2 < \Delta\varphi < 3.8$. The assigned systematic uncertainties range from 1% to 2% in pp collisions and 2% to 3% in p–Pb collisions and are indicated by dotted lines. These uncertainties are calculated by taking the difference of one standard deviation between the highest and lowest variation, as shown in equation 4.1. Additionally, the root mean square of the variations was also calculated as a cross-check and found to be consistent with or lower than the value of one standard deviation of

uniform distribution.

$$\text{One standard deviation } \% = |(\frac{\text{MaximumVariation} - \text{MinimumVariation}}{\sqrt{12}} - 1) \times 100| \tag{4.1}$$

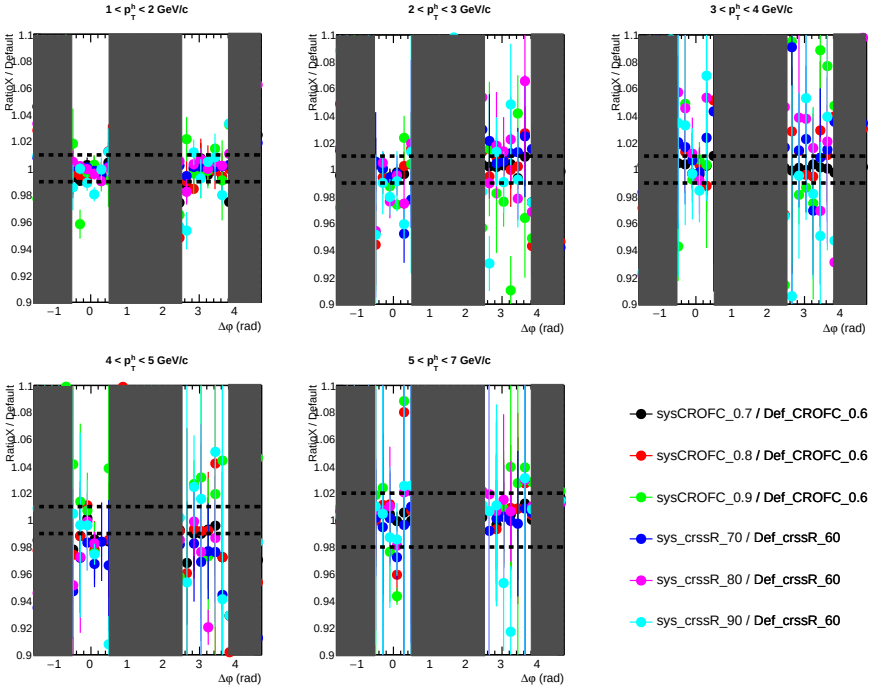

Figure 4.2: Ratio of the pedestal subtracted $\Delta\varphi$ distribution of different associated particle track cut values for $4 < p_{\mathrm{T}}^{\mathrm{e}} < 12$ GeV/c and $1 < p_{\mathrm{T}}^{\mathrm{assoc}} < 7$ GeV/c to the default cut values in pp collisions at $\sqrt{s} = 5.02$ TeV.

4.0.2 Electron track selection

To derive the $\Delta\varphi$ distribution for electrons, selection cuts are varied as listed in Table 4.2. To investigate the modifications in the near-side and away-side, a pedestal is first determined by fitting the $\Delta\varphi$ distribution using two generalized Gaussian functions and a constant. This pedestal is then subtracted from the $\Delta\varphi$ distribution to obtain a more precise representation of the data.

After subtracting the pedestal, the $\Delta\varphi$ distribution ratio for each variation in track cut relative to the default settings is obtained and presented in Figure 4.4 and 4.5 for pp and p–Pb collisions, respectively. To determine the systematic

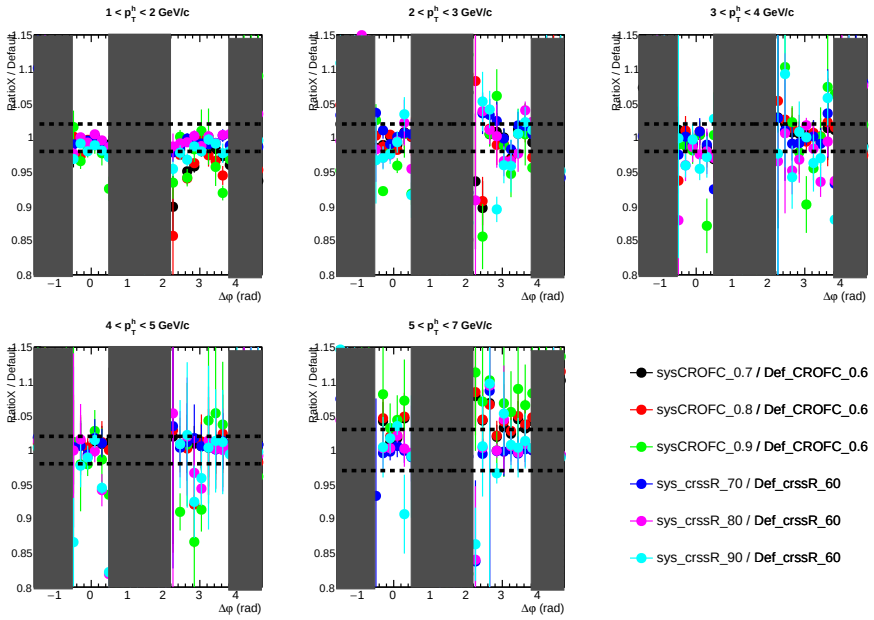

Figure 4.3: Ratio of the pedestal subtracted $\Delta\varphi$ distribution of different associated particle track cut values for $4 < p_{\mathrm{T}}^{\mathrm{e}} < 12$ GeV/c and $1 < p_{\mathrm{T}}^{\mathrm{assoc}} < 7$ GeV/c to the default cut values in p–Pb collisions at $\sqrt{s_{\mathrm{NN}}} = 5.02$ TeV.

Table 4.2: Electron track cut variations

Variables	Cut applied
Minimum number of TPC crossed rows required for the track	70 (default)
Minimum number of TPC crossed rows required for the track	80
Minimum number of TPC crossed rows required for the track	90
TPC crossed rows over findable clusters	0.8 (default)
TPC crossed rows over findable clusters	0.9

uncertainties, a 0^{th} order polynomial fit is performed on the ratio obtained after pedestal subtraction for the highest and lowest variation in the $\Delta\varphi$ range of $-0.5 < \Delta\varphi < 0.5$ and $2.2 < \Delta\varphi < 3.8$. The ratio of the pedestal-subtracted $\Delta\varphi$ distribution for each variation relative to the default settings is shown in Figure 4.4 and 4.5 for pp and p–Pb collisions, respectively. The assigned systematic uncertainties are 1% for pp collisions and 1% to 2% for p–Pb collisions, as indicated by the dotted lines

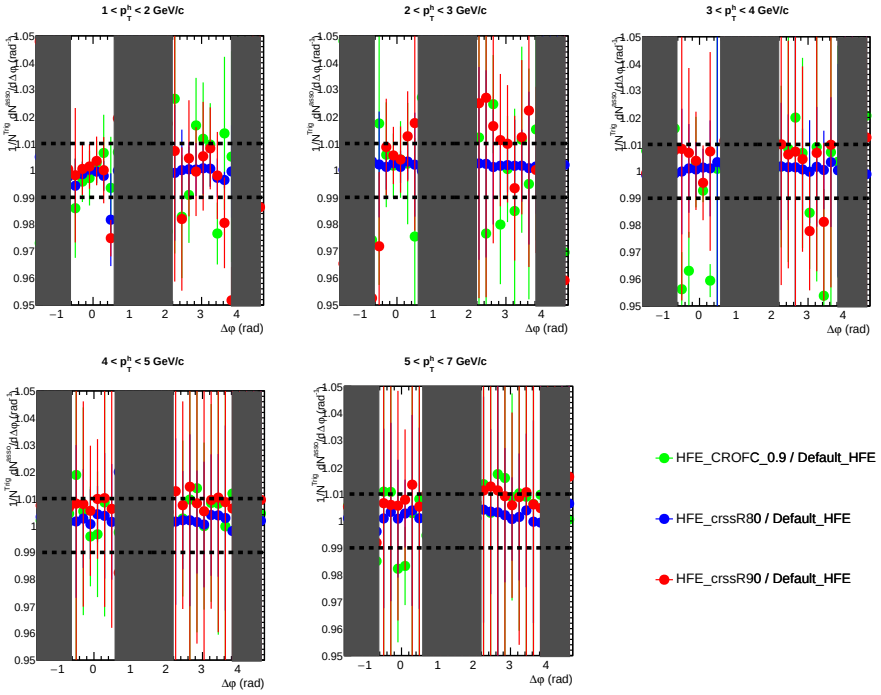

Figure 4.4: Ratio of the pedestal subtracted $\Delta\varphi$ distribution of different electron track cut values for $4 < p_{\mathrm{T}}^{\mathrm{e}} < 12$ GeV/c and $1 < p_{\mathrm{T}}^{\mathrm{assoc}} < 7$ GeV/c to the default cut values in pp collisions at $\sqrt{s} = 5.02$ TeV.

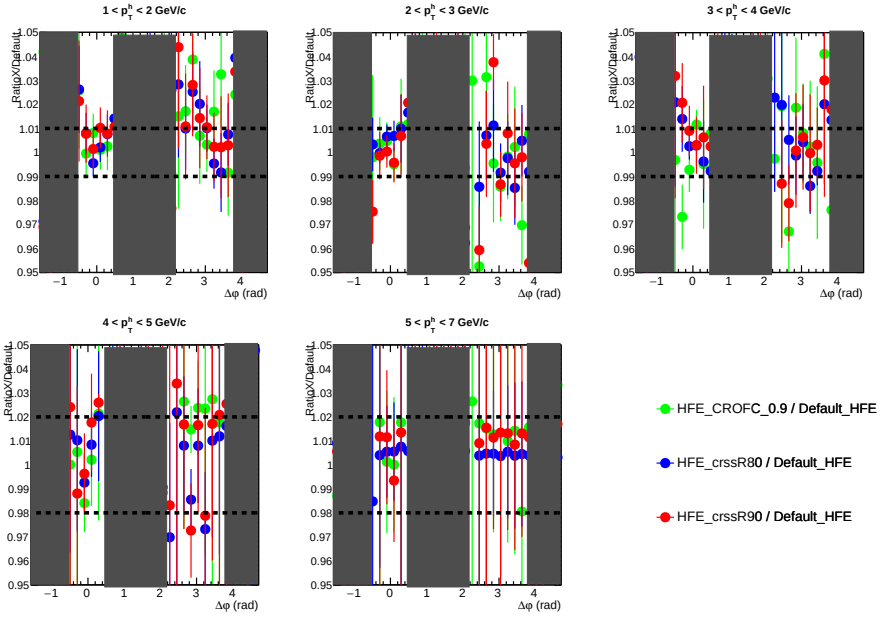

Figure 4.5: Ratio of the pedestal subtracted $\Delta\varphi$ distribution of different electron track cut values for $4 < p_{\mathrm{T}}^{\mathrm{e}} < 12$ GeV/c and $1 < p_{\mathrm{T}}^{\mathrm{assoc}} < 7$ GeV/c to the default cut values in p–Pb collisions at $\sqrt{s_{\mathrm{NN}}} = 5.02$ TeV.

4.0.3 Electron identification

The uncertainty is calculated by changing the criteria of electron identification, as presented in Table 4.3. Figure 4.6 shows the ratio of the HFE $\Delta\varphi$ distribution for each variation of the cut values to the default cut values after subtracting the pedestal in pp collisions. The distribution in p–Pb collisions is displayed in Figure 4.7. The dotted lines indicate the assigned systematic uncertainties, which are 3-6% in pp collisions and 2-4% in p–Pb collisions.

Table 4.3: Variations in electron identification criteria.

Variables	Condition applied
$n\sigma^{e}_{\mathrm{TPC-d}E/\mathrm{d}x}$	(-1,3) (default)
$n\sigma^{e}_{\mathrm{TPC-d}E/\mathrm{d}x}$	(-0.5,3)
$n\sigma^{e}_{\mathrm{TPC-d}E/\mathrm{d}x}$	(-0.75,3)
$n\sigma^{e}_{\mathrm{TPC-d}E/\mathrm{d}x}$	(-1.25,3)
E/p	(0.8,1.2) (default)
E/p	(0.75,1.2)
E/p	(0.85,1.2)
E/p	(0.9,1.2)
Shower shape (M02)	(0.02,0.9) (default)
Shower shape (M02)	(0.02,0.7)
Shower shape (M02)	(0.02,0.8)
Shower shape (M02)	(0.02,0.95)
Shower shape (M02)	(0.02,1.)
($n\sigma^{e}_{\mathrm{TPC-d}E/\mathrm{d}x}$) (Shower shape (M02))	(-1.25,3) (0.02,0.8)
($n\sigma^{e}_{\mathrm{TPC-d}E/\mathrm{d}x}$) (Shower shape (M02))(E/p)	(-0.75,3) (0.02,0.95) (0.85,1.2)
(Shower shape (M02))(E/p)	(0.02,0.85) (0.85,1.2)
($n\sigma^{e}_{\mathrm{TPC-d}E/\mathrm{d}x}$) (Shower shape (M02))(E/p)	(-0.75,3) (0.02,0.95) (0.75,1.2)

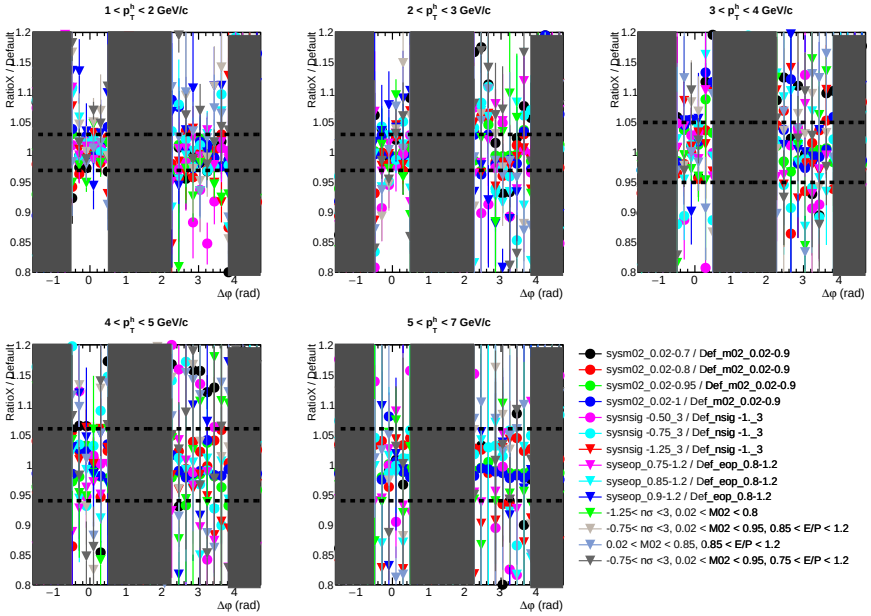

Figure 4.6: Ratio of the pedestal subtracted $\Delta\varphi$ distribution of different electron identification cut values for $4 < p_{\mathrm{T}}^{\mathrm{e}} < 12$ GeV/c and $1 < p_{\mathrm{T}}^{\mathrm{assoc}} < 7$ GeV/c to the default cut values in pp collisions at $\sqrt{s} = 5.02$ TeV.

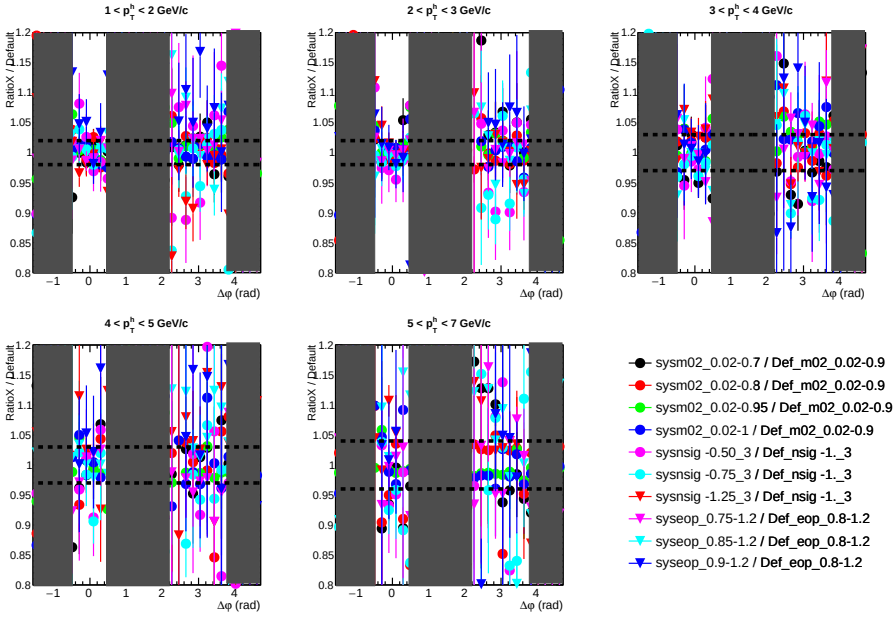

Figure 4.7: Ratio of the pedestal subtracted $\Delta\varphi$ distribution of different electron identification cut values for $4 < p_{\mathrm{T}}^{\mathrm{e}} < 12$ GeV/c and $1 < p_{\mathrm{T}}^{\mathrm{assoc}} < 7$ GeV/c to the default cut values in p–Pb collisions at $\sqrt{s_{\mathrm{NN}}} = 5.02$ TeV.

4.0.4 Non-HFE identification

The uncertainty is estimated by varying partner electron track cuts as shown in the Table 4.4. The HFE $\Delta\varphi$ distribution ratio for each cut variation to the default cut values after pedestal subtraction is shown in Figure 4.8 and 4.9 for pp and p–Pb. The assigned systematic uncertainties are 1% for both pp and p–Pb events as indicated with dotted lines.

Table 4.4: Variations of partner electron selection criteria.

Variables	Condition applied
Min p_{T} (MeV/c)	100 (default)
Min p_{T} (MeV/c)	50
Min p_{T} (MeV/c)	150
Max invariant mass (MeV/c^2)	140 (default)
Max invariant mass (MeV/c^2)	120
Max invariant mass (MeV/c^2)	130
Max invariant mass (MeV/c^2)	150
Max invariant mass (MeV/c^2)	160

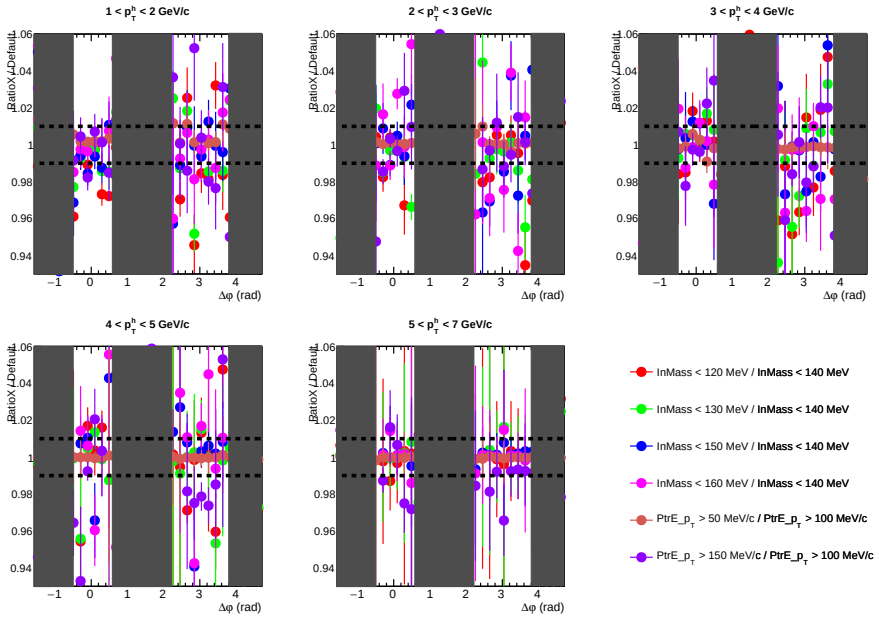

Figure 4.9: Ratio of the pedestal subtracted $\Delta\varphi$ distribution of different partner electron track cut values for $4 < p_{\mathrm{T}}^{\mathrm{e}} < 12$ GeV/c and $1 < p_{\mathrm{T}}^{\mathrm{assoc}} < 7$ GeV/c to the default cut values in p–Pb collisions at $\sqrt{s_{\mathrm{NN}}} = 5.02$ TeV.

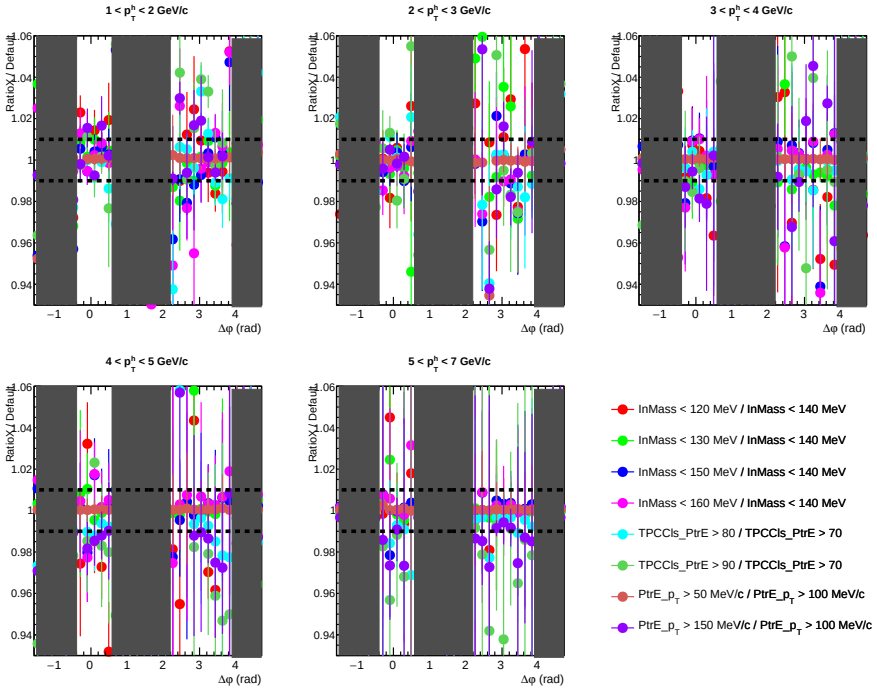

Figure 4.8: Ratio of the pedestal subtracted $\Delta\varphi$ distribution of different partner electron track cut values for $4 < p_{\mathrm{T}}^{\mathrm{e}} < 12$ GeV/c and $1 < p_{\mathrm{T}}^{\mathrm{assoc}} < 7$ GeV/c to the default cut values in pp collisions at $\sqrt{s} = 5.02$ TeV.

4.0.5 mixed-event correction

The mixed-event $(\Delta\eta, \Delta\varphi)$ distribution in the default method is normalized using its yield at $(\Delta\eta, \Delta\varphi) = (0, 0)$. To assess the uncertainty in the normalization factor, the yield is calculated by integrating over $\Delta\varphi$ for $\Delta\eta = 0$. As the mixed-event correction affects the pedestal and signal region similarly, the pedestal is not removed to estimate the uncertainty. For pp collisions, the red marker in Figure 4.10 displays the ratio of the HFE $\Delta\varphi$ distribution obtained using the modified normalizing factor for mixed-event correction to the default method.

Another check performed for mixed-event correction is by changing the binning for the mixed-event pool. The modified bins for pp and p–Pb are shown below.

Default pp mixed-event pool bins:

- Centrality bin : (0,100)
- VtxZ(cm) bin : (-10,-3), (-3,0.9), (0.9,3), (3,10)

pp mixed-event pool bins for systematic uncertainties:

- Centrality bin : (0,100)
- Vertex z(cm) : (-10,-5), (-5,0), (0,5), (5,10)

Default p–Pb mixed-event pool bins:

- Multiplicity bin : (0,25), (25,50), (50,75), (75,100)
- VtxZ(cm) bin : (-10,-4.6), (-4.6,-1.6), (-1.6,0.9), (0.9,3.4), (3.4,6.1), (6.1,10)

p–Pb mixed-event pool bins for systematic uncertainties:

- Centrality bin : (0,20), (20,40), (40,60), (60,100)
- Vertex z(cm) : (-10,-5), (-5,-2.5), (-2.5,0), (0,2.5), (2.5,5), (5,10)

The black marker in Figure 4.10 illustrates the ratio of the HFE $\Delta\varphi$ distribution obtained using the modified binning to the default one for pp collisions. The systematic uncertainties resulting from the mixed-event correction are calculated using the average method, in which the average is taken over all variations. The dotted lines indicate that the assigned systematic uncertainty is 1% for all p_{T}.

In Figure 4.11, the ratio of the HFE $\Delta\varphi$ distribution obtained using the modified normalizing factor for mixed-event correction and the ratio of $\Delta\varphi$ distribution of modified mixed-event pool bins to the default bins in p–Pb collisions are displayed. For both pp and p–Pb, a systematic uncertainty of 1% is assigned.

4.0.6 Pedestal estimation methods

The systematic uncertainty on the pedestal estimation of the $\Delta\varphi$ distribution is obtained by varying methods of pedestal estimation. These methods are:

- Fitting with polynomial of order “0” + Gaussian + Gaussian, as shown in Figure 4.12.

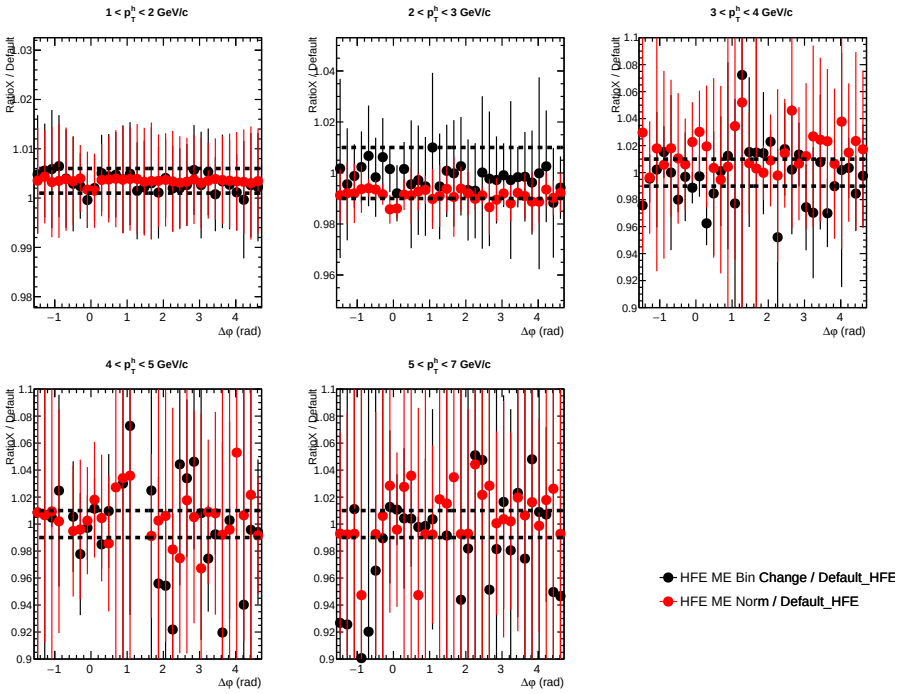

Figure 4.10: Ratio of the $\Delta\varphi$ distribution for $4 < p_{\mathrm{T}}^{\mathrm{e}} < 12$ GeV/c and $1 < p_{\mathrm{T}}^{\mathrm{assoc}} < 7$ GeV/c from the modified mixed-event pool binning to the default binning and ratio of modified normalisation factor to default in pp collisions at $\sqrt{s} = 5.02$ TeV.

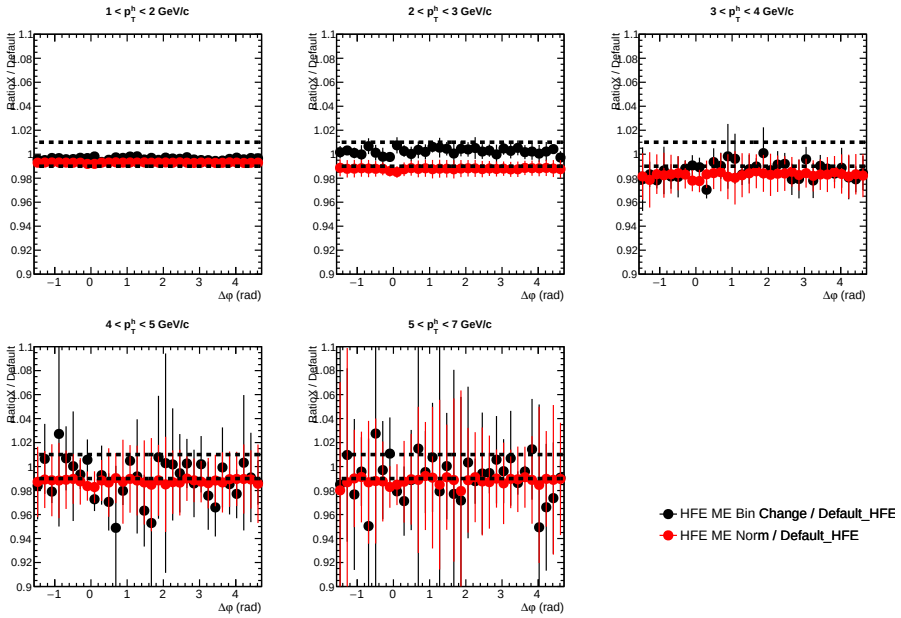

Figure 4.11: Ratio of the $\Delta\varphi$ distribution for $4 < p_{\mathrm{T}}^{\mathrm{e}} < 12$ GeV/c and $1 < p_{\mathrm{T}}^{\mathrm{assoc}} < 7$ GeV/c from the modified mixed-event pool binning to the default binning and ratio of modified normalisation factor to default in p–Pb collisions at $\sqrt{s_{\mathrm{NN}}} = 5.02$ TeV.

- Fitting with polynomial of order "0" + generalized Gaussian (with periodicity) + generalized Gaussian (with periodicity) after reflecting the $\Delta\varphi$ range

from $-\pi/2$ to $3\pi/2$ into 0 to π.

- Taking the average of the polynomial of order "0" fitting in the $\Delta\varphi$ region -1.5 to -1 and 1 to 1.5 (3 bins from each region), referred to as "AvgPed".

- Fitting polynomial of order "0" + Gaussian + Gaussian with different fit options [166], "I", "WL" shown in Figure A.8 and Figure A.9 in appendix. The default is χ^2 fit.

- Doubling the histogram bins to check for statistical fluctuations. The default is 32 bins, and the variation is with 64 bins, as depicted in Figure A.7 in appendix.

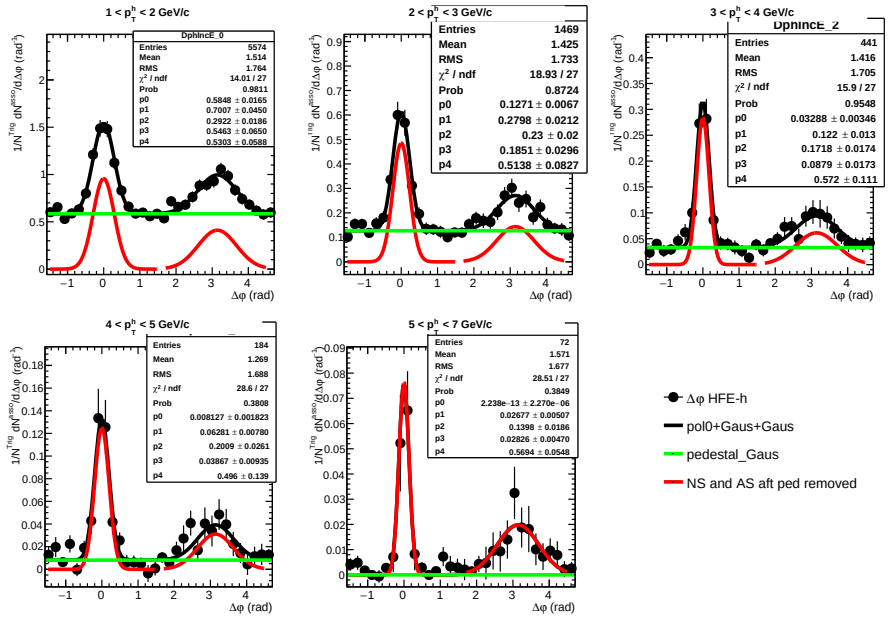

Figure 4.12: The $\Delta\varphi$ distribution fitted with double Gaussian function in pp collisions for $4 < p_{\mathrm{T}}^{\mathrm{e}} < 12$ GeV/c and $1 < p_{\mathrm{T}}^{\mathrm{assoc}} < 7$ GeV/c at $\sqrt{s} = 5.02$ TeV.

In all methods, a 0^{th} order polynomial (polynomial of order "0") represents the baseline (pedestal). The Pedestal value obtained for each variation for pp and p–Pb data sample is shown in Figure 4.15 and 4.16 respectively.

Systematic uncertainties due to the pedestal are calculated by taking the maximum deviation. The maximum deviation of the pedestal method variations from the default pedestal value for the different p_{T} bins vary from 0.0013 to 0.028 in pp and 0.0005 to 0.018 in p–Pb. The last p_{T} bin in pp collisions has a high pedestal

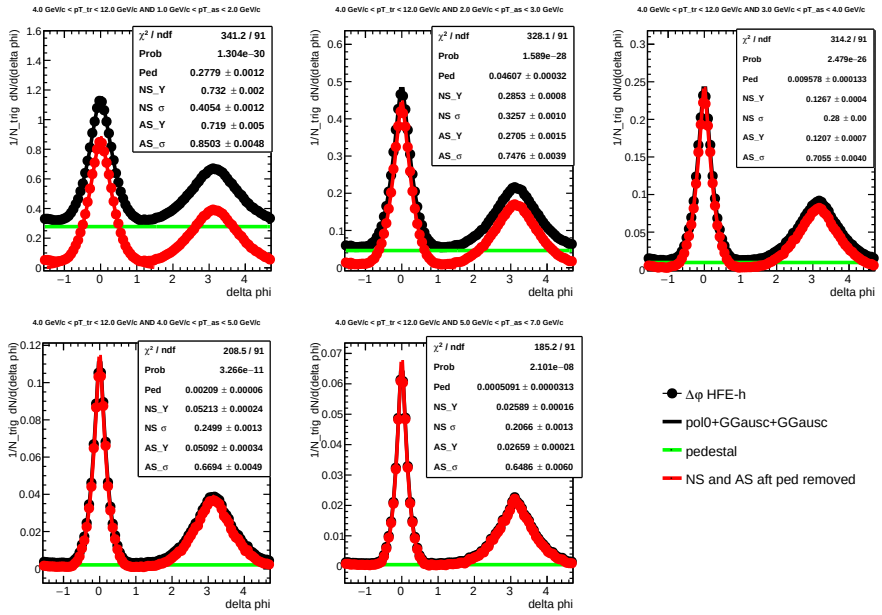

Figure 4.13: $\Delta\varphi$ distribution fitted with generalized Gaussian function by decreasing β by by 10% for $4 < p_{\mathrm{T}}^{\mathrm{e}} < 12$ GeV/c and $1 < p_{\mathrm{T}}^{\mathrm{assoc}} < 7$ GeV/c in pp collisions at $\sqrt{s} = 5.02$ TeV.

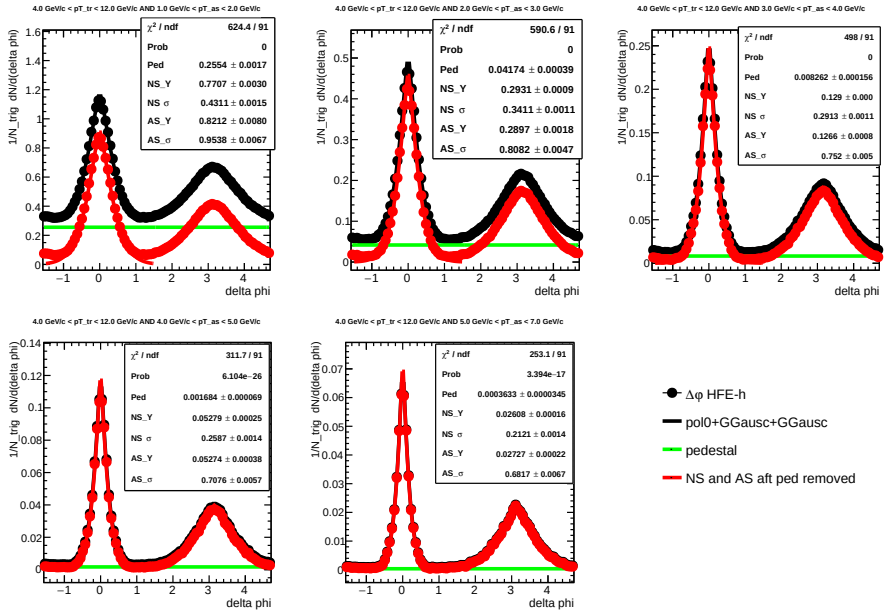

Figure 4.14: $\Delta\varphi$ distribution fitted with generalized Gaussian function by decreasing β by by 15% for $4 < p_{\mathrm{T}}^{\mathrm{e}} < 12$ GeV/c and $1 < p_{\mathrm{T}}^{\mathrm{assoc}} < 7$ GeV/c in pp collisions at $\sqrt{s} = 5.02$ TeV.

value from the AvgPed method due to the statistical fluctuations (Figure 4.15); hence this variation was not considered to assign systematic for that p_{T} bin.

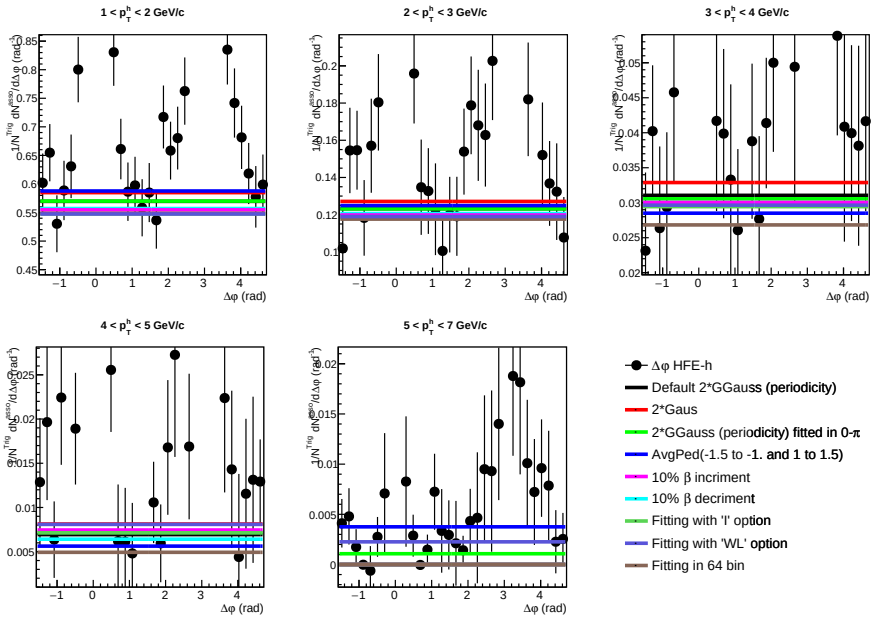

Figure 4.15: $\Delta\varphi$ distribution with pedestal values obtained using different methods for $4 < p_{\mathrm{T}}^{\mathrm{e}} < 12$ GeV/c and $1 < p_{\mathrm{T}}^{\mathrm{assoc}} < 7$ GeV/c in pp collisions at $\sqrt{s} = 5.02$ TeV.

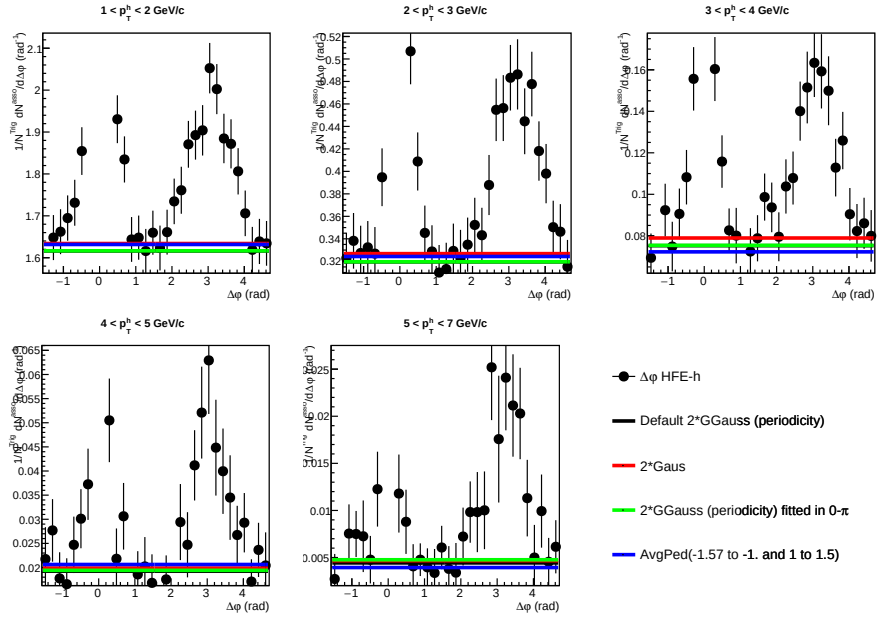

Figure 4.16: $\Delta\varphi$ distribution with pedestal values obtained using different methods for $4 < p_{\mathrm{T}}^{\mathrm{e}} < 12$ GeV/c and $1 < p_{\mathrm{T}}^{\mathrm{assoc}} < 7$ GeV/c in p–Pb collisions at $\sqrt{s_{\mathrm{NN}}} = 5.02$ TeV.

4.0.7 Beta variation

The value of β parameters is varied, and the corresponding pedestal is used for systematic estimation. The variation up to 10% is taken to estimate systematic, as higher variation results in a bad fit. This is cross-checked with MC (PYTHIA)

simulation. For example, fittings with 10% and 15% decrement are shown in Figure 4.13 and 4.14 respectively. By observing both figures, it is concluded that χ^2/NDF is much higher, and the pedestal is so low in the 15% beta variation.

4.0.8 Systematic uncertainties on near-side and away-side yields

The systematic uncertainty on the measurement of near-side and away-side yields (integral in the range $-3\sigma < \Delta\varphi < 3\sigma$ rad and $\pi - 3\sigma < \Delta\varphi < \pi + 3\sigma$ rad respectively) is estimated separately by calculating the near-side and away-side yields for each systematic variation and obtaining the ratio with respect to the yield from default settings. To illustrate the procedure, the systematic uncertainties from electron identification selection in pp and p–Pb is used as an example in the next sub-section. The absolute yields presented in this section do not incorporate width correction in the $\Delta\varphi$ distribution. Nonetheless, this effect is nullified when taking the ratio, and as such, it does not impact the values of systematic estimation.

4.0.9 Electron identification

The pedestal or the baseline on the HFE $\Delta\varphi$ distribution is subtracted to calculate the near-side and away-side yield. The near-side and away-side yield for each electron identification cut variations and the corresponding ratios to default yield are shown in figure 4.17 for pp and 4.18, 4.19 for p–Pb single and simultaneous variation respectively.

A systematic uncertainty of 3-6% (5-7%) for near-side (away-side) yield is assigned for pp, and after considering both single and simultaneous variation 4% systematic uncertainties are assigned for both near-side and away-side for p–Pb collisions.

4.0.10 Electron track selection

The ratios of near-side and away-side yield obtained by varying electron track cuts with respect to default cuts are shown in 4.20 and 4.21 for pp and p–Pb, respectively. Systematic uncertainties of 1% were assigned for near-side and away-side in both pp and p–Pb events.

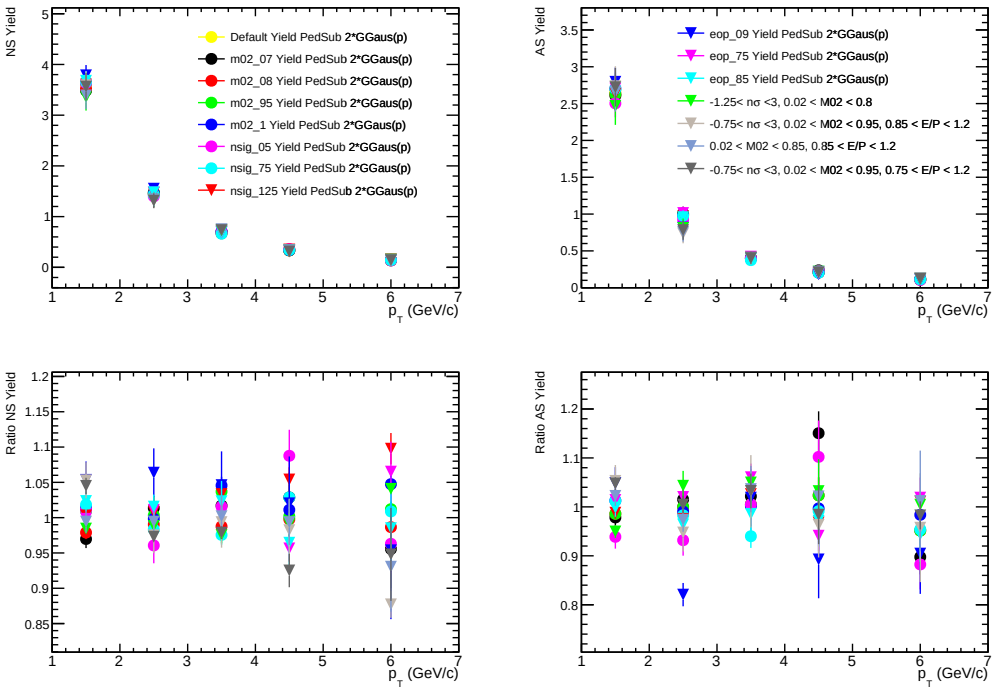

Figure 4.17: Ratio of near-side (left) and away-side (right) yield for $4 < p_{\mathrm{T}}^{\mathrm{e}} < 12$ GeV/c and $1 < p_{\mathrm{T}}^{\mathrm{assoc}} < 7$ GeV/c obtained from different electron identification cuts to the default value in central pp collisions at $\sqrt{s} = 5.02$ TeV.

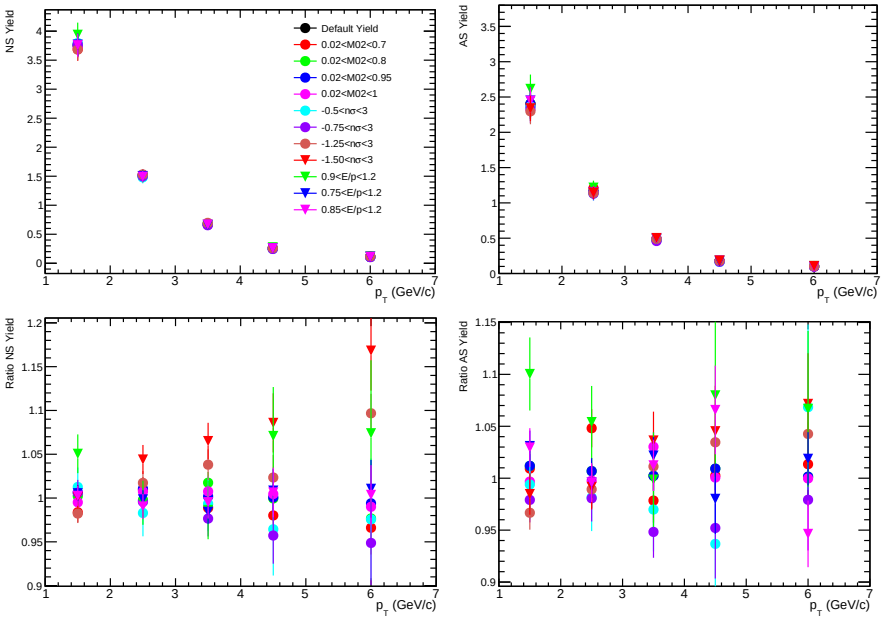

Figure 4.18: Ratio of near-side (left) and away-side (right) yield for $4 < p_{\mathrm{T}}^{\mathrm{e}} < 12$ GeV/c and $1 < p_{\mathrm{T}}^{\mathrm{assoc}} < 7$ GeV/c obtained from different electron identification cuts (single variation) to the default value in p–Pb collisions at $\sqrt{s_{\mathrm{NN}}} = 5.02$ TeV.

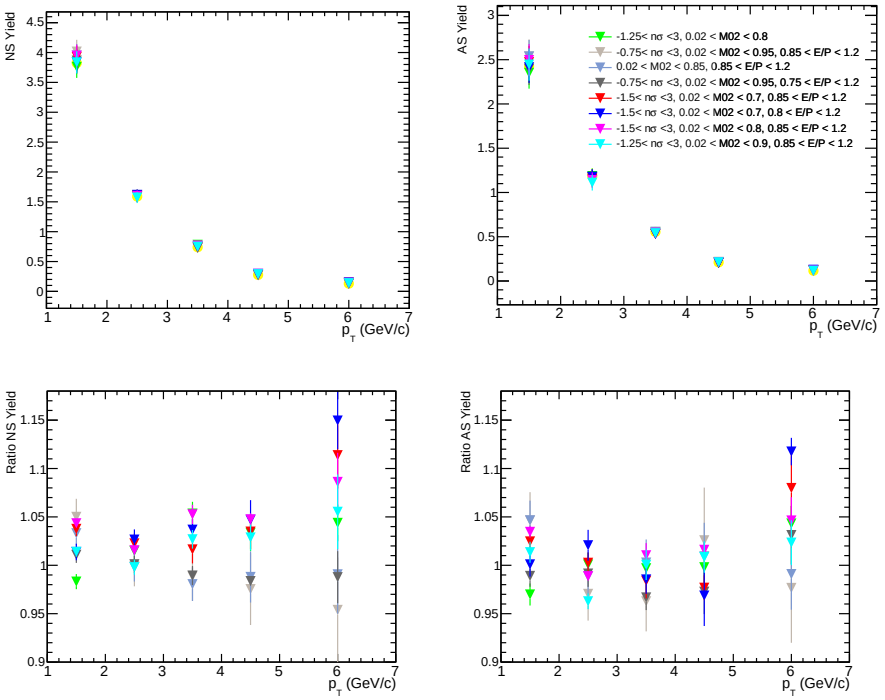

Figure 4.19: Ratio of near-side (left) and away-side (right) yield for $4 < p_{\mathrm{T}}^{\mathrm{e}} < 12$ GeV/c and $1 < p_{\mathrm{T}}^{\mathrm{assoc}} < 7$ GeV/c obtained from different electron identification cuts (simultaneous variation) to the default value in p–Pb collisions at $\sqrt{s_{\mathrm{NN}}} = 5.02$ TeV.

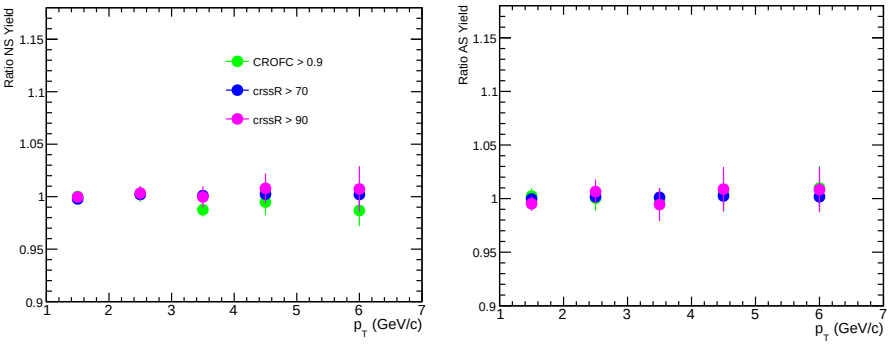

Figure 4.20: Near-side (left) and away-side (right) yield ratios by varying electron track cuts with respect to default for $4 < p_{\mathrm{T}}^{\mathrm{e}} < 12$ GeV/c and $1 < p_{\mathrm{T}}^{\mathrm{assoc}} < 7$ GeV/c in pp collisions at $\sqrt{s} = 5.02$ TeV.

4.0.11 Associated track selection

The Figures 4.22 and 4.23 illustrate the ratios of near-side and away-side yield, which were obtained by adjusting the associate track cuts (previously discussed) in comparison to default cuts, for pp and p–Pb events respectively. For near-side yield, a systematic uncertainty of 1-2% is assigned for pp and 2-4% in p–Pb collisions, while for away-side yield, a systematic uncertainty of 1-3% is assigned

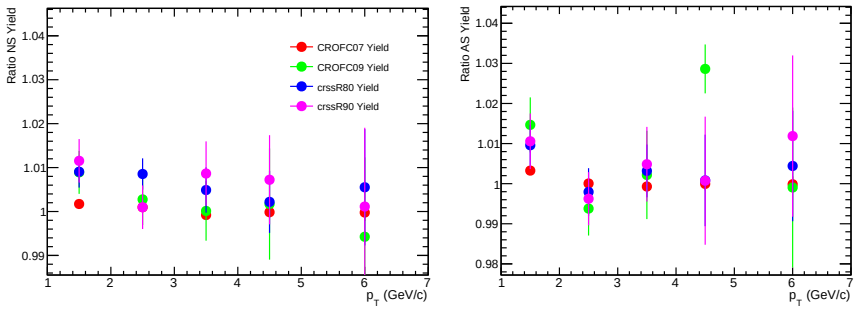

Figure 4.21: Near-side (left) and away-side (right) yield ratios by varying electron track cuts with respect to default for $4 < p_{\mathrm{T}}^{\mathrm{e}} < 12$ GeV/c and $1 < p_{\mathrm{T}}^{\mathrm{assoc}} < 7$ GeV/c in p–Pb collisions at $\sqrt{s_{\mathrm{NN}}} = 5.02$ TeV.

for pp and 2-4% in p–Pb collisions.

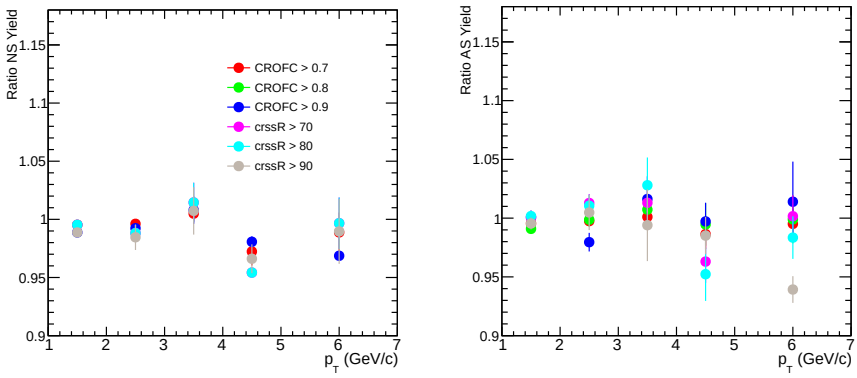

Figure 4.22: Near-side (left) and away-side (right) yield ratios by varying associate particles track cuts with respect to default for $4 < p_{\mathrm{T}}^{\mathrm{e}} < 12$ GeV/c and $1 < p_{\mathrm{T}}^{\mathrm{assoc}} < 7$ GeV/c in pp collisions at $\sqrt{s} = 5.02$ TeV.

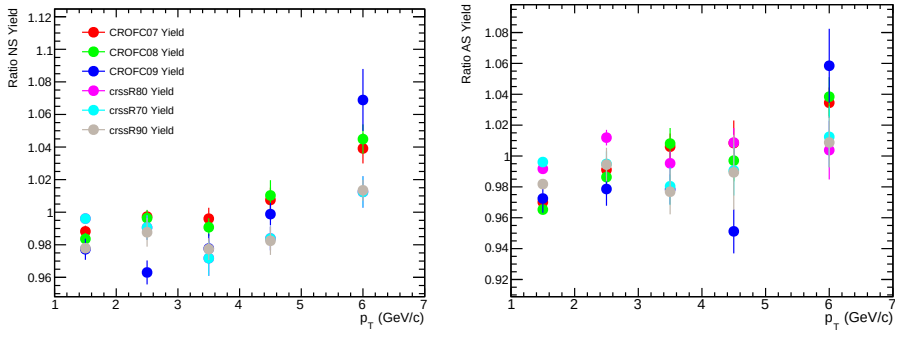

Figure 4.23: Near-side (left) and away-side (right) yield ratios by varying associate particles track cuts with respect to default for $4 < p_{\mathrm{T}}^{\mathrm{e}} < 12$ GeV/c and $1 < p_{\mathrm{T}}^{\mathrm{assoc}} < 7$ GeV/c in p–Pb collisions at $\sqrt{s_{\mathrm{NN}}} = 5.02$ TeV.

4.0.12 Non-HFE tagging

The Figures 4.24 and 4.25 display the ratios of near-side and away-side yield for various partner electron cut variations in comparison to default cuts for pp and p–Pb events, respectively. For near-side yield, a systematic uncertainty of 1% is assigned for both pp and p–Pb events, while for away-side yield, a systematic uncertainty of 1-2% is assigned for pp and 1% in p–Pb collisions.

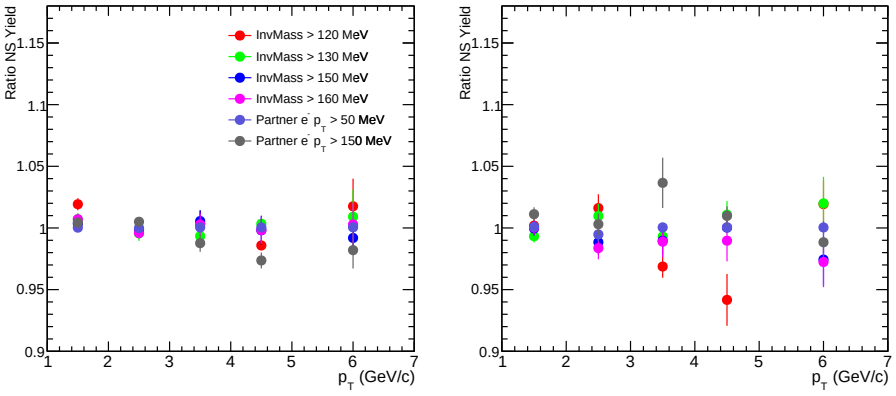

Figure 4.24: Near-side (left) and away-side (right) yield ratios by varying partner electron cuts for non-hfe estimation with respect to default for $4 < p_{\mathrm{T}}^{\mathrm{e}} < 12$ GeV/c and $1 < p_{\mathrm{T}}^{\mathrm{assoc}} < 7$ GeV/c in pp collisions at $\sqrt{s} = 5.02$ TeV.

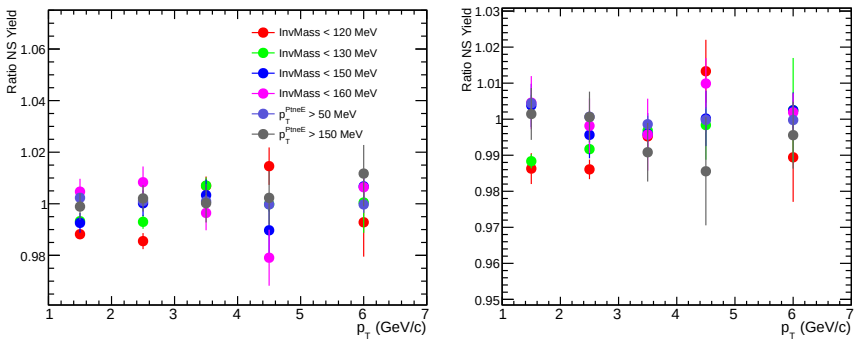

Figure 4.25: Near-side (left) and away-side (right) yield ratios by varying partner electron cuts for non-hfe estimation with respect to default for $4 < p_{\mathrm{T}}^{\mathrm{e}} < 12$ GeV/c and $1 < p_{\mathrm{T}}^{\mathrm{assoc}} < 7$ GeV/c in p–Pb collisions at $\sqrt{s_{\mathrm{NN}}} = 5.02$ TeV.

4.0.13 mixed-event correction

Figures 4.26 and 4.27 illustrate the ratio of near-side and away-side yield for different mixed-event correction methods in comparison to the default setting for pp and p–Pb events. For both near-side and away-side yield, a systematic uncer-

tainty of 1% is assigned for pp and p–Pb events. The systematic uncertainties are calculated as the average of the values obtained from the two methods.

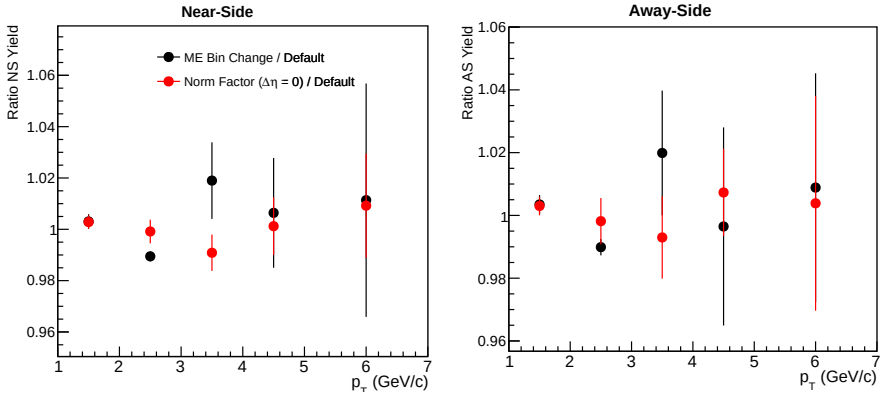

Figure 4.26: Ratio of near-side (left) and away-side (right) yield obtained from variation of mixed-event correction settings to the default settings for $4 < p_{\mathrm{T}}^{\mathrm{e}} < 12$ GeV/c and $1 < p_{\mathrm{T}}^{\mathrm{assoc}} < 7$ GeV/c in pp collisions at $\sqrt{s} = 5.02$ TeV.

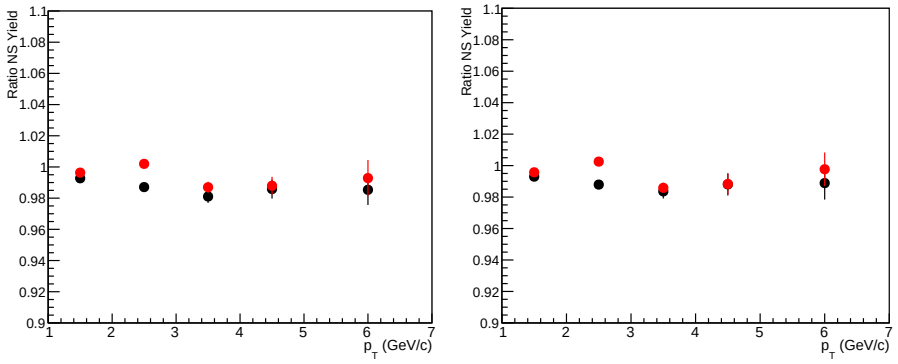

Figure 4.27: Ratio of near-side (left) and away-side (right) yield obtained from variation of mixed-event correction settings to the default settings for $4 < p_{\mathrm{T}}^{\mathrm{e}} < 12$ GeV/c and $1 < p_{\mathrm{T}}^{\mathrm{assoc}} < 7$ GeV/c in p–Pb collisions at $\sqrt{s_{\mathrm{NN}}} = 5.02$ TeV.

4.0.14 Beta variation

Figure 4.28 and 4.29 display the near and away-side yield obtained by increasing and decreasing the β parameters, as well as their corresponding ratios in comparison to the default setting for pp and p–Pb collisions. The systematic uncertainties are assigned by taking the full envelope of variation, and for near-side and away-side yield in pp events, the assigned systematic uncertainties range from 4-7% and 4-9%, respectively. In p–Pb events, the assigned systematic uncertainties for near-side and away-side yield range from 3-9% and 5-12% respectively.

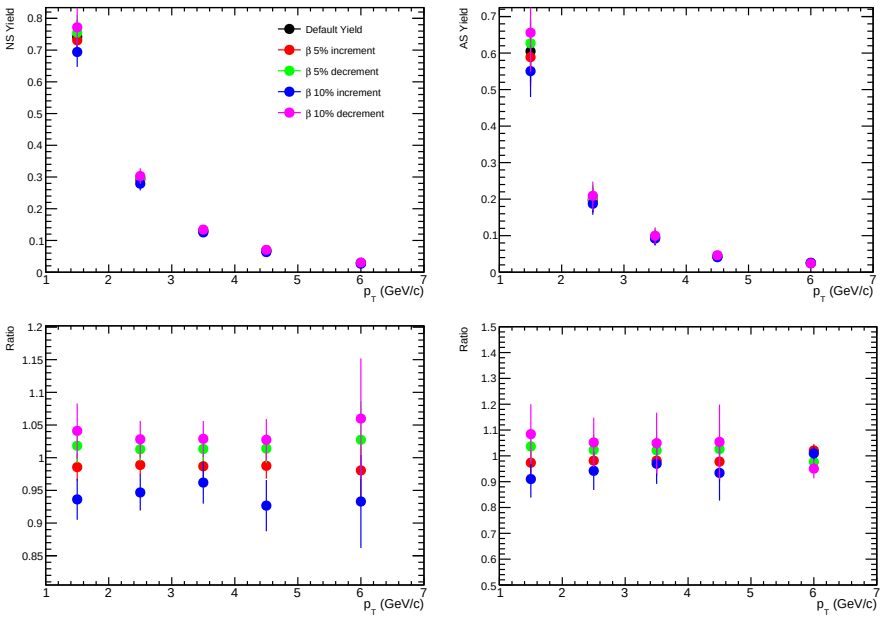

Figure 4.28: Near-side (upper left) and away-side (upper right) yields for each beta variation and corresponding ratio with respect to default for near-side (bottom left) and away-side (bottom right) for $4 < p_{\mathrm{T}}^{\mathrm{e}} < 12$ GeV/c and $1 < p_{\mathrm{T}}^{\mathrm{assoc}} < 7$ GeV/c in pp collisions at $\sqrt{s} = 5.02$ TeV.

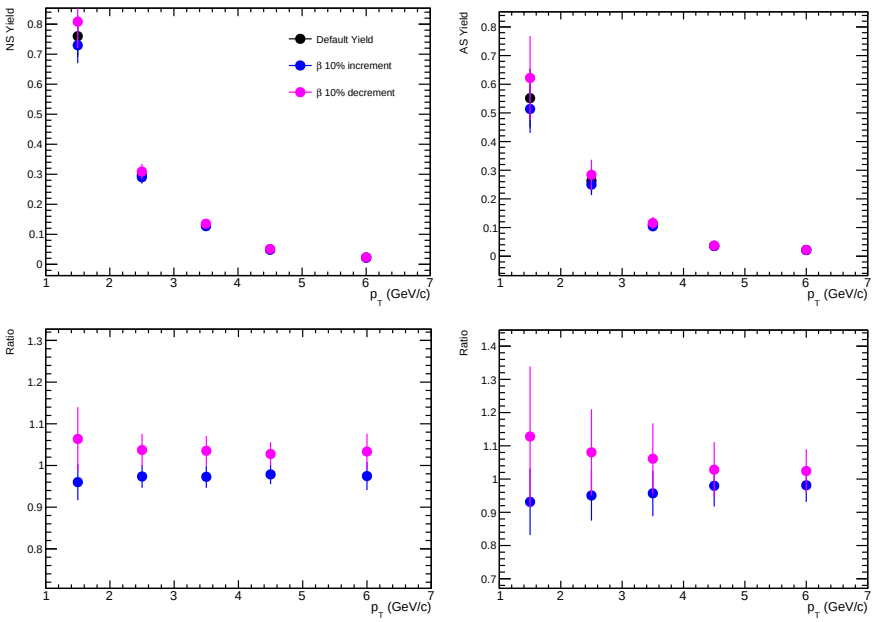

Figure 4.29: Near-side (upper left) and away-side (upper right) yields for each beta variation and corresponding ratio with respect to default for near-side (bottom left) and away-side (bottom right) for $4 < p_{\mathrm{T}}^{\mathrm{e}} < 12$ GeV/c and $1 < p_{\mathrm{T}}^{\mathrm{assoc}} < 7$ GeV/c in p–Pb collisions at $\sqrt{s_{\mathrm{NN}}} = 5.02$ TeV.

The generalized Gaussian function

To obtain the near-side and away-side yield, the baseline or pedestal in the HFE $\Delta\varphi$ distribution is subtracted. Figure 4.30 and 4.31 show the near-side and away-

side yield for each pedestal estimation, as well as the corresponding ratios to the default yield. The upper left plot displays the near-side yield, while the upper right plot shows the away-side yield. The bottom plots illustrate the ratio of yields from different pedestal values with respect to default for both near-side and away-side peaks. For pp, a systematic uncertainty of 3 to 15% is assigned for the near-side and away-side yields, while for p–Pb, a systematic uncertainty of 4 to 8% is assigned for the near-side yield and 6 to 12% for the away-side yield. The maximum deviation is used to determine the systematic uncertainties.

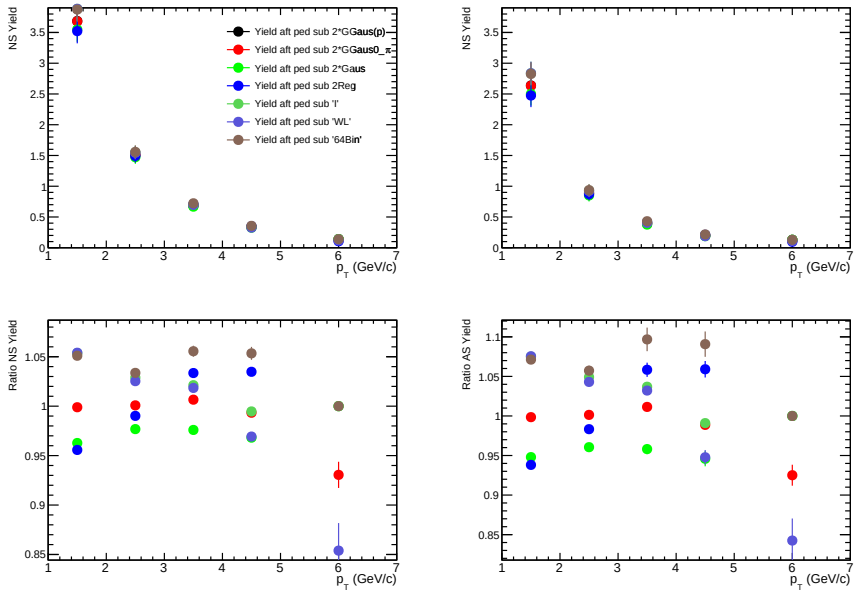

Figure 4.30: Near-side (Upper Left) and away-side (Upper Right) yields for each pedestal estimation methods and corresponding ratio with respect to default for near-side (Bottom Left) and away-side (Bottom Right) for $4 < p_{\mathrm{T}}^{\mathrm{e}} < 12$ GeV/c and $1 < p_{\mathrm{T}}^{\mathrm{assoc}} < 7$ GeV/c in pp collisions at $\sqrt{s} = 5.02$ TeV.

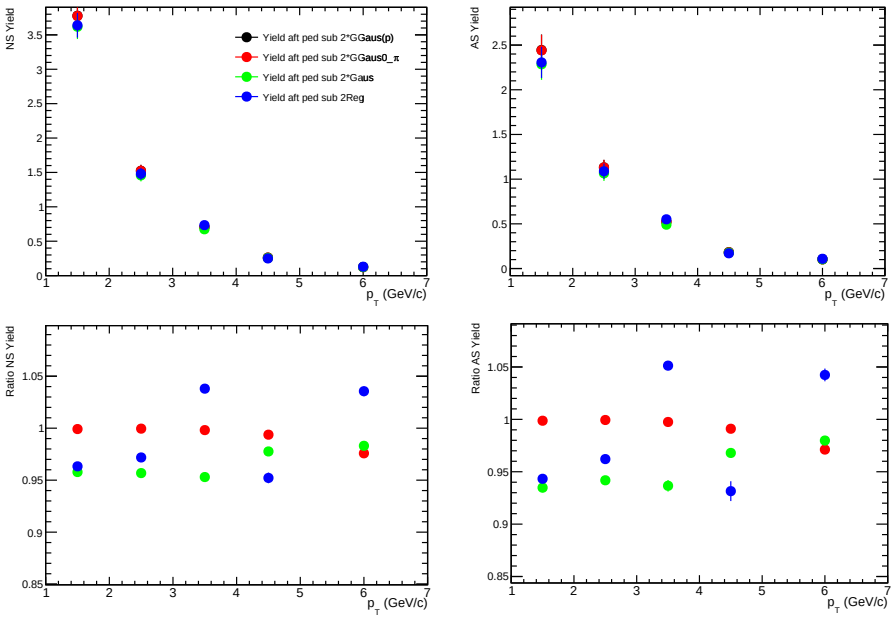

Figure 4.31: Near-side (upper left) and away-side (upper right) yields for each pedestal estimation methods and corresponding ratio with respect to default for near-side (bottom left) and away-side (bottom right) for $4 < p_{\mathrm{T}}^{\mathrm{e}} < 12$ GeV/c and $1 < p_{\mathrm{T}}^{\mathrm{assoc}} < 7$ GeV/c in p–Pb collisions at $\sqrt{s_{\mathrm{NN}}} = 5.02$ TeV.

4.0.15 Systematic uncertainties on near- and away-side width

To estimate the systematic uncertainty on the near-side and away-side width measurements, the near-side and away-side widths are calculated for each systematic variation, and the ratios with respect to the widths obtained from the default settings are determined. The near and away-side sigma values obtained from each electron identification cut and their corresponding ratios with respect to the default settings are shown in Figure 4.32 and 4.33 for pp and p–Pb events, respectively. The assigned systematic uncertainties are 3 to 4% for the near-side and 5% for the away-side in pp, and 2 to 4% for the near-side and 4-5% for the away-side in p–Pb events. The systematic uncertainties from electron track selection, Non-HFE tagging efficiency, and associated track variations are displayed in Figure 4.34, 4.35, and 4.36 for pp, and 4.37, 4.38, and 4.39 for p–Pb collisions. In pp, the systematic uncertainty on σ due to electron track selection is negligible, whereas for non-hfe selection, it is 0.3-1%, and for associated track selections, it is 0.2-3%. Similarly, in p–Pb collisions, the systematic uncertainties due to electron track, non-hfe selection, and associated track selections are 1%, 1%, and 1-4% for the near-side, and 1%, 1%, and 2% for the away-side, respectively.

The largest source of systematic uncertainty on σ is from the pedestal. The ratios of the sigma values for different fit parameters with respect to the default settings are shown in Figure 4.40 and 4.41 for pp and p–Pb events, respectively.

4.0.16 Fitting options (Pedestal) and parameters

The near and away-side sigma, obtained from the different fitting option and corresponding ratio compared to default is shown in Figure 4.40 and 4.41 for pp and p–Pb respectively. The assigned systematic uncertainties are 10% and 11% for $4 < p_{\mathrm{T}}^{\mathrm{e}} < 12$ GeV/c and $1 < p_{\mathrm{T}}^{\mathrm{assoc}} < 7$ GeV/c in pp and p–Pb.

The near and away-side sigma, obtained from the increment and decrement of the β parameter and corresponding ratio compared to default, is shown in Figure 4.42 and 4.43 for pp and p–Pb. Assigned systematic uncertainties are 3-

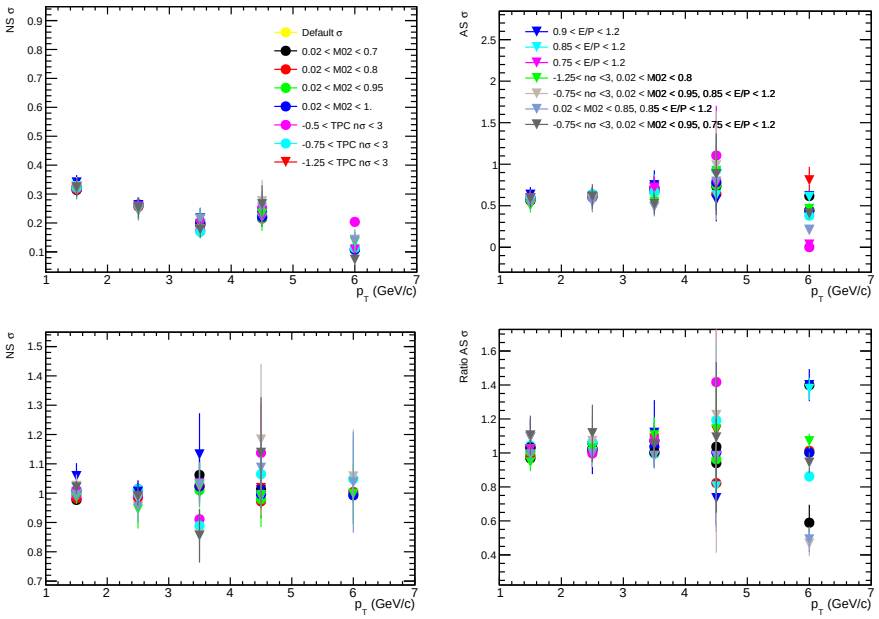

Figure 4.32: Near-side (upper left) and away-side (upper right) sigmas (σ) for each electron identification cut variations and corresponding ratio with respect to default for near-side (bottom left) and away-side (bottom right) for $4 < p_{\mathrm{T}}^{\mathrm{e}} < 12$ GeV/c and $1 < p_{\mathrm{T}}^{\mathrm{assoc}} < 7$ GeV/c in pp collisions at $\sqrt{s} = 5.02$ TeV.

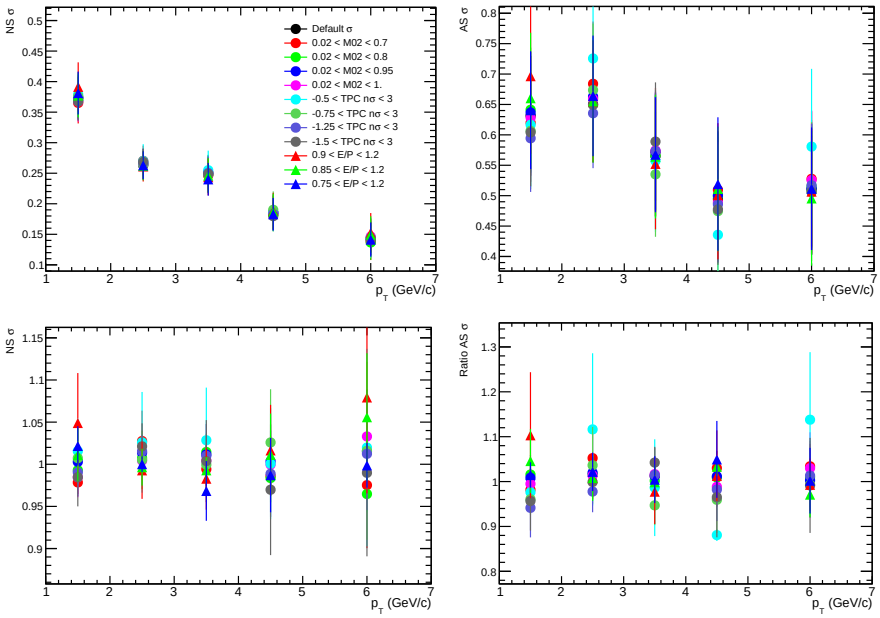

Figure 4.33: Near-side (upper left) and away-side (upper right) sigmas (σ) for each electron identification cut variations and corresponding ratio with respect to default for near-side (bottom left) and away-side (bottom right) for $4 < p_{\mathrm{T}}^{\mathrm{e}} < 12$ GeV/c and $1 < p_{\mathrm{T}}^{\mathrm{assoc}} < 7$ GeV/c in p–Pb collisions at $\sqrt{s_{\mathrm{NN}}} = 5.02$ TeV.

8% for near-side and 6-10% for away-side in pp. Similarly, for p–Pb, assigned systematic uncertainties are 3-9% for near-side and 5-12% for away-side.

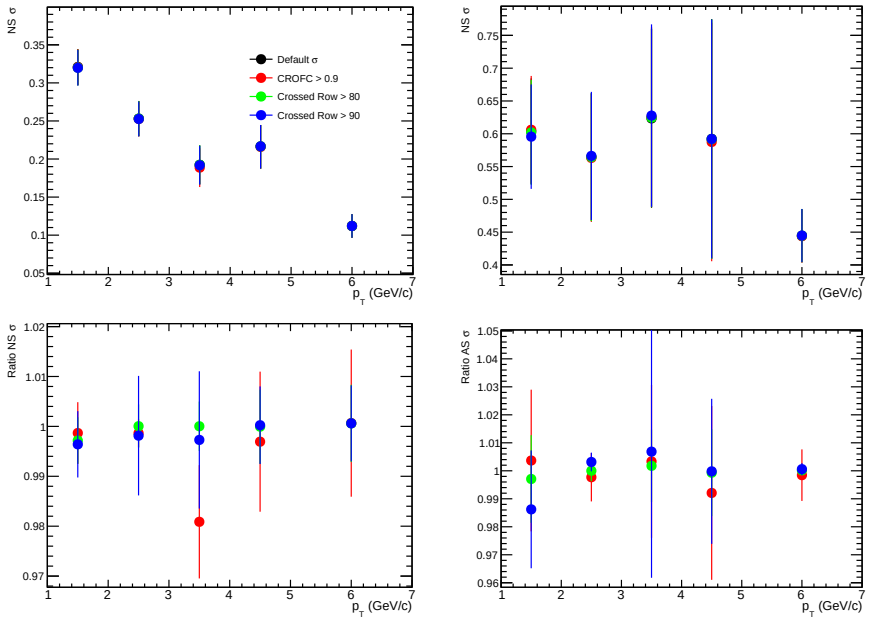

Figure 4.34: Near-side (upper left) and away-side (upper right) sigmas (σ) for each electron selection cut variations and corresponding ratio with respect to default for near-side (bottom left) and away-side (bottom right) for $4 < p_{\mathrm{T}}^{\mathrm{e}} < 12$ GeV/c and $1 < p_{\mathrm{T}}^{\mathrm{assoc}} < 7$ GeV/c in pp collisions at $\sqrt{s} = 5.02$ TeV.

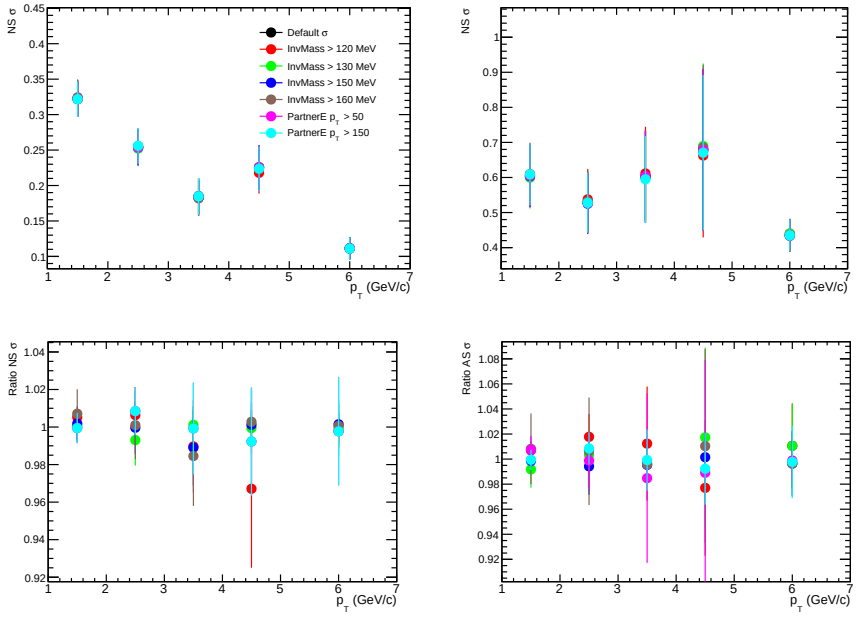

Figure 4.35: Near-side (upper left) and away-side (upper right) sigmas (σ) for each partner electron track selection cut variations and corresponding ratio with respect to default for near-side (bottom left) and away-side (bottom right) for $4 < p_{\mathrm{T}}^{\mathrm{e}} < 12$ GeV/c and $1 < p_{\mathrm{T}}^{\mathrm{assoc}} < 7$ GeV/c in pp collisions at $\sqrt{s} = 5.02$ TeV.

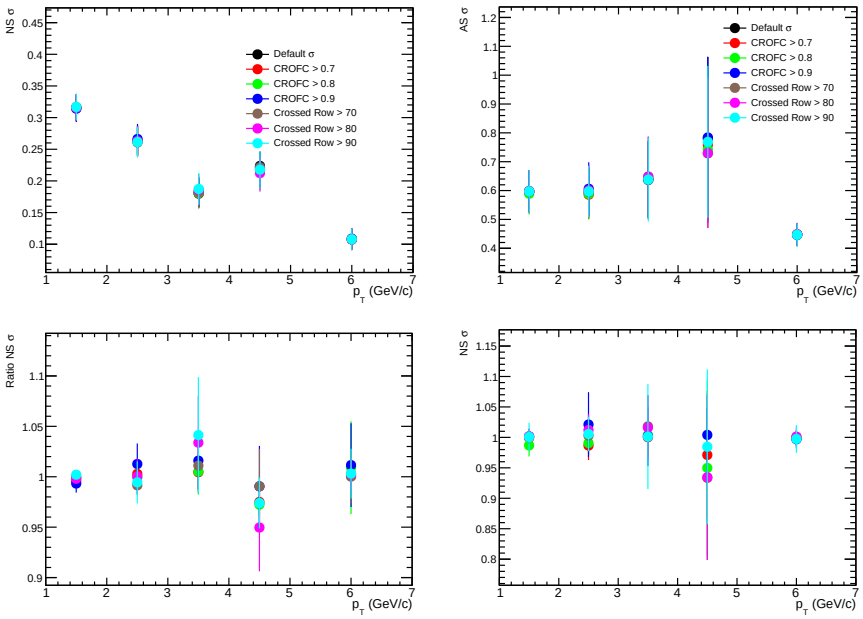

Figure 4.36: Near-side (upper left) and away-side (upper right) sigmas (σ) for each associate track selection cut variations and corresponding ratio with respect to default for near-side (bottom left) and away-side (bottom right) for $4 < p_{\mathrm{T}}^{\mathrm{e}} < 12$ GeV/c and $1 < p_{\mathrm{T}}^{\mathrm{assoc}} < 7$ GeV/c in pp collisions at $\sqrt{s} = 5.02$ TeV.

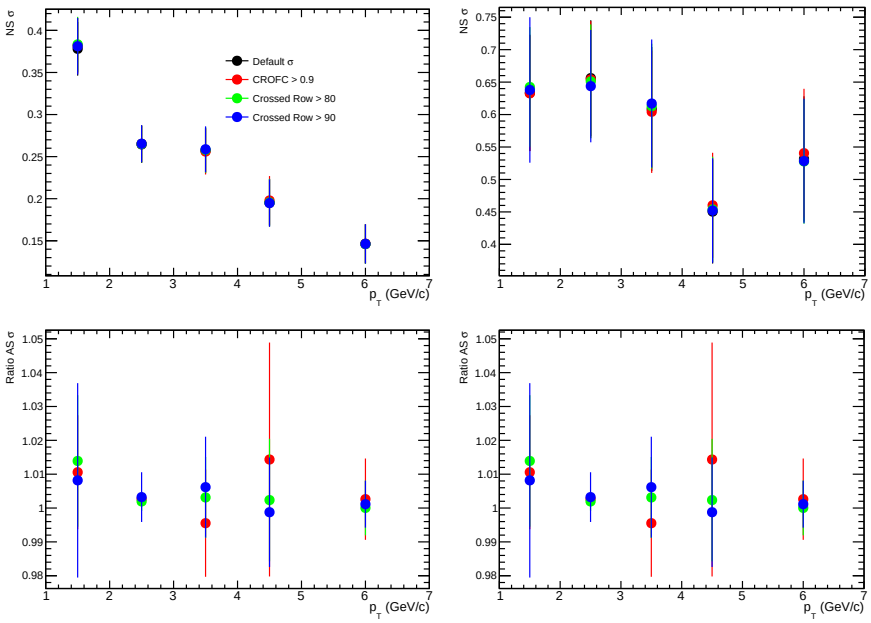

Figure 4.37: Near-side (upper left) and away-side (upper right) sigmas (σ) for each electron track selection cut variations and corresponding ratio with respect to default for near-side (bottom left) and away-side (bottom right) for $4 < p_{\mathrm{T}}^{\mathrm{e}} < 12$ GeV/c and $1 < p_{\mathrm{T}}^{\mathrm{assoc}} < 7$ GeV/c in p–Pb collisions at $\sqrt{s_{\mathrm{NN}}} = 5.02$ TeV.

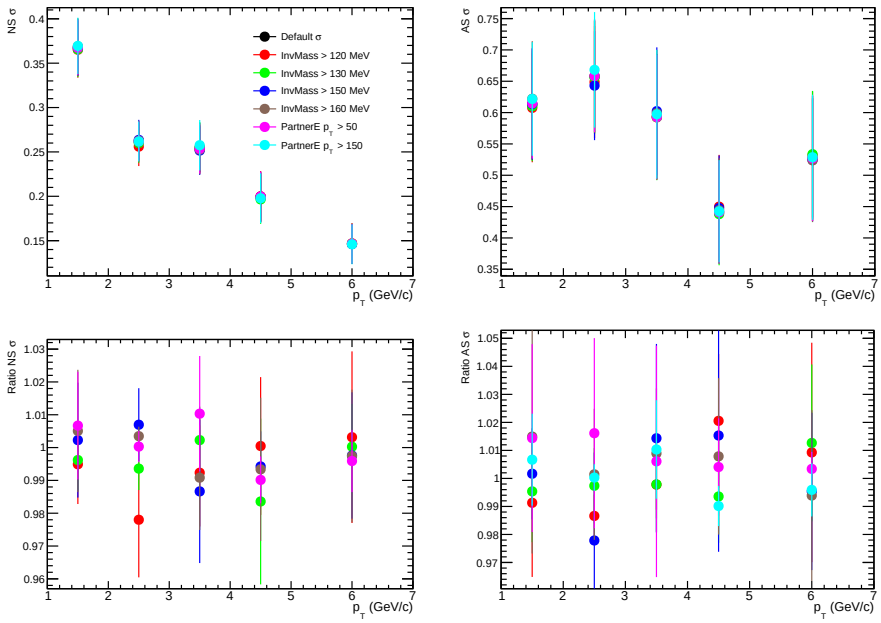

Figure 4.38: Near-side (upper left) and away-side (upper right) sigmas (σ) for each partner electron track selection cut variations and corresponding ratio with respect to default for near-side (bottom left) and away-side (bottom right) for $4 < p_{\mathrm{T}}^{\mathrm{e}} < 12$ GeV/c and $1 < p_{\mathrm{T}}^{\mathrm{assoc}} < 7$ GeV/c in p–Pb collisions at $\sqrt{s_{\mathrm{NN}}} = 5.02$ TeV.

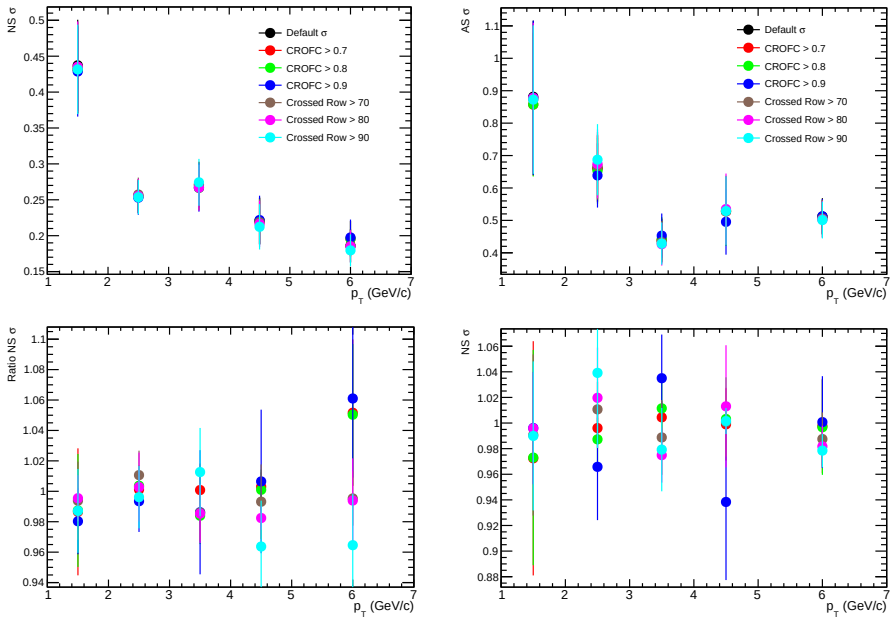

Figure 4.39: Near-side (upper left) and away-side (upper right) sigmas (σ) for each associate track selection cut variations and corresponding ratio with respect to default for near-side (bottom left) and away-side (bottom right) for $4 < p_{\mathrm{T}}^{\mathrm{e}} < 12$ GeV/c and $1 < p_{\mathrm{T}}^{\mathrm{assoc}} < 7$ GeV/c in p–Pb collisions at $\sqrt{s_{\mathrm{NN}}} = 5.02$ TeV.

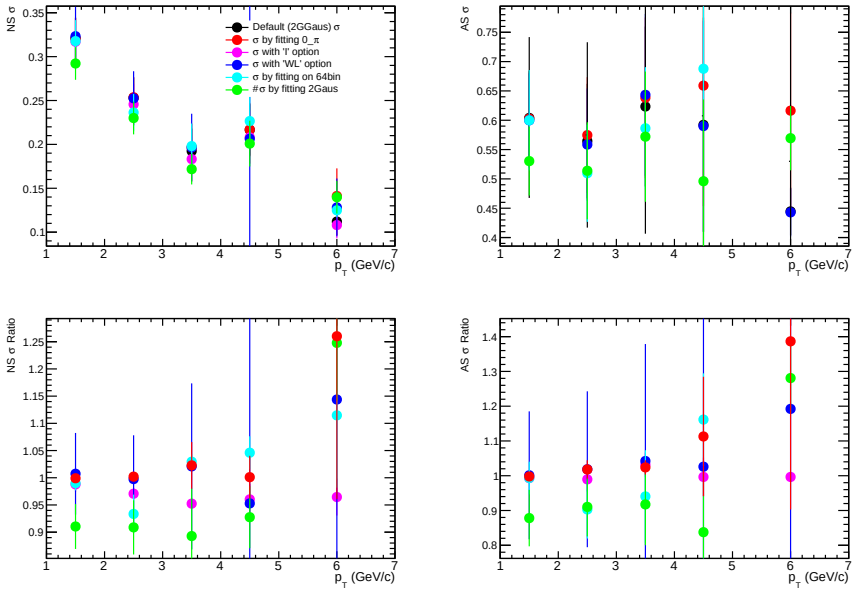

Figure 4.40: Near-side (upper left) and away-side (upper right) sigmas (σ) obtained from different fitting options and corresponding ratio with respect to default for near-side (bottom left) and away-side (bottom right) for $4 < p_{\mathrm{T}}^{\mathrm{e}} < 12$ GeV/c and $1 < p_{\mathrm{T}}^{\mathrm{assoc}} < 7$ GeV/c in pp collisions at $\sqrt{s} = 5.02$ TeV.

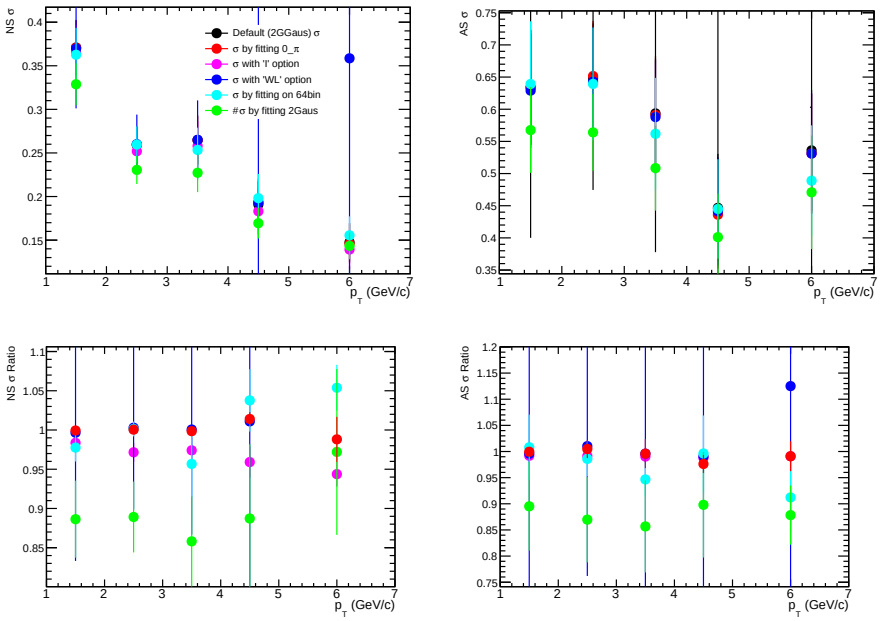

Figure 4.41: Near-side (upper left) and away-side (upper right) sigmas (σ) obtained from different fitting options and corresponding ratio with respect to default for near-side (bottom left) and away-side (bottom right) for $4 < p_{\mathrm{T}}^{\mathrm{e}} < 12$ GeV/c and $1 < p_{\mathrm{T}}^{\mathrm{assoc}} < 7$ GeV/c in p–Pb collisions at $\sqrt{s_{\mathrm{NN}}} = 5.02$ TeV.

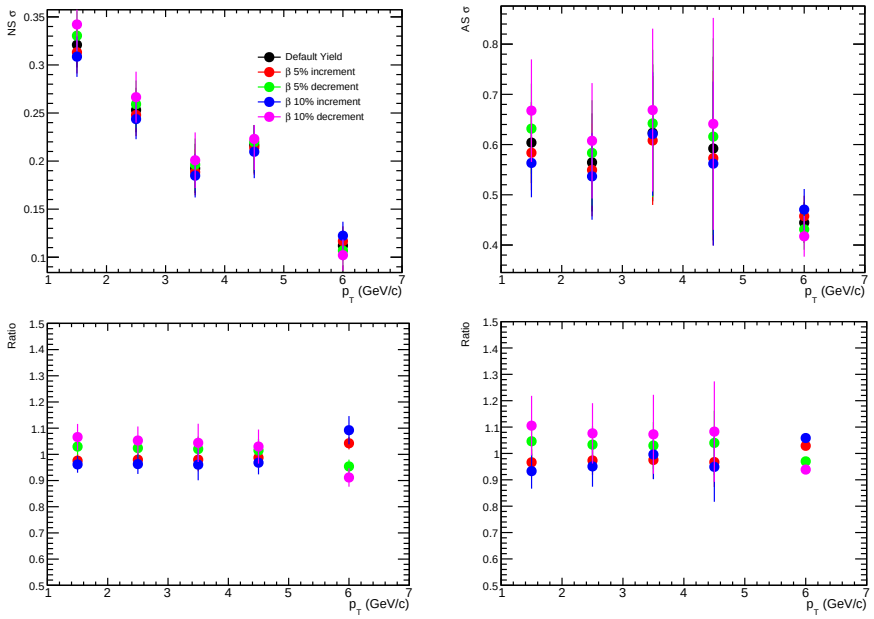

Figure 4.42: Near-side (upper left) and away-side (upper right) sigmas (σ) after changing beta values (β) and corresponding ratio with respect to default for near-side (bottom left) and away-side (bottom right) for $4 < p_{\mathrm{T}}^{\mathrm{e}} < 12$ GeV/c and $1 < p_{\mathrm{T}}^{\mathrm{assoc}} < 7$ GeV/c in pp collisions at $\sqrt{s} = 5.02$ TeV.

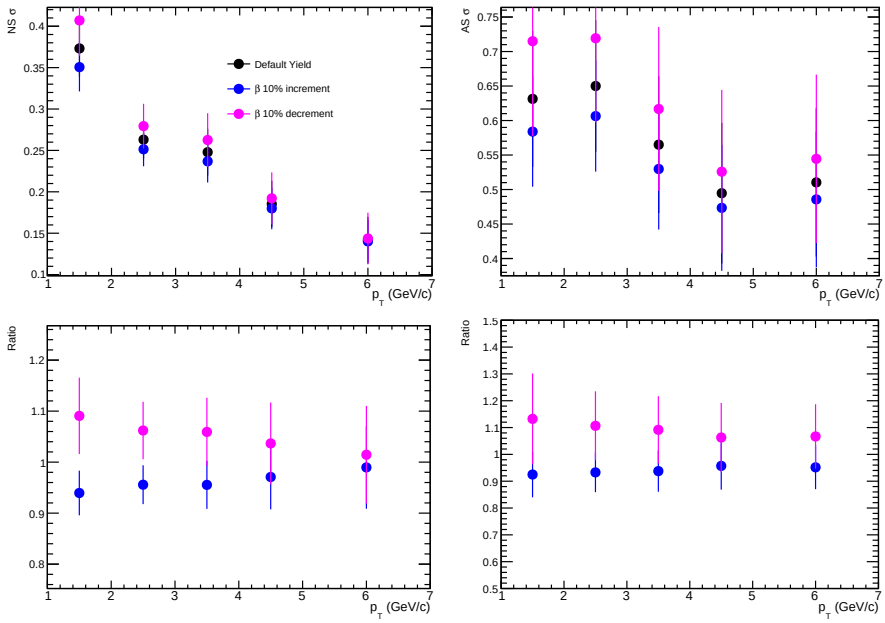

Figure 4.43: Near-side (upper left) and away-side (upper right) sigmas (σ) after changing beta values (β) and corresponding ratio with respect to default for near-side (bottom left) and away-side (bottom right) for $4 < p_{\mathrm{T}}^{\mathrm{e}} < 12$ GeV/c and $1 < p_{\mathrm{T}}^{\mathrm{assoc}} < 7$ GeV/c in p–Pb collisions at $\sqrt{s_{\mathrm{NN}}} = 5.02$ TeV.

A summary of the systematic uncertainties assigned for $\Delta\varphi$ distribution, near- and away-side yield, and width from each source in each p_{T} bin is given in Table 4.5 to 4.9 for pp collisions. Similarly, systematic uncertainties for p–Pb collisions are shown in Tabel 4.10 to 4.14.

It is to be noted that the final results used von Mises function as a default fit function in order to characterize the correlation peaks and estimation of near- and away-side observables; therefore, we no longer need of systematic uncertainties from the β variation in the final result plots.

Table 4.5: Summary of total systematic uncertainties in $\Delta\varphi$ assigned for each $p_{\mathrm{T}}^{\mathrm{assoc}}$ bin for pp collisions and pedestal estimation assigned as the difference of maximum deviation from the default, due to very small pedestal value from the default method at higher p_T.

Variables / $p_{\mathrm{T}}^{\mathrm{assoc}}$ (GeV/c)	$(1-2)$	$(2-3)$	$(3-4)$	$(4-5)$	$(5-7)$
Electron identification	3%	3%	3%	3%	5%
Non-HFE identification	1%	1%	1%	1%	1%
Electron track selection	1%	1%	1%	1%	1%
Associated track selection	1%	1%	1%	1%	2%
mixed-event	1%	1%	1%	1%	1%
Pedestal estimation	0.0208	0.0056	0.0042	0.0020	0.001

Table 4.6: Summary of total systematic uncertainties in near-side yields assigned for each $p_{\mathrm{T}}^{\mathrm{assoc}}$ bin for pp collisions at $\sqrt{s} = 5.02$ TeV.

Variables / $p_{\mathrm{T}}^{\mathrm{assoc}}$ (GeV/c)	$(1-2)$	$(2-3)$	$(3-4)$	$(4-5)$	$(5-7)$
Electron identification	2%	3%	3%	4%	4%
Non-HFE identification	1%	1%	1%	1%	1%
Electron track selection	1%	1%	1%	1%	1%
Associated track selection	1%	1%	1%	2%	2%
mixed-event	1%	1%	1%	1%	1%
Pedestal estimation	5%	4%	5%	5%	8%
β parameter	6%	6%	4%	7%	7%

It is to be noted that the final results used von Mises function as a default fit function in order to characterize the correlation peaks and estimation of near- and

Table 4.7: Summary of total systematic uncertainties in away-side yields assigned for each $p_{\mathrm{T}}^{\mathrm{assoc}}$ bin for pp collisions at $\sqrt{s} = 5.02$ TeV.

Variables / $p_{\mathrm{T}}^{\mathrm{assoc}}$ (GeV/c)	$(1-2)$	$(2-3)$	$(3-4)$	$(4-5)$	$(5-7)$
Electron identification	3%	5%	5%	6%	6%
Non-HFE identification	2%	2%	2%	2%	2%
Electron track selection	1%	1%	1%	1%	1%
Associated track selection	1%	2%	2%	3%	3%
mixed-event	1%	1%	1%	1%	1%
Pedestal estimation	8%	6%	10%	9%	8%
β parameter	9%	6%	4%	7%	5%

Table 4.8: Summary of total systematic uncertainties in near-side sigma assigned for each $p_{\mathrm{T}}^{\mathrm{assoc}}$ bin for pp collisions at $\sqrt{s} = 5.02$ TeV.

Variables / $p_{\mathrm{T}}^{\mathrm{assoc}}$ (GeV/c)	$(1-2)$	$(2-3)$	$(3-4)$	$(4-5)$	$(5-7)$
Electron identification	2%	2%	6%	6%	6%
Non-HFE identification	0.3%	0.6%	0.9%	1%	0.2%
Associated track selection	0.3%	0.7%	2%	3%	0.6%
Electron track selection	*Nil*	*Nil*	*Nil*	*Nil*	*Nil*
mixed-event	*Nil*	*Nil*	*Nil*	*Nil*	*Nil*
Pedestal estimation	10%	10%	10%	10%	10%
β parameter	6%	5%	4%	3%	8%

away-side observables; therefore, we no longer need of systematic uncertainties from the β variation.

A summary of the systematic uncertainties of the correlation distribution, NS and AS yields and widths for $4 < p_{\mathrm{T}}^{\mathrm{e}} < 12$ GeV/c are reported in Tables 4.35 and 4.36 for pp and p–Pb collisions, respectively. The $\Delta\varphi$ correlated and uncorrelated uncertainties are separately reported for the $\Delta\varphi$ distribution, and the total uncertainty from all sources is reported for the peak yields and widths.

By varying the selection criteria, one can study possible biases associated with the track quality selection for electrons used in the analysis, as mentioned in [2]. They observed an uncertainty of 1-2% in the correlation distribution as a

Table 4.9: Summary of total systematic uncertainties in away-side sigma assigned for each $p_{\mathrm{T}}^{\mathrm{assoc}}$ bin for pp collisions at $\sqrt{s} = 5.02$ TeV.

Variables / $p_{\mathrm{T}}^{\mathrm{assoc}}$ (GeV/c)	$(1-2)$	$(2-3)$	$(3-4)$	$(4-5)$	$(5-7)$
Electron identification	4%	4%	7%	7%	7%
Non-HFE identification	0.7%	0.8%	1%	1%	0.6%
Associated track selection	0.3%	0.7%	2%	3%	0.2%
Electron track selection	*Nil*	*Nil*	*Nil*	*Nil*	*Nil*
mixed-event	*Nil*	*Nil*	*Nil*	*Nil*	*Nil*
Pedestal estimation	10%	10%	10%	10%	10%
β parameter	10%	7%	7%	8%	6%

Table 4.10: Summary of total systematic uncertainties in $\Delta\varphi$ assigned for each $p_{\mathrm{T}}^{\mathrm{assoc}}$ bin for p–Pb collisions. and pedestal estimation assigned as the difference of maximum deviation from the default due to a very small pedestal value from the default method at higher p_T.

Variables / $p_{\mathrm{T}}^{\mathrm{assoc}}$ (GeV/c)	$(1-2)$	$(2-3)$	$(3-4)$	$(4-5)$	$(5-7)$
Electron identification	2%	2%	3%	3%	4%
Non-HFE identification	1%	1%	1%	1%	1%
Electron track selection	1%	1%	1%	2%	2%
Associated track selection	2%	2%	2%	2%	3%
mixed-event	1%	1%	1%	1%	1%
Pedestal estimation	0.02	0.0069	0.0035	0.0013	0.0005

function of $p_{\mathrm{T}}^{\mathrm{assoc}}$ for $4 < p_{\mathrm{T}}^{\mathrm{e}} < 12$ GeV/c in both collision systems. The uncertainty in the range of 1-2% was also estimated for NS and AS yields. However, the uncertainty from track selection on NS and AS widths was found to be insignificant.

To assess the uncertainty due to electron identification using TPC and EMCAL signals, researchers varied the selection criteria for $n\sigma^{\mathrm{TPC}}$e, E/p, and M02. These variations changed the efficiency by a maximum of approximately 20%. For $4 < p_{\mathrm{T}}^{\mathrm{e}} < 12$ GeV/c in pp and p–Pb collisions, a total uncertainty of 2-5% was obtained for the correlation distribution as a function of $p_{\mathrm{T}}^{\mathrm{assoc}}$. The resulting uncertainties ranged from 2% to 6% for NS and AS yields and between 2% and 7%

Table 4.11: Summary of total systematic uncertainties in near-side yields assigned for each $p_{\mathrm{T}}^{\mathrm{assoc}}$ bin for p–Pb collisions at $\sqrt{s_{\mathrm{NN}}} = 5.02$ TeV.

Variables / $p_{\mathrm{T}}^{\mathrm{assoc}}$ (GeV/c)	$(1-2)$	$(2-3)$	$(3-4)$	$(4-5)$	$(5-7)$
Electron identification	4%	4%	4%	4%	4%
Non-HFE identification	1%	1%	1%	1%	1%
Electron track selection	1%	1%	1%	1%	1%
Associated track selection	2%	2%	2%	2%	4%
mixed-event	1%	1%	1%	1%	1%
Pedestal estimation	4%	4%	5%	5%	5%
β parameter	6%	4%	4%	3%	3%

Table 4.12: Summary of total systematic uncertainties in away-side yields assigned for each $p_{\mathrm{T}}^{\mathrm{assoc}}$ bin for p–Pb collisions at $\sqrt{s_{\mathrm{NN}}} = 5.02$ TeV.

Variables / $p_{\mathrm{T}}^{\mathrm{assoc}}$ (GeV/c)	$(1-2)$	$(2-3)$	$(3-4)$	$(4-5)$	$(5-7)$
Electron identification	4%	4%	4%	4%	4%
Non-HFE identification	1%	1%	1%	1%	1%
Electron track selection	1%	1%	1%	1%	1%
Associated track selection	2%	3%	3%	4%	4%
mixed-event	1%	1%	1%	1%	1%
Pedestal estimation	6%	6%	7%	7%	5%
β parameter	13%	8%	6%	3%	3%

for NS and AS widths.

We estimated the contribution from background electrons using the invariant-mass method. We varied the selection criteria of the partner electron tracks, including the minimum p_{T} and the invariant-mass window of the electron-positron pairs, to obtain the systematic uncertainty of the procedure, which mainly affects the average tagging efficiency. The variation affected the tagging efficiency by about 5%. A resulting systematic uncertainty of 1-2% was obtained as a function of $p_{\mathrm{T}}^{\mathrm{assoc}}$ on the correlation distribution, the peak yields, and their widths for $4 < p_{\mathrm{T}}^{\mathrm{e}} < 12$ GeV/c in pp and p–Pb collisions.

By adjusting the charged track selection criteria, including requiring a hit

Table 4.13: Summary of total systematic uncertainties in near-side sigma assigned for each $p_{\mathrm{T}}^{\mathrm{assoc}}$ bin for p–Pb collisions at $\sqrt{s_{\mathrm{NN}}} = 5.02$ TeV.

Variables / $p_{\mathrm{T}}^{\mathrm{assoc}}$ (GeV/c)	$(1-2)$	$(2-3)$	$(3-4)$	$(4-5)$	$(5-7)$
Electron identification	2%	2%	2%	2%	4%
Non-HFE identification	1%	1%	1%	1%	1%
Associated track selection	1%	1%	1%	2%	4%
Electron track selection	1%	1%	1%	1%	1%
mixed-event	*Nil*	*Nil*	*Nil*	*Nil*	*Nil*
Pedestal estimation	11%	11%	11%	11%	11%
β parameter	9%	8%	8%	5%	3%

Table 4.14: Summary of total systematic uncertainties in away-side sigma assigned for each $p_{\mathrm{T}}^{\mathrm{assoc}}$ bin for p–Pb collisions at $\sqrt{s_{\mathrm{NN}}} = 5.02$ TeV.

Variables / $p_{\mathrm{T}}^{\mathrm{assoc}}$ (GeV/c)	$(1-2)$	$(2-3)$	$(3-4)$	$(4-5)$	$(5-7)$
Electron identification	4%	4%	4%	5%	5%
Non-HFE identification	1%	1%	1%	1%	1%
Associated track selection	2%	2%	2%	2%	2%
Electron track selection	1%	1%	1%	1%	1%
mixed-event	*Nil*	*Nil*	*Nil*	*Nil*	*Nil*
Pedestal estimation	11%	11%	11%	11%	11%
β parameter	12%	10%	10%	9%	5%

Table 4.15: Summary of total systematic uncertainties in $\Delta\varphi$ assigned for $p_{\mathrm{T}}^{\mathrm{Trigger}}$: 4-7 GeV/$c$ in each $p_{\mathrm{T}}^{\mathrm{assoc}}$ bin for pp collisions and pedestal estimation assigned as the difference of maximum deviation from the default, due to very small pedestal value from the default method at higher p_T.

Variables / $p_{\mathrm{T}}^{\mathrm{assoc}}$ (GeV/c)	$(1-2)$	$(2-3)$	$(3-4)$	$(4-5)$	$(5-7)$
Electron identification	3%	3%	3%	3%	5%
Non-HFE identification	1%	1%	1%	1%	1%
Electron track selection	1%	1%	1%	1%	1%
Associated track selection	1%	1%	1%	1%	2%
Pedestal estimation	0.009	0.0027	0.0013	0.00065	0.0

Table 4.16: Summary of total systematic uncertainties in $\Delta\varphi$ assigned for $p_{\mathrm{T}}^{\mathrm{Trigger}}$: 4-7 GeV/$c$ in each $p_{\mathrm{T}}^{\mathrm{assoc}}$ bin for p–Pb collisions. and pedestal estimation assigned as the difference of maximum deviation from the default, due to very small pedestal value from the default method at higher p_T.

Variables / $p_{\mathrm{T}}^{\mathrm{assoc}}$ (GeV/c)	$(1-2)$	$(2-3)$	$(3-4)$	$(4-5)$	$(5-7)$
Electron identification	3%	3%	5%	5%	6%
Non-HFE identification	1%	1%	1%	1%	1%
Electron track selection	1%	1%	1%	2%	2%
Associated track selection	2%	2%	2%	2%	3%
Pedestal estimation	0.0199	0.004	0.0005	0.0004	0.0001

Table 4.17: Summary of total systematic uncertainties in near-side yields assigned for $p_{\mathrm{T}}^{\mathrm{Trigger}}$: 4-7 GeV/$c$ in each $p_{\mathrm{T}}^{\mathrm{assoc}}$ bin for pp collisions at $\sqrt{s} = 5.02$ TeV.

Variables / $p_{\mathrm{T}}^{\mathrm{assoc}}$ (GeV/c)	$(1-2)$	$(2-3)$	$(3-4)$	$(4-5)$	$(5-7)$
Electron identification	3%	3%	5%	5%	5%
Non-HFE identification	1%	1%	1%	1%	1%
Electron track selection	1%	1%	1%	1%	1%
Associated track selection	2%	2%	2%	2%	4%
Pedestal estimation	3%	2%	2%	3%	0%

Table 4.18: Summary of total systematic uncertainties in near-side yields assigned for $p_{\mathrm{T}}^{\mathrm{Trigger}}$: 4-7 GeV/$c$ in each $p_{\mathrm{T}}^{\mathrm{assoc}}$ bin for p–Pb collisions at $\sqrt{s_{\mathrm{NN}}} = 5.02$ TeV.

Variables / $p_{\mathrm{T}}^{\mathrm{assoc}}$ (GeV/c)	$(1-2)$	$(2-3)$	$(3-4)$	$(4-5)$	$(5-7)$
Electron identification	3%	3%	3%	3%	4%
Non-HFE identification	1%	1%	1%	1%	1%
Electron track selection	1%	1%	1%	1%	1%
Associated track selection	1%	1%	3%	3%	3%
Pedestal estimation	5%	3%	4%	3%	2%

in one of the two SPD layers of the ITS and varying the selection on the distance of the closest approach, the uncertainty associated with the specific selection of associated particles was estimated. This uncertainty is considered to be correlated in $\Delta\varphi$, and for $4 < p_{\mathrm{T}}^{\mathrm{e}} < 12$ GeV/c, the uncertainties were 1-2% and 2-3% for the correlation distribution in pp and p–Pb collisions, respectively. For NS and AS

Table 4.19: Summary of total systematic uncertainties in away-side yields assigned for $p_{\mathrm{T}}^{\mathrm{Trigger}}$: 4-7 GeV/$c$ in each $p_{\mathrm{T}}^{\mathrm{assoc}}$ bin for pp collisions at $\sqrt{s} = 5.02$ TeV.

Variables / $p_{\mathrm{T}}^{\mathrm{assoc}}$ (GeV/c)	$(1-2)$	$(2-3)$	$(3-4)$	$(4-5)$	$(5-7)$
Electron identification	3%	3%	4%	7%	7%
Non-HFE identification	1%	1%	2%	3%	3%
Electron track selection	1%	1%	1%	1%	1%
Associated track selection	1%	1%	1%	2%	2%
Pedestal estimation	4%	4%	4%	3%	0%

Table 4.20: Summary of total systematic uncertainties in away-side yields assigned for $p_{\mathrm{T}}^{\mathrm{Trigger}}$: 4-7 GeV/$c$ in each $p_{\mathrm{T}}^{\mathrm{assoc}}$ bin for p–Pb collisions at $\sqrt{s_{\mathrm{NN}}} = 5.02$ TeV.

Variables / $p_{\mathrm{T}}^{\mathrm{assoc}}$ (GeV/c)	$(1-2)$	$(2-3)$	$(3-4)$	$(4-5)$	$(5-7)$
Electron identification	4%	4%	4%	4%	4%
Non-HFE identification	1%	1%	1%	1%	1%
Electron track selection	1%	1%	1%	1%	1%
Associated track selection	2%	2%	2%	2%	2%
Pedestal estimation	8%	4%	4%	3%	2%

Table 4.21: Summary of total systematic uncertainties in near-side sigma assigned for $p_{\mathrm{T}}^{\mathrm{Trigger}}$: 4-7 GeV/$c$ in each $p_{\mathrm{T}}^{\mathrm{assoc}}$ bin for pp collisions at $\sqrt{s} = 5.02$ TeV.

Variables / $p_{\mathrm{T}}^{\mathrm{assoc}}$ (GeV/c)	$(1-2)$	$(2-3)$	$(3-4)$	$(4-5)$	$(5-7)$
Electron identification	2%	2%	3%	4%	4%
Non-HFE identification	1%	1%	1%	1%	1%
Associated track selection	1%	1%	1%	2%	2%
Electron track selection	1%	1%	1%	1%	1%
Pedestal estimation	6%	9%	9%	5%	5%

yields, uncertainties of 1-3% and 1-4% were estimated for pp and p–Pb collisions, respectively, while uncertainties of less than 3% and 4% were obtained for the NS and AS widths in pp and p–Pb collisions, respectively.

The mixed-event technique was used to correct for effects induced by limited detector acceptance and its local inhomogeneities. The normalization factor, β, was varied by calculating the integrated yield over the full $\Delta\varphi$ range for $|\Delta\eta| <$

Table 4.22: Summary of total systematic uncertainties in away-side sigma assigned for $p_{\mathrm{T}}^{\mathrm{Trigger}}$: 4-7 GeV/$c$ in each $p_{\mathrm{T}}^{\mathrm{assoc}}$ bin for pp collisions at $\sqrt{s} = 5.02$ TeV.

Variables / $p_{\mathrm{T}}^{\mathrm{assoc}}$ (GeV/c)	$(1-2)$	$(2-3)$	$(3-4)$	$(4-5)$	$(5-7)$
Electron identification	5%	5%	8%	8%	8%
Non-HFE identification	1%	1%	2%	2%	2%
Associated track selection	1%	1%	1%	2%	2%
Electron track selection	1%	1%	1%	1%	1%
Pedestal estimation	8%	6%	8%	6%	12%

Table 4.23: Summary of total systematic uncertainties in near-side sigma assigned for $p_{\mathrm{T}}^{\mathrm{Trigger}}$: 4-7 GeV/$c$ in each $p_{\mathrm{T}}^{\mathrm{assoc}}$ bin for p–Pb collisions at $\sqrt{s_{\mathrm{NN}}} = 5.02$ TeV.

Variables / $p_{\mathrm{T}}^{\mathrm{assoc}}$ (GeV/c)	$(1-2)$	$(2-3)$	$(3-4)$	$(4-5)$	$(5-7)$
Electron identification	2%	2%	3%	4%	4%
Non-HFE identification	1%	1%	1%	1%	1%
Associated track selection	1%	1%	1%	1%	1%
Electron track selection	1%	1%	1%	1%	1%
Pedestal estimation	11%	9%	12%	7%	13%

Table 4.24: Summary of total systematic uncertainties in away-side sigma assigned for $p_{\mathrm{T}}^{\mathrm{Trigger}}$: 4-7 GeV/$c$ in each $p_{\mathrm{T}}^{\mathrm{assoc}}$ bin for p–Pb collisions at $\sqrt{s_{\mathrm{NN}}} = 5.02$ TeV.

Variables / $p_{\mathrm{T}}^{\mathrm{assoc}}$ (GeV/c)	$(1-2)$	$(2-3)$	$(3-4)$	$(4-5)$	$(5-7)$
Electron identification	4%	4%	4%	5%	5%
Non-HFE identification	2%	2%	2%	2%	2%
Associated track selection	1%	1%	1%	1%	1%
Electron track selection	1%	1%	1%	1%	1%
Pedestal estimation	11%	9%	12%	7%	7%

0.01. For the correlation distribution and the peak yields in pp and p–Pb collisions, a correlated uncertainty of 1% in $\Delta\varphi$ was obtained. No uncertainty was assigned for the NS and AS widths.

The v_2 of HFe and charged particles can affect the $\Delta\varphi$ distribution. However, as there are no previous measurements of HFe v_2 in minimum bias pp and p–Pb collisions, a conservative estimate was obtained using measurements in 0-20%

Table 4.25: Summary of total systematic uncertainties in $\Delta\varphi$ assigned for $p_{\mathrm{T}}^{\mathrm{Trigger}}$: 7-16 GeV/$c$ in each $p_{\mathrm{T}}^{\mathrm{assoc}}$ bin for pp collisions and pedestal estimation assigned as the difference of maximum deviation from the default, due to very small pedestal value from the default method at higher p_T.

Variables / $p_{\mathrm{T}}^{\mathrm{assoc}}$ (GeV/c)	$(1-2)$	$(2-3)$	$(3-4)$	$(4-5)$	$(5-7)$
Electron identification	5%	5%	5%	5%	5%
Non-HFE identification	1%	1%	1%	1%	1%
Electron track selection	1%	1%	1%	1%	1%
Associated track selection	1%	1%	1%	1%	2%
Pedestal estimation	0.008	0.004	0.003	0.00	0.00

Table 4.26: Summary of total systematic uncertainties in $\Delta\varphi$ assigned for $p_{\mathrm{T}}^{\mathrm{Trigger}}$: 7-16 GeV/$c$ in each $p_{\mathrm{T}}^{\mathrm{assoc}}$ bin for p–Pb collisions. and pedestal estimation assigned as the difference of maximum deviation from the default due to a very small pedestal value from the default method at higher p_T.

Variables / $p_{\mathrm{T}}^{\mathrm{assoc}}$ (GeV/c)	$(1-2)$	$(2-3)$	$(3-4)$	$(4-5)$	$(5-7)$
Electron identification	4%	4%	4%	4%	4%
Non-HFE identification	1%	1%	1%	1%	1%
Electron track selection	1%	1%	1%	2%	2%
Associated track selection	2%	2%	2%	2%	2%
Pedestal estimation	0.01	0.007	0.002	0.0015	0.0008

Table 4.27: Summary of total systematic uncertainties in near-side yields assigned for $p_{\mathrm{T}}^{\mathrm{Trigger}}$: 7-16 GeV/$c$ in each $p_{\mathrm{T}}^{\mathrm{assoc}}$ bin for pp collisions at $\sqrt{s} = 5.02$ TeV.

Variables / $p_{\mathrm{T}}^{\mathrm{assoc}}$ (GeV/c)	$(1-2)$	$(2-3)$	$(3-4)$	$(4-5)$	$(5-7)$
Electron identification	5%	5%	5%	5%	5%
Non-HFE identification	1%	1%	1%	1%	1%
Electron track selection	1%	1%	1%	1%	1%
Associated track selection	2%	2%	2%	2%	4%
Pedestal estimation	2%	2%	2%	2%	5%

central p–Pb collisions from Ref. [167]. Including v_2 has a minimal impact of less than 1% on the baseline and peak yields and does not alter the NS and AS widths.

To investigate the stability of the fit to the correlation distributions, several

Table 4.28: Summary of total systematic uncertainties in away-side yields assigned for $p_{\mathrm{T}}^{\mathrm{Trigger}}$: 7-16 GeV/$c$ in each $p_{\mathrm{T}}^{\mathrm{assoc}}$ bin for pp collisions at $\sqrt{s} = 5.02$ TeV.

Variables / $p_{\mathrm{T}}^{\mathrm{assoc}}$ (GeV/c)	$(1-2)$	$(2-3)$	$(3-4)$	$(4-5)$	$(5-7)$
Electron identification	5%	5%	5%	5%	5%
Non-HFE identification	1%	1%	1%	2%	2%
Electron track selection	1%	1%	1%	1%	1%
Associated track selection	1%	1%	1%	2%	2%
Pedestal estimation	4%	4%	4%	9%	1%

Table 4.29: Summary of total systematic uncertainties in near-side yields assigned for $p_{\mathrm{T}}^{\mathrm{Trigger}}$: 7-16 GeV/$c$ in each $p_{\mathrm{T}}^{\mathrm{assoc}}$ bin for p–Pb collisions at $\sqrt{s_{\mathrm{NN}}} = 5.02$ TeV.

Variables / $p_{\mathrm{T}}^{\mathrm{assoc}}$ (GeV/c)	$(1-2)$	$(2-3)$	$(3-4)$	$(4-5)$	$(5-7)$
Electron identification	3%	3%	4%	5%	5%
Non-HFE identification	1%	1%	1%	1%	1%
Electron track selection	1%	1%	1%	1%	1%
Associated track selection	3%	3%	1%	1%	1%
Pedestal estimation	6%	2%	1%	4%	3%

Table 4.30: Summary of total systematic uncertainties in away-side yields assigned for $p_{\mathrm{T}}^{\mathrm{Trigger}}$: 7-16 GeV/$c$ in each $p_{\mathrm{T}}^{\mathrm{assoc}}$ bin for p–Pb collisions at $\sqrt{s_{\mathrm{NN}}} = 5.02$ TeV.

Variables / $p_{\mathrm{T}}^{\mathrm{assoc}}$ (GeV/c)	$(1-2)$	$(2-3)$	$(3-4)$	$(4-5)$	$(5-7)$
Electron identification	5%	5%	5%	5%	5%
Non-HFE identification	2%	2%	2%	2%	2%
Electron track selection	1%	1%	1%	1%	1%
Associated track selection	4%	4%	4%	4%	4%
Pedestal estimation	9%	12%	5%	5%	2%

checks were performed. The NS and AS peaks were fitted using alternative functions, such as a Gaussian and a generalized Gaussian, instead of the von Mises function. Additionally, alternative fits were carried out by fixing the baseline value to the average of the points in the transverse region ($\pi/3 < |\Delta\varphi| < \pi/2$) to examine its stability with respect to statistical fluctuations.

The NS and AS yields were obtained by integrating the fit functions in the

Table 4.31: Summary of total systematic uncertainties in near-side sigma assigned for $p_{\mathrm{T}}^{\mathrm{Trigger}}$: 7-16 GeV/$c$ in each $p_{\mathrm{T}}^{\mathrm{assoc}}$ bin for pp collisions at $\sqrt{s} = 5.02$ TeV.

Variables / $p_{\mathrm{T}}^{\mathrm{assoc}}$ (GeV/c)	$(1-2)$	$(2-3)$	$(3-4)$	$(4-5)$	$(5-7)$
Electron identification	2%	3%	4%	4%	4%
Non-HFE identification	1%	1%	1%	1%	1%
Associated track selection	1%	1%	1%	1%	1%
Electron track selection	1%	1%	1%	1%	1%
Pedestal estimation	6%	9%	9%	5%	5%

Table 4.32: Summary of total systematic uncertainties in away-side sigma assigned for $p_{\mathrm{T}}^{\mathrm{Trigger}}$: 7-16 GeV/$c$ in each $p_{\mathrm{T}}^{\mathrm{assoc}}$ bin for pp collisions at $\sqrt{s} = 5.02$ TeV.

Variables / $p_{\mathrm{T}}^{\mathrm{assoc}}$ (GeV/c)	$(1-2)$	$(2-3)$	$(3-4)$	$(4-5)$	$(5-7)$
Electron identification	6%	6%	6%	6%	6%
Non-HFE identification	2%	2%	2%	2%	2%
Associated track selection	2%	2%	1%	1%	1%
Electron track selection	1%	1%	1%	1%	1%
Pedestal estimation	8%	6%	8%	6%	12%

Table 4.33: Summary of total systematic uncertainties in near-side sigma assigned for $p_{\mathrm{T}}^{\mathrm{Trigger}}$: 7-16 GeV/$c$ in each $p_{\mathrm{T}}^{\mathrm{assoc}}$ bin for p–Pb collisions at $\sqrt{s_{\mathrm{NN}}} = 5.02$ TeV.

Variables / $p_{\mathrm{T}}^{\mathrm{assoc}}$ (GeV/c)	$(1-2)$	$(2-3)$	$(3-4)$	$(4-5)$	$(5-7)$
Electron identification	4%	4%	4%	4%	4%
Non-HFE identification	1%	1%	1%	1%	1%
Associated track selection	3%	3%	3%	3%	3%
Electron track selection	1%	1%	1%	1%	1%
Pedestal estimation	9%	8%	7%	9%	9%

range $-3\sigma_{\mathrm{NS}} < \Delta\varphi < 3\sigma_{\mathrm{NS}}$ and $-3\sigma_{\mathrm{AS}} < \Delta\varphi - \pi < 3\sigma_{\mathrm{AS}}$, rather than using the default bin counting procedure. The overall systematic uncertainty was calculated by taking the maximum variation of the results. The uncertainty from the baseline estimation on the correlation distribution was quoted as absolute numbers that affect all $\Delta\varphi$ bins by the same value. For $4 < p_{\mathrm{T}}^{\mathrm{e}} < 12$ GeV/c, the uncertainty of the NS and AS yields and width varied in the range of 4–9% and 10–11% for pp

Table 4.34: Summary of total systematic uncertainties in away-side sigma assigned for $p_{\mathrm{T}}^{\mathrm{Trigger}}$: 7-16 GeV/$c$ in each $p_{\mathrm{T}}^{\mathrm{assoc}}$ bin for p–Pb collisions at $\sqrt{s_{\mathrm{NN}}} = 5.02$ TeV.

Variables / $p_{\mathrm{T}}^{\mathrm{assoc}}$ (GeV/c)	$(1-2)$	$(2-3)$	$(3-4)$	$(4-5)$	$(5-7)$
Electron identification	3%	3%	3%	3%	3%
Non-HFE identification	1%	1%	1%	1%	1%
Associated track selection	5%	5%	2%	2%	1%
Electron track selection	1%	1%	1%	1%	1%
Pedestal estimation	9%	7%	10%	6%	10%

and p–Pb collisions, respectively.

Similar procedures were applied to estimate the systematic uncertainties from the aforementioned sources on the correlation distribution, NS and AS yields, and widths for $4 < p_{\mathrm{T}}^{\mathrm{e}} < 7\mathrm{GeV}/c$ and $7 < p_{\mathrm{T}}^{\mathrm{e}} < 16\mathrm{GeV}/c$. The uncertainty values were found to be comparable to those obtained for $4 < p_{\mathrm{T}}^{\mathrm{e}} < 12\mathrm{GeV}/c$ in both collision systems.

Table 4.35: Systematic uncertainties of the correlation distribution, the peak yields, and their widths for $4 < p_{\mathrm{T}}^{\mathrm{e}} < 12$ GeV/c in pp collisions. The individual sources of systematic uncertainties depend on the associated particle p_{T}. The values are presented as a range corresponding to the lowest and highest $p_{\mathrm{T}}^{\mathrm{assoc}}$ interval. For the correlation distribution, the systematic uncertainty from the baseline estimation is given as an absolute value, and the total uncertainties from correlated and uncorrelated sources are reported separately.

Source	Correlation distribution	NS yield	AS yield	NS width	AS width
Electron track selection	1%	1%	1%	0%	0%
Electron identification	3–5%	2–4%	3–6%	2–6%	4–7%
Background electron	1%	1%	2%	1%	1%
Associated particle selection	1–2%	1–2%	1–3%	1–3%	1–3%
Mixed-event correction	1%	1%	1%	0%	0%
Fit routine / Baseline estimation	0.001–0.02 (rad^{-1})	5–8%	8–9%	10%	10%
Total (correlated sources)	1–2%				
Total (uncorrelated sources)	3–5%				
Total		6–9%	9–11%	10–12%	11–13%

Table 4.36: Systematic uncertainties of the correlation distribution, the peak yields, and their widths for $4 < p_{\mathrm{T}}^{\mathrm{e}} < 12$ GeV/c in p–Pb collisions. The individual sources of systematic uncertainties depend on the associated particle p_{T}. The values presented as a range corresponding to the lowest and highest $p_{\mathrm{T}}^{\mathrm{assoc}}$ interval. The systematic uncertainty of the correlation distribution from the baseline estimation is given as absolute values. For the correlation distribution, the systematic uncertainty from the baseline estimation is given as an absolute value, and the total uncertainties from correlated and uncorrelated sources are reported separately.

Source	Correlation distribution	NS yield	AS yield	NS width	AS width
Electron track selection	1–2%	1%	1%	1%	1%
Electron identification	2–4%	4%	4%	2–4%	4–5%
Background electron	1%	1%	1%	1%	1%
Associated particle selection	2–3%	2–4%	2–4%	1–4%	2%
Mixed-event correction	1%	1%	1%	0%	0%
Fit routine / Baseline estimation	0.0005–0.02 (rad^{-1})	4–5%	6–7%	11%	11%
Total (correlated sources)	2–3%				
Total (uncorrelated sources)	2–5%				
Total		6–8%	8–9%	11–13%	12%

Chapter 5

Results

This chapter presents the findings of the research study and highlights the outcomes of the azimuthal correlation between heavy flavour hadron decay electrons with charged particle with ALICE at the LHC. Results in this chapter include the analysis performed in section 3 with systematic uncertainties that are calculated in section 4. In this chapter first, we will compare results from pp collisions to p–Pb collisions, then model comparison, and finally, the dependency of correlation distribution on the transverse momentum of heavy flavour hadron decay electrons.

5.1 Comparison of the results in pp and p–Pb collisions

The azimuthal-correlation distributions for $|\Delta\eta| < 1$ with trigger electron in the interval $4 < p_{\mathrm{T}}^{\mathrm{e}} < 12$ GeV/c and for different associated particle p_{T} ranges together with their fit functions are shown in Fig. 5.1 and 5.2 (for selected $p_{\mathrm{T}}^{\mathrm{assoc}}$ ranges) for pp (top panels) and p–Pb (bottom panels) collisions. The correlated systematic uncertainties from the associated particle selection and mixed-event correction are reported as text for each $p_{\mathrm{T}}^{\mathrm{assoc}}$ interval. The baseline is shown by the horizontal green line. The absolute systematic uncertainty of the baseline estimation is shown as a solid box at $\Delta\varphi \sim -2$ rad. The near- and away-side peaks are well described by the von Mises fit function in all $p_{\mathrm{T}}^{\mathrm{assoc}}$ ranges. While the baseline contribution is higher in p–Pb collisions (due to the larger charged-particle multiplicity), its absolute value reduces with increasing $p_{\mathrm{T}}^{\mathrm{assoc}}$ in both pp and p–Pb collisions. As a large fraction of the baseline is from the underlying event processes, the pairs

contributing to it are dominated by low p_{T} particles.

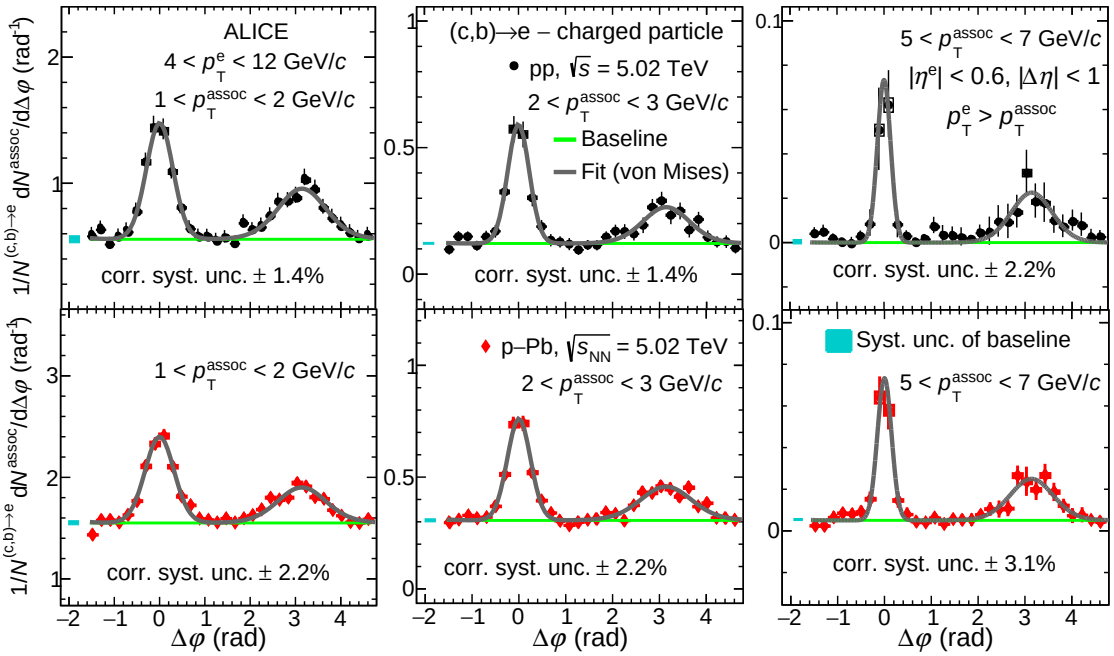

Figure 5.1: The azimuthal-correlation distribution for $4 < p_{\mathrm{T}}^{\mathrm{e}} < 12$ GeV/c fitted with a constant function for the baseline (green line) and von Mises functions for AS and NS peaks (grey curves) for different associated p_{T} ranges in pp collisions at $\sqrt{s} = 5.02$ TeV (top panels) and p–Pb collisions at $\sqrt{s_{\mathrm{NN}}} = 5.02$ TeV (bottom panels). The statistical (uncorrelated systematic) uncertainties are shown as vertical lines (empty boxes). The uncertainties of the baseline estimation are shown as solid boxes at $\Delta\varphi \sim -2$ rad.

To compare the NS and AS peaks of the $\Delta\varphi$ correlation distribution between pp and p–Pb collisions, the baseline-subtracted distributions from the two collision systems are shown together in Fig. 5.3 and 5.4 , for $4 < p_{\mathrm{T}}^{\mathrm{e}} < 12$ GeV/c and for different $p_{\mathrm{T}}^{\mathrm{assoc}}$ ranges. It can be seen that the peak heights of the NS and AS decrease with increasing $p_{\mathrm{T}}^{\mathrm{assoc}}$. A tendency for a more pronounced collimation of the NS peak with increasing $p_{\mathrm{T}}^{\mathrm{assoc}}$ is visible. The profile of the correlation peaks is consistent in pp and p–Pb collisions within the statistical and systematic uncertainties. This indicates that cold-nuclear matter effects do not impact heavy-quark fragmentation and hadronization in the measured p_{T} range, in minimum bias collisions. This observation is consistent with previous measurements of D-meson correlations with charged particles [11, 12].

To perform a quantitative comparison of the correlation peaks between pp and p–Pb collisions, the per-trigger NS and AS peak yields (first row) and widths (third row) are shown in Fig. 5.5, superimposed for the two collision systems, as a

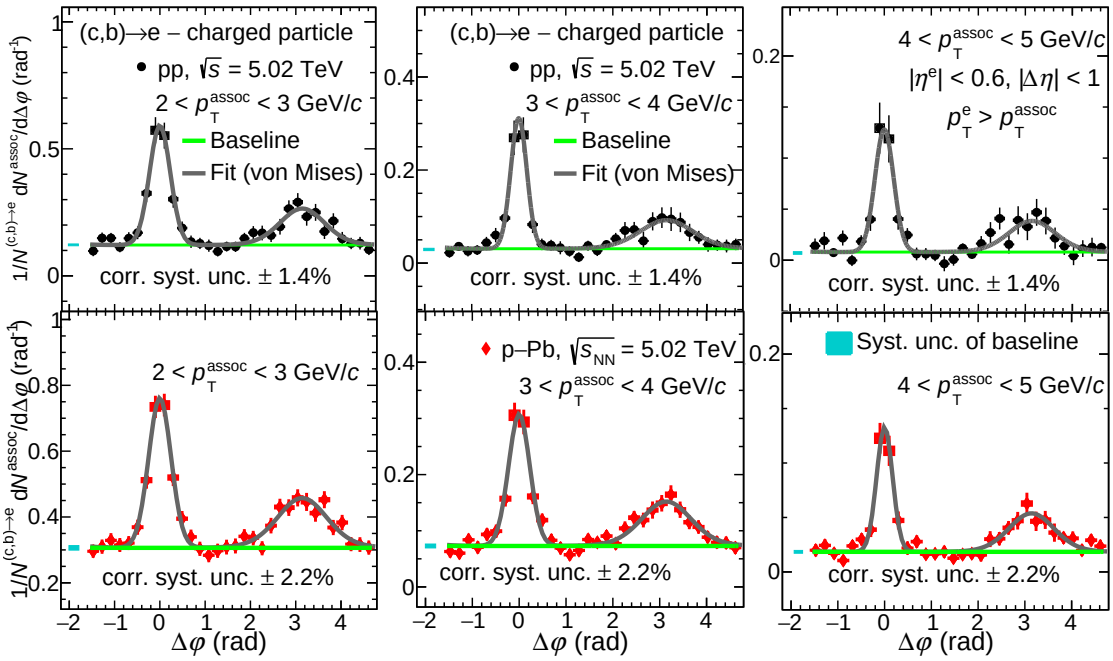

Figure 5.2: The azimuthal-correlation distribution for $4 < p_{\mathrm{T}}^{\mathrm{e}} < 12$ GeV/c fitted with a constant function for the baseline (green line) and von Mises functions for AS and NS peaks (grey curves) for remaining associated p_{T} ranges in pp collisions at $\sqrt{s} = 5.02$ TeV (top panels) and p–Pb collisions at $\sqrt{s_{\mathrm{NN}}} = 5.02$ TeV (bottom panels). The statistical (uncorrelated systematic) uncertainties are shown as vertical lines (empty boxes). The uncertainties of the baseline estimation are shown as solid boxes at $\Delta\varphi \sim -2$ rad.

function of $p_{\mathrm{T}}^{\mathrm{assoc}}$ for $4 < p_{\mathrm{T}}^{\mathrm{e}} < 12$ GeV/c. The ratios between pp and p–Pb yields (second row) and widths (fourth row) are also shown in this figure. The systematic uncertainties on the ratio of the yields and widths were obtained by considering all sources except for the baseline estimation as uncorrelated between pp and p–Pb collisions. The partially correlated uncertainty of the baseline estimation, obtained by using different fit functions, was estimated on the ratio. The total uncertainty was obtained by taking the quadratic sum of the correlated and uncorrelated uncertainties. While the NS and AS yields decrease with increasing $p_{\mathrm{T}}^{\mathrm{assoc}}$ for both pp and p–Pb collisions, the measured yields are consistent within uncertainties between the two collision systems for all the $p_{\mathrm{T}}^{\mathrm{assoc}}$ ranges, as can be seen in the ratio panels of Fig. 5.5.

The decrease in yields with increasing $p_{\mathrm{T}}^{\mathrm{assoc}}$ can be understood considering that, as the heavy quarks have on average a hard fragmentation into heavy-flavor hadrons, it is far more likely that the associated particles accompanying the decay

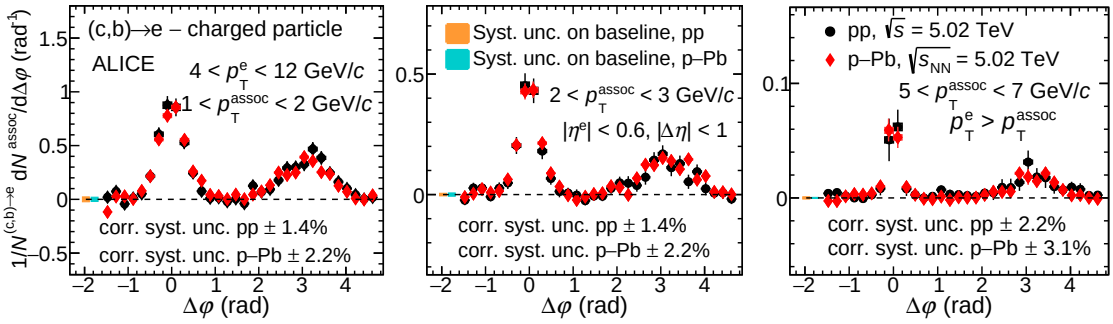

Figure 5.3: Comparison of azimuthal-correlation distribution after baseline subtraction for $4 < p_{\mathrm{T}}^{\mathrm{e}} < 12$ GeV/c and for different associated p_{T} ranges in pp collisions at $\sqrt{s} = 5.02$ TeV and p–Pb collisions at $\sqrt{s_{\mathrm{NN}}} = 5.02$ TeV. The statistical (uncorrelated systematic) uncertainties are shown as vertical lines (empty boxes). The uncertainties of the baseline estimation are shown as solid boxes at $\Delta\varphi \sim -2$ rad.

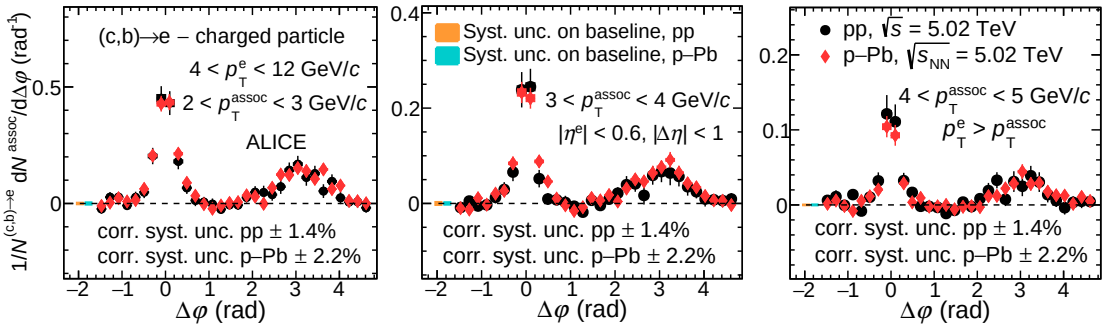

Figure 5.4: Azimuthal-correlation distributions after baseline subtraction for $4 < p_{\mathrm{T}}^{\mathrm{e}} < 12$ GeV/c and for remaining associated p_{T} ranges in pp collisions at $\sqrt{s} = 5.02$ TeV and p–Pb collisions at $\sqrt{s_{\mathrm{NN}}} = 5.02$ TeV. The statistical (systematic) uncertainties are shown as vertical lines (empty boxes). The uncertainties of the baseline are shown as solid boxes at $\Delta\varphi \sim$ -2 rad.

electron are preferentially produced at lower p_{T}, due to the limited energy remaining to the parton. The NS width values tend to decrease with increasing $p_{\mathrm{T}}^{\mathrm{assoc}}$, with a value of about 0.3 at $p_{\mathrm{T}}^{\mathrm{assoc}} = 1$ GeV/c and narrowing to a value of roughly 0.15 at 6 GeV/c, with a significance of about 3σ, for both pp and p–Pb collisions. The significance is calculated on the difference between the widths in the lowest and highest $p_{\mathrm{T}}^{\mathrm{assoc}}$ intervals, taking into account both statistical and systematic uncertainties. The AS widths are independent of $p_{\mathrm{T}}^{\mathrm{assoc}}$, and have a value of about 0.5. The NS peak distribution is closely connected to the fragmentation of the jet containing the trigger particle. The narrowing of the NS width with increasing $p_{\mathrm{T}}^{\mathrm{assoc}}$ indicates that higher p_{T} particles tend to be closer to the jet-axis, whose direction can be approximated by the trigger electron. This is in turn related to

higher p_{T} emissions from the heavy quark being more collinear to it. The AS peak is less sensitive to the fragmentation of a specific parton, as it could have contributions from different production processes, including non back-to-back ones, possibly with different relative fractions for different particle p_{T}. The NS and AS widths are similar in pp and p–Pb collisions, as can be seen in the ratio plots.

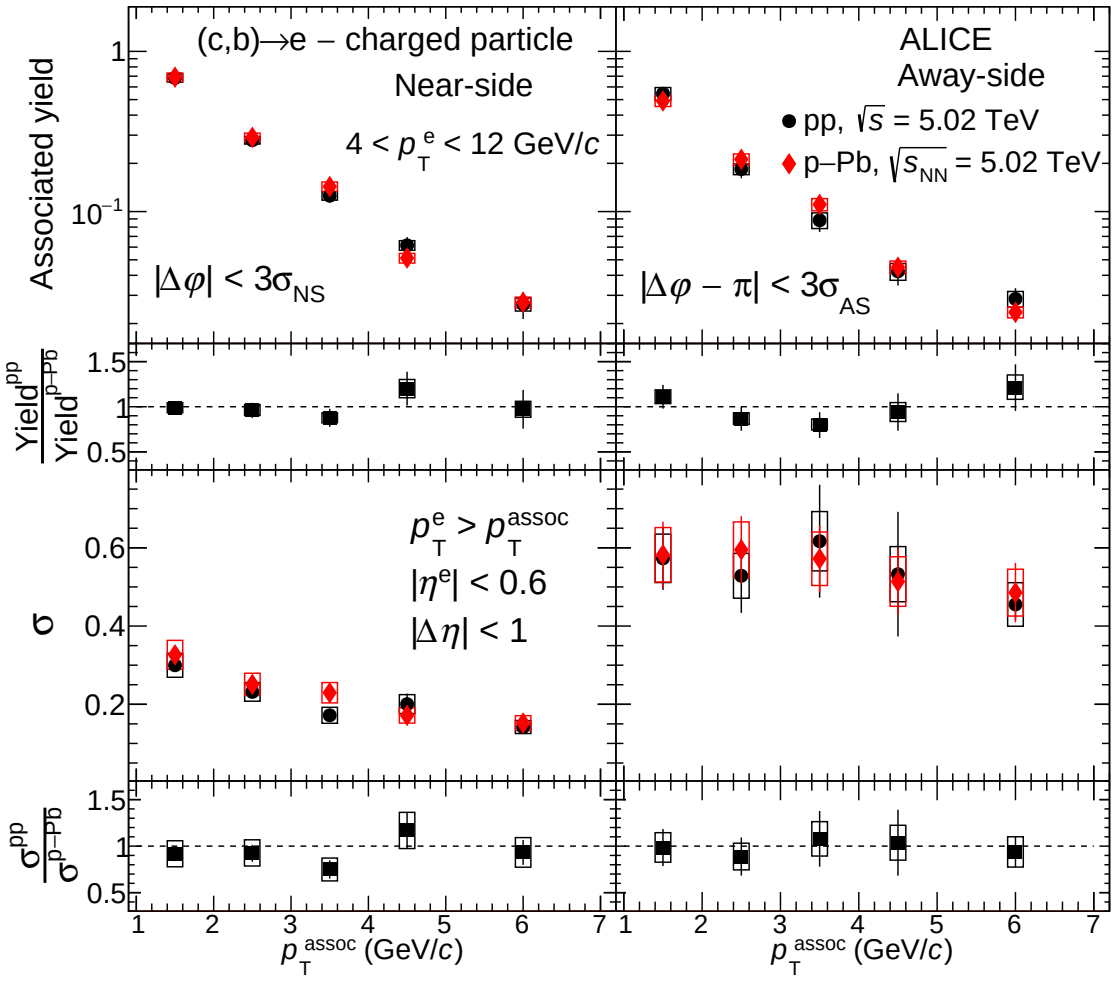

Figure 5.5: Comparison of near- and away-side per-trigger yields (first row) and widths (third row) as a function of $p_{\mathrm{T}}^{\mathrm{assoc}}$ for $4 < p_{\mathrm{T}}^{\mathrm{e}} < 12$ GeV/c in pp collisions at $\sqrt{s} = 5.02$ TeV and p–Pb collisions at $\sqrt{s_{\mathrm{NN}}} = 5.02$ TeV. The ratios between pp and p–Pb yields and widths are shown in the second and fourth row, respectively. The statistical (systematic) uncertainties are shown as vertical lines (empty boxes).

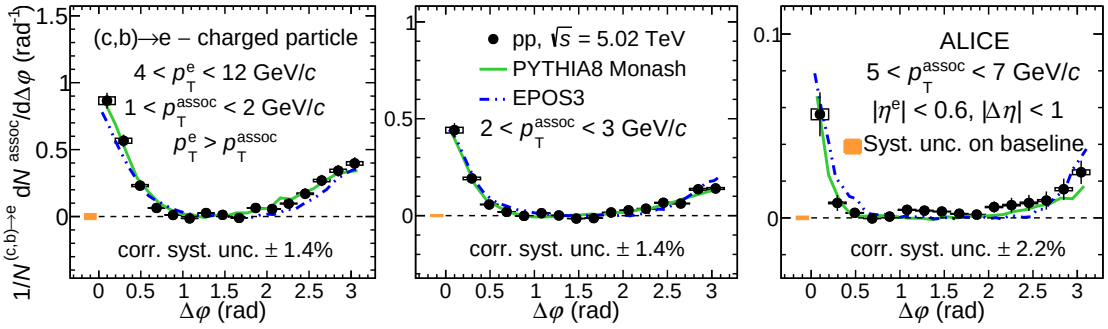

Figure 5.6: Comparison of the azimuthal-correlation distribution with model predictions after baseline subtraction for $4 < p_{\mathrm{T}}^{\mathrm{e}} < 12$ GeV/c in different $p_{\mathrm{T}}^{\mathrm{assoc}}$ ranges in pp collisions at $\sqrt{s} = 5.02$ TeV. The statistical (uncorrelated systematic) uncertainties are shown as vertical lines (empty boxes). The uncertainties of the baseline are shown as solid boxes near $\Delta\varphi \sim 0$ rad.

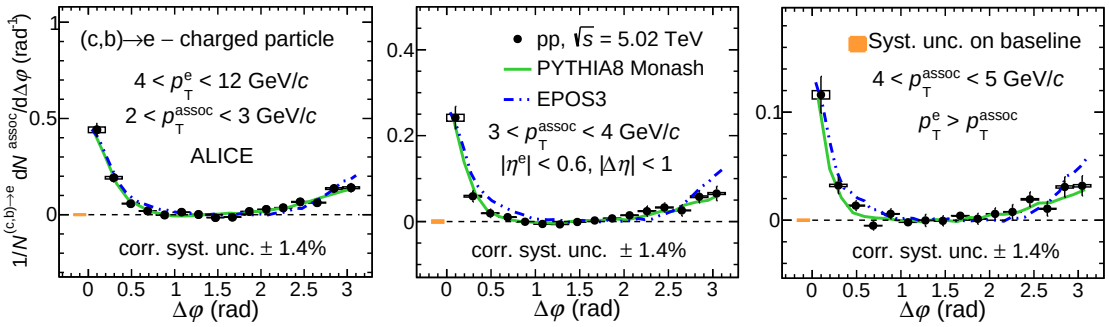

Figure 5.7: Azimuthal-correlation distributions after baseline subtraction for $4 < p_{\mathrm{T}}^{\mathrm{e}} < 12$ GeV/c and for remaining associated p_{T} ranges compared with predictions from PYTHIA8 Monash and EPOS3 in pp collisions at $\sqrt{s} = 5.02$ TeV. The statistical (systematic) uncertainties are shown as vertical lines (empty boxes). The uncertainties of the baseline are shown as solid boxes at $\Delta\varphi \sim 0$ rad.

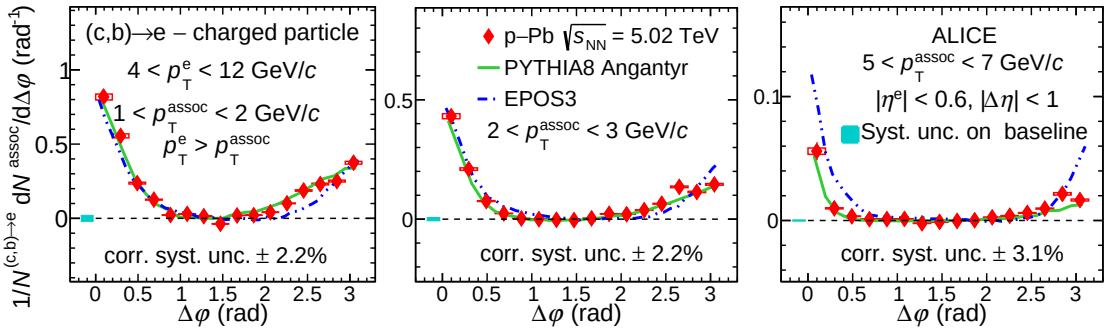

Figure 5.8: Comparison of the azimuthal-correlation distribution with model predictions after baseline subtraction for $4 < p_{\mathrm{T}}^{\mathrm{e}} < 12$ GeV/c in different $p_{\mathrm{T}}^{\mathrm{assoc}}$ ranges in p–Pb collisions at $\sqrt{s_{\mathrm{NN}}} = 5.02$ TeV. The statistical (uncorrelated systematic) uncertainties are shown as vertical lines (empty boxes). The uncertainties of the baseline are shown as solid boxes near $\Delta\varphi \sim 0$ rad.

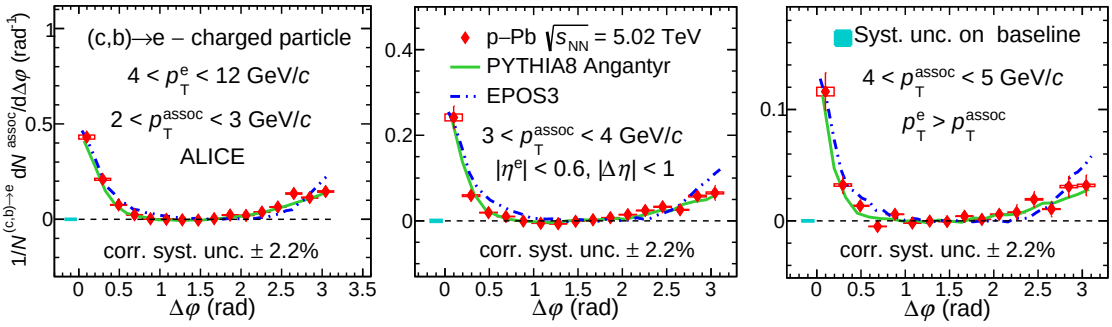

Figure 5.9: Azimuthal-correlation distributions after baseline subtraction for $4 < p_{\mathrm{T}}^{\mathrm{e}} < 12$ GeV/c and for remaining associated p_{T} ranges compared with predictions from PYTHIA8 Angantyr and EPOS3 in p–Pb collisions at $\sqrt{s_{\mathrm{NN}}} = 5.02$ TeV. The statistical (systematic) uncertainties are shown as vertical lines (empty boxes). The uncertainties of the baseline are shown as solid boxes near $\Delta\varphi \sim 0$ rad.

5.2 Comparison with predictions from MC event generators

The near- and away-side peaks of the azimuthal-correlation distribution in pp and p–Pb collisions are compared with predictions from different MC event generators. This allows verifying the implementation of the processes of charm- and beauty-quark production, fragmentation, and hadronization, which have an impact on the observables studied in this paper. The models used for this comparison are PYTHIA8 with the Monash tune [78, 113, 114] and EPOS 3.117 [117, 118]. The prediction of these models for correlations of D mesons with charged particles can be found in Refs. [11, 12]. In this work, the Angantyr [148, 165] model is used to simulate ultra-relativistic p–Pb collisions with the PYTHIA8 event generator. PYTHIA8 does not natively support collisions involving nuclei; this feature is implemented in the Angantyr model, which combines several nucleon−nucleon collisions to build a proton–nucleus (p–A) or nucleus–nucleus (A–A) collision. In this model, some modifications are made over the dynamics of pp collisions. The Angantyr model improves the inclusive definition of collision types of the FRITIOF model [168, 169]. In this model, a projectile nucleon can interact with several target nucleons where one primary collision looks like a typical pp non-diffractive (ND) collision. ND collisions refer to collisions between particles that do not undergo diffractive scattering. Diffractive scattering occurs when a par-

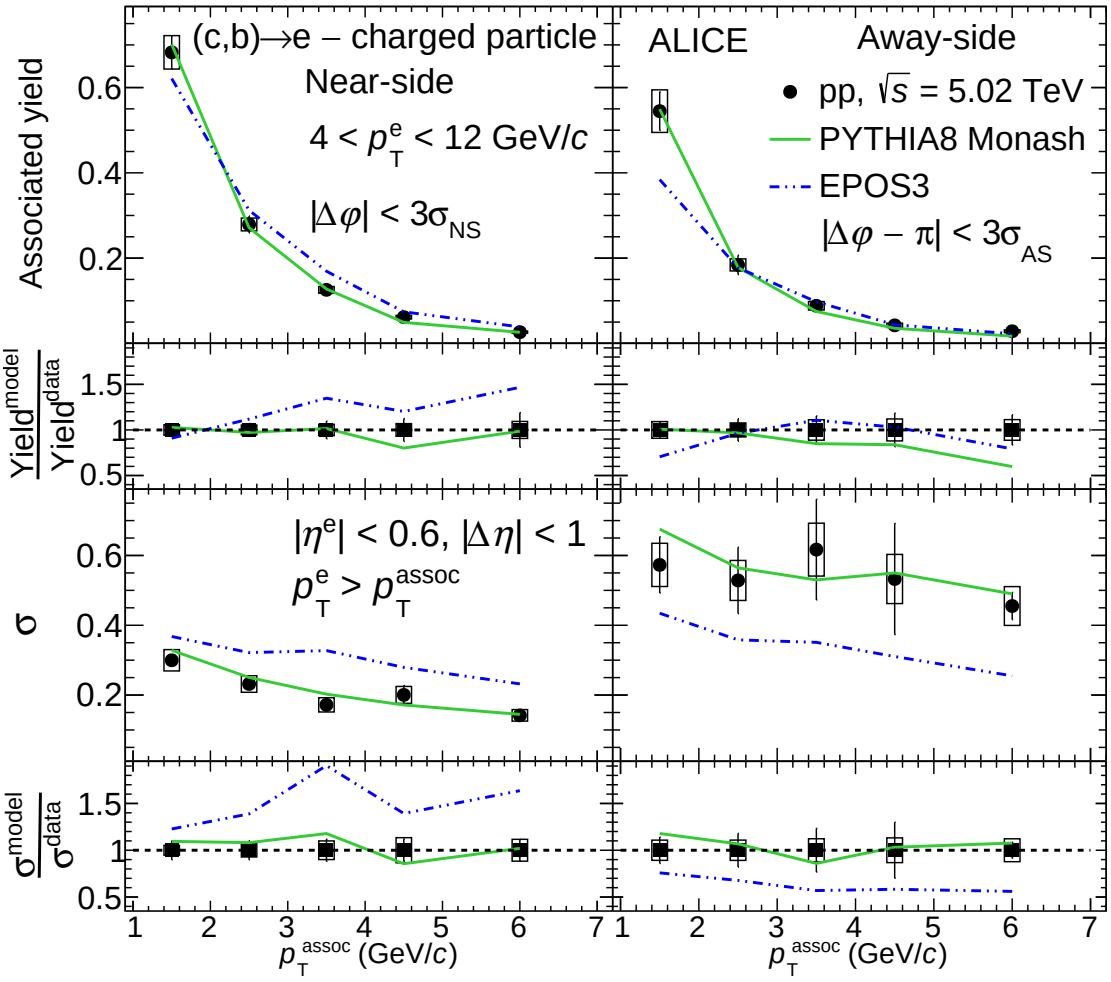

Figure 5.10: Near- and away-side per-trigger yields (first row) and widths (third row) as a function of $p_{\mathrm{T}}^{\mathrm{assoc}}$ for $4 < p_{\mathrm{T}}^{\mathrm{e}} < 12$ GeV/c compared with predictions from PYTHIA8 Monash tune and EPOS3 in pp collisions at $\sqrt{s} = 5.02$ TeV. The ratios between model predictions and data are shown in the second and fourth row for the yields and widths, respectively. The statistical (systematic) uncertainties are shown as vertical lines (empty boxes).

ticle is scattered by an object or target without being absorbed or changing its identity. However, other target nucleons may also undergo ND collisions with the projectile. The Angantyr model treats secondary ND collisions as modified single-diffractive (SD) interactions. For every p–A or A–A collision, nucleons are distributed randomly inside a nucleus according to a Glauber formalism similar to the one described in Ref. [170]. This model is able to correctly reproduce final-state observables of heavy-ion collisions, i.e., multiplicity and p_{T} distributions [171]. As collectivity is not incorporated in this model, its predictions serve as a baseline for studying observables sensitive to collective behavior in p–A and A–A systems.

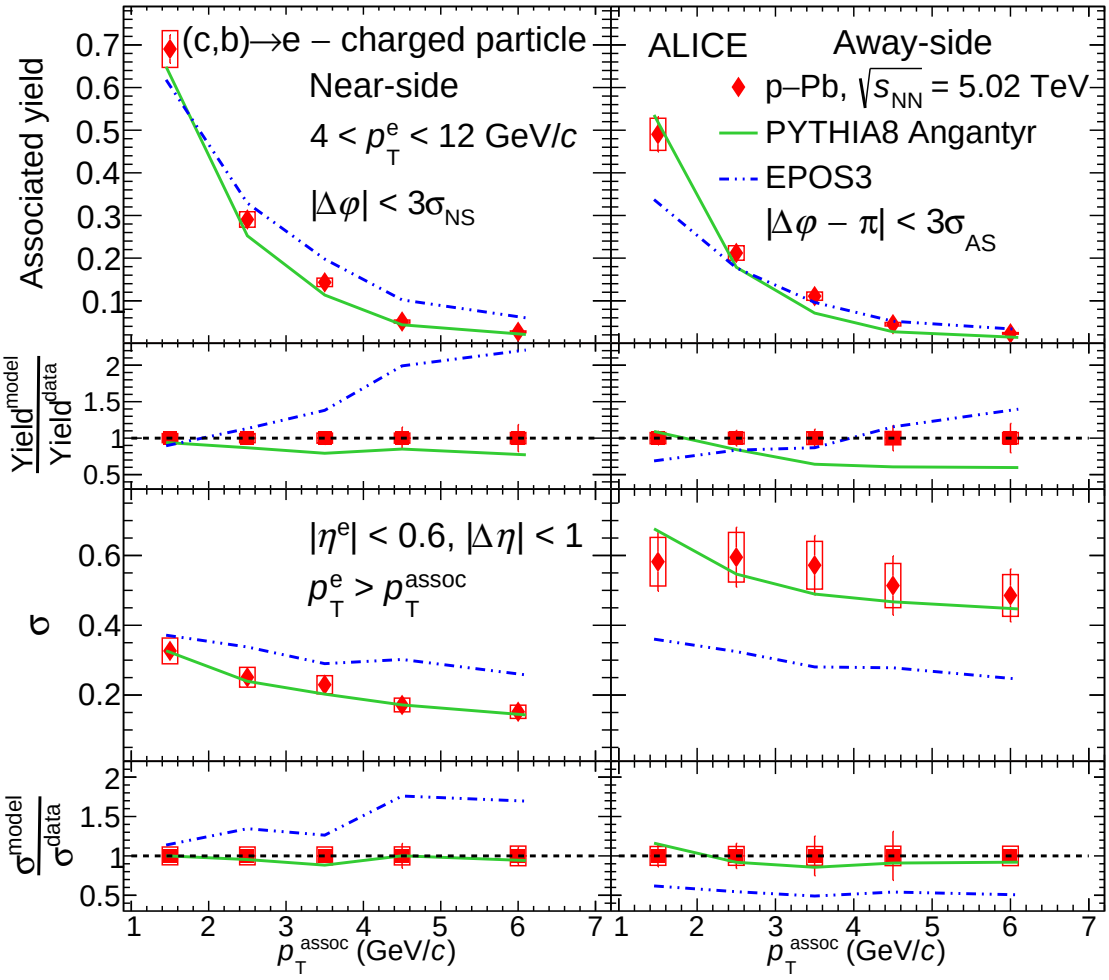

Figure 5.11: Near- and away-side per-trigger yields (first row) and widths (third row) as a function of $p_{\mathrm{T}}^{\mathrm{assoc}}$ for $4 < p_{\mathrm{T}}^{\mathrm{e}} < 12$ GeV/c compared with predictions from PYTHIA8 Angantyr and EPOS3 in p–Pb collisions at $\sqrt{s_{\mathrm{NN}}} = 5.02$ TeV. The ratios between model predictions and data are shown in the second and fourth row for the yields and widths, respectively. The statistical (systematic) uncertainties are shown as vertical lines (empty boxes).

For PYTHIA8 simulations, the correlation distributions for electrons from charm- and beauty-hadron decays are obtained separately, and summed after weighting their relative fractions based on FONLL calculations [64, 119, 172, 173].

The EPOS3 event generator is largely used for the description of ultra-relativistic heavy-ion collisions. It employs a core-corona description of the fireball produced in these collisions: in the "core", its inner part, a quark–gluon plasma is formed, which follows a hydrodynamic behavior, while in the external regions of the "corona" the partons fragment and hadronize independently. A study of radial flow performed with the EPOS3 event generator in proton–proton collisions

at $\sqrt{s} = 7$ TeV [174] has shown that the energy density reached in such collisions is large enough to grant the applicability of the hydrodynamic evolution to the core of the collision.

In the models, the azimuthal correlation function of trigger electrons from charm- and beauty-hadron decays with charged particles is evaluated using the same prescriptions applied for data analysis in terms of kinematic and particle-species selections. The peak properties of the correlation functions are obtained by following the same approach employed in data, i.e., by fitting the distributions with two von Mises functions and a constant term.

In Figs. 5.6, 5.7 and 5.8, 5.9, the baseline-subtracted azimuthal-correlation distribution measured in pp and p–Pb collisions, reflected in the $0 < \Delta\varphi < \pi$ range, is compared with predictions from PYTHIA8 and EPOS3 generators for $4 < p_{\mathrm{T}}^{\mathrm{e}} < 12$ GeV/c in three different $p_{\mathrm{T}}^{\mathrm{assoc}}$ ranges. From this qualitative comparison, both MC generators give a good overall description of the data in all the $p_{\mathrm{T}}^{\mathrm{assoc}}$ intervals, even though the EPOS3 predictions show some deviation from the measured NS and AS peaks in the highest $p_{\mathrm{T}}^{\mathrm{assoc}}$ interval. The peak yields and widths extracted from the measured distribution are also compared with model predictions in Figs. 5.10 and 5.11 for pp and p–Pb collisions, respectively. From here on, PYTHIA8/Angantyr will be used to refer to PYTHIA8 Monash simulations in pp collisions and PYTHIA8 Angantyr simulations in p–Pb collisions together. PYTHIA8/Angantyr simulations provide NS widths decreasing with increasing $p_{\mathrm{T}}^{\mathrm{assoc}}$ consistent with data in both collision systems. The AS widths show a slightly decreasing trend with $p_{\mathrm{T}}^{\mathrm{assoc}}$ that is consistent with data within statistical and systematic uncertainties in both collision systems. The NS and AS yields from PYTHIA8/Angantyr simulations decrease with increasing $p_{\mathrm{T}}^{\mathrm{assoc}}$ and are consistent with data within statistical and systematic uncertainties. The EPOS3 simulations overestimate the NS widths and underestimate the AS widths for all $p_{\mathrm{T}}^{\mathrm{assoc}}$ ranges in pp and p–Pb collisions. The NS and AS yields predicted by the EPOS3 model qualitatively describe the data within statistical and systematic uncertainties in pp collisions. In p–Pb collisions, the NS yield is overestimated at high $p_{\mathrm{T}}^{\mathrm{assoc}}$ while the AS yield is consistent with data within statistical and systematic uncertainties.

5.3 Dependence of the correlation distribution on the $p_{\mathrm{T}}^{\mathrm{e}}$

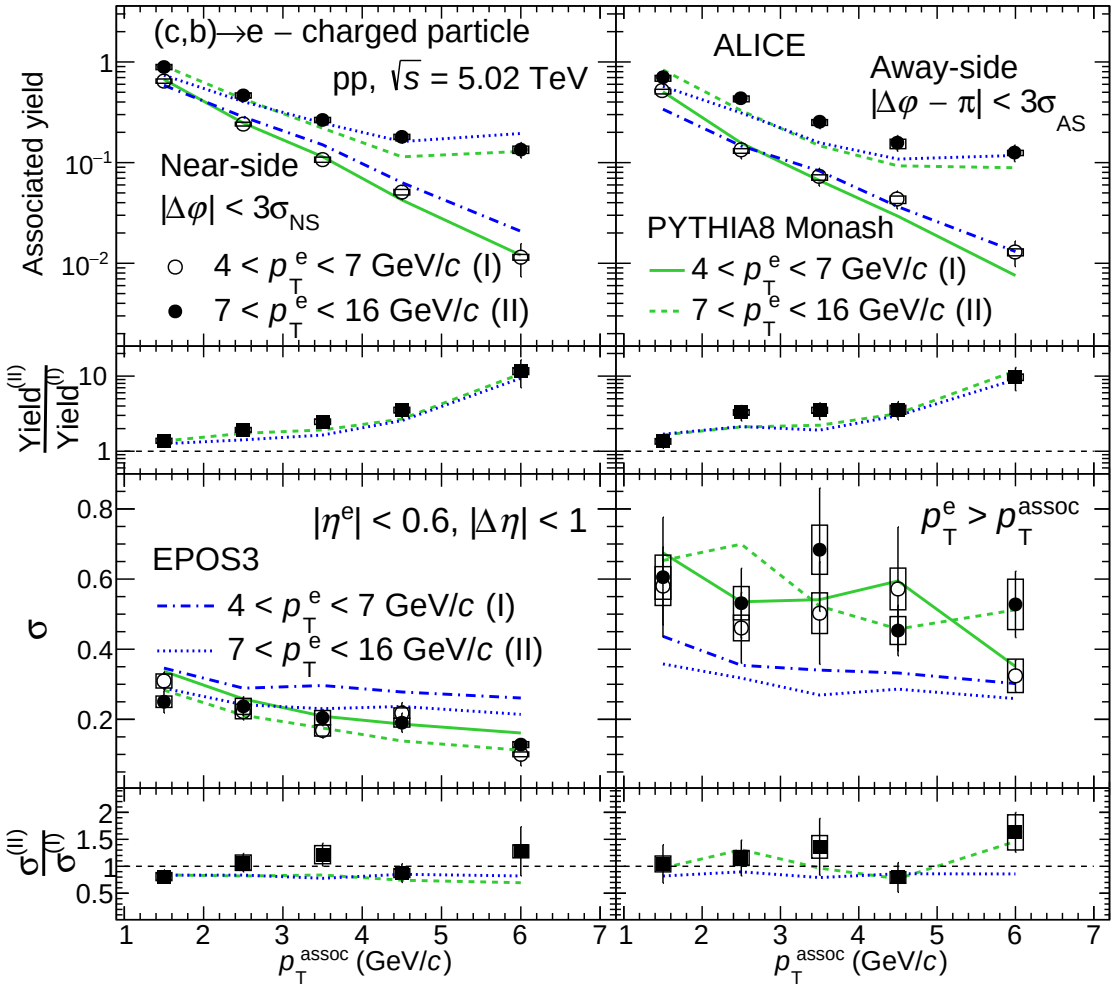

Figure 5.12: Comparison of NS and AS per-trigger yields (first row) and widths (third row) for two $p_{\mathrm{T}}^{\mathrm{e}}$ ranges $4 < p_{\mathrm{T}}^{\mathrm{e}} < 7$ GeV/c and $7 < p_{\mathrm{T}}^{\mathrm{e}} < 16$ GeV/c, as a function of $p_{\mathrm{T}}^{\mathrm{assoc}}$ in pp collisions. The ratios between the $7 < p_{\mathrm{T}}^{\mathrm{e}} < 16$ GeV/c and $4 < p_{\mathrm{T}}^{\mathrm{e}} < 7$ GeV/c yields and widths are shown in the second and fourth rows, respectively. The data are compared with PYTHIA8 Monash and EPOS3 predictions. The statistical (systematic) uncertainties are shown as vertical lines (empty boxes).

The relative fractions of electrons produced by charm- and beauty-hadron decays have a strong p_{T} dependence [119]. The fraction of electrons from beauty-hadron decays at $p_{\mathrm{T}}^{\mathrm{e}} = 4$ GeV/c accounts for about 40% of the HFe yield, increasing to 60–70% for $p_{\mathrm{T}}^{\mathrm{e}} > 8$ GeV/c. A dependence of the correlation distribution on the flavor of the quark from which the trigger electron originates can be expected, due to the different fragmentation of charm and beauty quarks and different fraction

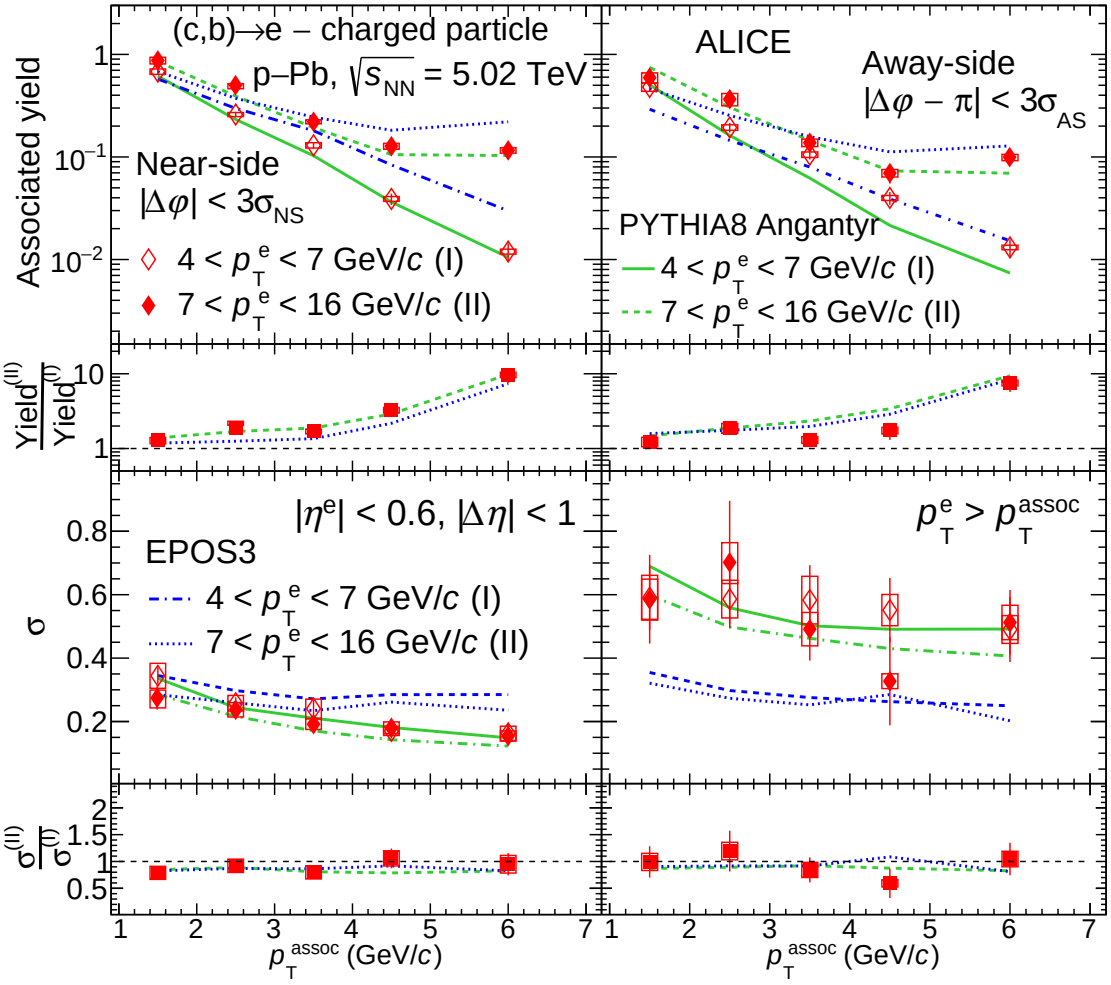

Figure 5.13: Comparison of NS and AS per-trigger yields (first row) and widths (third row) for two p_T^e ranges $4 < p_T^e < 7$ GeV/c and $7 < p_T^e < 16$ GeV/c, as a function of p_T^{assoc} in p–Pb collisions. The ratios between the $7 < p_T^e < 16$ GeV/c and $4 < p_T^e < 7$ GeV/c yields and widths are shown in the second and fourth rows, respectively. The data are compared with PYTHIA8 Angantyr and EPOS3 predictions. The statistical (systematic) uncertainties are shown as vertical lines (empty boxes).

of LO and NLO processes involved in their production. The correlation distributions for electrons from a given quark flavor can also have a trigger-particle p_T dependence due to the different energy of the original parton, and different relative contribution of LO and NLO production processes for the hard scattering producing the parton. These effects are studied by measuring the correlation distributions for trigger electrons in the p_T ranges $4 < p_T^e < 7$ GeV/c and $7 < p_T^e < 16$ GeV/c, where the latter p_T^e range is dominated by electrons from beauty-hadron decays. The azimuthal correlation distributions for these two p_T^e ranges are presented in Figs. 5.15, 5.17, 5.16, and 5.18. It is observed that the shape of peaks

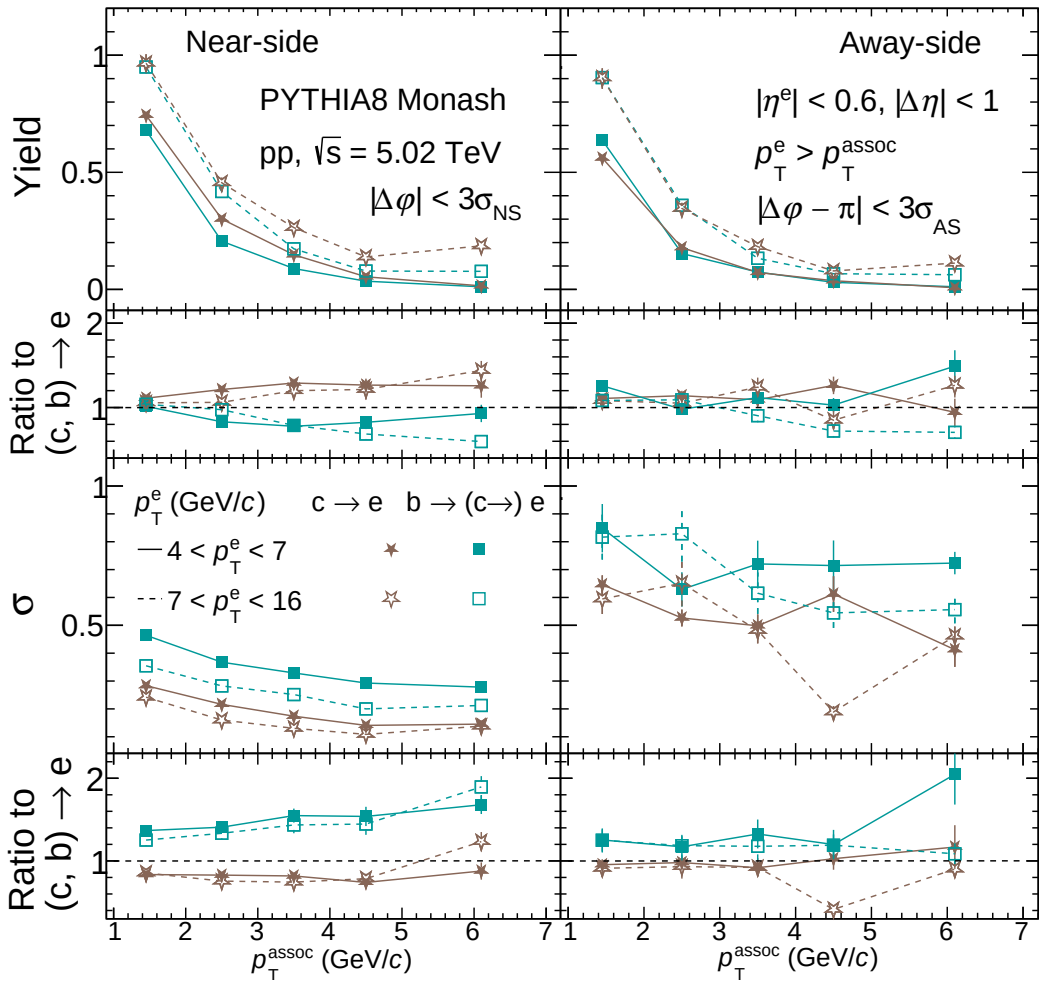

Figure 5.14: Comparison of PYTHIA8 Monash prediction for NS and AS per-trigger yields (first row) and widths (third row) in the two $p_{\mathrm{T}}^{\mathrm{e}}$ ranges $4 < p_{\mathrm{T}}^{\mathrm{e}} < 7$ GeV/c and $7 < p_{\mathrm{T}}^{\mathrm{e}} < 16$ GeV/c for electrons from charm- and beauty-hadron decays, as a function of $p_{\mathrm{T}}^{\mathrm{assoc}}$ in pp collisions. The ratios to c, b $\rightarrow$ e yields and widths are shown in the second and fourth rows, respectively. The statistical uncertainties are shown as vertical lines.

looks the same for both $p_{\mathrm{T}}^{\mathrm{e}}$ ranges, but the peak heights are higher for $7 < p_{\mathrm{T}}^{\mathrm{e}}$ 16 GeV/c compared to $4 < p_{\mathrm{T}}^{\mathrm{e}}$ 7 GeV/c. To study the quantitative effects, NS and AS widths and yields for the two $p_{\mathrm{T}}^{\mathrm{e}}$ intervals are obtained following the same procedure described in Sec. 3.9.

The comparisons of the yields (first row) and widths (third row) for the two $p_{\mathrm{T}}^{\mathrm{e}}$ bins are shown in Figs. 5.12 and 5.13 for pp and p–Pb collisions, respectively. While the NS width values decrease with $p_{\mathrm{T}}^{\mathrm{assoc}}$, they are similar for the two trigger electron p_{T} ranges. The AS widths are also observed to be similar for the two trigger electron p_{T} ranges and to have an almost flat trend with $p_{\mathrm{T}}^{\mathrm{assoc}}$. It should be noted that the kinematic bias induced due to the condition of $p_{\mathrm{T}}^{\mathrm{assoc}} < p_{\mathrm{T}}^{\mathrm{e}}$ affects

the correlation distributions for the two trigger electron p_{T} ranges differently. While none of the correlation distributions for higher $p_{\mathrm{T}}^{\mathrm{e}}$ interval are affected by the bias, the distributions for $4 < p_{\mathrm{T}}^{\mathrm{e}} < 7$ GeV/c and $4 < p_{\mathrm{T}}^{\mathrm{assoc}} < 7$ GeV/c would miss some associated particles because of the selection.

The per-trigger NS and AS yields are systematically higher for the $7 < p_{\mathrm{T}}^{\mathrm{e}} < 16$ GeV/c range compared to the values obtained for $4 < p_{\mathrm{T}}^{\mathrm{e}} < 7$ GeV/c, for both pp and p–Pb collisions. The ratio between the $7 < p_{\mathrm{T}}^{\mathrm{e}} < 16$ GeV/c and $4 < p_{\mathrm{T}}^{\mathrm{e}} < 7$ GeV/c yields is shown in the second row of Figs. 5.12 and 5.13. It can be observed that the yield is higher for the higher $p_{\mathrm{T}}^{\mathrm{e}}$ interval, and the ratio increases from 1.3 at low $p_{\mathrm{T}}^{\mathrm{assoc}}$ to ~ 10 in the highest $p_{\mathrm{T}}^{\mathrm{assoc}}$ interval, for both pp and p–Pb collisions. This can be explained by considering that higher-p_{T} electrons are typically produced by more energetic heavy quarks, and the additional parton energy on average leads to a larger number of associated fragmentation particles.

The NS and AS yields and widths of the correlation distributions as a function of $p_{\mathrm{T}}^{\mathrm{assoc}}$ for the two $p_{\mathrm{T}}^{\mathrm{e}}$ ranges are compared with PYTHIA8/Angantyr and EPOS3 MC simulations for pp and p–Pb collisions. The PYTHIA8/Angantyr predictions describe the data within uncertainties for both $p_{\mathrm{T}}^{\mathrm{e}}$ ranges. The NS width trend from EPOS3 is slightly flatter as a function of $p_{\mathrm{T}}^{\mathrm{assoc}}$ compared to that of data, while the model provides NS and AS yields consistent with data for both $p_{\mathrm{T}}^{\mathrm{e}}$ intervals. Similar to what was observed for $4 < p_{\mathrm{T}}^{\mathrm{e}} < 12$ GeV/c, the NS width is overestimated, while the AS width is underestimated compared to data for both $p_{\mathrm{T}}^{\mathrm{e}}$ ranges. The ratio of the yields and widths of the two $p_{\mathrm{T}}^{\mathrm{e}}$ ranges are well described by both MC event generators.

To understand the effect of the different charm and beauty fragmentation on the observed $p_{\mathrm{T}}^{\mathrm{e}}$ dependence, the correlation distributions were obtained for electrons from charm- and beauty-hadron decays separately for the two $p_{\mathrm{T}}^{\mathrm{e}}$ intervals using PYTHIA8 MC simulations. The NS and AS yields and widths of the correlation distributions for electrons from charm- and beauty-hadron decays, and their ratios to the combined ones (HFe), are shown in Fig. 5.14. For both $p_{\mathrm{T}}^{\mathrm{e}}$ intervals, the NS yields for trigger electrons from beauty-hadron decays are lower than those from charm-hadron decays, by about 5% for the first $p_{\mathrm{T}}^{\mathrm{assoc}}$ interval, with a

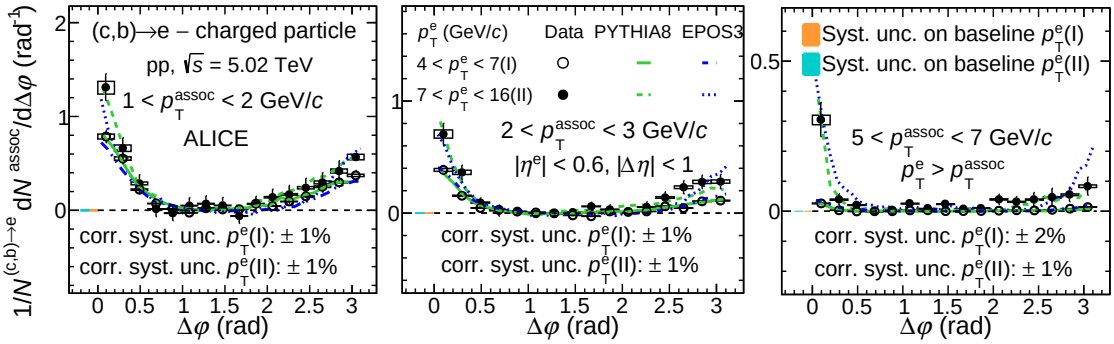

Figure 5.15: Azimuthal-correlation distributions after baseline subtraction for two $p_{\mathrm{T}}^{\mathrm{e}}$ intervals, $4 < p_{\mathrm{T}}^{\mathrm{e}} < 7$ GeV/c and $7 < p_{\mathrm{T}}^{\mathrm{e}} < 16$ GeV/c , and for different associated p_{T} ranges within $1 < p_{\mathrm{T}}^{\mathrm{assoc}} < 7$ GeV/c compared with predictions from PYTHIA8 Monash and EPOS3 in pp collisions at $\sqrt{s} = 5.02$ TeV. The statistical (systematic) uncertainties are shown as vertical lines (empty boxes). The uncertainties of the baseline are shown as solid boxes at $\Delta\varphi \sim 0$ rad.

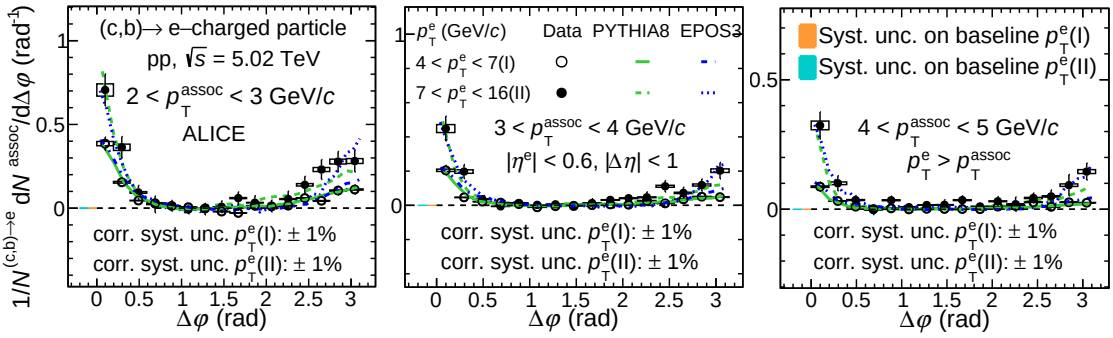

Figure 5.16: Azimuthal-correlation distributions after baseline subtraction for two $p_{\mathrm{T}}^{\mathrm{e}}$ intervals, $4 < p_{\mathrm{T}}^{\mathrm{e}} < 7$ GeV/c and $7 < p_{\mathrm{T}}^{\mathrm{e}} < 16$ GeV/c, and for remaining associated p_{T} ranges compared with predictions from PYTHIA8 Monash and EPOS3 in pp collisions at $\sqrt{s} = 5.02$ TeV. The statistical (systematic) uncertainties are shown as vertical lines (empty boxes). The uncertainties of the baseline are shown as solid boxes at $\Delta\varphi \sim 0$ rad.

tendency for an increased difference for larger $p_{\mathrm{T}}^{\mathrm{assoc}}$, about 40% for the last $p_{\mathrm{T}}^{\mathrm{assoc}}$ range. This can be expected due to the harder fragmentation of beauty quarks to beauty hadrons compared to that of charm quarks, with less energy remaining for the production of other particles in the parton shower. This indicates that the yield increase at higher $p_{\mathrm{T}}^{\mathrm{e}}$ observed in Figs. 5.12 and 5.13 is largely due to the higher energy of the initial heavy quark. The NS and AS widths of the correlation distributions decrease with increasing $p_{\mathrm{T}}^{\mathrm{e}}$ for both charm- and beauty-hadron decays, but the widths for electrons from beauty-hadron decays are wider than for electrons from charm-hadron decays for both $p_{\mathrm{T}}^{\mathrm{e}}$ intervals. These two opposing

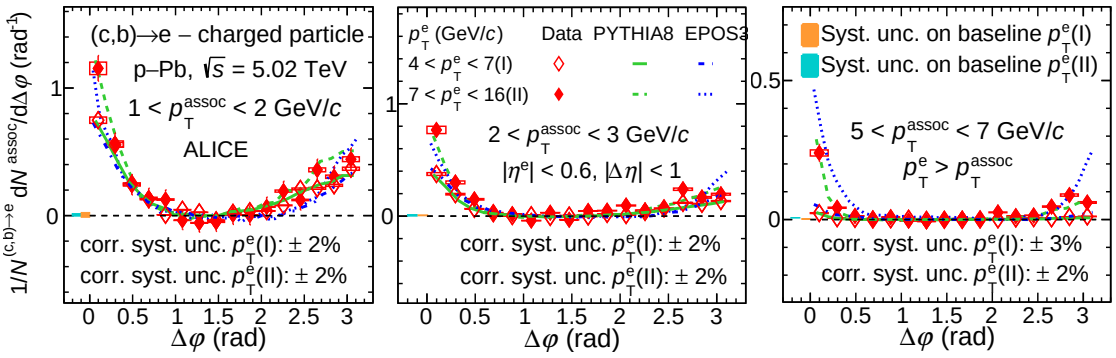

Figure 5.17: Azimuthal-correlation distributions after baseline subtraction for two $p_{\mathrm{T}}^{\mathrm{e}}$ intervals, $4 < p_{\mathrm{T}}^{\mathrm{e}} < 7$ GeV/c and $7 < p_{\mathrm{T}}^{\mathrm{e}} < 16$ GeV/c, and for different associated p_{T} ranges within $1 < p_{\mathrm{T}}^{\mathrm{assoc}} < 7$ GeV/c compared with predictions from PYTHIA8 Angantyr and EPOS3 in p–Pb collisions at $\sqrt{s_{\mathrm{NN}}} = 5.02$ TeV. The statistical (systematic) uncertainties are shown as vertical lines (empty boxes). The uncertainties of the baseline are shown as solid boxes at $\Delta\varphi \sim 0$ rad.

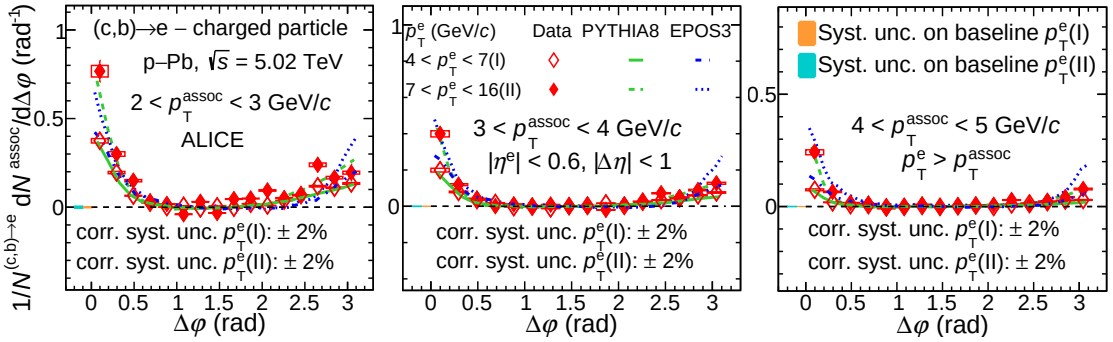

Figure 5.18: Azimuthal-correlation distributions after baseline subtraction for two $p_{\mathrm{T}}^{\mathrm{e}}$ intervals, $4 < p_{\mathrm{T}}^{\mathrm{e}} < 7$ GeV/c and $7 < p_{\mathrm{T}}^{\mathrm{e}} < 16$ GeV/c, and for remaining associated p_{T} ranges compared with predictions from PYTHIA8 Angantyr and EPOS3 in p–Pb collisions at $\sqrt{s_{\mathrm{NN}}} = 5.02$ TeV. The statistical (systematic) uncertainties are shown as vertical lines (empty boxes). The uncertainties of the baseline are shown as solid boxes at $\Delta\varphi \sim 0$ rad.

effects lead to similar widths for the two $p_{\mathrm{T}}^{\mathrm{e}}$ intervals in Figs. 5.12 and 5.13.

Chapter 6

Phenomenology using PYTHIA8

Although experiments are essential for studying particle physics, they often have limitations due to technical constraints and statistics. Therefore, we use simulations to supplement experimental results and gain deeper insights into the behavior of particles.

In this chapter, we aimed to establish the PYTHIA8 Angantyr for heavy-ion collisions, and then we will proceed to study the fragmentation of heavy flavors using two particle azimuthal correlation. PYTHIA8 Angantyr event generator is commonly used in high-energy physics for simulations, particularly for the study of heavy-ion collisions. By simulating high-energy collisions, one can study the behavior of particles in a controlled environment, which can help improve our understanding of the underlying physics.

In a pp collision, more than one distinct hard-parton interaction can occur, and proton remnants can also scatter again on each other. Such processes are called multi-parton interactions (MPI) and are responsible for the production of a large fraction of the particles. The MPI implementation used in PYTHIA8 [114] (which also drives the MPI process in POWHEG+PYTHIA8 simulations [175]), charm-quark production can occur not only from the first (hardest) hard scattering but also from hard processes in the various MPI occurring in the collisions, ordered with decreasing hardness. There is also some correlation between FSR+ISR and MPI processes since initial- and final-state radiations are generated from all the parton interactions occurring in the collision and are thus enhanced in the presence of MPI.

An initial and important observable is the multiplicity distribution

($\mathrm{d}N_{\mathrm{ch}}/d\eta$) of the charged particles, which is essential to extract the properties of produced particles and their interactions [176]. Such distributions in a particular pseudorapidity range were measured in the CERN proton anti-proton ($\mathrm{p\overline{p}}$) collider experiments in 1980's [177–180]. These measurements provide information on the energy density and centrality of the colliding system. The centrality is directly related to the initial overlap region geometry, which correspond to the number of participating nucleons and binary collisions[181].

For the final-state charged particles, the rapidity (y) or pseudorapidity (η) and transverse momentum (p_{T}) spectra are known to reflect the degrees of longitudinal extension and transverse excitation of the interacting system, respectively[103, 182]. Distributions in low p_{T} ranges let us inspect the transverse excitation and soft processes, whereas higher p_{T} corresponds to hard scattering processes. In low-energy collisions, one can neglect hard processes, as most of the contribution comes from soft processes. At the high center of mass energies, hard processes have finite contribution albeit, the soft processes are predominant [183]. From the final state charged particle p_{T} spectra, one can extract information about the thermal nature of the interacting system [184, 185], and can comment on the formation and characteristic properties of the formed matter. According to the Maxwell-Boltzmann distribution law, the p_{T} spectra are related to the temperature of the system formed in these collisions. The N_{ch} of charged particles formed in ultra-relativistic collisions also depends on the system's temperature and density. Since most of the final state charged particles are part of a locally thermalized medium, the mean transverse momentum $\langle p_{\mathrm{T}} \rangle$ distribution vs. N_{ch} is expected to be more or less flat in heavy-ion systems like Pb–Pb at high N_{ch}. The contributions at lower N_{ch} are mostly from the peripheral collisions where a QGP is less likely to be produced.

The ratios of yields of identified hadrons are important to understand the mechanism of hadron production. The ratio of proton to pion (p/π) and kaon to pion (K/π) characterize the relative baryon and meson production, respectively. Additionally, K/π, Λ/π, Σ^0/π, Ξ^0/π, and Ω/π ratios represent the strangeness production at higher multiplicities, indicating a universal underlying dynamics in hadron production for different quark-gluon final states. Strangeness enhancement

is proposed as a signature of QGP formation in heavy-ion collisions [109, 186, 187] because of the faster equilibration of strangeness production processes in a QGP than any other process in a hadron gas [188, 189]. This is observed to be more prominent for multi-strange hadrons [25]. The production mechanism of strange hadrons provides a way to investigate the properties of the hot QCD matter.

Another essential medium characteristic is anisotropic flow, considered the proof of collective behavior of partons and hadrons[102, 190, 191]. In a heavy-ion collision, the hydrodynamic expansion is a consequence of the transverse pressure gradient. This transverse flow shifts the produced particles to higher momenta, and due to the higher gain in momenta of heavy particles from flow velocity, the increment is more for heavier particles. This effect is seen commonly for heavy-ion systems and even high multiplicity pp and p–Pb collisions [25].

Other than light-flavours, this section also explores heavy-flavours. The heavy-flavour hadron production is sensitive to the charm and bottom fragmentation functions and to the hadronization mechanisms of these heavy-flavour hadrons [192, 193]. These heavy quarks hadronize on a shorter time scale as they traverse the medium. This phenomenon can lead to a modification in the fragmentation function of the heavy quarks. In order to quantify the medium effects, studies of high-p_{T} jet fragmentation are done via angular correlations of heavy flavor particles in heavy-ion collisions [13, 194]. Azimuthal angular correlation study is an effective tool for studying jet events. A jet event can consist of atleast a single jet, the particles from which will produce a large correlation at $\Delta\varphi = 0$, or a back-to-back di-jet in which the particles will produce a correlation at $\Delta\varphi = \pi$. The correlation function is obtained by correlating each trigger particle with the associated charged particle. These correlations appear as peaks in a $\Delta\varphi$ distribution, generally known as the "near-side" ($\Delta\varphi = 0$) and "away-side" ($\Delta\varphi = \pi$) peaks.

The recent measurement of angular correlations between D mesons and charged particles by the STAR collaboration shows a significant modification of the near-side peak width and associated yield, which increases from peripheral to central Au–Au collisions [195]. Similar measurements were later carried out

by LHC, which investigated the possible modifications in jet properties due to the medium effects [196]. The measurements show suppression for the away-side peak, suggesting energy loss of the recoil-jet parton traversing through the medium. The amount of suppression can be quantified by the near- and away-side yield ratios taken for p–Pb and Pb–Pb systems over pp where medium effects are not present. We inspect the contribution of MPI and various CR phenomena with PYTHIA8+Angantyr [148] in the regime of perturbative QCD.

In this section, we have explored all the above-mentioned aspects of particle production and fragmentation using PYTHIA8 with the Angantyr model. The Angantyr model is the heavy-ion extension of the PYTHIA8, extensively used for pp collisions. The aim of this study is to see the possibility of using the Angantyr model for heavy-ion collisions.

6.1 Dynamics of particle production in Pb–Pb collisions at $\sqrt{s_{NN}} = 2.76$ TeV using PYTHIA8 Angantyr model

We have generated around 2 million events in Pb–Pb at $\sqrt{s_{\rm NN}}$= 2.76 TeV. The inelastic, non-diffractive component of the total cross-section for all soft QCD processes is used with the switch `SoftQCD:all = on` with MPI based scheme of color reconnection (`ColorReconnection:mode(0)`). For string shoving, under the rope hadronization framework(`Ropewalk:RopeHadronization = on`), we switch string shoving via `Ropewalk:doShoving = on` and turn off flavour ropes by `Ropewalk:doFlavour = off`. The classes based on charged particle multiplicities ($N_{\rm ch}$) have been chosen within the pseudorapidity window of $-0.8 < \eta < 0.8$ to match the acceptance of the TPC detector in ALICE [102]. The events generated using these cuts are divided into nine multiplicity classes, each class containing 10% of total events except the first two classes, which contain 5% of total events as used in [102]. The $N_{\rm ch}$ classes corresponding to different centralities are tabulated in TABLE 6.1. Heavy strange particles are chosen from their specific decay channels and PDG codes.

Table 6.1: Centrality classes and the corresponding charged particle multiplicities ($N_{\rm ch}$) in PYTHIA8+Angantyr with MPI+CR and string shoving in Pb–Pb collisions at $\sqrt{s_{\rm NN}} = 2.76$ TeV.

S.No.	Centrality (%)	MPI+CR	Shoving
I	0-5	2314-3050	2117-2900
II	5-10	1947-2314	1782-2117
III	10-20	1387-1947	1270-1782
IV	20-30	967-1387	885-1270
V	30-40	644-967	590-885
VI	40-50	399-644	367-590
VII	50-60	224-399	205-367
VIII	60-70	108-224	99-205
IX	70-80	43-108	39-99

Table 6.2: Mean and RMS of charged particle multiplicity in different PYTHIA8 tunes in Pb–Pb collisions at $\sqrt{s_{\rm NN}} = 2.76$ TeV.

	MPI+CR	CR-off	MPI-off	(MPI+CR)-off	Shoving
Mean	704.1	882.8	276.6	276.6	647.6
RMS	759.5	961.2	274.3	274.3	697.8

The charged-particle multiplicity distributions for different PYTHIA8 tunes within $|\eta| < 0.8$) are shown in FIG. 6.1. To see the effect of different PYTHIA tunes, we consider the following configurations: MPI with/without CR, No MPI, and both MPI and CR off and string shoving. It is observed that results from MPI+CR and string shoving tunes are compatible with ALICE data. MPI without CR overestimates, whereas the tune without MPI is seen to underestimate our results. We also observe that there is no effect of CR if MPI is off. The particle production increases with MPI due to inter-partonic interactions; on the other hand, when turning CR off, particle production increases. In the color reconnection (CR) scheme, the string lengths are reduced; in consequence, when CR is kept on, particle production lessens [14]. Turning MPI off removes the strings between the partons. As a result, we do not observe any effect of CR. String shoving

shows the best agreement with the data among all the tunes. The fragmentation of longer strings leads to higher particle production. To quantify the effect of the tunes used, the mean and RMS of the multiplicity distributions are measured and reported in TABLE 6.2. The mean for MPI+CR is around 2.5 times larger without MPI and around 3.2 times larger without CR compared to without MPI. A similar comparison can be made for the RMS values between these settings. For MPI+CR turned off, we report similar values for mean and RMS, which confirms our statement made earlier. The results from string shoving are closer than any other tune to ALICE data. This is accredited to the higher effective length of the color ropes, leading to higher particle production via fragmentation.

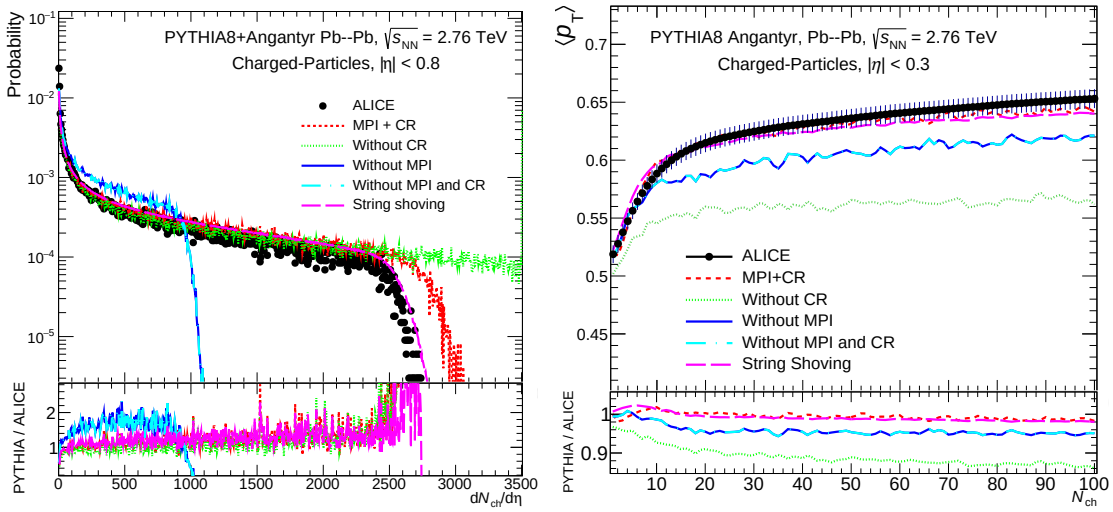

Figure 6.1: (Color Online) (Left) Multiplicity distribution of charged particles from PYTHIA8 Angantyr with different tunes and ALICE data. (Right) $\langle p_{\mathrm{T}} \rangle$ distribution vs. charged-particle multiplicity in different PYTHIA8 tunes and ALICE data. The lower panels show the ratio of PYTHIA Angantyr predictions over data for the different configurations considered in Pb–Pb collisions at $\sqrt{s_{\mathrm{NN}}} =$ 2.76 TeV.

By observing different tunes in FIG. 6.1 (Left), we can conclude that with MPI and CR mode of hadronization and hadronization via string shoving in rope hadronization framework are favorable settings to describe ALICE data [102]. We also observed similar results after comparing $\langle p_{\mathrm{T}} \rangle$ distribution as a function of charged-particle multiplicity using simulated PYTHIA8 Angantyr and experimental data, as shown in FIG. 6.1 (Right). Distributions obtained from PYTHIA8 are scaled with a constant (1.138) factor for better visualization and to compare the slope of different distributions with data [197]. The $\langle p_{\mathrm{T}} \rangle$ distributions with

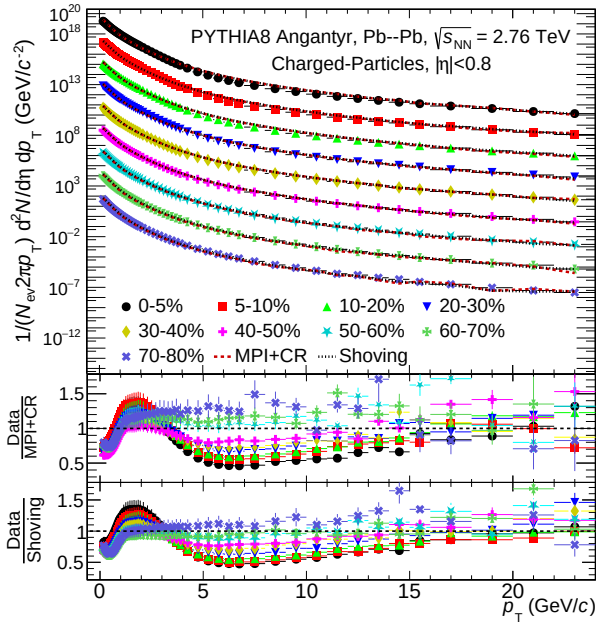

Figure 6.2: (Color Online) Charged-particle p_{T} spectra in nine centrality classes described in TABLE 6.1 from PYTHIA Angantyr and ALICE data. The middle and lower panels represent the deviation of PYTHIA Angantyr predictions from MPI+CR and string shoving, respectively, with data in Pb–Pb collisions at $\sqrt{s_{\mathrm{NN}}} = 2.76$ TeV.

MPI+CR and string shoving describe the data very well, even without hydrodynamics. $\langle p_{\mathrm{T}} \rangle$ with MPI off (or MPI and CR off) describe data below $N_{\mathrm{ch}} = 10$ very well but deviates at higher values, becoming almost flat at high multiplicities. This is probably due to the large production of low multiplicity events when MPI is kept off. A similar trend is seen for CR turned off; however, the ratio of $\langle p_{\mathrm{T}} \rangle$ over data decreases as we go to higher values in multiplicity, as reconnection occurs in such a way that the strings between partons are as small as possible. This attribute is credited to CR, where a correlation between N_{ch} and $\langle p_{\mathrm{T}} \rangle$ can be seen [198]. Preceding hadronization, strings fuse to form high p_{T} hadrons. With CR off, fewer strings fuse to form hadrons during hard scatterings, explaining the increment of $\langle p_{\mathrm{T}} \rangle$ at higher multiplicities. For hadronization via string shoving, the trend for $\langle p_{\mathrm{T}} \rangle$ is very close to MPI+CR tune, describing the data very well. This concludes that MPI+CR and string shoving frameworks have similar outcomes when it comes to particle production.

To further check the compatibility of simulated data, we compare the p_{T} spectra of final state charged particle with ALICE measurements in different centrality classes within experimental kinematic selections, which is shown in FIG. 6.2.

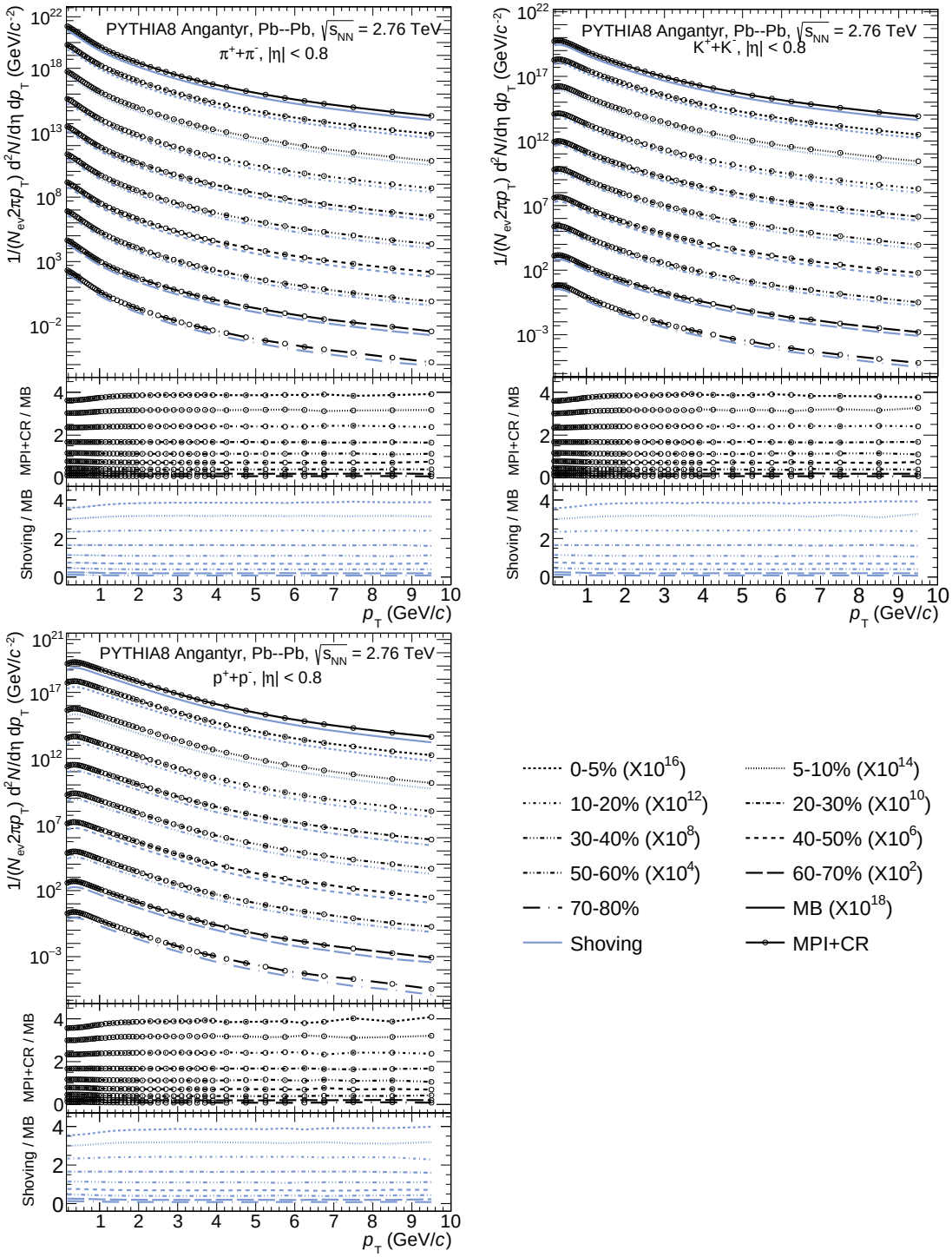

Figure 6.3: (Color Online) p_{T} spectra of identified charged-particles ($\pi^{\pm}$, $\mathrm{K}^{\pm}$, $p(\bar{p})$) in various centrality classes. The middle and lower panels show the ratios for each centrality class to MB for MPI+CR and string shoving, respectively in Pb–Pb collisions at $\sqrt{s_{\mathrm{NN}}} = 2.76$ TeV.

The p_{T} spectra of each centrality class are scaled to the slope with ALICE measurements for clearer visualization and comparison. From the lower panels of FIG. 6.2, it is observed that the experimental to simulated data is comparable

within statistical uncertainties.

With the assurance of the quality of the simulated data discussed above, we now move on to study the transverse momentum spectra of identified particles, p_{T} integrated yield of identified and strange particles, and particle ratios with PYTHIA8+Angantyr.

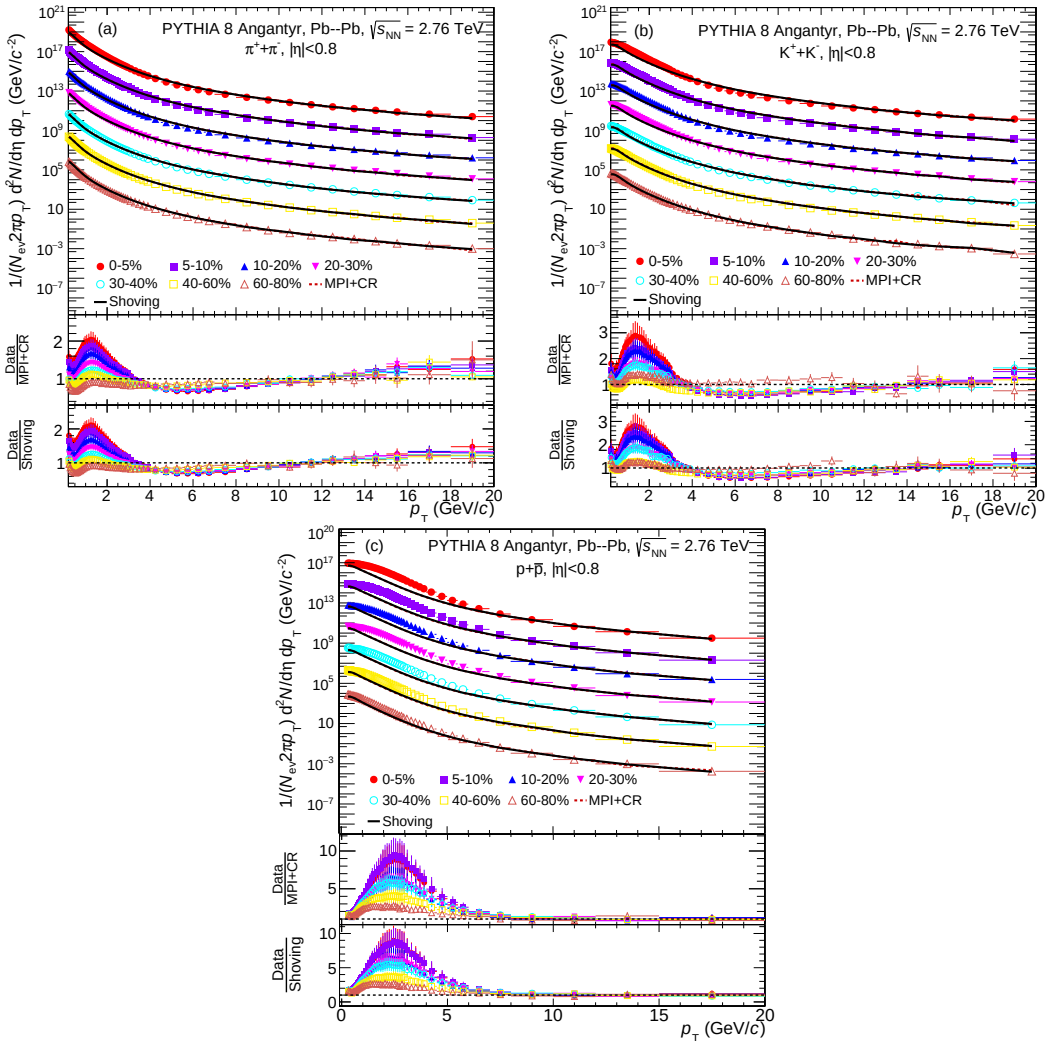

Figure 6.4: (Color Online) p_{T} spectra of identified charged-particles ($\pi^{\pm}$,K$^{\pm}$, p($\bar{\mathrm{p}}$)). The middle and lower panels show the ratios for different centrality classes to data with MPI+CR and string shoving in Pb–Pb collisions at $\sqrt{s_{\mathrm{NN}}}$ = 2.76 TeV.

6.1.1 Transverse momentum spectra of identified particles

FIG. 6.3. shows the p_{T} spectra of identified charge-particles $\pi^{\pm}$,$K^{\pm}$, and $p(\bar{p})$ in different centrality classes and for minimum bias (MB). The spectra were obtained

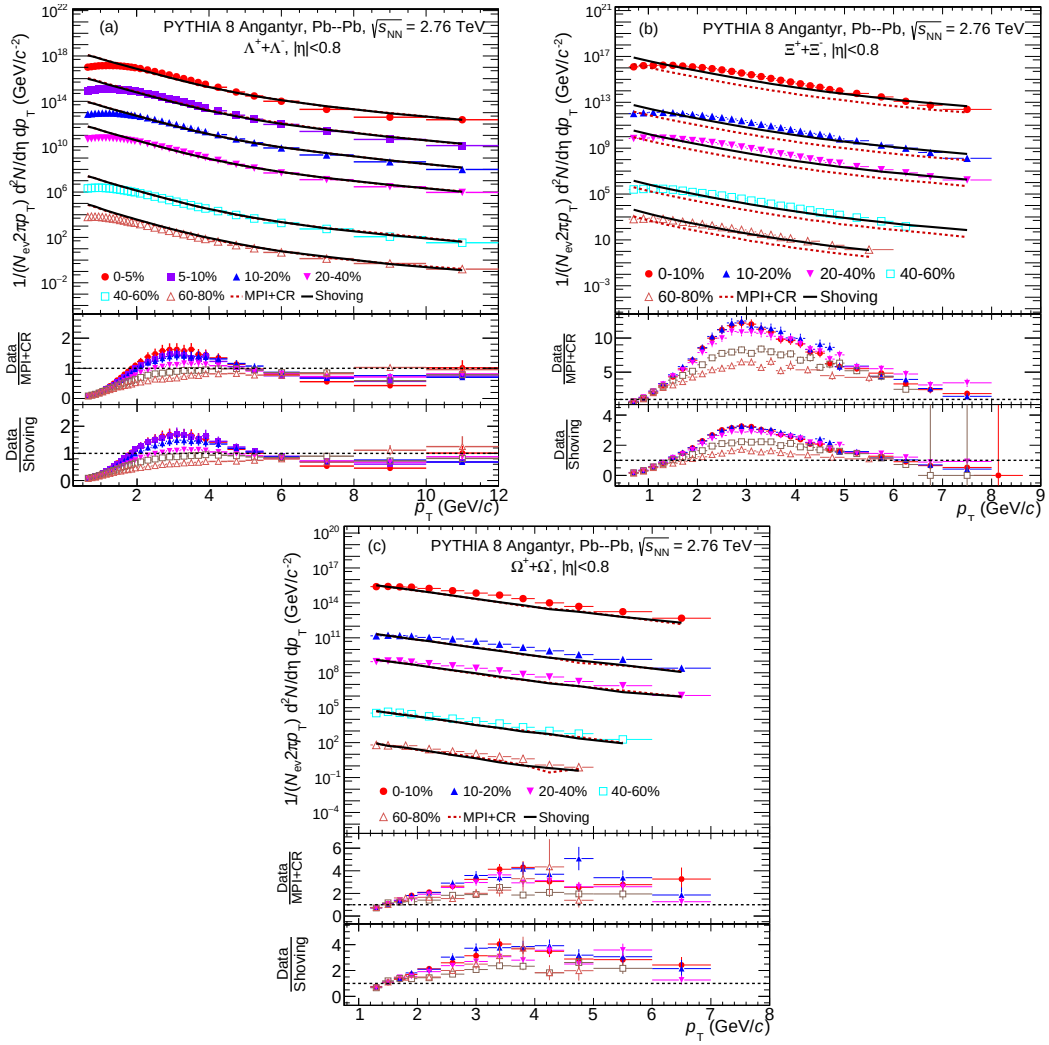

Figure 6.5: (Color Online) p_{T} spectra of strange and multi-strange baryons ($\Lambda^{\pm}$, $\Xi^{\pm}$, $\Omega^{\pm}$). The middle and lower panels show the ratios for different centrality classes to data with MPI+CR and string shoving in Pb–Pb collisions at $\sqrt{s_{\mathrm{NN}}}$ = 2.76 TeV.

using the same selection cuts in all charged-particles species. To visualize better, we multiplied scale factors to each p_{T} spectra. From the lower panel of FIG. 6.3., the p_{T} spectra corresponding to (30-40)% centrality is seen to coincide with the MB spectra. For the threshold centrality class (30-40)%, classes (0-5)%, (5-10)%, (10-20)%, (20-30)% are harder while classes (40-50)%, (50-60)%, (60-70)% and (70-80)% are softer with respect to MB. It is to be noted that a similar trend is observed for all the identified particles. We report a shift in the hardness of the p_{T} spectra from most central to peripheral collisions. The ratios change from low p_{T} to high p_{T} and this change is $\sim$ 5% down to $\sim$ 20% for 0-5% and 70-80% central events respectively. This is due to the loss of hard processes in peripheral

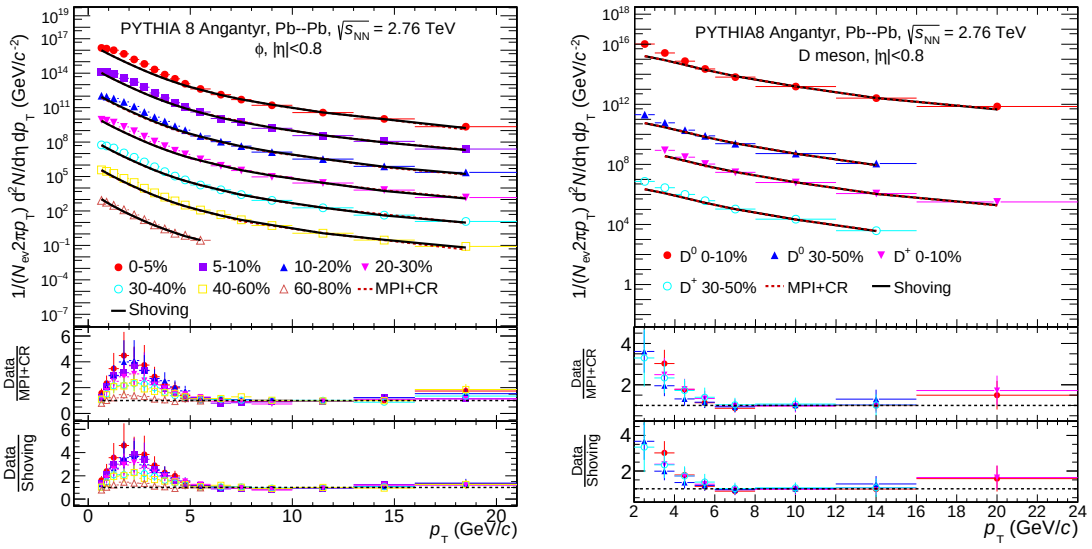

Figure 6.6: (Color Online) p_{T} spectra of ϕ and D-mesons. The middle and lower panels show the ratios for each centrality class to data with MPI+CR and string shoving in Pb–Pb collisions at $\sqrt{s_{\mathrm{NN}}} = 2.76$ TeV.

collisions, which reflects in high p_{T} particle production.

The p_{T} spectra of hadrons obtained at the final state are compared to measurements from the ALICE. In FIG. 6.4. the PYTHIA predictions find a good match with the data for pions, kaons and protons, however an underestimation at low p_{T} is observed. The hump at low p_{T} is probably due to the pQCD implementation of PYTHIA, whereas we expect NRQCD effects in this regime. The effects of radial flow and other medium effects are contributing factors, which can explain the bump at low p_{T} as reported in [199, 200]. We also compare strange baryon p_{T} spectra (Λ, Ξ, Ω) with ALICE in all centrality ranges considered, as shown in FIG. 6.5. The ratios show a similar peak at p_{T} ~3 GeV/c. It is also observed that the width of the hump increases with strangeness and mass, especially for central and semi-central events. At higher centralities, the strange baryons show good compatibility. In FIG. 6.6., we compare the ϕ meson and D-meson (D^0, D^+) p_{T} spectra, where the ϕ meson spectra are seen to be consistent with ALICE measurements in all centralities. As ϕ mesons decay outside a produced fireball, medium effects do not affect the production process [201]. A thermalised QGP state is not a part of PYTHIA-Angantyr, which may result in a good description of experimental results. In the case of D-mesons, we see PYTHIA predictions depart at low p_{T}, however in good agreement at intermediate-higher values. This

helps us to conclude that the more prominent peaks observed for strange baryons (FIG. 6.5.) have a strangeness dependence rather than mass. In a comparison between the tunes, there is no noticeable difference between the results from MPI+CR and string shoving, showing identical ratios for data over model calculations for all aforementioned species, except Ξ. The p_{T} spectra for Ξ from string shoving describe the experimental measurements better than MPI+CR tune.

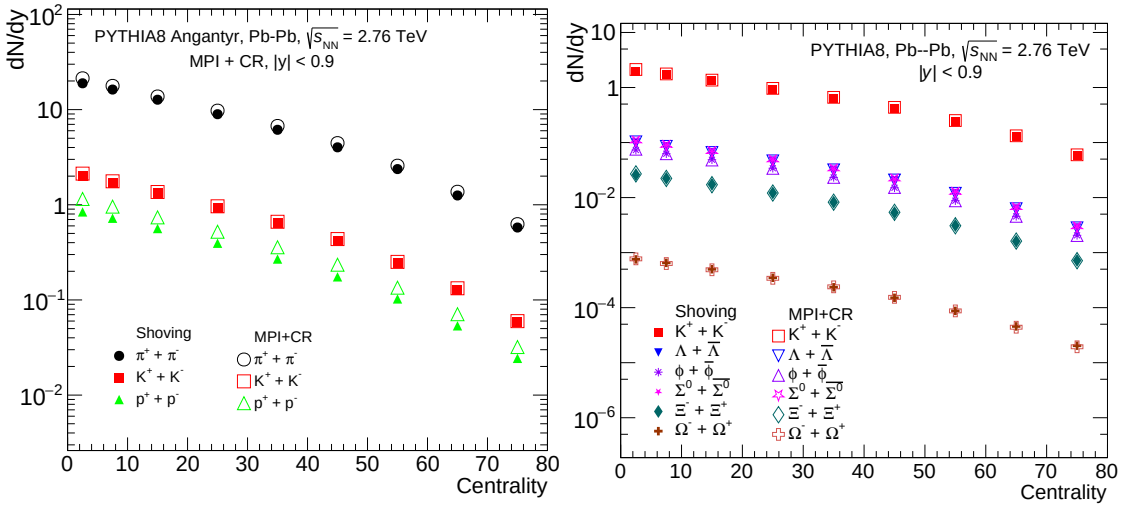

Figure 6.7: (Color Online) Yield of identified particles (Left) and strange particles (Right) as a function of centrality with MPI+CR and string shoving in Pb–Pb collisions at $\sqrt{s_{\mathrm{NN}}} = 2.76$ TeV.

6.1.2 p_{T} integrated yield of identified and strange particles

The p_{T} integrated yields of $\pi^{\pm}$, $K^{\pm}$ and $p(\bar{p})$ are shown in FIG. 6.7 (Left) within rapidity range -0.9 $< y <$ 0.9 normalized by the total number of events. It is observed that the yields of different particles are increasing going from peripheral to most central. We can see a clear mass ordering in yields, with lower mass pions having higher yields, while protons being heavier have lower yields. This is expected towards central collisions; the probability for hard scatterings will be higher, resulting in high particle production. Production of a lighter particle requires lesser energy as compared to a heavier particle and will be more dominant in peripheral collisions. The PYTHIA+Angantyr configurations show minor deviations in proton and π yields, with a slightly higher yield in Angantyr.

In FIG. 6.7 (Right), p_{T}-integrated yields of strange particles are shown. One can see the same features in strange particles like that of identified particles observed in FIG. 6.7 (Left). Production of strange particles is seen to reduce towards peripheral collisions with a similar trend in mass, except for ϕ mesons.

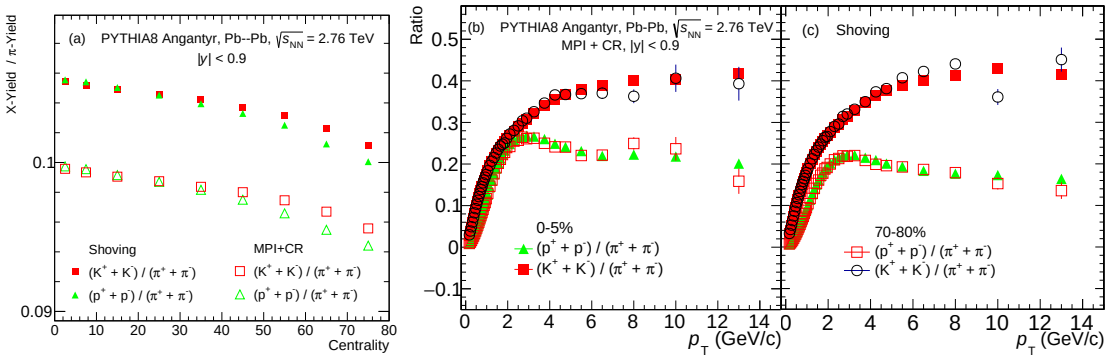

Figure 6.8: (Color Online) Ratio of yields of identified particles over $\pi^+ + \pi^-$ as a function of centrality (a) and as a function of transverse momentum with (b) MPI+CR and (c) string shoving in Pb–Pb collisions at $\sqrt{s_{\mathrm{NN}}}$ = 2.76 TeV.

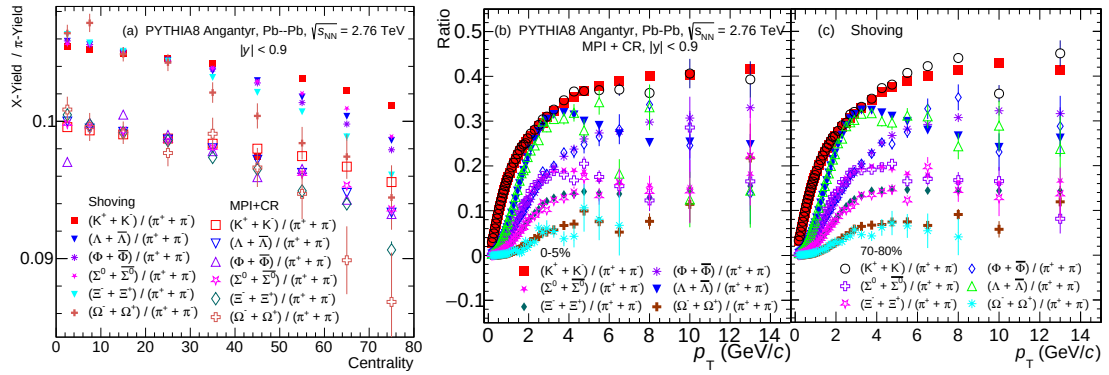

Figure 6.9: (Color Online) Ratio of yields of strange particles over $\pi^+ + \pi^-$ as a function of centrality in (a) and as a function of transverse momentum with (b) MPI+CR and (c) string shoving in Pb–Pb collisions at $\sqrt{s_{\mathrm{NN}}}$ = 2.76 TeV.

6.1.3 Particle ratios

By the bare yield distribution, we cannot quantitatively measure the enhancement or suppression of different particle species. The best way to do this is to estimate the yield with respect to other particles. We measure the ratio of proton and kaon yields over pions to inspect the variation over centrality and p_{T}. FIG. 6.8 shows the measured yield ratios vs. centrality (a) and p_{T} ((b) and (c)). We scale proton over pion ratios for every centrality class for better comparison with the

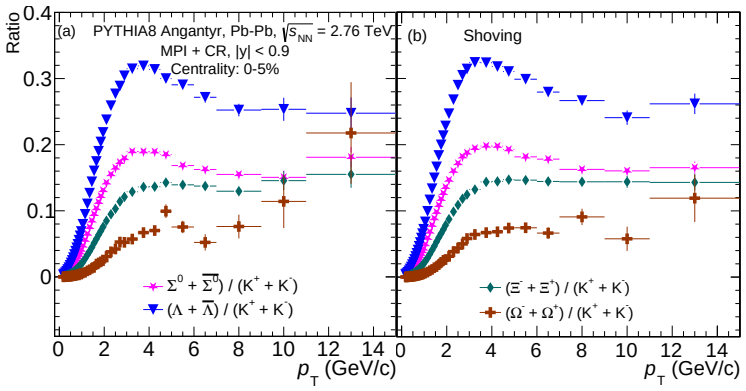

Figure 6.10: (Color Online) Ratio of yields of strange particles over $(K^+ + K^-)$ as a function of transverse momentum with (a) MPI+CR and (b)string shoving in Pb–Pb collisions at $\sqrt{s_{\rm NN}} = 2.76$ TeV.

corresponding quantity versus $p_{\rm T}$ (a). The scale factor is calculated using the formula:

$$Scale\ factor = \frac{K/\pi}{X/\pi}$$

Here X refers to different particle species. We can see from this FIG. 6.8. that both ratios are increasing towards most central; however proton over pion (p/π) ratio drops rapidly than kaon over pion (K/π). There is a visible deviation of $\sim 5\%$ between MPI+CR and string shoving. The reason could be slight over-estimation of π and proton yields for MPI+CR compared to string shoving. As a function of $p_{\rm T}$, K/π ratio increases at lower $p_{\rm T}$ but decreases at higher $p_{\rm T}$, showing a bump around 3 GeV/c. In heavy-ion collisions, this is the consequence of radial flow, but in PYTHIA, this is attributed to the string interactions in color reconnection or string shoving. We can argue that CR or string shoving could be another mechanism of flow where a longitudinal boost is implemented at the initial state (partonic state), prior to hadronization. Understanding this mechanism is important, as it can provide an explanation of flow-like patterns in PYTHIA. At higher $p_{\rm T}$, more particles correspond to jets, in which these particles become insensitive to the hadronization mechanism. If one increases MPI, we see an enhancement in the bump region. In contrast to experimental measurements [202], we do not observe any bump in the K/π ratio. A similar behavior is seen for meson to pion ratios. For baryon to pion ratios however, the bump is seen to shift

further in p_{T} with increasing mass. The results are shown for both the tunes, showing close similarity between the results. This is a qualitative attempt with PYTHIA+Angantyr to describe meson and baryon over meson ratios. Studies report this effect can also be observed in meson to meson ratios with further tuning. [14]. Similarly, we show yield ratios of strange particles over pions as a function of centrality in FIG. 6.9 (a). Each yield ratio of different particles is scaled with a similar method as mentioned before. A $\sim 5\%$ deviation between the tunes is seen here due to the slightly higher π yields. We observe a clear strangeness enhancement as we go from most central to peripheral collisions. Heavy strange particle ratios are showing more enhancement, as reported in FIG. 6.9 (a), slopes of strange particle ratios increase towards heavier strange particles. This is due to overlapping color strings forming (ropes) at higher densities [148]. In FIG. 6.9, we show yield ratios of strange particles as a function of transverse momentum in two different centrality classes at 0-5% and 70-80%. For all strange particles, yield ratios increase towards higher p_{T}. As expected, the ratio of yields is lesser for strange heavy particles. We also conclude by observing FIG. 6.8 (Right) and FIG. 6.9 (Right) that meson to pion ratios are not showing the bump but shows for baryon to pion ratios.

In FIG. 6.10 we show the ratio of strange particles over $(K^+ + K^-)$ mesons. The ratio increases as p_{T} increases, and after a peak close to 3-4 GeV/c, it decreases. The position of the peak shift towards higher p_{T} for strange heavy particles. A study reports a similar type of observation seen in experimental data for Pb–Pb collisions [203]. This effect is generally seen in heavy-ion collisions as a consequence of radial flow [204].

6.2 Jet fragmentation via azimuthal angular correlations of heavy flavor decay electrons in pp, p–Pb, and Pb–Pb collisions using PYTHIA8+Angantyr

In this article, the heavy-flavor hadron decay electrons (c,b$\rightarrow e$) are used to study the parton shower of heavy quarks. It will contribute to a better understanding of heavy flavour parton showers and offer predictions for measurements of the heavy-flavor correlation. This study is important from the perspective of experimental measurements at high energies in heavy flavor correlations, which are currently available only for charm mesons. By varying the trigger and associated particle p_{T}, this work aims to investigate how soft and hard fragmentation showers interplay. The correlation peaks are described using a novel fitting function (von Mises). As the BLC tunes increase the peak amplitude for baryon-tagged correlation, predictions from the new color reconnection (BLC) tunes are compared to the default (Monash) ones to see the behavior of fragmentation functions in the presence of baryon decay electrons. Further, the effect of partonic and hadronic level processes on heavy flavor jet fragmentation is studied.

Initial hard scatterings in pp, p–Pb, and Pb–Pb collisions produce heavy-flavours, namely charm (c) and beauty (b) [182, 192, 205–207]. Their early production can be attributed to their large mass, which allows them to traverse through the QGP and interact with the partons of the hot medium. The production cross-section of these heavy quarks is usually calculated using the factorization theorem

$$d\sigma^{\mathrm{hard}}_{AB\rightarrow C} = \Sigma_{a,b,X} f_{a/A}(x_a, Q^2) \otimes f_{b/B}(x_b, Q^2) \otimes d\sigma^{\mathrm{hard}}_{ab\rightarrow cX}(x_a, x_b, Q^2) \otimes D_{c\rightarrow C}(z, Q^2) \tag{6.1}$$

where, $f_{a/A}(x_a, Q^2)$ and $f_{b/B}(x_b, Q^2)$ are the parton distribution functions which give the probability of finding parton "a"(b) inside the particle "A"(B) for given x (fraction of particle momentum taken by parton) and factorization scale (Q^2), $d\sigma^{\mathrm{hard}}_{ab\rightarrow cX}(x_a, x_b, Q^2)$ is the partonic hard scattering cross-section, and

$D_{c\to C}(z, Q^2)$ is the fragmentation function of the produced parton (particle). This leads to universal hadronization, but new PYTHIA8 tunes have incorporated different hadronization models based on beyond-leading color approximation (BLC tunes) and rope hadronization (Shoving) which do not assume universal hadronization. The high momentum (p_{T}) partons through fragmentation (parton showering) [12, 13, 208] and hadronization form a cluster of final state particles known as a jet. The study of high-pT jets reveals how parton fragments into various particles and allows the study of the parton's interaction with the medium.

The CR mechanism of hadronization can be investigated further by looking at the string topology between the partons. The Leading Color (LC) approximation assigns a unique index to quarks and antiquarks connected by a colored string. This guarantees a fixed number of colored strings, ensuring that no two quarks (antiquarks) have the same color. The same is true for gluons, which are represented by a pair of colored quark-antiquark. This model is extended to non-LC topologies, also known as Beyond-LC (BLC) [78], in which colored strings can form between LC and non-LC connected partons. This opened the possibility of a string being linked to partons of matching indexes other than the LC parton. Three modes of Color Reconnection in the BLC approximation are used with the different constraints on the allowed string reconnections, taking into account causal connections of dipoles involved in a reconnection and time dilation effects caused by relative boosts between string pieces [78, 209]. We investigated different PYTHIA8/Angantyr tunes, i.e., LC (MONASH 2013 [209], and 4C [210]), BLC (Mode0, Mode2, Mode3), and rope hadronization (Shoving) [211–214]. In our study, similar results were obtained with the LC tunes 4C and Monash, and different BLC tunes were also consistent with one another; therefore, for this investigation, we used the Monash, Mode2, and Shoving tunes and investigated how different hadronization processes affected the results.

Leading order (LO) perturbative scattering processes of gluon fusion ($gg \to Q\overline{Q}$) or pair annihilation ($q\overline{q} \to Q\overline{Q}$) is used for the production of heavy-flavours in PYTHIA. PYTHIA also approximates certain higher-order contributions within its LO framework via flavour excitations ($gQ \to Qg$), or gluon splittings ($g \to Q\overline{Q}$) which give rise to heavy-flavour production during high p_{T} parton showers [182,

192].

One of the methods to study interactions of heavy-flavours with partons of hot QCD matter is two-particle angular correlation function [215–218], i.e. the distribution of the differences in azimuthal angles, $\Delta\varphi = \varphi_{assoc} - \varphi_{trig}$, and pseudorapidities, $\Delta\eta = \eta_{assoc} - \eta_{trig}$, where φ_{assoc} (η_{assoc}) and φ_{trig} (η_{trig}) are the azimuthal angles (pseudorapidities) of the associated and trigger particles respectively. The structure of the correlation function usually contains a "near side" (NS) peak and an "away side" (AS) peak at $\Delta\varphi = 0$ and $\Delta\varphi = \pi$ respectively over a wide range of $\Delta\eta$. In QCD, leading order (LO) heavy-flavour production processes imply back to back correlations at $\Delta\varphi = 0$ and $\Delta\varphi = \pi$ with the same distribution parameters, however next-to-leading order (NLO) processes like gluon splitting and flavour excitation can lead to change in the away side peak. Additionally, the production of heavy-flavour hadrons is sensitive to both the charm and beauty fragmentation functions as well as the hadronization mechanisms; for these reasons, the two-particle angular correlation function not only enables us to study how heavy-flavours interact with QGP in Pb–Pb collisions but also to characterize the production, fragmentation, and hadronization of heavy-flavour hadrons in pp collisions [192]. Apart from above mentioned reasons, modification of the correlation function is also possible in the case of p–Pb due to cold-nuclear matter effects (nuclear shadowing and gluon saturation) [219–221]. After measuring the nuclear modification factor of D mesons and electrons from heavy-flavour hadron decay in p–Pb collisions at $\sqrt{s_{NN}} = 5.02$ TeV, a small influence of cold-nuclear matter effects on heavy-flavour quark production at midrapidity was observed [3, 222–225].

In this article, we present the study of the azimuthal correlation function of prompt D mesons/baryons and B mesons with charged hadrons in pp collisions at $\sqrt{s} = 7$ TeV using PYTHIA8, where "prompt" refers to D mesons produced from the fragmentation of charm-quark generated in initial hard scattering, including those from the decay of excited charmed resonances and excluding D mesons produced from beauty hadron weak decays. In terms of particle multiplicity and angular profile, the near-side correlation peak is a suitable probe for characterizing charm jets and their internal structure. Probing the near-side peak [226] features as a function of charged-particle transverse momentum (p_{T}), possibly up to values

of a few GeV/c, can provide insight into the transverse-momentum distribution of the jet constituents. These features are useful to decifer how the jet momentum fraction not carried by the D mesons is shared among the other particles produced by charm fragmentation, as well as the correlation between the p_{T} of these particles and their radial displacement from the jet axis. Variations in the amplitude and width of the away-side peak also shed light on the dynamics of heavy-flavour production mechanism [227].

Various event generators in high energy physics mainly use either string model or cluster model for the description of hadronization [228–230]. This study aims to understand and compare the fragmentation and hadronization of D mesons/baryons and B mesons using different tunes of PYTHIA8. In PYTHIA8, the LUND string hadronization model with parameters tuned using $e^{+}e^{-}$ data is used for the fragmentation process [113, 114, 230, 231]. Different tunes of PYTHIA8 such as Monash, 4C, Mode(0,2,3), and shoving differ in implementations of string hadronization which are discussed in the next section. The production and the fragmentation of charmed baryons and beauty mesons is inherently different owing to the difference in their quark content. It will be interesting not only to see which of these models gives a better description of charmed mesons data but also their predictions for charmed baryons and beauty mesons. In the literature, the hadronization of these particles is also explained by $3 \rightarrow 1$ and $2 \rightarrow 1$ coalescence model [232, 233]. As far as the comparison between charmed mesons and beauty mesons is concerned, global fragmentation functions based on Next to Leading Logarithmic (NLL) calculations contain the parameter which is a function of the inverse square of heavy-flavour mass [234–238]. We anticipate that the effect of mass hierarchy between charm and beauty quark should also be visible in azimuthal angular correlation.

We used PYTHIA version 8.3 and PYTHIA8+Angantyr to generate around 50 million events for pp and p–Pb collisions at $\sqrt{s_{\mathrm{NN}}}$= 5.02 TeV, respectively. For Pb–Pb, approximately 5 million events were generated using PYTHIA8+Angantyr at $\sqrt{s_{\mathrm{NN}}}$= 5.02 TeV. The reported results are the predictions for the ALICE experiment. Therefore, the electrons from heavy flavor hadrons ($c, b \rightarrow e$) decays are selected within $|\eta| < 0.6$ as trigger particles due to the acceptance of the

electromagnetic calorimeter (EMCal) detector in ALICE. The trigger particles are selected from 4 to 20 GeV/c. In order to increase the statistics of heavy-flavor decay electrons, the hard QCD processes are turned on to enable charm and beauty quark production with the minimum phase space cut of 9 GeV/c, which is a safe choice for LHC energies. The number of electrons from beauty and charm hadrons is corrected using FONLL prediction [172] [173] [64], as the decay kinematics and fragmentation of charm and beauty are different. The correlation distribution of heavy-flavor decay electrons is generated by correlating each heavy flavor electron to the associated particles from 1 to 7 GeV/c. Here, associated particles are the physical primary particles.

To validate these settings of PYTHIA, a comparison of azimuthal correlation ($\Delta\varphi$ distribution) of prompt D-meson and charged particles with ALICE data is shown in Fig. 6.17. In the figure, the $\Delta\varphi$ distribution obtained from PYTHIA8 Monash tune is compared with ALICE published data for the $\sqrt{s}$ = 7 TeV in the $p_{\rm T}$ trigger 5-8 GeV/c ($p_{\rm T}^{\rm e}$) for associate particles $p_{\rm T}$ 0.3-1 GeV/c ($p_{\rm T}^{\rm assoc}$) [11]. Here, the range of $\Delta\varphi$ distribution is taken from 0 to π to match with ALICE data. The pedestal (baseline) is subtracted from the generalized Gaussian function considering the physical minima around $\pi/4$ to $\pi/2$. The result from PYTHIA shows a good agreement with ALICE data which motivates us to give a prediction on heavy-flavor electron correlation with charged particles.

6.2.1 Baseline estimation and near- and away-side observable extraction

The correlation analysis is performed by correlating each heavy-flavor decay electron with its associated charged particles. In order to measure both the near- and away-side peaks with full ranges, the $\Delta\varphi$ distribution is obtained in the range $-\pi/2 < \Delta\varphi < 3\pi/2$, where the near-side peak is observed at $\Delta\varphi = 0$, formed by the charged particle associated with the electron of high transverse momentum ($p_{\rm T}^{\rm e}$) particle, whereas the away-side peak appears at $\Delta\varphi = \pi$ due to back to back di-jets produced by LO processes. A flat region also appears between the peaks formed under the signal region by the uncorrelated pairs of trigger particles

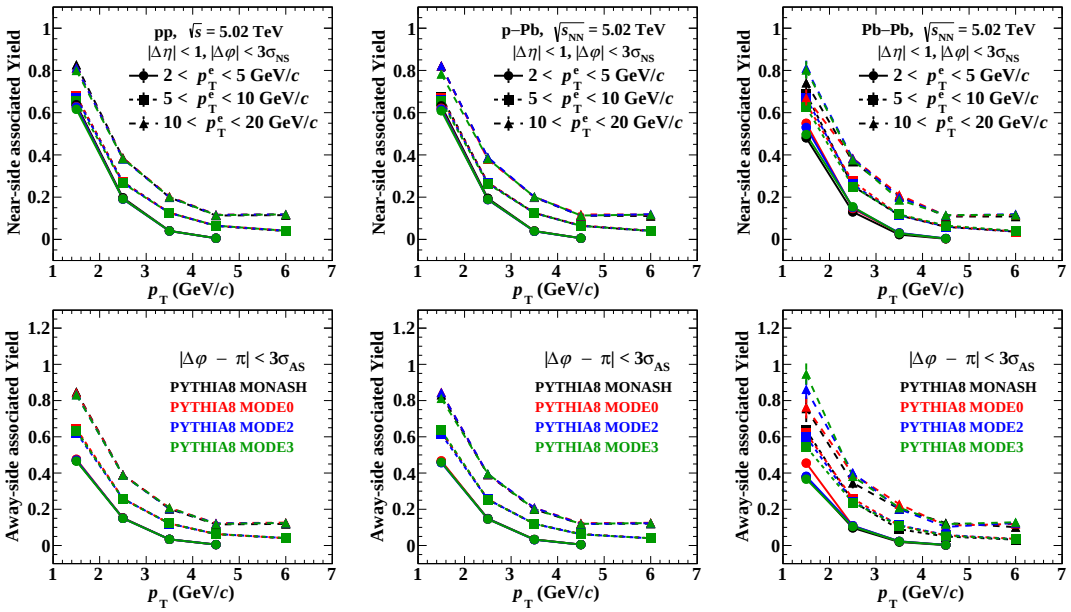

Figure 6.11: The near- and away-side yields of correlation peaks from PYTHIA8 for different trigger $p_{\mathrm{T}}^{\mathrm{e}}$ ranges $2 < p_T^e < 5$, $5 < p_T^e < 10$, and $10 < p_T^e < 20$ GeV/c for different associated $p_{\mathrm{T}}^{\mathrm{assoc}}$ ranges between $1 < p_T^{assoc} < 7$ GeV/c in pp, p–Pb and Pb–Pb collisions at $\sqrt{s_{\mathrm{NN}}}$= 5.02 TeV.

and associated particles. Most of the contribution in the baseline comes from the soft processes. The baseline subtraction and measurement of near- and away-side observables are performed by fitting the raw $\Delta\varphi$ distribution (included baseline) with the von Mises function, as shown in FIG. 6.15. The function is defined as:

$$f(\Delta\varphi) = b + \frac{e^{\kappa_{NS}\cos(\Delta\varphi)}}{2\pi I_0(\kappa_{NS})} + \frac{e^{\kappa_{AS}\cos(\Delta\varphi-\pi)}}{2\pi I_0(\kappa_{AS})} \tag{6.2}$$

Here, b is the baseline, κ is the reciprocal of dispersion, which means it gives a measure of the concentration, I_0 is the 0^{th} order modified Bessel function. The mean for near- and away-side peaks are fixed to "0" and "π," respectively.

Earlier, a double Gaussian, double generalized Gaussian, and generalized Gaussian + Gaussian functions, along with a constant term, were employed in these measurements to measure the near- and away-side observables as well as to estimate the baseline. But due to the triangular structure of the near-side correlation peak, the Gaussian function is not suitable as a fit function. The generalized Gaussian function is discarded as the number of free parameters is

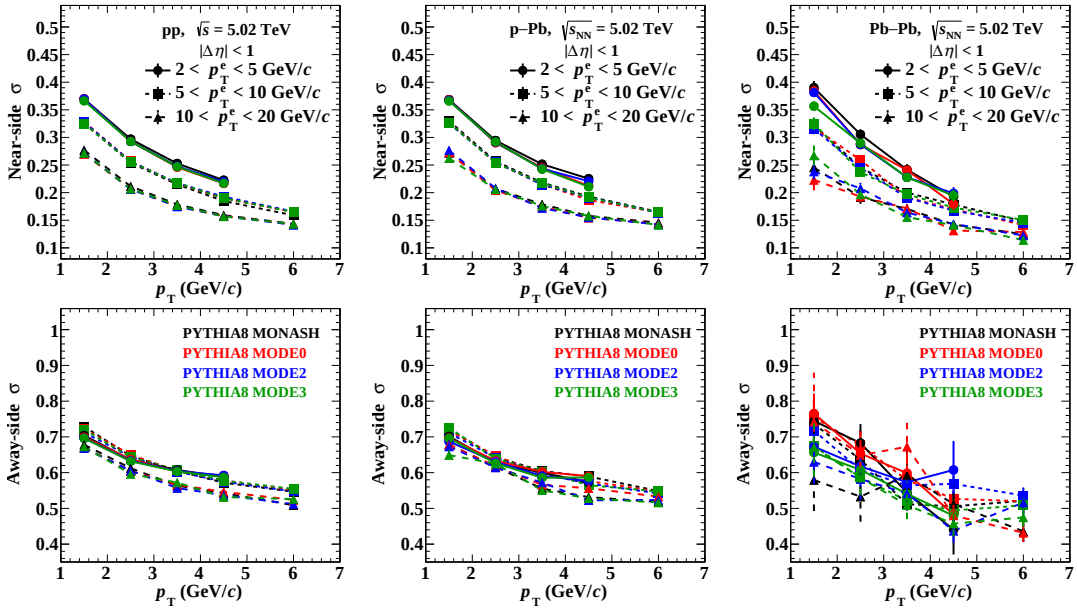

Figure 6.12: The near- and away-side widths (σ) of correlation peaks from PYTHIA8 for different trigger $p_{\mathrm{T}}^{\mathrm{e}}$ ranges $2 < p_T^e < 5$, $5 < p_T^e < 10$, and $10 < p_T^e < 20$ GeV/c for different associated $p_{\mathrm{T}}^{\mathrm{assoc}}$ ranges between $1 < p_T^{assoc} < 7$ GeV/c in pp, p–Pb and Pb–Pb collisions at $\sqrt{s_{\mathrm{NN}}}$= 5.02 TeV.

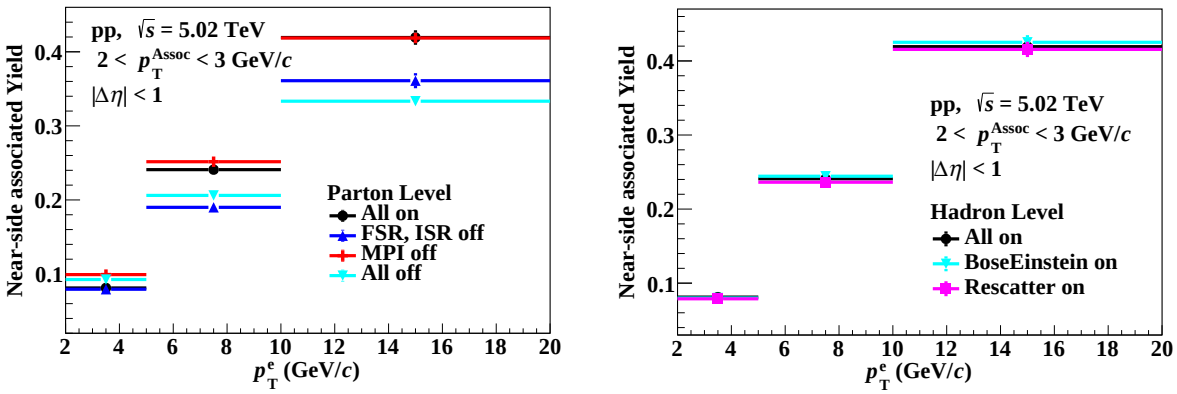

Figure 6.13: The near-side yields of correlation peaks from PYTHIA8 for different parton level (Up) and hadron level (Down) processes for trigger $p_{\mathrm{T}}^{\mathrm{e}}$ ranges between $2 < p_T^e < 20$ GeV/c and for associated $p_{\mathrm{T}}^{\mathrm{assoc}}$ range $2 < p_T^{assoc} < 3$ GeV/c in pp collisions at $\sqrt{s}$= 5.02 TeV.

larger than that of the von Mises function, which may bias the near- and away-side observables, especially the width, as the shape parameters of the generalized Gaussian have an anti-correlation with the width of the peaks. Another advantage of the von Mises function is that it can adjust the shape according to correlation peaks, as the shape of the near-side peak is near to triangular, whereas the away-side peak is almost Gaussian. In the measurements of D meson correlation, authors used two different functions, a generalized Gaussian for near-side peak (triangular) and a Gaussian for away-side peak, where the von Mises function does not need to club with other functions.

The near- and away-side width is estimated by measuring the sigma (σ) from the von Mises function as by the given relation:

$$\sigma = \sqrt{-2 \log \frac{I_1(\kappa)}{I_0(\kappa)}} \tag{6.3}$$

Here, I_0 and I_1 are the modified Bessel function of 0^{th} order and 1^{st} order, and κ is measured by the von Mises function fit parameter.

The error in the width (dσ) is propagated by the relation:

$$\mathrm{d}\sigma = \frac{1}{\sigma} \times \left(\frac{\mathrm{I_1}}{\mathrm{I_0}} - \frac{\mathrm{I_0}}{\mathrm{I_1}} + \frac{1}{\kappa} \right) \mathrm{d}\kappa \tag{6.4}$$

Where dκ is the uncertainty in κ, obtained by von Mises function fitting.

In this work, we are presenting the $\Delta\varphi$ distribution, near- and away-side yields and widths (σ) in three different $p_{\mathrm{T}}^{\mathrm{e}}$ intervals corresponding 4-7 GeV/c, 7-10 GeV/c and 10-20 GeV/c with five $p_{\mathrm{T}}^{\mathrm{assoc}}$ intervals corresponding 1-2, 2-3, 3-4, 4-5 and 5-7 GeV/c. The $\Delta\varphi$ distribution obtained within $\mid \Delta\eta \mid < 1.$ range. A condition $p_{\mathrm{T}}^{\mathrm{assoc}} < p_{\mathrm{T}}^{\mathrm{e}}$ is applied while correlating the particles to avoid the double-counting of trigger electrons in correlation. These results are obtained with three different tunes of color reconnection along with the default Monash tune.

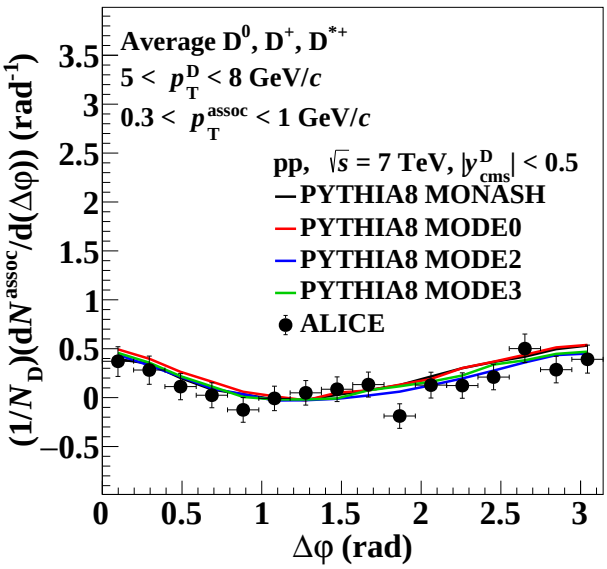

Figure 6.14: Comparison of average D-meson azimuthal-correlation distribution at mid-rapidity with PYTHIA8 Monash for trigger $p_{\mathrm{T}}^{\mathrm{D}}$ range $5 < p_{\mathrm{T}}^{\mathrm{D}} < 8$ GeV/c and $p_{\mathrm{T}}^{\mathrm{assoc}}$ range $0.3 < p_{\mathrm{T}}^{\mathrm{D}} < 1$ GeV/c in pp collisions at $\sqrt{s}$= 7 TeV.

6.3 Heavy-flavour hadron decay electron correlation with charged particles

The shape and height of the correlation peaks can be compared in pp, p–Pb, and Pb–Pb collisions to provide information about the possible system size dependence on the modification of jet fragmentation. On the away-side, it reflects the survival probability of recoil partons while passing through the medium. It can be seen in Fig. 6.16 that there are no significant differences among different color reconnection tunes in pp and p–Pb collisions; however, a small increment of peak height is observed in Pb–Pb collisions with BLC tunes. This might be because an additional junction was added to BLC tunes, showing the effect at high-density strings in Pb-Pb collisions. However, more study is required in this direction to make a strong claim. It is observed that the particles associated with the high $p_{\mathrm{T}}^{\mathrm{e}}$ have higher peaks compared to low p_{T} trigger particles. Also, the peaks are narrower for the high $p_{\mathrm{T}}^{\mathrm{e}}$ particle due to the initial boost. The difference between the correlation pattern can be quantified more efficiently by comparing near- and away-side yields and widths.

The near- and away-side width of $\Delta\varphi$ distribution peaks are obtained for all

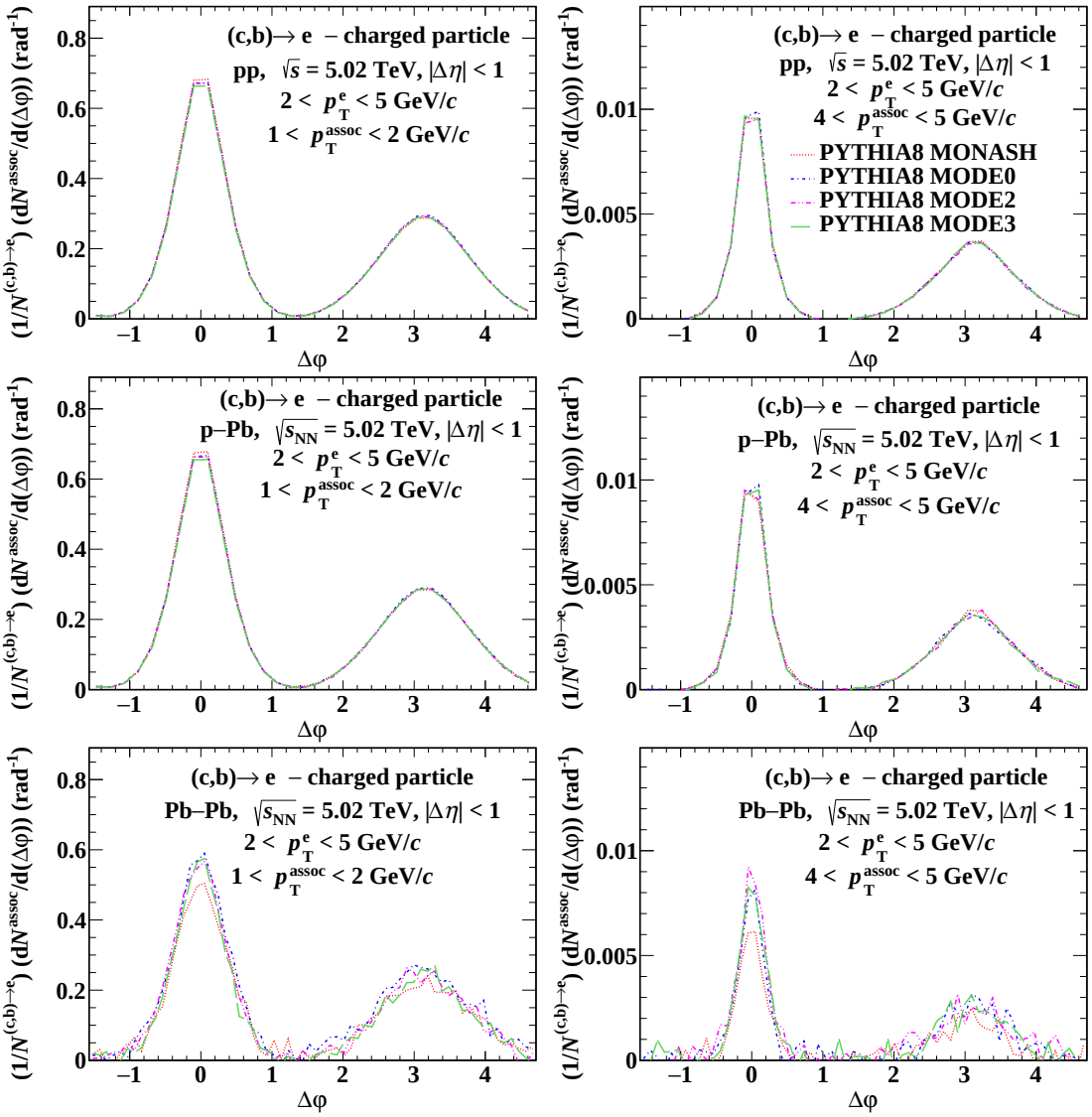

Figure 6.16: (Color online) The azimuthal-correlation distribution from the PYTHIA8 for trigger $p_{\mathrm{T}}^{\mathrm{e}}$ range $2 < p_T^e < 5$ GeV/c and for associated $p_{\mathrm{T}}^{\mathrm{assoc}}$ ranges $1 < p_T^{assoc} < 2$ and $4 < p_T^{assoc} < 5$ GeV/c in pp, p–Pb and Pb–Pb collisions at $\sqrt{s_{\mathrm{NN}}}$= 5.02 TeV.

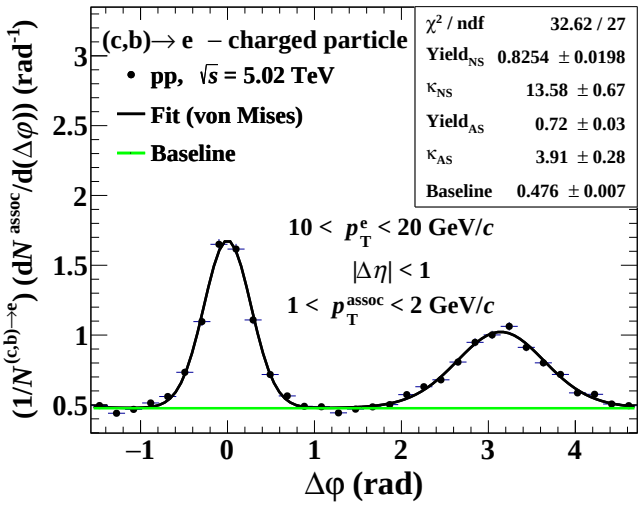

Figure 6.15: (Color online) The azimuthal-correlation distribution ($\Delta\varphi$) fitted with the von Mises function is shown for trigger $p_{\rm T}^{\rm e}$ range $10 < p_T^e < 20$ GeV/c and for associated $p_{\rm T}$ range $1 < p_T^e < 2$ GeV/c in pp collisions at $\sqrt{s}$= 5.02 TeV.

the tunes with different triggers and associated $p_{\rm T}$ intervals, as shown in Figs. 6.12 for pp, p–Pb, and Pb–Pb collisions. By observing all the figures, it is clear that for each $p_{\rm T}^{\rm e}$ bin, widths decrease as increasing associate particles $p_{\rm T}$, which is reflected by the decreasing of broadness. On the other hand, peaks associated with high $p_{\rm T}^{\rm e}$ particles have lower widths than low $p_{\rm T}^{\rm e}$ particles due to the initial boost in the transverse direction. Different color-reconnection tunes are not showing significant changes in width, and the spreads of the widths due to the various tunes are treated as a band of systematic uncertainties.

Similarly, yields are extracted for the near- and away-side peaks. The yields are measured by the bin counting method within the three sigma ($< 3\sigma$) region from the mean value of the peaks. The σ for the concerned peak is obtained by using eq 6.3 with the help of the von Mises function. The near- and away-side yields for the different $p_{\rm T}^{\rm e}$ are shown in Figs. 6.11 for pp, p-Pb, and Pb-Pb, respectively. It is observed that a high $p_{\rm T}^{\rm e}$ particle shows a higher yield compared to a low $p_{\rm T}^{\rm e}$ particle. This is expected as the available energy to fragment into associate particles is more prominent in high $p_{\rm T}^{\rm e}$ particles.

Moreover, the difference in charm and beauty fragmentation could affect the yields of low and high $p_{\rm T}^{\rm e}$ particles. The yields are decreasing towards higher $p_{\rm T}^{\rm assoc}$ intervals, suggesting that fragmentation into low $p_{\rm T}^{\rm assoc}$ particles is higher than high $p_{\rm T}^{\rm assoc}$ particles due to the production cross-section. As the process

of heavy quark fragmenting to heavy flavor hadrons is very rare, the emission of high p_{T} associated particles becomes limited, and most of the accompanying associated particles are softer. By comparing these yields in different systems, it is observed that the results from pp and p-Pb are consistent with each other, which is also seen in the D-meson and charged particle correlation performed by ALICE experiment [11] [13]. The D-h correlation measurement performed by the ALICE experiment does not show any deviation in pp and p-Pb collision results, which suggests that there is no major modification in the fragmentation due to the cold nuclear matter effect. We see the same result by using PYTHIA8 Angantyr. In contrast, yields from Pb-Pb are slightly lower, especially for low $p_{\mathrm{T}}^{\mathrm{e}}$ particles. It must be noted that the suppression of yields (jet quenching) in Pb-Pb is due to MPI+CR and higher particle density, as a thermalized medium is not implemented in the PYTHIA8 Angantyr model.

Further, results are obtained for different partonic and hadronization processes and compared with themselves. It provides a detailed view of the correlation function from the hard-scattering outgoing partons and their hadronization. In fig. 6.13, the near-side yields are obtained from the bin-counting method using the fit function discussed above for both parton level and hadron level processes. The top figure shows the comparison between different partonic processes, i.e., ISR, FSR, and MPI. Before hard scatterings occur, partons from the incident protons beams can radiate gluons in the initial-state radiation (ISR) process. Similarly, outgoing partons from hard-scattering processes can produce a shower of softer particles via a final-state radiation (FSR) process. Since hadrons are composite objects, more than one distinct hard-parton interaction can occur in a pp collision, and proton remnants can also scatter again on each other. Such processes are called multi-parton interactions (MPI) and are responsible for producing a large fraction of the particles. Heavy quarks in PYTHIA can occur not only from the first hard (hardest) scattering but also from hard processes in the various MPI occurring in the collisions, ordered with decreasing hardness [239].

It is observed that the near side yields using all partonic processes on (default) are similar to the yields for MPI off, especially at higher p_{T}. This is because particles produced from MPI are uncorrelated to the trigger particle; hence it

contributes to the baseline. A significant decrease in yields is seen while switching off to ISR and FSR processes, as higher momentum particles contribute to more collinear particle production with these processes. This points towards a relevant role of hadronization in shaping the correlation peaks in the absence of these processes. Switching MPI off with these processes (All off) has no significant difference. The difference which we are seeing at high $p_{\mathrm{T}}^{\mathrm{e}}$ could be due to fluctuation. In the bottom figure, different hadron level processes are shown, i.e., Bose-Einstein (BE) effect and Rescattering effect [240] [241] [242]. In the phenomenological Lund Model, the BE effect is approximated by a semi-classical momentum-dependent correlation function, which effectively acts as an attractive force between two mesons. The BE class in PYTHIA performs shifts of momenta of identical particles to provide a crude estimate of BE effects. In the rescattering phenomena, it is assumed that the hadrons produced can scatter against each other on the way out before the fragmenting system has had time to expand enough that the hadrons get free. This is happening in parallel with rapid decays. It is interesting to see that no significant impact of the hadronization processes is observed in the yields. It is to be noted that in this figure, "All on" means all the default hadronic processes are on; however, BE and Rescatter are off.

6.4 Jet fragmentation via azimuthal angular correlations of heavy-flavours in pp collisions at $\sqrt{s} = 7$ TeV

We used PYTHIA version 8.3 to generate around 1B events for each tune in pp collisions at $\sqrt{s} = 7$ TeV. heavy-flavour hadrons are selected within $|y| < 0.5$. The p_{T} of trigger particle (heavy-flavour) is selected in three intervals, i.e., 3-5, 5-8, and 8-16 GeV/c, while associate particles are selected in the ranges 0.3-50, 0.3-1, 1-50 GeV/c. The inelastic, non-diffractive component of the total cross-section for all soft QCD processes is used with the switch `SoftQCD:all = on` with MPI. Correlation distribution was obtained by correlating each trigger particle with all the associated charged particles. It is to be noted that the decay product of the

trigger particle is excluded from the correlation function. The $\Delta\eta$ is selected in the range from -1 to 1. The correlation distribution is fitted with the generalized Gaussian function for the near-side peak, Gaussian function for the away-side peak, and 0^{th} order polynomial the baseline identification as shown in the eq. 6.5.

$$f(\Delta\varphi) = b + \frac{Y_{\rm NS} \times \beta_{\rm NS}}{2\alpha_{\rm NS}\Gamma(1/\beta_{\rm NS})} \times e^{-(\frac{\Delta\varphi}{\alpha_{\rm NS}})^{\beta_{\rm NS}}} + \frac{Y_{\rm AS}}{\sqrt{2\pi}\sigma_{\rm AS}} \times e^{-(\frac{\Delta\varphi-\pi}{\sqrt{2}\sigma_{\rm AS}})^2} \tag{6.5}$$

Where Y_{NS} and Y_{AS} are the yields for NS and AS peaks, β_{NS} is the shape parameter for near-side peak, and α_{NS} is related to the σ_{NS} (width) of the peak by the given relation:

$$\sigma_{\rm NS} = \alpha_{\rm NS}\sqrt{\Gamma(3/\beta_{\rm NS})/\Gamma(1/\beta_{\rm NS})} \tag{6.6}$$

In this contribution, we tried to study the fragmentation and hadronization of heavy-flavours via jet-like azimuthal correlation of heavy-flavour hadrons with the charged particle in pp at $\sqrt{s} = 7$ TeV. Charm mesons species which are selected for the comparisons are D^0, D^+ and D^{*+}, similarly charm baryons species are Λ_c^+, Σ_c^0, Σ_c^+, Ξ_c^+, Ξ_c^0, Ω_c^0, Ω_c^{0*}, and beauty mesons species are B^0, B^+, B_s^0 and B^{*+} with their anti-particles.

The jet-like two-particle correlation measurement is an alternative tool to study the jet properties even at low $p_{\rm T}$ where direct jet measurement is not possible [243]. The correlation measurements provide insight into particle production from the different processes, i.e., pair creation (LO), gluon-splitting, and flavour-excitation (NLO).

The ALICE measurements of azimuthal correlations for charm mesons are compared with PYTHIA prediction in the following subsection. The measurements of charm mesons are independently compared to charm baryons and beauty mesons to spot any potential alterations in jet fragmentation.

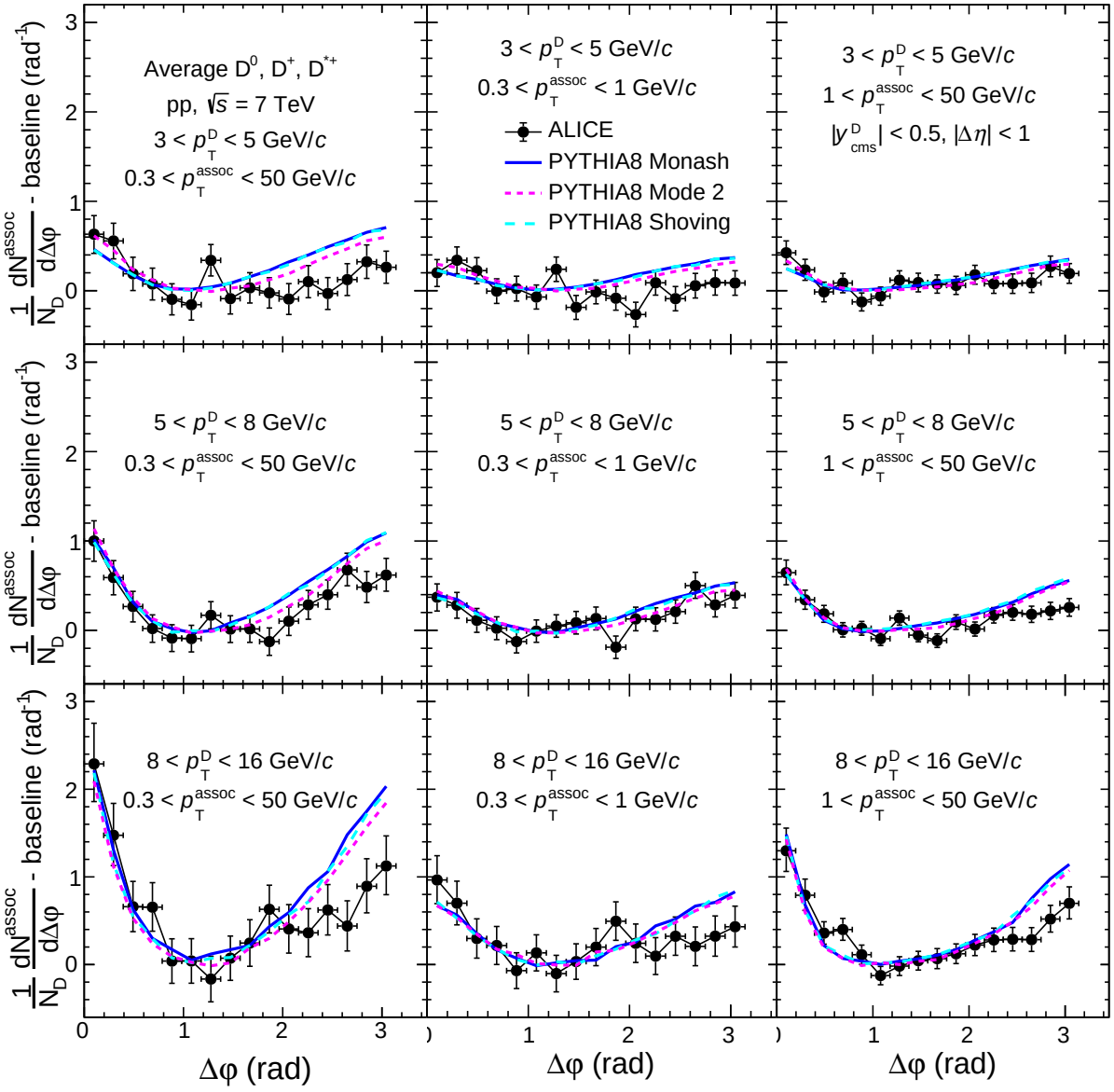

Figure 6.17: Comparison of ALICE results of average D meson azimuthal-correlation distribution with PYTHIA8 (Monash, Mode 2, and Shoving) after baseline subtraction for $3 < p_{\mathrm{T}}^{\mathrm{D}} < 16$ GeV/c and for different associated $p_{\mathrm{T}}^{\mathrm{assoc}}$ ranges in pp collisions at $\sqrt{s} = 7$ TeV.

6.4.1 Comparison with ALICE data

In order to validate the settings of PYTHIA that are used for this study, the azimuthal correlation between D meson and charged particles from the PYTHIA event generator with different color reconnection (CR) schemes and rope hadronization (RH) model is compared with the measurements of ALICE experiment [11]. In the FIG 6.17, baseline subtracted $\Delta\varphi$ distribution compared with ALICE data in triggered D mesons $p_{\mathrm{T}}^{\mathrm{D}}$ intervals 3-5, 5-8 and 8-16 GeV/c

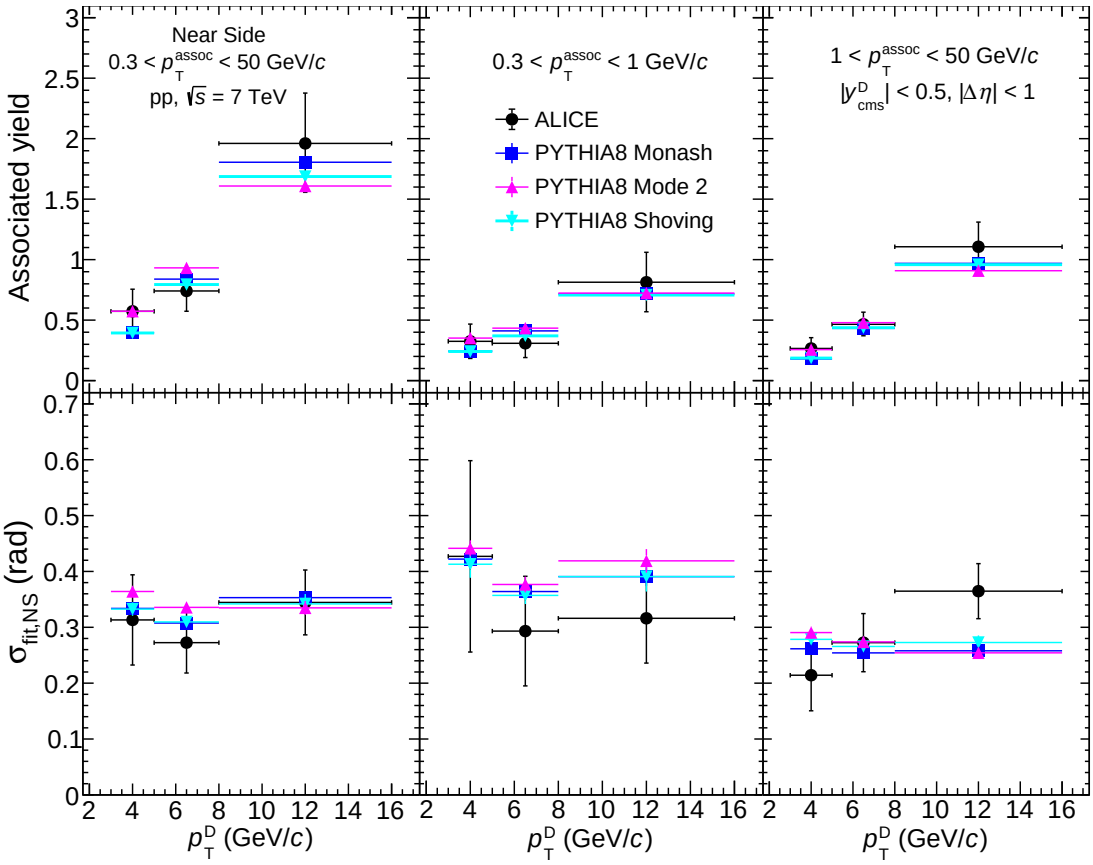

Figure 6.18: Comparison of ALICE result of average D meson near-side yields (top) and widths (σ) with PYTHIA8 (Monash, Mode 2, and Shoving) in pp collisions at $\sqrt{s} = 7$ TeV for $3 < p_{\mathrm{T}}^{\mathrm{D}} < 16$ GeV/c in different associated $p_{\mathrm{T}}^{\mathrm{assoc}}$ ranges.

and associate $p_{\mathrm{T}}^{\mathrm{assoc}}$ intervals 0.3-50, 0.3-1, and 1-50 GeV/c in the rapidity range $|y^D_{cms}| < 0.5$. Most of the fraction in the baseline is contributed by the underlying event and dominated by low p_{T} particles. The qualitative shape of the correlation function and the evolution of the near- and away-side peaks with trigger and associated particle p_{T} are consistent with ALICE measurement. However, PYTHIA measurements overestimate the away-side peak, especially at high $p_{\mathrm{T}}^{\mathrm{D}}$. This study suggests that PYTHIA needs to reform the fragmentation of particles produced at the recoiling jet. All the tunes of PYTHIA provide the same results for D meson and charged particle correlation. It is observed that the height of the correlation peak is increasing with $p_{\mathrm{T}}^{\mathrm{D}}$, which suggests the production of a higher number of particles in the jet accompanying the fragmenting charm quark when the energy of the trigger particle increases. However, no significant difference was observed among different CR and RH tunes in D mesons correlation measurements.

A more quantitative comparison of the near- and away-side peak features

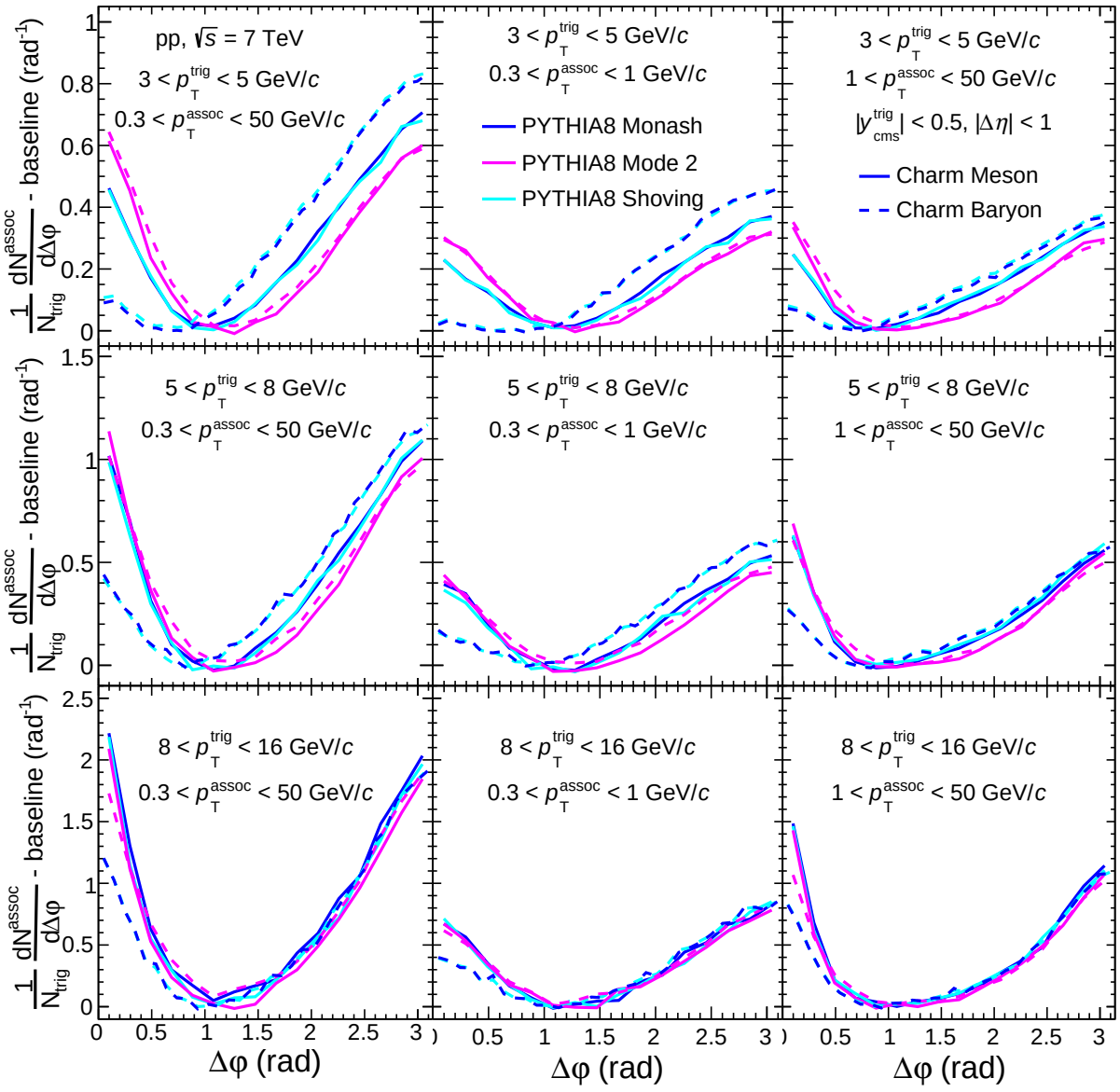

Figure 6.19: Comparison of average charmed meson and baryon azimuthal-correlation distribution derived from PYTHIA8 (Monash, Mode 2, and Shoving) after baseline subtraction for $3 < p_{\mathrm{T}}^{\mathrm{trig}} < 16$ GeV/c and for different associated $p_{\mathrm{T}}^{\mathrm{assoc}}$ ranges in pp collisions at $\sqrt{s} = 7$ TeV.

and the p_{T} evolution can be made by measuring the yields and widths of the peaks. As we discussed, the yields and widths are obtained by fitting with the generalized Gaussian function. Yield and width (σ) of the near-side peaks of D meson and charged particles correlation are shown in FIG 6.18 with different tunes and compared with ALICE results. The peak's yield is shown in the top panel, whereas widths are shown in the bottom panel. The per trigger associated yields of the peak are increasing with increasing trigger particle $p_{\mathrm{T}}^{\mathrm{D}}$. This is expected, as high energetic particles are, in general, produced by high energetic partons,

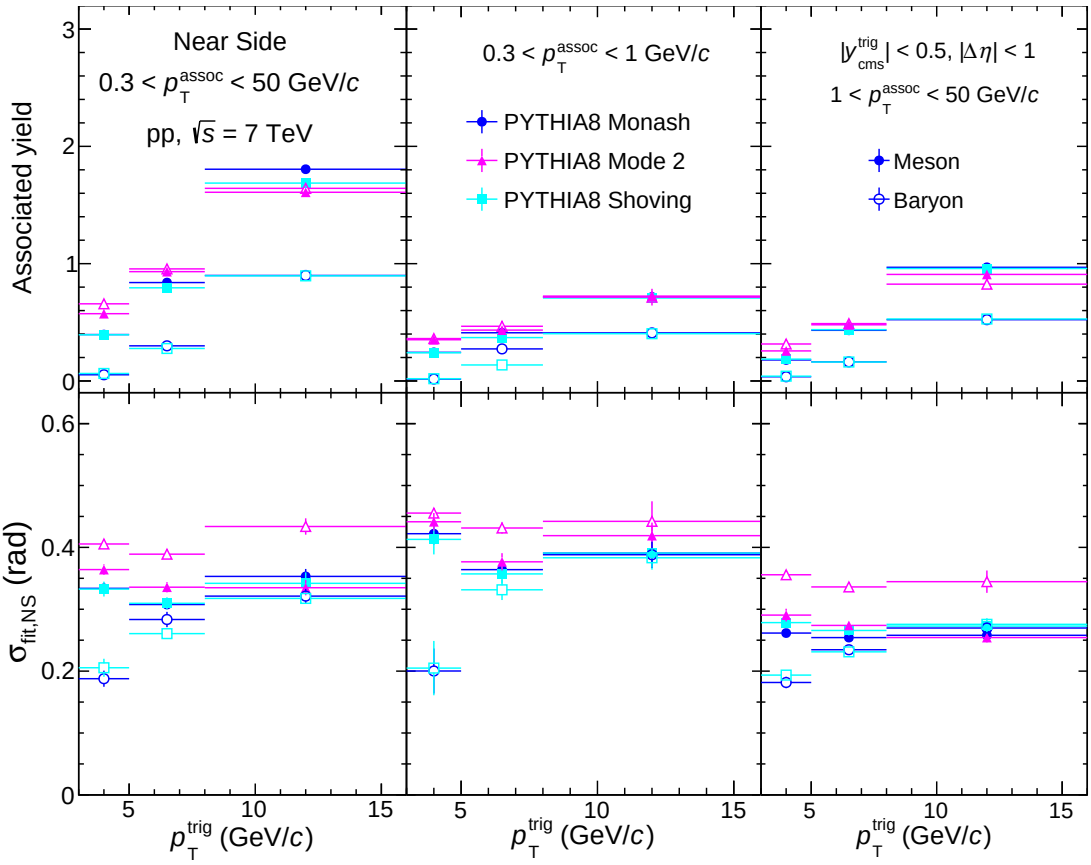

Figure 6.20: Comparison of average charmed meson and baryon near-side yields and widths (σ), derived from PYTHIA8 (Monash, Mode 2, and Shoving) after baseline subtraction in pp collisions at $\sqrt{s} = 7$ TeV for $3 < p_{\mathrm{T}}^{\mathrm{D}} < 16$ GeV/c in different associated $p_{\mathrm{T}}^{\mathrm{assoc}}$ ranges.

which in turn fragment into a more significant number of particles. Furthermore, as $p_{\mathrm{T}}^{\mathrm{assoc}}$ increases, the associated yield decreases. This is because heavy flavor quarks occupy a larger portion of the phase space during fragmentation. Hence, the remaining phase space for emitting further high p_{T} particles is limited, and most of the accompanying associated particles are softer. The near-side peak width (σ) is shown in the bottom panel of FIG 6.18. The widths estimated by PYTHIA and from the ALICE measurement are almost flat and consistent with each other within statistical uncertainty.

6.4.2 Comparison with charm baryons

Currently, statistics are not enough to measure the azimuthal correlation of charm baryons experimentally. However, it may be feasible in the upcoming LHC run

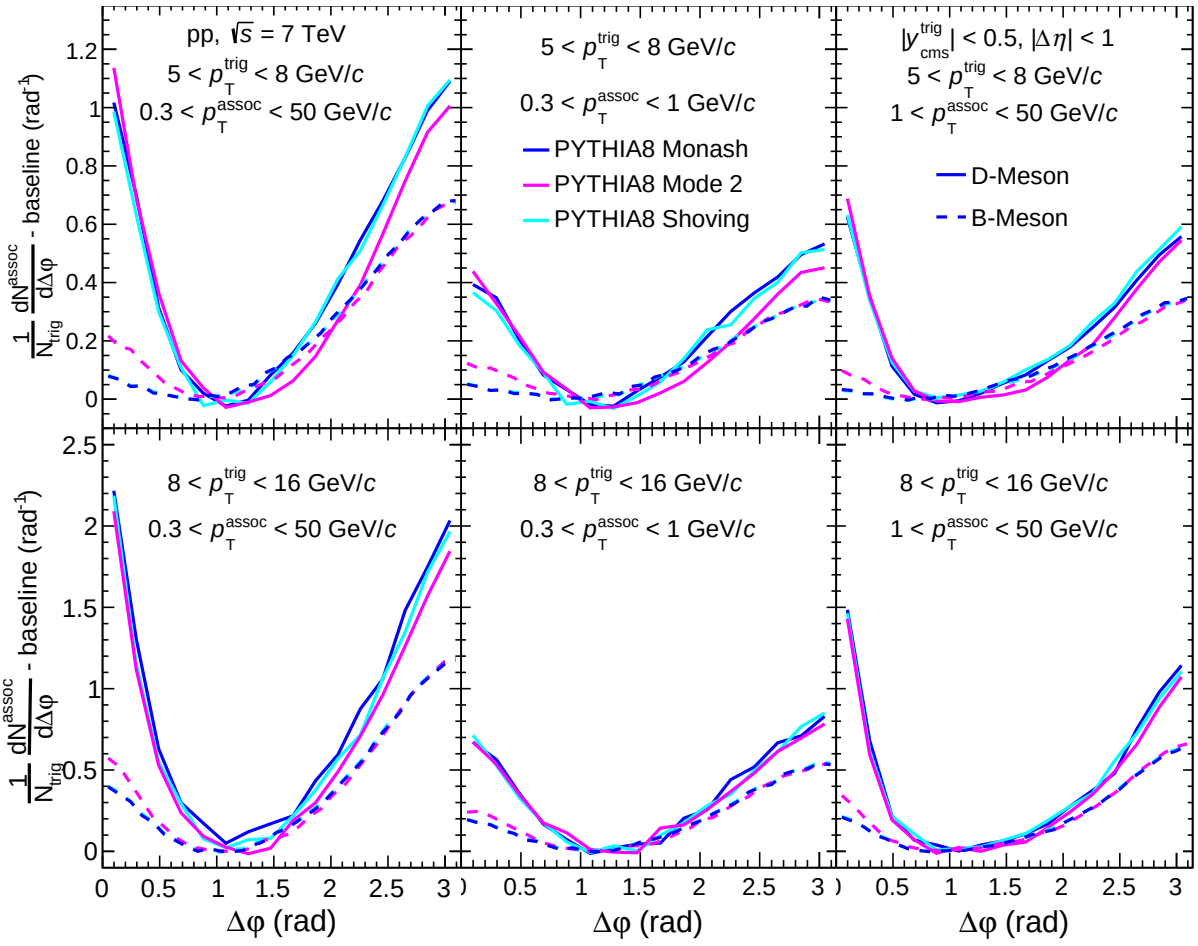

Figure 6.21: Comparison of average charm and beauty meson azimuthal-correlation distribution derived from PYTHIA8 (Monash, Mode 2, and Shoving) after baseline subtraction for $5 < p_{\mathrm{T}}^{\mathrm{trig}} < 16$ GeV/c in different associated $p_{\mathrm{T}}^{\mathrm{assoc}}$ ranges in pp collisions at $\sqrt{s} = 7$ TeV.

3. In the FIG 6.19, we attempt to provide a prediction for charm baryons fragmentation and modification of fragmentation compared to charm mesons. It is observed that the height of the near-side peaks is largely suppressed for charm baryons, derived by using default tune Monash and rope hadronization Shoving, whereas the height of the away-side peak is increased compared to charm mesons. In mode 2, charm meson and baryon peaks are consistent with each other.

Similar to the previous section, the near-side observables obtained from fitting are shown in FIG 6.20. It is clearly seen that the associated yield of charm baryons is almost half estimated from Monash and Shoving. In contrast, in mode 2, charm baryons yield is consistent with charm mesons yield. On the other hand, near-side widths from Monash and Shoving are suppressed with respect to mode 2 for baryons at low $p_{\mathrm{T}}^{\mathrm{trig}}$, whereas, at higher $p_{\mathrm{T}}^{\mathrm{trig}}$, widths are consistent with charm

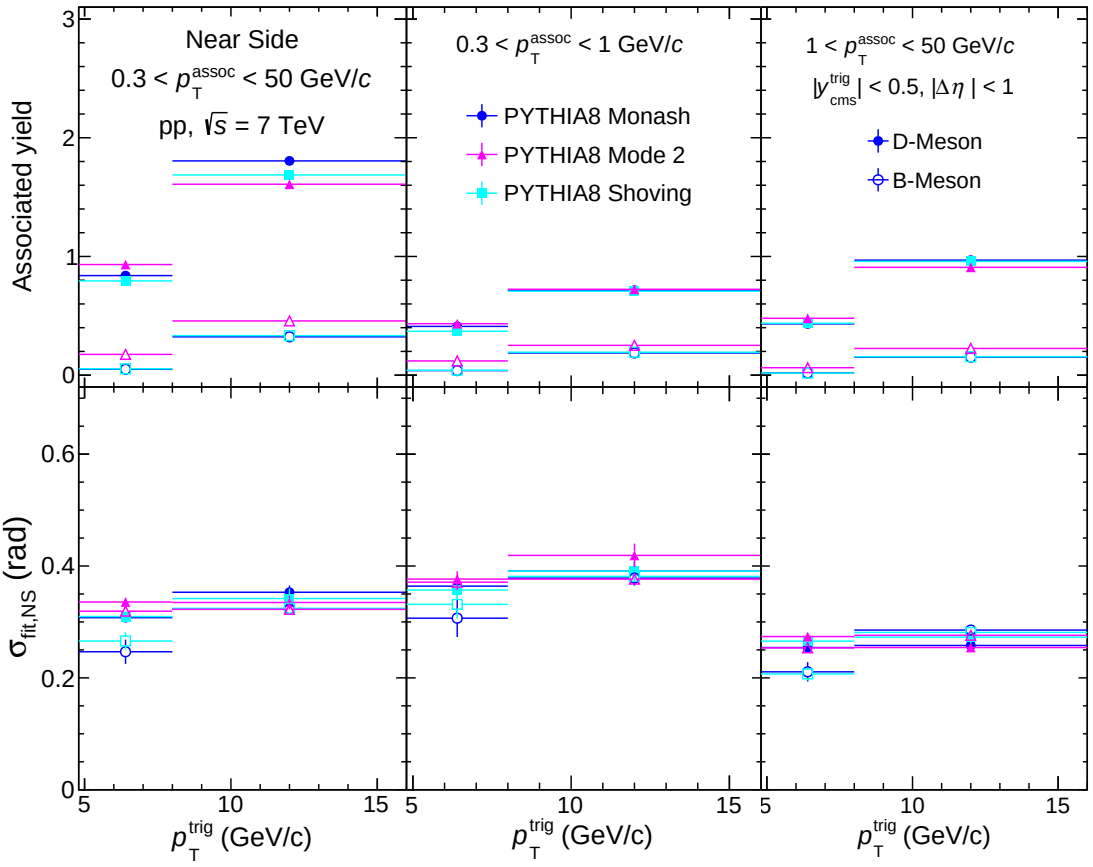

Figure 6.22: Comparison of average charm and beauty meson yields and widths (σ) derived from PYTHIA8 (Monash, Mode 2, and Shoving) after baseline subtraction in pp collisions at $\sqrt{s} = 7$ TeV for $5 < p_{\mathrm{T}}^{\mathrm{trig}} < 16$ GeV/c in different associated $p_{\mathrm{T}}^{\mathrm{assoc}}$ ranges.

mesons. A higher width of charm baryons can be seen from the Mode 2 tune for all the $p_{\mathrm{T}}^{\mathrm{trig}}$ and $p_{\mathrm{T}}^{\mathrm{assoc}}$ intervals. The trend was very similar to the production cross sections of charm baryons normalized by D^0 meson, where tune Monash underestimates the ALICE measurement, on the other hand, Mode 2 is in good agreement with the data, especially for Λ_c baryon [244]. The new CR tunes introduce new color reconnection topologies, including junctions, that enhance baryon production and charmonia, to a lesser extent. At the same time, multi-parton interactions (MPI) are observed in PYTHIA8 to increase the charm quark production significantly. This leads to the modification of the relative abundances of the charm hadron species. The relative baryon enhancement is only observed when the MPI is coupled to a color reconnection mode beyond the leading color approximation. It is observed that for the charm mesons, predictions from the PYTHIA8 generator with the different tunes are reasonably similar.

6.4.3 Comparison with beauty mesons

A similar comparison is made between charm and beauty meson correlation features. The $\Delta\varphi$ distribution of charm mesons with charged particles and beauty mesons with charged particles are shown in FIG 6.21 for $p_{\mathrm{T}}^{\mathrm{trig}}$ 5-8 and 8-16 GeV/c. Here, a comparison between charm and beauty mesons fragmentation for the $p_{\mathrm{T}}^{\mathrm{trig}}$ 3-5 GeV/c is not shown as the mass of beauty is $\sim$ 5 GeV/c, which results in almost a flat near-side peak. The height of the near- and away-side peaks of the correlation function obtained for B mesons are very small compared to D mesons correlation peaks as the available energy of B mesons for fragmentation is small compared to D mesons in the same p_{T} range. A more quantitative comparison of correlation peaks from D mesons and B mesons fragmentation can be seen in FIG. 6.22. Yields from D mesons are about 4-5 times higher than from B mesons. One of the reasons for the difference in yield can be attributed to the mass hierarchy between charm and beauty quarks, this hierarchy creeps into the global fragmentation function as a factor of an inverse mass square. At higher $p_{\mathrm{T}}^{\mathrm{trig}}$, B mesons associated yield increases more rapidly than D mesons. It is also seen that B mesons associated yield for the near-side peak is larger with Mode 2 compared to Shoving and Monash. The correlation peaks exhibit nearly uniform widths, indicating no discernible distinction between D mesons and B mesons. This observation suggests that the dead-cone effect does not have a significant impact on the current level of precision. The dead-cone effect is an inherent characteristic of gauge field theories, whereby radiation from an emitter with mass m and energy E is suppressed at angular scales smaller than m/E relative to the emitter's direction. However, it remains intriguing to investigate whether the dead-cone effect will have a notable influence on the width of light flavor correlations.

Chapter 7

Summary and outlook

The aim of this thesis is to investigate the correlations between heavy-flavour particles in systems of different sizes, ranging from small to large. The study of these correlations can provide valuable insights into the properties of direct jets and the dynamics of initial partons. By measuring the distribution of azimuthal angles between high transverse-momentum trigger particles and associated charged particles, it is possible to identify a "near-side" peak at $\Delta\varphi = 0$ and an "away-side" peak at $\Delta\varphi = \pi$, which are indicative of the fragmentation of the same parton and the other parton produced in the hard scattering, respectively. In this thesis, the azimuthal correlation distributions between heavy-flavour hadron decay electrons and associated charged particles are measured in pp, p–Pb, and Pb–Pb collisions at $\sqrt{s_{\rm NN}} = 5.02$ TeV using the ALICE subdetectors. The results are reported for electrons with transverse momentum between 4 and 16 GeV/c and pseudorapidity between -0.6 and 0.6, and associated charged particles with transverse momentum between 1 and 7 GeV/c and a relative pseudorapidity separation with the leading electron of less than 1. The correlation measurements are performed to study and characterize the fragmentation and hadronization of heavy quarks, and the correlation structures are characterized using a constant and two von Mises functions for each peak. The measurements from pp collisions are compared with results from p–Pb and Pb–Pb collisions systems. Finally, the $\Delta\varphi$ distribution and peak observables in pp and p–Pb collisions are compared with calculations from Monte Carlo event generators such as PYTHIA8 and EPOS3. The findings of this thesis is summarized below

- The measurement of heavy flavour hadron decay electron with charged particle shows consistent results for pp and p–Pb collisions systems, while a

modification is seen in Pb–Pb collisions.

- The correlation function's near- and away-side peaks show similar evolution in pp and p–Pb collisions across all considered kinematic ranges, indicating the absence of observable modifications to heavy quark fragmentation and hadronization due to cold-nuclear-matter effects within the current measurement precision.

- Per-trigger yields decrease with increasing $p_{\mathrm{T}}^{\mathrm{assoc}}$, and the near-side width tends to decrease with $p_{\mathrm{T}}^{\mathrm{assoc}}$, while the away-side width does not show a pronounced trend in both collision systems.

- The results are compared with predictions from Monte Carlo event generators PYTHIA8 (with Monash tune for pp and Angantyr for p–Pb collisions) and EPOS3, and the PYTHIA8 model provides the best description for both yields and widths of the peaks. The relative fractions of electrons from charm- and beauty-hadron decays have a strong dependence on p_{T}, and the correlation distribution was studied in the kinematic regions $4 < p_{\mathrm{T}}^{\mathrm{e}} < 7$ GeV/c and $7 < p_{\mathrm{T}}^{\mathrm{e}} < 16$ GeV/c, where the latter range is dominated by beauty-hadron decays.

- The per-trigger yields in pp and p–Pb collisions exhibit a systematic increase for the $7 < p_{\mathrm{T}}^{\mathrm{e}} < 16$ GeV/c range in comparison to the $4 < p_{\mathrm{T}}^{\mathrm{e}} < 7$ range. This can be attributed to the higher energy of the initial heavy quark, which enables the generation of more particles in the parton shower.

- The larger boost of the initial heavy quark causes stronger collimation of the peaks with increasing $p_{\mathrm{T}}^{\mathrm{e}}$ for both charm- and beauty-origin contributions, which compensates the broader peak widths for trigger electrons originating from beauty-hadron decays. This effect increases with $p_{\mathrm{T}}^{\mathrm{e}}$.

- The study of identified particle at $\sqrt{s_{\mathrm{NN}}} = 2.76$ TeV, aimed to establish the Angantyr model for heavy-ion collisions and to examine how multi-parton interactions (MPI) and color reconnection (CR) influence experimentally measured quantities. We also looked into the role of string shoving within the rope hadronization framework and its effects on particle production.

The Angantyr model combines several nucleon-nucleon collisions to build a proton–nucleus (p–A) or nucleus–nucleus (A–A) collision and investigates medium-like properties without relying on hydrodynamics.

- The results demonstrate that MPI with CR and string shoving configurations produce testable results, as seen in the charged-particle multiplicity (N_{ch}) and mean transverse momentum ($\langle p_{\mathrm{T}} \rangle$) distributions. We were able to explain these distributions well using PYTHIA8 Angantyr with appropriate tuning.

- The collective nature of the produced particles is investigated by examining the ratio of particle yields to pions and kaons. Our findings suggest that PYTHIA8 Angantyr with MPI+CR and hadronization via string shoving can mimic signs of collectivity. We observed a peak around 3 GeV/c in the ratio of proton over pion, which is consistent with the radial flow observed in experimental data. We also observed a similar rise in all the strange baryon over pion ratios. We conclude that PYTHIA+Angantyr provides favorable tunes for studying relevant observables in heavy-ion collisions. However, we found that the model fails in the low p_{T} regime compared to measurements from ALICE.

- It is observed that the slope of strange particles to pion ratio as a function of centrality is more significant for strange heavy particles. We report that the peak of strange baryon to pion ratio and strange baryon to kaon as a function of p_{T} shifts toward higher p_{T} for heavier strange particles. This shows that strangeness enhancement is dominant in strange heavy particles, which is a consequence of color strings overlapping at higher densities in accordance with CR and string shoving.

- To investigate the production of heavy-flavour hadrons in different colliding systems, we used the PYTHIA+Angantyr model to study the azimuthal angular correlations of electrons in pp, p–Pb, and Pb–Pb collisions at $\sqrt{s_{\mathrm{NN}}}$ = 5.02 TeV.

- By analyzing the yields and widths associated with the near-side and away-

side correlation peaks as a function of the associated p_{T} for various trigger p_{T} ranges, we observed small jet-quenching in Pb–Pb collisions compared with pp collisions, likely due to MPI+CR and higher density string medium.

- Furthermore, we found that beyond leading color reconnection modes show a small increment of peak height in Pb–Pb collisions. It is observed that MPI has no significant effect on fragmentation, as MPI mostly contributes to the baseline through soft processes.

- The associated yields are significantly increased by initial and final state radiation effects, as these radiations contribute to more collinear particle production. No significant modifications were observed in fragmentation due to hadron-level processes, i.e., BE effect and rescatter effect, indicating that associated yields per trigger particle are mainly generated by parton fragmentation. Overall, our findings suggest that the PYTHIA+Angantyr model provides valuable insights into the production of heavy-flavour hadrons in different colliding systems.

- The fragmentation of heavy quarks explored by analyzing the azimuthal angular correlations of heavy-flavour hadrons (such as charm and beauty mesons, and charm baryons) in pp collisions at $\sqrt{s} = 7$ TeV using PYTHIA8. The inclusion of various particle species allowed us to isolate possible modifications in particle production and fragmentation due to the differences in quark contents and mass. We investigated heavy-flavour jet production using different PYTHIA8 tunes, and calculated the correlations of heavy-flavour hadrons at different triggers and associated p_{T} intervals. Using double generalized Gaussian functions, we calculated yields and widths for the near-side and away-side correlation peaks and studied their dependence on associated p_{T} for different trigger p_{T} ranges.

- We found that PYTHIA8's near-side correlation distributions and observables for D mesons were consistent with ALICE measurements, but the away-side observable was slightly overestimated due to the lack of explicit inclusion of NLO.

- The low $p_{\mathrm{T}}^{\mathbf{assoc}}$ particles have a higher production rate than high $p_{\mathrm{T}}^{\mathbf{assoc}}$ particles due to limited phase space, yields were found to be higher at low $p_{\mathrm{T}}^{\mathrm{assoc}}$ for the same $p_{\mathrm{T}}^{\mathrm{trig}}$.

- Compared to charm meson yields, near-side associated yields of charm baryons were suppressed in Monash and Shoving tunes, but negligible in Mode 2. These results align with the charm baryons production cross sections calculated by the ALICE experiment.

- Near-side yields from D mesons were 4-5 times greater than B mesons yields for the same $p_{\mathrm{T}}^{\mathrm{trig}}$, which could be due to the availability of more energy for D meson fragmentation.

- We found no significant difference between D and B mesons widths in the same trigger and associated p_{T} ranges. The dead cone effect did not have a major impact on the widths of D and B mesons as they are both heavy particles. Nonetheless, investigating the dead-cone effect in heavy quarks while comparing it with light quarks correlation distribution would be of interest.

The outlook of my experimental work is to study the potential modification of jet fragmentation function in the hot and dense quark-gluon plasma medium. Currently, we are conducting a correlation study on Pb–Pb collisions. Additionally, we are collecting the run 3 ALICE data, which features high luminosity and statistics. To analyze this data at a high rate, we are developing our analysis task into the O2 framework, which is also ongoing. Our research also involves conducting phenomenological studies to gain more insight into fragmentation and hadronization, as well as to further explore the QGP medium.

Bibliography

[1] **ALICE** Collaboration, "The ALICE experiment – A journey through QCD," arXiv:2211.04384 [nucl-ex]. iii, 2

[2] **ALICE** Collaboration, S. Acharya *et al.*, "Measurement of electrons from semileptonic heavy-flavour hadron decays at midrapidity in pp and Pb-Pb collisions at $\sqrt{s_{\rm NN}} = 5.02$ TeV," *Phys. Lett. B* **804** (2020) 135377, arXiv:1910.09110 [nucl-ex]. 2, 142

[3] **CMS** Collaboration, A. M. Sirunyan *et al.*, "Nuclear modification factor of $\rm D^0$ mesons in PbPb collisions at $\sqrt{s_{\rm NN}} = 5.02$ TeV," *Phys. Lett. B* **782** (2018) 474–496, arXiv:1708.04962 [nucl-ex]. 188

[4] **LHCb** Collaboration, R. Aaij *et al.*, "Measurements of prompt charm production cross-sections in pp collisions at $\sqrt{s} = 13$ TeV," *JHEP* **03** (2016) 159, arXiv:1510.01707 [hep-ex]. [Erratum: JHEP 09, 013 (2016), Erratum: JHEP 05, 074 (2017)].

[5] **ALICE** Collaboration, S. Acharya *et al.*, "Measurement of inclusive charged-particle b-jet production in pp and p-Pb collisions at $\sqrt{s_{\rm NN}} = 5.02$ TeV," *JHEP* **01** (2022) 178, arXiv:2110.06104 [nucl-ex].

[6] **ALICE** Collaboration, S. Acharya *et al.*, "Measurement of the production of charm jets tagged with $\rm D^0$ mesons in pp collisions at $\sqrt{s} = 5.02$ and 13 TeV," *JHEP* **06** (2023) 133, arXiv:2204.10167 [nucl-ex]. iii, 2

[7] B. A. Kniehl, G. Kramer, I. Schienbein, and H. Spiesberger, "Finite-mass effects on inclusive B meson hadroproduction," *Phys. Rev. D* **77** (2008) 014011, arXiv:0705.4392 [hep-ph]. iii, 2

[8] M. Cacciari, S. Frixione, M. L. Mangano, P. Nason, and G. Ridolfi, "QCD

analysis of first b cross-section data at 1.96-TeV," *JHEP* **07** (2004) 033, arXiv:hep-ph/0312132.

[9] B. A. Kniehl, G. Kramer, I. Schienbein, and H. Spiesberger, "Collinear subtractions in hadroproduction of heavy quarks," *Eur. Phys. J. C* **41** (2005) 199–212, arXiv:hep-ph/0502194.

[10] M. Cacciari and P. Nason, "Charm cross-sections for the Tevatron Run II," *JHEP* **09** (2003) 006, arXiv:hep-ph/0306212. iii, 2

[11] **ALICE** Collaboration, J. Adam *et al.*, "Measurement of azimuthal correlations of D mesons and charged particles in pp collisions at $\sqrt{s} = 7$ TeV and p-Pb collisions at $\sqrt{s_{\rm NN}} = 5.02$ TeV," *Eur. Phys. J. C* **77** no. 4, (2017) 245, arXiv:1605.06963 [nucl-ex]. iv, 29, 156, 161, 190, 197, 200

[12] **ALICE** Collaboration, S. Acharya *et al.*, "Azimuthal correlations of prompt D mesons with charged particles in pp and p–Pb collisions at $\sqrt{s_{NN}} = 5.02$ TeV," *Eur. Phys. J. C* **80** no. 10, (2020) 979, arXiv:1910.14403 [nucl-ex]. 29, 98, 156, 161, 187

[13] **ALICE** Collaboration, S. Acharya *et al.*, "Investigating charm production and fragmentation via azimuthal correlations of prompt D mesons with charged particles in pp collisions at $\sqrt{\mathbf{s}} = \mathbf{13}$ TeV," *Eur. Phys. J. C* **82** no. 4, (2022) 335, arXiv:2110.10043 [nucl-ex]. iv, 29, 173, 187, 197

[14] A. Ortiz Velasquez, P. Christiansen, E. Cuautle Flores, I. Maldonado Cervantes, and G. Paić, "Color Reconnection and Flowlike Patterns in *pp* Collisions," *Phys. Rev. Lett.* **111** no. 4, (2013) 042001, arXiv:1303.6326 [hep-ph]. vi, 61, 175, 185

[15] R. Singh, S. Khade, and A. Roy, "Jet fragmentation via azimuthal angular correlations of heavy flavors in pp collisions at s=7 TeV," *Phys. Rev. C* **107** no. 2, (2023) 025206, arXiv:2301.12881 [hep-ph]. viii, 29

[16] "Suman Deb, Thesis, https://cds.cern.ch/record/2838698?ln=en,". vii, xxix, 5, 38

[17] S. Bethke, "Determination of the QCD coupling α_s," *J. Phys. G* **26** (2000) R27, arXiv:hep-ex/0004021. vii, 8

[18] **Particle Data Group** Collaboration, K. A. Olive *et al.*, "Review of Particle Physics," *Chin. Phys. C* **38** (2014) 090001. vii, 8

[19] B. Betz, "Jet Propagation and Mach-Cone Formation in (3+1)-dimensional Ideal Hydrodynamics," other thesis, 10, 2009. vii, 9, 14

[20] P. Petreczky, "Lattice QCD at non-zero temperature," *J. Phys. G* **39** (2012) 093002, arXiv:1203.5320 [hep-lat]. vii, 11

[21] **HotQCD** Collaboration, A. Bazavov *et al.*, "Equation of state in (2+1)-flavor QCD," *Phys. Rev. D* **90** (2014) 094503, arXiv:1407.6387 [hep-lat]. vii, 11

[22] **ALICE** Collaboration, B. Abelev *et al.*, "D meson elliptic flow in non-central Pb-Pb collisions at $\sqrt{s_{\rm NN}} = 2.76$TeV," *Phys. Rev. Lett.* **111** (2013) 102301, arXiv:1305.2707 [nucl-ex]. viii, 18, 19

[23] Y.-J. Lee, "Jet Quenching at RHIC and the LHC," *J. Phys. Conf. Ser.* **446** (2013) 012001. viii, 23

[24] **ALICE** Collaboration, K. Aamodt *et al.*, "Particle-yield modification in jet-like azimuthal di-hadron correlations in Pb-Pb collisions at $\sqrt{s_{NN}} = 2.76$ TeV," *Phys. Rev. Lett.* **108** (2012) 092301, arXiv:1110.0121 [nucl-ex]. viii, 25, 26

[25] **ALICE** Collaboration, J. Adam *et al.*, "Enhanced production of multi-strange hadrons in high-multiplicity proton-proton collisions," *Nature Phys.* **13** (2017) 535–539, arXiv:1606.07424 [nucl-ex]. viii, 22, 27, 173

[26] **CMS** Collaboration, V. Khachatryan *et al.*, "Measurement of long-range near-side two-particle angular correlations in pp collisions at $\sqrt{s}$ =13 TeV," *Phys. Rev. Lett.* **116** no. 17, (2016) 172302, arXiv:1510.03068 [nucl-ex]. viii, 28

[27] "The CERN accelerator complex:, https://cds.cern.ch/record/2197559.,". viii, 34

[28] "ALICE detector:, https://alice-figure.web.cern.ch/node/11218.,". viii, 36

[29] P. G. Kuijer, "Commissioning and Prospects for Early Physics with ALICE," *Nucl. Phys. A* **830** (2009) 81C–88C, arXiv:0907.5060 [hep-ex]. viii, 37

[30] **ALICE** Collaboration, K. Aamodt *et al.*, "Alignment of the ALICE Inner Tracking System with cosmic-ray tracks," *JINST* **5** (2010) P03003, arXiv:1001.0502 [physics.ins-det]. viii, 39, 40

[31] "ITS performance:, https://alice-figure.web.cern.ch/node/9865.,". ix, 42

[32] **ALICE** Collaboration, A. Mathis, "Study of the dE/dx resolution of a GEM Readout Chamber prototype for the upgrade of the ALICE TPC," *EPJ Web Conf.* **174** (2018) 01002, arXiv:1707.05779 [physics.ins-det]. ix, 42

[33] A. Maire, *Production des baryons multi-étranges au LHC dans les collisions proton-proton avec l'expérience ALICE*. PhD thesis, Strasbourg U., 2011. ix, 42

[34] C. Lippmann, "Performance of the ALICE Time Projection Chamber," *Phys. Procedia* **37** (2012) 434–441. ix, 44

[35] **ALICE** Collaboration, R. Schicker, "Overview of ALICE results in pp, pA and AA collisions," *EPJ Web Conf.* **138** (2017) 01021, arXiv:1701.04810 [nucl-ex]. ix, 46

[36] **ALICE** Collaboration, P. Cortese *et al.*, "ALICE electromagnetic calorimeter technical design report,". ix, 46

[37] **ALICE** Collaboration, A. Fantoni, "The ALICE Electromagnetic Calorimeter: EMCAL," *J. Phys. Conf. Ser.* **293** (2011) 012043. ix, 46

[38] **ALICE** Collaboration, P. Cortese *et al.*, "ALICE technical design report on forward detectors: FMD, T0 and V0,". ix, 49

[39] T. R. P.-R. Aronsson, *Cross section of bottom electrons in proton-proton collisions in the ALICE experiment*. PhD thesis, Yale U., 2014. ix, 53, 54, 55

[40] "ALICE trigger data-acquisition high-level trigger and control system : Technical Design Report, https://cds.cern.ch/record/684651,". x, 57

[41] **ALICE** Collaboration, B. Abelev *et al.*, "Measurement of electrons from semileptonic heavy-flavour hadron decays in pp collisions at \sqrts = 7 TeV," *Phys. Rev. D* **86** (2012) 112007, arXiv:1205.5423 [hep-ex]. x, 2, 76, 77

[42] **ALICE** Collaboration, B. B. Abelev *et al.*, "Performance of the ALICE Experiment at the CERN LHC," *Int. J. Mod. Phys. A* **29** (2014) 1430044, arXiv:1402.4476 [nucl-ex]. xxix, 38

[43] S. F. Novaes, "Standard model: An Introduction," in *10th Jorge Andre Swieca Summer School: Particle and Fields*, pp. 5–102. 1, 1999. arXiv:hep-ph/0001283. 1, 33

[44] H. Satz, "The Quark-Gluon Plasma: A Short Introduction," *Nucl. Phys. A* **862-863** (2011) 4–12, arXiv:1101.3937 [hep-ph]. 1

[45] **STAR** Collaboration, J. Adams *et al.*, "Experimental and theoretical challenges in the search for the quark gluon plasma: The STAR Collaboration's critical assessment of the evidence from RHIC collisions," *Nucl. Phys. A* **757** (2005) 102–183, arXiv:nucl-ex/0501009. 1, 11, 13, 18

[46] **ALICE** Collaboration, S. Acharya *et al.*, "Measurement of D^0 , D^+ , D^{*+} and D_s^+ production in pp collisions at $\sqrt{s}$ = 5.02 TeV with ALICE," *Eur. Phys. J. C* **79** no. 5, (2019) 388, arXiv:1901.07979 [nucl-ex]. 2

[47] **ALICE** Collaboration, S. Acharya *et al.*, "Production of muons from heavy-flavour hadron decays in pp collisions at $\sqrt{s} = 5.02$ TeV," *JHEP* **09** (2019) 008, arXiv:1905.07207 [nucl-ex].

[48] **ALICE** Collaboration, S. Acharya *et al.*, "Measurement of beauty and charm production in pp collisions at $\sqrt{s} = 5.02$ TeV via non-prompt and prompt D mesons," *JHEP* **05** (2021) 220, arXiv:2102.13601 [nucl-ex].

[49] **ALICE** Collaboration, B. Abelev *et al.*, "Heavy flavour decay muon production at forward rapidity in proton–proton collisions at $\sqrt{s} = 7$ TeV," *Phys. Lett. B* **708** (2012) 265–275, arXiv:1201.3791 [hep-ex].

[50] **ALICE** Collaboration, B. Abelev *et al.*, "Measurement of charm production at central rapidity in proton-proton collisions at $\sqrt{s} = 2.76$ TeV," *JHEP* **07** (2012) 191, arXiv:1205.4007 [hep-ex].

[51] **LHCb** Collaboration, R. Aaij *et al.*, "Measurements of prompt charm production cross-sections in pp collisions at $\sqrt{s} = 5$ TeV," *JHEP* **06** (2017) 147, arXiv:1610.02230 [hep-ex].

[52] **ALICE** Collaboration, B. Abelev *et al.*, "Measurement of electrons from beauty hadron decays in *pp* collisions at $\sqrt{s} = 7$ TeV," *Phys. Lett. B* **721** (2013) 13–23, arXiv:1208.1902 [hep-ex]. [Erratum: Phys.Lett.B 763, 507–509 (2016)].

[53] **ALICE** Collaboration, B. B. Abelev *et al.*, "Measurement of electrons from semileptonic heavy-flavor hadron decays in *pp* collisions at $\sqrt{s} = 2.76$ TeV," *Phys. Rev. D* **91** no. 1, (2015) 012001, arXiv:1405.4117 [nucl-ex].

[54] **LHCb** Collaboration, R. Aaij *et al.*, "Measurement of the $B^{\pm}$ production cross-section in *pp* collisions at $\sqrt{s} = 7$ TeV," *JHEP* **04** (2012) 093, arXiv:1202.4812 [hep-ex].

[55] **ATLAS** Collaboration, G. Aad *et al.*, "Measurement of the b-hadron production cross section using decays to $D^*\mu^- X$ final states in pp collisions at sqrt(s) = 7 TeV with the ATLAS detector," *Nucl. Phys. B* **864** (2012) 341–381, arXiv:1206.3122 [hep-ex].

[56] **ATLAS** Collaboration, G. Aad *et al.*, "Measurement of the differential

cross-section of B^+ meson production in pp collisions at $\sqrt{s} = 7$ TeV at ATLAS," *JHEP* **10** (2013) 042, arXiv:1307.0126 [hep-ex].

[57] **CMS** Collaboration, S. Chatrchyan *et al.*, "Measurement of the Inclusive Cross Section $\sigma(pp \to b\bar{b}X \to \mu\mu X')$ at $\sqrt{s} = 7$ TeV," *JHEP* **06** (2012) 110, arXiv:1203.3458 [hep-ex].

[58] **CMS** Collaboration, V. Khachatryan *et al.*, "Measurement of the B^+ Production Cross Section in pp Collisions at $\sqrt{s} = 7$˜TeV," *Phys. Rev. Lett.* **106** (2011) 112001, arXiv:1101.0131 [hep-ex].

[59] **CMS** Collaboration, S. Chatrchyan *et al.*, "Measurement of the B^0 production cross section in pp Collisions at $\sqrt{s} = 7$ TeV," *Phys. Rev. Lett.* **106** (2011) 252001, arXiv:1104.2892 [hep-ex].

[60] **CMS** Collaboration, S. Chatrchyan *et al.*, "Measurement of the Strange B Meson Production Cross Section with J/Psi ϕ Decays in pp Collisions at $\sqrt{s} = 7$ TeV," *Phys. Rev. D* **84** (2011) 052008, arXiv:1106.4048 [hep-ex].

[61] **CMS** Collaboration, V. Khachatryan *et al.*, "Measurement of the total and differential inclusive B^+ hadron cross sections in pp collisions at $\sqrt{s} = 13$ TeV," *Phys. Lett. B* **771** (2017) 435–456, arXiv:1609.00873 [hep-ex]. 2

[62] B. A. Kniehl, G. Kramer, I. Schienbein, and H. Spiesberger, "Inclusive Charmed-Meson Production at the CERN LHC," *Eur. Phys. J. C* **72** (2012) 2082, arXiv:1202.0439 [hep-ph]. 2

[63] B. A. Kniehl, G. Kramer, I. Schienbein, and H. Spiesberger, "Inclusive B-Meson Production at the LHC in the GM-VFN Scheme," *Phys. Rev. D* **84** (2011) 094026, arXiv:1109.2472 [hep-ph].

[64] M. Cacciari, S. Frixione, N. Houdeau, M. L. Mangano, P. Nason, and G. Ridolfi, "Theoretical predictions for charm and bottom production at the LHC," *JHEP* **10** (2012) 137, arXiv:1205.6344 [hep-ph]. 2, 163, 190

[65] **ALICE** Collaboration, S. Acharya *et al.*, "First measurement of Λc+ production down to pT=0 in pp and p-Pb collisions at sNN=5.02 TeV," *Phys. Rev. C* **107** no. 6, (2023) 064901, arXiv:2211.14032 [nucl-ex]. 2

[66] **ALICE** Collaboration, "First measurement of Ω_c^0 production in pp collisions at $\sqrt{s} = 13$ TeV," arXiv:2205.13993 [nucl-ex].

[67] **ALICE** Collaboration, S. Acharya *et al.*, "Measurement of Prompt D^0, Λ_c^+, and $\Sigma_c^{0,++}(2455)$ Production in Proton–Proton Collisions at $\sqrt{s} =$ 13 TeV," *Phys. Rev. Lett.* **128** no. 1, (2022) 012001, arXiv:2106.08278 [hep-ex].

[68] **ALICE** Collaboration, S. Acharya *et al.*, "Observation of a multiplicity dependence in the pT-differential charm baryon-to-meson ratios in proton–proton collisions at s=13 TeV," *Phys. Lett. B* **829** (2022) 137065, arXiv:2111.11948 [nucl-ex].

[69] **LHCb** Collaboration, R. Aaij *et al.*, "Prompt charm production in pp collisions at sqrt(s)=7 TeV," *Nucl. Phys. B* **871** (2013) 1–20, arXiv:1302.2864 [hep-ex].

[70] **ALICE** Collaboration, S. Acharya *et al.*, "Λ_c^+ production in pp collisions at $\sqrt{s} = 7$ TeV and in p-Pb collisions at $\sqrt{s_{\rm NN}} = 5.02$ TeV," *JHEP* **04** (2018) 108, arXiv:1712.09581 [nucl-ex].

[71] **ALICE** Collaboration, S. Acharya *et al.*, "Λ_c^+ Production and Baryon-to-Meson Ratios in pp and p-Pb Collisions at $\sqrt{s_{NN}}$=5.02 TeV at the LHC," *Phys. Rev. Lett.* **127** no. 20, (2021) 202301, arXiv:2011.06078 [nucl-ex].

[72] **ALICE** Collaboration, S. Acharya *et al.*, "Λ_c^+ production in *pp* and in *p*-Pb collisions at $\sqrt{s_{NN}}$=5.02 TeV," *Phys. Rev. C* **104** no. 5, (2021) 054905, arXiv:2011.06079 [nucl-ex].

[73] **CMS** Collaboration, A. M. Sirunyan *et al.*, "Production of Λ_c^+ baryons in proton-proton and lead-lead collisions at $\sqrt{s_{\rm NN}} = 5.02$ TeV," *Phys. Lett. B* **803** (2020) 135328, arXiv:1906.03322 [hep-ex].

[74] **ALICE** Collaboration, S. Acharya *et al.*, "First measurement of Ξ_c^0 production in pp collisions at $\sqrt{s} = 7$ TeV," *Phys. Lett. B* **781** (2018) 8–19, arXiv:1712.04242 [hep-ex].

[75] **ALICE** Collaboration, S. Acharya *et al.*, "Measurement of the production cross section of prompt Ξ_c^0 baryons at midrapidity in pp collisions at $\sqrt{s} =$ 5.02 TeV," *JHEP* **10** (2021) 159, arXiv:2105.05616 [nucl-ex].

[76] **ALICE** Collaboration, S. Acharya *et al.*, "Measurement of the Cross Sections of Ξ_c^0 and Ξ_c^+ Baryons and of the Branching-Fraction Ratio $\mathrm{BR}(\Xi_c^0 \to \Xi^- e^+ \nu_e)/\mathrm{BR}(\Xi_c^0 \to \Xi^- \pi^+)$ in pp collisions at 13 TeV," *Phys. Rev. Lett.* **127** no. 27, (2021) 272001, arXiv:2105.05187 [nucl-ex]. 2

[77] L. Ravagli and R. Rapp, "Quark Coalescence based on a Transport Equation," *Phys. Lett. B* **655** (2007) 126–131, arXiv:0705.0021 [hep-ph]. 2

[78] J. R. Christiansen and P. Z. Skands, "String Formation Beyond Leading Colour," *JHEP* **08** (2015) 003, arXiv:1505.01681 [hep-ph]. 2, 161, 187

[79] M. He and R. Rapp, "Charm-Baryon Production in Proton-Proton Collisions," *Phys. Lett. B* **795** (2019) 117–121, arXiv:1902.08889 [nucl-th]. 2

[80] D. Ebert, R. N. Faustov, and V. O. Galkin, "Spectroscopy and Regge trajectories of heavy baryons in the relativistic quark-diquark picture," *Phys. Rev. D* **84** (2011) 014025, arXiv:1105.0583 [hep-ph]. 2

[81] **CMS** Collaboration, S. Chatrchyan *et al.*, "Observation of a New Boson at a Mass of 125 GeV with the CMS Experiment at the LHC," *Phys. Lett. B* **716** (2012) 30–61, arXiv:1207.7235 [hep-ex]. 4

[82] W. J. Marciano and H. Pagels, "Quantum Chromodynamics: A Review," *Phys. Rept.* **36** (1978) 137. 5

[83] G. Punetha and H. C. Chandola, "Dual Meissner Effect and Quark Confinement Potential in SU(3) Dual QCD Formalism," *Acta Phys. Polon. B* **50** (2019) 1483–1500, arXiv:1909.09776 [hep-ph]. 6

[84] M. Chaichian and K. Nishijima, "Does color confinement imply massive gluons?," *Eur. Phys. J. C* **47** (2006) 737–743, arXiv:hep-th/0504050. 6

[85] D. J. Gross and F. Wilczek, "Ultraviolet Behavior of Nonabelian Gauge Theories," *Phys. Rev. Lett.* **30** (1973) 1343–1346. 6

[86] G. 't Hooft, "A Planar Diagram Theory for Strong Interactions," *Nucl. Phys. B* **72** (1974) 461. 6

[87] J. Alwall, R. Frederix, S. Frixione, V. Hirschi, F. Maltoni, O. Mattelaer, H. S. Shao, T. Stelzer, P. Torrielli, and M. Zaro, "The automated computation of tree-level and next-to-leading order differential cross sections, and their matching to parton shower simulations," *JHEP* **07** (2014) 079, arXiv:1405.0301 [hep-ph]. 7

[88] A. A. Andrianov, D. Espriu, and X. Planells, "An effective QCD Lagrangian in the presence of an axial chemical potential," *Eur. Phys. J. C* **73** no. 1, (2013) 2294, arXiv:1210.7712 [hep-ph]. 7

[89] M. G. Alford, A. Schmitt, K. Rajagopal, and T. Schäfer, "Color superconductivity in dense quark matter," *Rev. Mod. Phys.* **80** (2008) 1455–1515, arXiv:0709.4635 [hep-ph]. 10

[90] K. Fukushima and T. Hatsuda, "The phase diagram of dense QCD," *Rept. Prog. Phys.* **74** (2011) 014001, arXiv:1005.4814 [hep-ph]. 10

[91] **ALICE** Collaboration, K. Aamodt *et al.*, "The ALICE experiment at the CERN LHC," *JINST* **3** (2008) S08002. 11, 13, 34, 35, 39, 67

[92] **CBM** Collaboration, T. Ablyazimov *et al.*, "Challenges in QCD matter physics –The scientific programme of the Compressed Baryonic Matter experiment at FAIR," *Eur. Phys. J. A* **53** no. 3, (2017) 60, arXiv:1607.01487 [nucl-ex]. 11

[93] L. P. Csernai, D. J. Wang, M. Bleicher, and H. Stöcker, "Vorticity in peripheral collisions at the Facility for Antiproton and Ion Research and at the JINR Nuclotron-based Ion Collider fAcility," *Phys. Rev. C* **90** no. 2, (2014) 021904. 11

[94] H. Stoecker and W. Greiner, "High-Energy Heavy Ion Collisions: Probing the Equation of State of Highly Excited Hadronic Matter," *Phys. Rept.* **137** (1986) 277–392. 12

[95] **ALICE** Collaboration, S. Acharya *et al.*, "Characterizing the initial conditions of heavy-ion collisions at the LHC with mean transverse momentum and anisotropic flow correlations," *Phys. Lett. B* **834** (2022) 137393, arXiv:2111.06106 [nucl-ex]. 12

[96] F. Gelis, E. Iancu, J. Jalilian-Marian, and R. Venugopalan, "The Color Glass Condensate," *Ann. Rev. Nucl. Part. Sci.* **60** (2010) 463–489, arXiv:1002.0333 [hep-ph]. 13

[97] B. K. Patra, J.-e. Alam, P. Roy, S. Sarkar, and B. Sinha, "Space-time evolution of ultrarelativistic heavy ion collisions and hadronic spectra," *Nucl. Phys. A* **709** (2002) 440–450, arXiv:nucl-th/0201047. 13

[98] A. Jaiswal and V. Roy, "Relativistic hydrodynamics in heavy-ion collisions: general aspects and recent developments," *Adv. High Energy Phys.* **2016** (2016) 9623034, arXiv:1605.08694 [nucl-th]. 15

[99] J. Xu and C. M. Ko, "Chemical freeze-out in relativistic heavy-ion collisions," *Phys. Lett. B* **772** (2017) 290–293, arXiv:1704.04934 [nucl-th]. 15

[100] R. Averbeck, "Heavy-flavor production in heavy-ion collisions and implications for the properties of hot QCD matter," *Prog. Part. Nucl. Phys.* **70** (2013) 159–209, arXiv:1505.03828 [nucl-ex]. 16

[101] **ALICE** Collaboration, S. Acharya *et al.*, "Direct observation of the dead-cone effect in quantum chromodynamics," *Nature* **605** no. 7910, (2022) 440–446, arXiv:2106.05713 [nucl-ex]. [Erratum: Nature 607, E22 (2022)]. 17

[102] **ALICE** Collaboration, K. Aamodt *et al.*, "Elliptic flow of charged particles in Pb-Pb collisions at 2.76 TeV," *Phys. Rev. Lett.* **105** (2010) 252302, arXiv:1011.3914 [nucl-ex]. 18, 173, 174, 176

[103] **PHENIX** Collaboration, K. Adcox *et al.*, "Formation of dense partonic matter in relativistic nucleus-nucleus collisions at RHIC: Experimental evaluation by the PHENIX collaboration," *Nucl. Phys. A* **757** (2005) 184–283, arXiv:nucl-ex/0410003. 18, 172

[104] **ATLAS** Collaboration, G. Aad *et al.*, "Measurement of the nuclear modification factor for muons from charm and bottom hadrons in Pb+Pb collisions at 5.02 TeV with the ATLAS detector," *Phys. Lett. B* **829** (2022) 137077, arXiv:2109.00411 [nucl-ex]. 19

[105] A. Mocsy, P. Petreczky, and M. Strickland, "Quarkonia in the Quark Gluon Plasma," *Int. J. Mod. Phys. A* **28** (2013) 1340012, arXiv:1302.2180 [hep-ph]. 20

[106] R. Rapp, D. Blaschke, and P. Crochet, "Charmonium and bottomonium production in heavy-ion collisions," *Prog. Part. Nucl. Phys.* **65** (2010) 209–266, arXiv:0807.2470 [hep-ph]. 21

[107] **PHENIX** Collaboration, A. Adare *et al.*, "J/ψ suppression at forward rapidity in Au+Au collisions at $\sqrt{s_{NN}} = 200$ GeV," *Phys. Rev. C* **84** (2011) 054912, arXiv:1103.6269 [nucl-ex]. 21

[108] A. Singh, P. K. Srivastava, G. Devi, and B. K. Singh, "Production and enhancement of (multi-) strange hadrons in Au+Au collisions at sNN=200 GeV RHIC energy and Pb+Pb collisions at sNN=2.76 TeV LHC energy," *Phys. Rev. C* **107** no. 2, (2023) 024906. 21

[109] P. Koch, B. Muller, and J. Rafelski, "Strangeness in Relativistic Heavy Ion Collisions," *Phys. Rept.* **142** (1986) 167–262. 22, 173

[110] **ALICE** Collaboration, S. Acharya *et al.*, "Multiplicity dependence of (multi-)strange hadron production in proton-proton collisions at $\sqrt{s} = 13$ TeV," *Eur. Phys. J. C* **80** no. 2, (2020) 167, arXiv:1908.01861 [nucl-ex]. 27

[111] **ALICE** Collaboration, S. Acharya *et al.*, "Multiplicity dependence of

K*(892)^0 and ϕ(1020) production in pp collisions at $\sqrt{s}$ =13 TeV," *Phys. Lett. B* **807** (2020) 135501, arXiv:1910.14397 [nucl-ex]. 28

[112] **ALICE** Collaboration, A. Khuntia, "Latest results on the production of hadronic resonances in ALICE at the LHC," *Nucl. Phys. A* **1005** (2021) 121939, arXiv:2001.09023 [hep-ex]. 28

[113] T. Sjostrand, S. Mrenna, and P. Z. Skands, "PYTHIA 6.4 Physics and Manual," *JHEP* **05** (2006) 026, arXiv:hep-ph/0603175. 29, 51, 60, 68, 161, 189

[114] T. Sjostrand, S. Mrenna, and P. Z. Skands, "A Brief Introduction to PYTHIA 8.1," *Comput. Phys. Commun.* **178** (2008) 852–867, arXiv:0710.3820 [hep-ph]. 29, 161, 171, 189

[115] B. P. Kersevan and E. Richter-Was, "The Monte Carlo event generator AcerMC versions 2.0 to 3.8 with interfaces to PYTHIA 6.4, HERWIG 6.5 and ARIADNE 4.1," *Comput. Phys. Commun.* **184** (2013) 919–985, arXiv:hep-ph/0405247. 29

[116] J. Bellm *et al.*, "Herwig 7.0/Herwig++ 3.0 release note," *Eur. Phys. J. C* **76** no. 4, (2016) 196, arXiv:1512.01178 [hep-ph]. 29

[117] K. Werner, I. Karpenko, T. Pierog, M. Bleicher, and K. Mikhailov, "Event-by-Event Simulation of the Three-Dimensional Hydrodynamic Evolution from Flux Tube Initial Conditions in Ultrarelativistic Heavy Ion Collisions," *Phys. Rev. C* **82** (2010) 044904, arXiv:1004.0805 [nucl-th]. 29, 161

[118] H. J. Drescher, M. Hladik, S. Ostapchenko, T. Pierog, and K. Werner, "Parton based Gribov-Regge theory," *Phys. Rept.* **350** (2001) 93–289, arXiv:hep-ph/0007198. 29, 161

[119] **ALICE** Collaboration, B. B. Abelev *et al.*, "Beauty production in pp collisions at $\sqrt{s}$ = 2.76 TeV measured via semi-electronic decays," *Phys. Lett. B* **738** (2014) 97–108, arXiv:1405.4144 [nucl-ex]. 29, 163, 165

[120] J. R. Ellis, "Beyond the standard model with the LHC," *Nature* **448** (2007) 297–301. 33

[121] A. Nisati and G. Tonelli, "The discovery of the Higgs boson at the Large Hadron Collider," *Riv. Nuovo Cim.* **38** no. 11, (2015) 507–573. 33

[122] "LHC Machine," *JINST* **3** (2008) S08001. 33

[123] R. D. Heuer, "Electron positron colliders," *Int. J. Mod. Phys. A* **17** (2002) 3469–3482, arXiv:hep-ex/0111070. 34

[124] G. Apollinari, O. Brüning, T. Nakamoto, and L. Rossi, "High Luminosity Large Hadron Collider HL-LHC," *CERN Yellow Rep.* no. 5, (2015) 1–19, arXiv:1705.08830 [physics.acc-ph]. 34

[125] **ATLAS** Collaboration, G. Aad *et al.*, "The ATLAS Experiment at the CERN Large Hadron Collider," *JINST* **3** (2008) S08003. 35

[126] **CMS** Collaboration, S. Chatrchyan *et al.*, "The CMS Experiment at the CERN LHC," *JINST* **3** (2008) S08004. 35

[127] **LHCb** Collaboration, A. A. Alves, Jr. *et al.*, "The LHCb Detector at the LHC," *JINST* **3** (2008) S08005. 35

[128] **ALICE** Collaboration, G. Dellacasa *et al.*, "ALICE: Technical design report of the time projection chamber,". 42

[129] J. Alme *et al.*, "The ALICE TPC, a large 3-dimensional tracking device with fast readout for ultra-high multiplicity events," *Nucl. Instrum. Meth. A* **622** (2010) 316–367, arXiv:1001.1950 [physics.ins-det]. 42

[130] **ALICE** Collaboration, P. Cortese *et al.*, "ALICE: Physics performance report, volume I," *J. Phys. G* **30** (2004) 1517–1763. 43

[131] W. Blum, L. Rolandi, and W. Riegler, *Particle detection with drift chambers*. Particle Acceleration and Detection. 2008. 45

[132] S. Singha, *Identified particle production in Pb-Pb and pp collisions at LHC energies*. PhD thesis, Bhubaneswar, NISER, 9, 2014. 45

[133] **ALICE** Collaboration, E. Abbas *et al.*, "Performance of the ALICE VZERO system," *JINST* **8** (2013) P10016, arXiv:1306.3130 [nucl-ex]. 49

[134] S. van der Meer, "Calibration of the Effective Beam Height in the ISR,". 50

[135] "ROOT webpage:, http://root.cern.ch.,". 50

[136] "ALICE offline webpage:, http://aliceinfo.cern.ch/Offline/.,". 51

[137] T. Sjöstrand, S. Ask, J. R. Christiansen, R. Corke, N. Desai, P. Ilten, S. Mrenna, S. Prestel, C. O. Rasmussen, and P. Z. Skands, "An introduction to PYTHIA 8.2," *Comput. Phys. Commun.* **191** (2015) 159–177, arXiv:1410.3012 [hep-ph]. 51

[138] T. Pierog and K. Werner, "EPOS Model and Ultra High Energy Cosmic Rays," *Nucl. Phys. B Proc. Suppl.* **196** (2009) 102–105, arXiv:0905.1198 [hep-ph]. 51

[139] M. Gyulassy and X.-N. Wang, "HIJING 1.0: A Monte Carlo program for parton and particle production in high-energy hadronic and nuclear collisions," *Comput. Phys. Commun.* **83** (1994) 307, arXiv:nucl-th/9502021. 51

[140] R. Brun, R. Hagelberg, M. Hansroul, and J. C. Lassalle, "Geant: Simulation Program for Particle Physics Experiments. User Guide and Reference Manual,". 51

[141] **GEANT4** Collaboration, S. Agostinelli *et al.*, "GEANT4–a simulation toolkit," *Nucl. Instrum. Meth. A* **506** (2003) 250–303. 51

[142] **ALICE** Collaboration, M. Monteno, "Particle multiplicity in proton-proton collisions with ALICE," *J. Phys. Conf. Ser.* **5** (2005) 209–218. 52

[143] R. Fruhwirth, "Application of Kalman filtering to track and vertex fitting," *Nucl. Instrum. Meth. A* **262** (1987) 444–450. 52

[144] T. C. Awes, F. E. Obenshain, F. Plasil, S. Saini, S. P. Sorensen, and G. R. Young, "A Simple method of shower localization and identification in laterally segmented calorimeters," *Nucl. Instrum. Meth. A* **311** (1992) 130–138. 54

[145] **ALICE** Collaboration, S. Acharya *et al.*, "Production of π^0 and η mesons up to high transverse momentum in pp collisions at 2.76 TeV," *Eur. Phys. J. C* **77** no. 5, (2017) 339, arXiv:1702.00917 [hep-ex]. 54, 55

[146] **ALICE** Collaboration, J. F. Grosse-Oetringhaus, C. Zampolli, A. Colla, and F. Carminati, "The ALICE online-offline framework for the extraction of conditions data," *J. Phys. Conf. Ser.* **219** (2010) 022010. 56

[147] **ALICE** Collaboration, F. Carena *et al.*, "The ALICE data acquisition system," *Nucl. Instrum. Meth. A* **741** (2014) 130–162. 56

[148] C. Bierlich, G. Gustafson, L. Lönnblad, and H. Shah, "The Angantyr model for Heavy-Ion Collisions in PYTHIA8," *JHEP* **10** (2018) 134, arXiv:1806.10820 [hep-ph]. 59, 61, 161, 174, 185

[149] S. G. Weber, A. Dubla, A. Andronic, and A. Morsch, "Elucidating the multiplicity dependence of J/ψ production in proton–proton collisions with PYTHIA8," *Eur. Phys. J. C* **79** no. 1, (2019) 36, arXiv:1811.07744 [nucl-th]. 60

[150] **BaBar** Collaboration, J. P. Lees *et al.*, "Measurement of initial-state–final-state radiation interference in the processes $e^+e^-ß^{+-}$ and $e^+e^-ß^{+-}$," *Phys. Rev. D* **92** no. 7, (2015) 072015, arXiv:1508.04008 [hep-ex]. 60

[151] M. Martinez, "Coherence effects between the initial and final state radiation in a dense QCD medium," *Nucl. Phys. A* **926** (2014) 242–249, arXiv:1401.1806 [hep-ph]. 60

[152] N. K. Behera, R. K. Nayak, and S. Dash, "Baseline study for net-proton number fluctuations at top energies available at the BNL Relativistic Heavy Ion Collider and at the CERN Large Hadron Collider with the

Angantyr model," *Phys. Rev. C* **101** no. 6, (2020) 064903, arXiv:1909.12113 [hep-ph]. 61

[153] F. Carena *et al.*, "The ALICE Electronic Logbook," in *17th IEEE NPSS Real Time Conference*, IEEE Nucl.Sci.Symp.Conf.Rec., p. 5750476. 2010. 67

[154] **ALICE** Collaboration, "ALICE luminosity determination for pp collisions at $\sqrt{s} = 13$ TeV,". 67

[155] **ALICE** Collaboration, "ALICE 2017 luminosity determination for pp collisions at $\sqrt{s} = 5$ TeV,". 68

[156] **ALICE** Collaboration, B. B. Abelev *et al.*, "Measurement of visible cross sections in proton-lead collisions at $\sqrt{s_{\rm NN}} = 5.02$ TeV in van der Meer scans with the ALICE detector," *JINST* **9** no. 11, (2014) P11003, arXiv:1405.1849 [nucl-ex]. 68

[157] P. Z. Skands, "Tuning Monte Carlo Generators: The Perugia Tunes," *Phys. Rev. D* **82** (2010) 074018, arXiv:1005.3457 [hep-ph]. 68

[158] X.-N. Wang and M. Gyulassy, "HIJING: A Monte Carlo model for multiple jet production in p p, p A and A A collisions," *Phys. Rev. D* **44** (1991) 3501–3516. 68

[159] R. Brun, F. Bruyant, M. Maire, A. C. McPherson, and P. Zanarini, "GEANT3,". 68

[160] P. Astier, A. Cardini, R. D. Cousins, A. Letessier-Selvon, B. A. Popov, and T. Vinogradova, "Kalman filter track fits and track break point analysis," *Nucl. Instrum. Meth. A* **450** (2000) 138–154, arXiv:physics/9912034. 70

[161] D. Leermakers, "Systematic study of track quality cuts at ALICE. (2015), https://cds.cern.ch/record/2045797.,". 71

[162] "Performance study of EMCal shower shape parameters to identify high$-p_{\rm T}$ electrons in EMCal-triggered events in pp collisions (ALICE Analysis note), https://aliceinfo.cern.ch/Notes/node/547,". 72

[163] R. Rafelski, J. Hagedorn, "From hadron gas to quark matter, 2. (1981), http://cds.cern.ch/record/126179.,". 80

[164] **ALICE** Collaboration, "The ALICE definition of primary particles,". 95

[165] R. Singh, Y. Bailung, S. K. Kundu, and A. Roy, "Jet fragmentation via azimuthal angular correlations of electrons from heavy flavor decay in pp, p-Pb, and Pb-Pb collisions using PYTHIA8+Angantyr calculations," *Phys. Rev. C* **107** no. 2, (2023) 024911, arXiv:2301.13068 [hep-ph]. 99, 161

[166] "Fitting histogram, https://root.cern.ch/root/htmldoc/guides/users-guide/FittingHistograms.html,". 121

[167] **ALICE** Collaboration, S. Acharya *et al.*, "Azimuthal Anisotropy of Heavy-Flavor Decay Electrons in p-Pb Collisions at $\sqrt{s_{\rm NN}} = 5.02$ TeV," *Phys. Rev. Lett.* **122** no. 7, (2019) 072301, arXiv:1805.04367 [nucl-ex]. 149

[168] B. Andersson, G. Gustafson, and B. Nilsson-Almqvist, "A Model for Low p(t) Hadronic Reactions, with Generalizations to Hadron - Nucleus and Nucleus-Nucleus Collisions," *Nucl. Phys. B* **281** (1987) 289–309. 161

[169] H. Pi, "An Event generator for interactions between hadrons and nuclei: FRITIOF version 7.0," *Comput. Phys. Commun.* **71** (1992) 173–192. 161

[170] M. Alvioli and M. Strikman, "Color fluctuation effects in proton-nucleus collisions," *Phys. Lett. B* **722** (2013) 347–354, arXiv:1301.0728 [hep-ph]. 162

[171] R. Singh, Y. Bailung, and A. Roy, "Dynamics of particle production in Pb-Pb collisions at sNN=2.76 TeV using the PYTHIA8 Angantyr model," *Phys. Rev. C* **105** no. 3, (2022) 035202, arXiv:2108.08626 [nucl-th]. 162

[172] M. Cacciari, M. Greco, and P. Nason, "The P(T) spectrum in heavy flavor hadroproduction," *JHEP* **05** (1998) 007, arXiv:hep-ph/9803400. 163, 190

[173] M. Cacciari, S. Frixione, and P. Nason, "The p(T) spectrum in heavy flavor photoproduction," *JHEP* **03** (2001) 006, arXiv:hep-ph/0102134. 163, 190

[174] A. Ortiz, G. Bencedi, and H. Bello, "Revealing the source of the radial flow patterns in proton–proton collisions using hard probes," *J. Phys. G* **44** no. 6, (2017) 065001, arXiv:1608.04784 [hep-ph]. 164

[175] S. Frixione, P. Nason, and C. Oleari, "Matching NLO QCD computations with Parton Shower simulations: the POWHEG method," *JHEP* **11** (2007) 070, arXiv:0709.2092 [hep-ph]. 171

[176] **PHOBOS** Collaboration, B. B. Back *et al.*, "The PHOBOS perspective on discoveries at RHIC," *Nucl. Phys. A* **757** (2005) 28–101, arXiv:nucl-ex/0410022. 172

[177] **UA5** Collaboration, R. E. Ansorge *et al.*, "Charged Particle Multiplicity Distributions at 200-GeV and 900-GeV Center-Of-Mass Energy," *Z. Phys. C* **43** (1989) 357. 172

[178] **UA1** Collaboration, C. Albajar *et al.*, "A Study of the General Characteristics of $p\bar{p}$ Collisions at $\sqrt{s} = 0.2$-TeV to 0.9-TeV," *Nucl. Phys. B* **335** (1990) 261–287.

[179] **UA5** Collaboration, G. J. Alner *et al.*, "Scaling of Pseudorapidity Distributions at c.m. Energies Up to 0.9-TeV," *Z. Phys. C* **33** (1986) 1–6.

[180] **UA1** Collaboration, G. Arnison *et al.*, "Transverse Momentum Spectra for Charged Particles at the CERN Proton anti-Proton Collider," *Phys. Lett. B* **118** (1982) 167–172. 172

[181] M. L. Miller, K. Reygers, S. J. Sanders, and P. Steinberg, "Glauber modeling in high energy nuclear collisions," *Ann. Rev. Nucl. Part. Sci.* **57** (2007) 205–243, arXiv:nucl-ex/0701025. 172

[182] P. Braun-Munzinger, K. Redlich, and J. Stachel, "Particle production in heavy ion collisions," arXiv:nucl-th/0304013. 172, 186, 187

[183] F.-H. Liu, Y.-H. Chen, H.-R. Wei, and B.-C. Li, "Transverse Momentum Distributions of Final-State Particles Produced in Soft Excitation Process in High Energy Collisions," *Adv. High Energy Phys.* **2013** (2013) 965735. 172

[184] J. Cleymans and D. Worku, "Relativistic Thermodynamics: Transverse Momentum Distributions in High-Energy Physics," *Eur. Phys. J. A* **48** (2012) 160, arXiv:1203.4343 [hep-ph]. 172

[185] J. Cleymans and D. Worku, "The Tsallis Distribution in Proton-Proton Collisions at $\sqrt{s} = 0.9$ TeV at the LHC," *J. Phys. G* **39** (2012) 025006, arXiv:1110.5526 [hep-ph]. 172

[186] S. Soff, S. A. Bass, M. Bleicher, L. Bravina, M. Gorenstein, E. Zabrodin, H. Stoecker, and W. Greiner, "Strangeness enhancement in heavy ion collisions: Evidence for quark gluon matter?," *Phys. Lett. B* **471** (1999) 89–96, arXiv:nucl-th/9907026. 173

[187] A. Capella, "Strangeness enhancement in heavy ion collisions," *Phys. Lett. B* **364** (1995) 175–180, arXiv:hep-ph/9501331. 173

[188] E. Cuautle and G. Paić, "The energy density representation of the strangeness enhancement from p+p to Pb+Pb," arXiv:1608.02101 [hep-ph]. 173

[189] G. Torrieri, "Phenomenology of Strangeness enhancement in heavy ion collisions," *J. Phys. G* **36** (2009) 064007, arXiv:0901.0221 [nucl-th]. 173

[190] P. Huovinen, P. F. Kolb, U. W. Heinz, P. V. Ruuskanen, and S. A. Voloshin, "Radial and elliptic flow at RHIC: Further predictions," *Phys. Lett. B* **503** (2001) 58–64, arXiv:hep-ph/0101136. 173

[191] **STAR** Collaboration, J. Adams *et al.*, "Azimuthal anisotropy in Au+Au collisions at s(NN)**(1/2) = 200-GeV," *Phys. Rev. C* **72** (2005) 014904, arXiv:nucl-ex/0409033. 173

[192] E. Norrbin and T. Sjostrand, "Production and hadronization of heavy quarks," *Eur. Phys. J. C* **17** (2000) 137–161, arXiv:hep-ph/0005110. 173, 186, 188

[193] **ALICE, ATLAS, CMS, LHCb** Collaboration, M. Faggin, "Heavy-flavour hadron production," *PoS* **LHCP2021** (2021) 086, arXiv:2109.09348 [hep-ex]. 173

[194] **ALICE** Collaboration, R. Singh, "Angular correlations of heavy-flavour hadron decay electrons and charged particles in pp collisions at $\sqrt{s} = 5.02$ TeV with ALICE at the LHC," *PoS* **LHCP2021** (2021) 191, arXiv:2109.09318 [hep-ex]. 173

[195] **STAR** Collaboration, J. Adam *et al.*, "Measurement of D^0-meson + hadron two-dimensional angular correlations in Au+Au collisions at $\sqrt{s_{NN}}$ = 200 GeV," *Phys. Rev. C* **102** no. 1, (2020) 014905, arXiv:1911.12168 [nucl-ex]. 173

[196] S. Cao and X.-N. Wang, "Jet quenching and medium response in high-energy heavy-ion collisions: a review," *Rept. Prog. Phys.* **84** no. 2, (2021) 024301, arXiv:2002.04028 [hep-ph]. 174

[197] **ALICE** Collaboration, B. B. Abelev *et al.*, "Multiplicity dependence of the average transverse momentum in pp, p-Pb, and Pb-Pb collisions at the LHC," *Phys. Lett. B* **727** (2013) 371–380, arXiv:1307.1094 [nucl-ex]. 176

[198] **ALICE** Collaboration, B. Abelev *et al.*, "Centrality Dependence of Charged Particle Production at Large Transverse Momentum in Pb–Pb Collisions at $\sqrt{s_{NN}} = 2.76$ TeV," *Phys. Lett. B* **720** (2013) 52–62, arXiv:1208.2711 [hep-ex]. 177

[199] X. Zhu, F. Meng, H. Song, and Y.-X. Liu, "Hybrid model approach for strange and multistrange hadrons in 2.76A TeV Pb+Pb collisions," *Phys. Rev. C* **91** no. 3, (2015) 034904, arXiv:1501.03286 [nucl-th]. 181

[200] K. Werner, I. Karpenko, M. Bleicher, T. Pierog, and S. Porteboeuf-Houssais, "Jets, Bulk Matter, and their Interaction in Heavy Ion Collisions at Several TeV," *Phys. Rev. C* **85** (2012) 064907, arXiv:1203.5704 [nucl-th]. 181

[201] M. Nasim, V. Bairathi, M. K. Sharma, B. Mohanty, and A. Bhasin, "A Review on ϕ Meson Production in Heavy-Ion Collision," *Adv. High Energy Phys.* **2015** (2015) 197930. 181

[202] **ALICE** Collaboration, B. B. Abelev *et al.*, "Production of charged pions, kaons and protons at large transverse momenta in pp and Pb–Pb collisions at $\sqrt{s_{\rm NN}}$ =2.76 TeV," *Phys. Lett. B* **736** (2014) 196–207, arXiv:1401.1250 [nucl-ex]. 184

[203] **ALICE** Collaboration, B. B. Abelev *et al.*, "K^0_S and Λ production in Pb-Pb collisions at $\sqrt{s_{NN}}$ = 2.76 TeV," *Phys. Rev. Lett.* **111** (2013) 222301, arXiv:1307.5530 [nucl-ex]. 185

[204] R. J. Fries and B. Muller, "Heavy ions at LHC: Theoretical issues," *Eur. Phys. J. C* **34** (2004) S279–S285, arXiv:nucl-th/0307043. 185

[205] S. Frixione, M. L. Mangano, P. Nason, and G. Ridolfi, "Heavy quark production," *Adv. Ser. Direct. High Energy Phys.* **15** (1998) 609–706, arXiv:hep-ph/9702287. 186

[206] W. M. Alberico, A. Beraudo, A. De Pace, A. Molinari, M. Monteno, M. Nardi, F. Prino, and M. Sitta, "Heavy flavors in AA collisions: production, transport and final spectra," *Eur. Phys. J. C* **73** (2013) 2481, arXiv:1305.7421 [hep-ph].

[207] P. Levai and V. Skokov, "Nonperturbative enhancement of heavy quark-pair production in a strong SU(2) color field," *Phys. Rev. D* **82** (2010) 074014, arXiv:0909.2323 [hep-ph]. 186

[208] **CMS** Collaboration, A. M. Sirunyan *et al.*, "Measurement of b jet shapes in proton-proton collisions at $\sqrt{s}$ = 5.02 TeV," *JHEP* **05** (2021) 054, arXiv:2005.14219 [hep-ex]. 187

[209] P. Skands, S. Carrazza, and J. Rojo, "Tuning PYTHIA 8.1: the Monash 2013 Tune," *Eur. Phys. J. C* **74** no. 8, (2014) 3024, arXiv:1404.5630 [hep-ph]. 187

[210] R. Corke and T. Sjostrand, "Interleaved Parton Showers and Tuning Prospects," *JHEP* **03** (2011) 032, arXiv:1011.1759 [hep-ph]. 187

[211] C. Bierlich, G. Gustafson, and L. Lönnblad, "A shoving model for collectivity in hadronic collisions," arXiv:1612.05132 [hep-ph]. 187

[212] C. Bierlich, G. Gustafson, and L. Lönnblad, "Collectivity without plasma in hadronic collisions," *Phys. Lett. B* **779** (2018) 58–63, arXiv:1710.09725 [hep-ph].

[213] C. Bierlich, G. Gustafson, L. Lönnblad, and A. Tarasov, "Effects of Overlapping Strings in pp Collisions," *JHEP* **03** (2015) 148, arXiv:1412.6259 [hep-ph].

[214] C. Bierlich and J. R. Christiansen, "Effects of color reconnection on hadron flavor observables," *Phys. Rev. D* **92** no. 9, (2015) 094010, arXiv:1507.02091 [hep-ph]. 187

[215] A. Beraudo, A. De Pace, M. Monteno, M. Nardi, and F. Prino, "Heavy flavors in heavy-ion collisions: quenching, flow and correlations," *Eur. Phys. J. C* **75** no. 3, (2015) 121, arXiv:1410.6082 [hep-ph]. 188

[216] **PHENIX** Collaboration, A. Adare *et al.*, "Measurement of two-particle correlations with respect to second- and third-order event planes in Au+Au collisions at $\sqrt{s_{NN}} = 200$ GeV," *Phys. Rev. C* **99** no. 5, (2019) 054903, arXiv:1803.01749 [hep-ex].

[217] L.-Y. Zhang, J.-H. Chen, Z.-W. Lin, Y.-G. Ma, and S. Zhang, "Two-particle angular correlations in heavy ion collisions from a multiphase transport model," *Phys. Rev. C* **99** no. 5, (2019) 054904, arXiv:1904.08603 [nucl-th].

[218] L.-Y. Zhang, J.-H. Chen, Z.-W. Lin, Y.-G. Ma, and S. Zhang, "Two-particle angular correlations in pp and p-Pb collisions at energies

available at the CERN Large Hadron Collider from a multiphase transport model," *Phys. Rev. C* **98** no. 3, (2018) 034912, arXiv:1808.10641 [nucl-th]. 188

[219] **PHENIX** Collaboration, A. Adare *et al.*, "Cold Nuclear Matter Effects on J/ψ Yields as a Function of Rapidity and Nuclear Geometry in Deuteron-Gold Collisions at $\sqrt{s_{NN}} = 200$ GeV," *Phys. Rev. Lett.* **107** (2011) 142301, arXiv:1010.1246 [nucl-ex]. 188

[220] K. J. Eskola, V. J. Kolhinen, and R. Vogt, "Obtaining the nuclear gluon distribution from heavy quark decays to lepton pairs in pA collisions," *Nucl. Phys. A* **696** (2001) 729–746, arXiv:hep-ph/0104124.

[221] D. Kharzeev and K. Tuchin, "Signatures of the color glass condensate in J/psi production off nuclear targets," *Nucl. Phys. A* **770** (2006) 40–56, arXiv:hep-ph/0510358. 188

[222] **ALICE** Collaboration, J. Adam *et al.*, "Measurement of electrons from heavy-flavour hadron decays in p-Pb collisions at $\sqrt{s_{\rm NN}} = 5.02$ TeV," *Phys. Lett. B* **754** (2016) 81–93, arXiv:1509.07491 [nucl-ex]. 188

[223] **ALICE** Collaboration, S. Acharya *et al.*, "Measurement of $\rm D^0$, $\rm D^+$, $\rm D^{*+}$ and $\rm D_s^+$ production in Pb-Pb collisions at $\sqrt{\rm s_{NN}} = 5.02$ TeV," *JHEP* **10** (2018) 174, arXiv:1804.09083 [nucl-ex].

[224] **STAR** Collaboration, L. Adamczyk *et al.*, "Observation of D^0 Meson Nuclear Modifications in Au+Au Collisions at $\sqrt{s_{NN}} = 200$ GeV," *Phys. Rev. Lett.* **113** no. 14, (2014) 142301, arXiv:1404.6185 [nucl-ex]. [Erratum: Phys.Rev.Lett. 121, 229901 (2018)].

[225] H. Fujii and K. Watanabe, "Heavy quark pair production in high energy pA collisions: Open heavy flavors," *Nucl. Phys. A* **920** (2013) 78–93, arXiv:1308.1258 [hep-ph]. 188

[226] **ATLAS** Collaboration, G. Aad *et al.*, "Observation of Associated Near-Side and Away-Side Long-Range Correlations in $\sqrt{s_{NN}}$=5.02 TeV

Proton-Lead Collisions with the ATLAS Detector," *Phys. Rev. Lett.* **110** no. 18, (2013) 182302, arXiv:1212.5198 [hep-ex]. 188

[227] J. L. Albacete, G. Giacalone, C. Marquet, and M. Matas, "Forward dihadron back-to-back correlations in pA collisions," *Phys. Rev. D* **99** no. 1, (2019) 014002, arXiv:1805.05711 [hep-ph]. 189

[228] B. Andersson, G. Gustafson, and B. Soderberg, "A General Model for Jet Fragmentation," *Z. Phys. C* **20** (1983) 317. 189

[229] R. C. Hwa, "Clustering and Hadronization of Quarks: A Treatment of the Low p(t) Problem," *Phys. Rev. D* **22** (1980) 1593.

[230] A. Buckley *et al.*, "General-purpose event generators for LHC physics," *Phys. Rept.* **504** (2011) 145–233, arXiv:1101.2599 [hep-ph]. 189

[231] J. M. Campbell *et al.*, "Event Generators for High-Energy Physics Experiments," in *Snowmass 2021*. 3, 2022. arXiv:2203.11110 [hep-ph]. 189

[232] T. S. Biro, P. Levai, and J. Zimanyi, "ALCOR: A Dynamic model for hadronization," *Phys. Lett. B* **347** (1995) 6–12. 189

[233] R. J. Fries, V. Greco, and P. Sorensen, "Coalescence Models For Hadron Formation From Quark Gluon Plasma," *Ann. Rev. Nucl. Part. Sci.* **58** (2008) 177–205, arXiv:0807.4939 [nucl-th]. 189

[234] B. A. Kniehl, G. Kramer, I. Schienbein, and H. Spiesberger, "Finite-mass effects on inclusive B meson hadroproduction," *Phys. Rev. D* **77** (2008) 014011, arXiv:0705.4392 [hep-ph]. 189

[235] M. Salajegheh, S. M. Moosavi Nejad, H. Khanpour, B. A. Kniehl, and M. Soleymaninia, "B-hadron fragmentation functions at next-to-next-to-leading order from a global analysis of e^+e^- annihilation data," *Phys. Rev. D* **99** no. 11, (2019) 114001, arXiv:1904.08718 [hep-ph].

[236] M. Epele, C. García Canal, and R. Sassot, "Heavy quark mass effects in parton-to-kaon hadronization probabilities," *Phys. Lett. B* **790** (2019) 102–107, arXiv:1807.07495 [hep-ph].

[237] G. Kramer and H. Spiesberger, "b-hadron production in the general-mass variable-flavour-number scheme and LHC data," *Phys. Rev. D* **98** no. 11, (2018) 114010, arXiv:1809.04297 [hep-ph].

[238] G. Kramer and H. Spiesberger, "Study of heavy meson production in p–Pb collisions at $\sqrt{S}$= 5.02 TeV in the general-mass variable-flavour-number scheme," *Nucl. Phys. B* **925** (2017) 415–430, arXiv:1703.04754 [hep-ph]. 189

[239] **ALICE** Collaboration, J. Adam *et al.*, "Measurement of charm and beauty production at central rapidity versus charged-particle multiplicity in proton-proton collisions at $\sqrt{s} = 7$ TeV," *JHEP* **09** (2015) 148, arXiv:1505.00664 [nucl-ex]. 197

[240] K. Fialkowski and R. Wit, "Bose-Einstein effect from asymmetric sources in Monte Carlo generators," *Acta Phys. Polon. B* **32** (2001) 1233, arXiv:hep-ph/0012356. 198

[241] L. Lonnblad and T. Sjostrand, "Modeling Bose-Einstein correlations at LEP-2," *Eur. Phys. J. C* **2** (1998) 165–180, arXiv:hep-ph/9711460. 198

[242] S. Ferreres-Solé and T. Sjöstrand, "The space–time structure of hadronization in the Lund model," *Eur. Phys. J. C* **78** no. 11, (2018) 983, arXiv:1808.04619 [hep-ph]. 198

[243] M. Connors, C. Nattrass, R. Reed, and S. Salur, "Jet measurements in heavy ion physics," *Rev. Mod. Phys.* **90** (2018) 025005, arXiv:1705.01974 [nucl-ex]. 199

[244] **ALICE** Collaboration, S. Acharya *et al.*, "Charm-quark fragmentation fractions and production cross section at midrapidity in pp collisions at the LHC," *Phys. Rev. D* **105** no. 1, (2022) L011103, arXiv:2105.06335 [nucl-ex]. 205

Appendix A

Appendix

The Appendix section is dedicated to figures that provide additional follow-up details regarding the analysis work conducted in this thesis. Given the significant number of figures, their inclusion in the main body of the thesis might hinder the smooth progression of the accompanying text. Therefore, to maintain clarity and readability, these figures have been compiled and presented in the Appendix section.

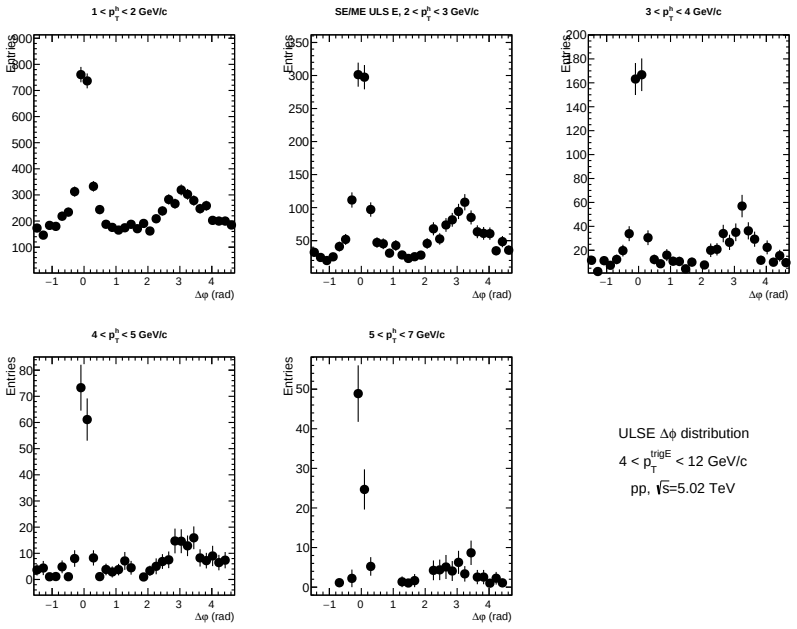

Figure A.1: $\Delta\varphi$ distribution for electrons (positrons) that form ULS pairs with other positrons (electrons) for pp events.

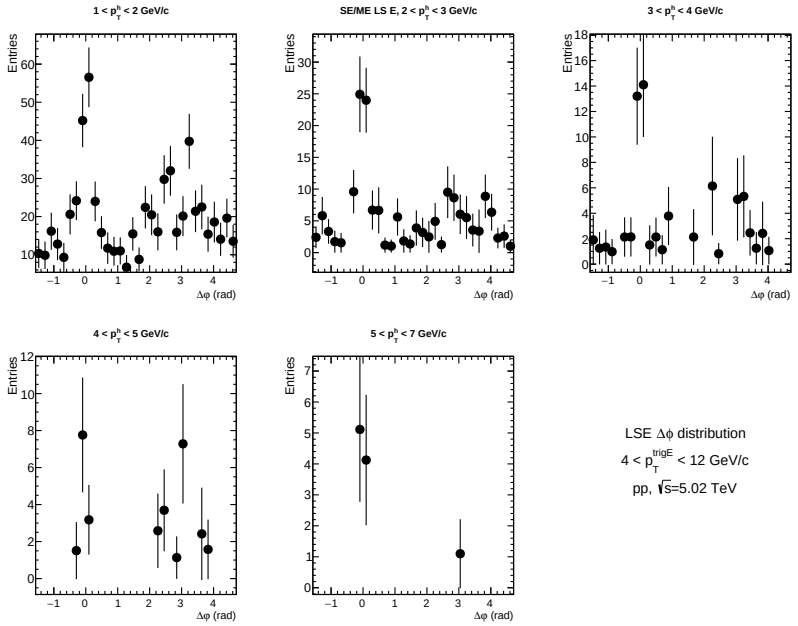

Figure A.2: $\Delta\varphi$ distribution for electrons that form LS pairs with other electrons for pp events.

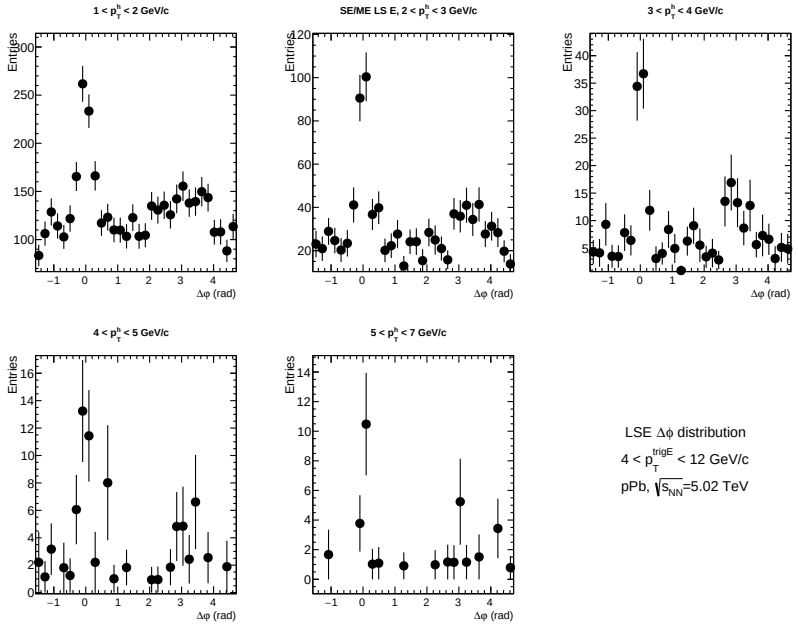

Figure A.4: $\Delta\varphi$ distribution for electrons that form LS pairs with other electrons for p–Pb events.

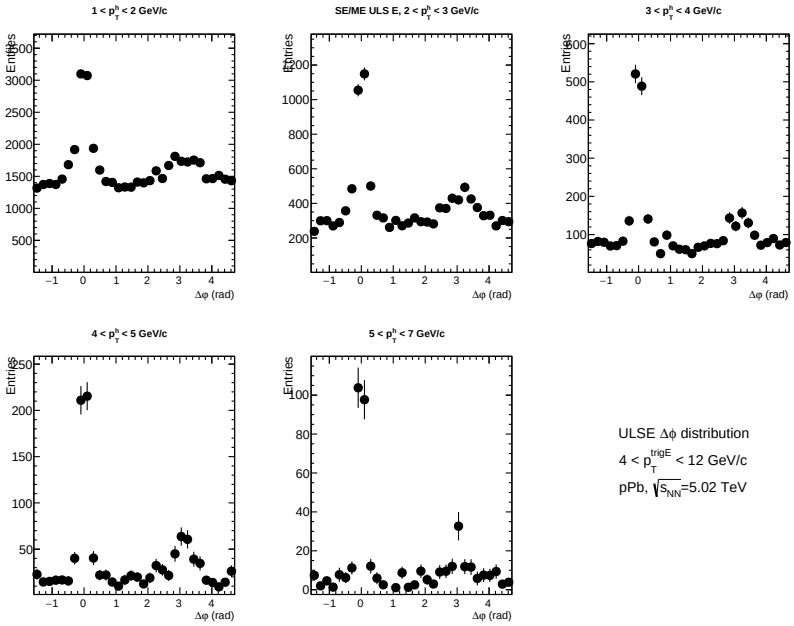

Figure A.3: $\Delta\varphi$ distribution for electrons (positrons) that form ULS pairs with other positrons (electrons) for p–Pb events.

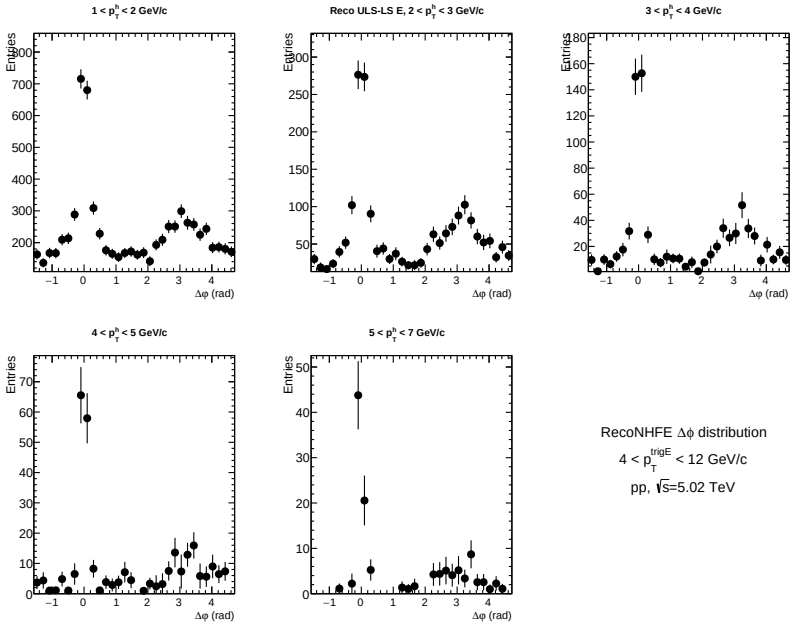

Figure A.5: $\Delta\varphi$ distribution for reconstructed non-heavy flavour electron background (Non-$\mathrm{Hf_r}$) for pp events.

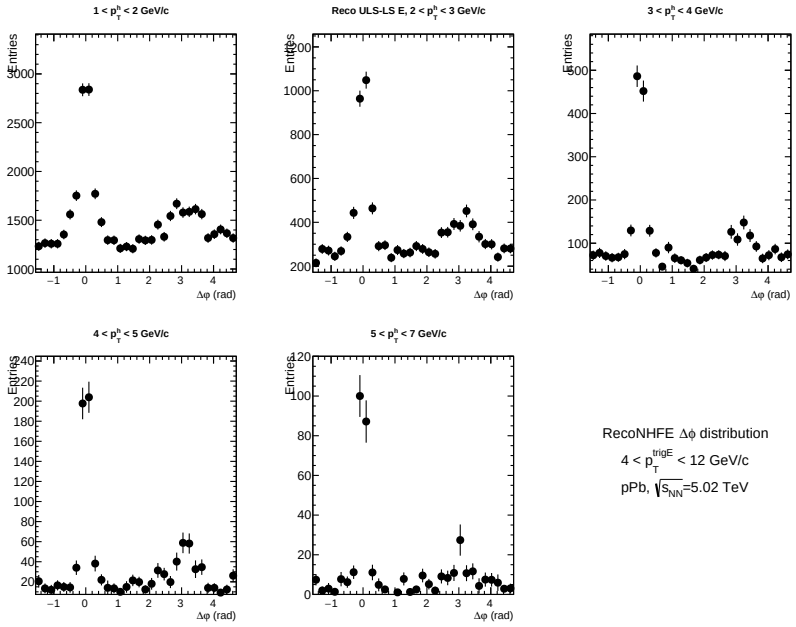

Figure A.6: $\Delta\varphi$ distribution for reconstructed non-heavy flavour electron background (Non-Hf$_r$) for p–Pb events.

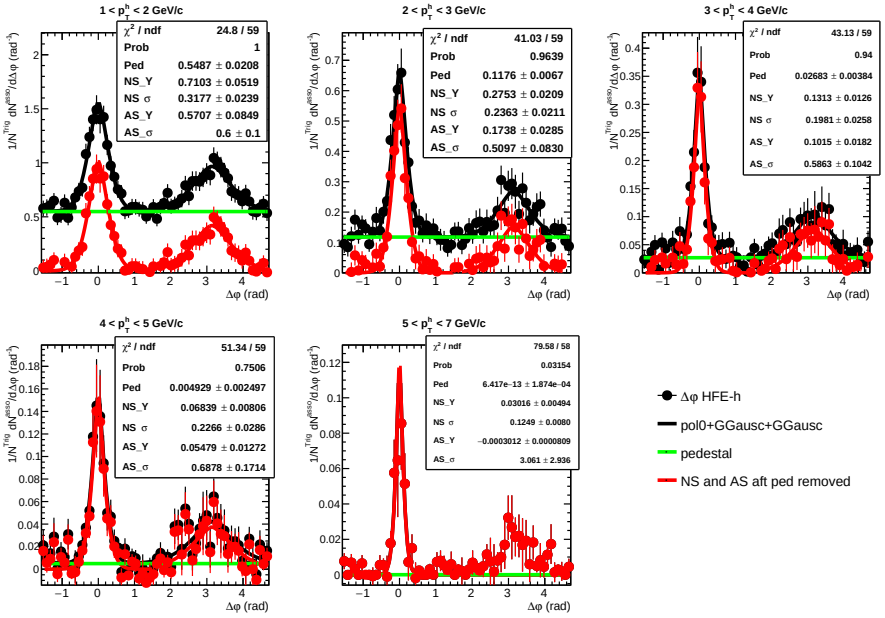

Figure A.7: $\Delta\varphi$ distribution with 64 bins fitted with generalized Gaussian function in pp events.

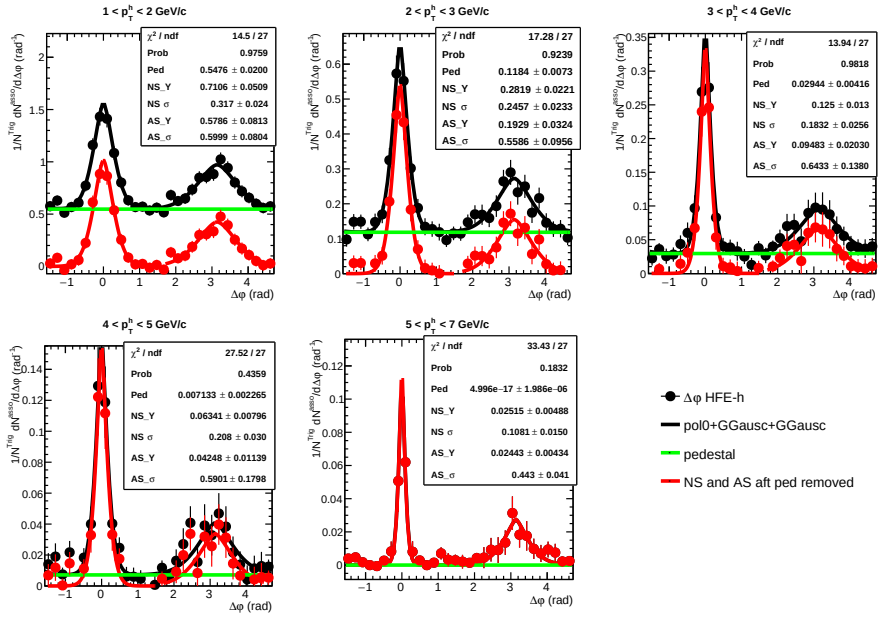

Figure A.8: $\Delta\varphi$ distribution fitted with "I" option by generalized Gaussian function in pp events.

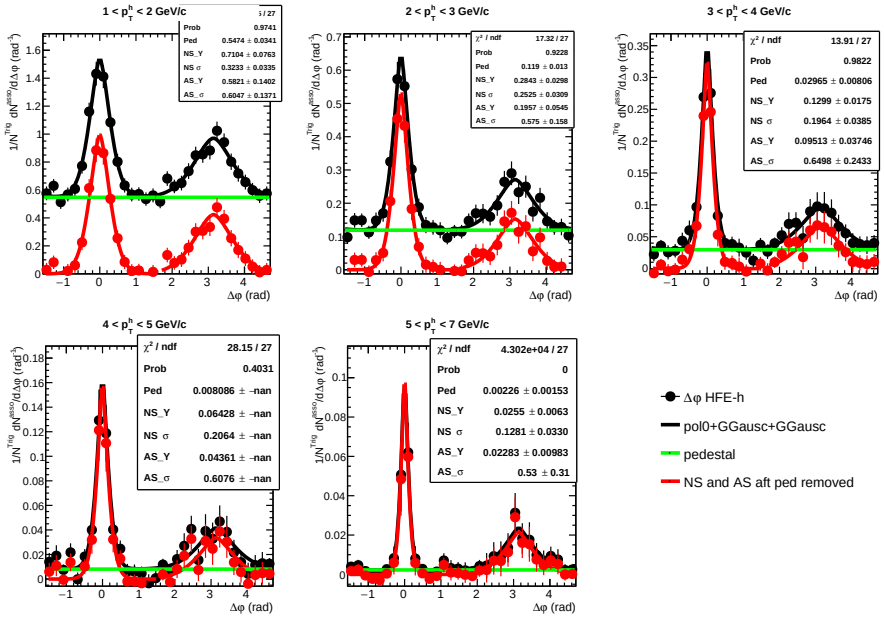

Figure A.9: $\Delta\varphi$ distribution fitted with "WL" option by generalized Gaussian function in pp events.